
Electromagnetic Observables and Open-Shell Nuclei from the In-Medium No-Core Shell Model

Vom Fachbereich Physik
der Technischen Universität Darmstadt

zur Erlangung des Grades
Doctor rerum naturalium (Dr. rer. nat.)

**genehmigte Dissertation von
Klaus Vobig**

Erstgutachter: Prof. Dr. Robert Roth
Zweitgutachter: Prof. Dr. Achim Schwenk

Darmstadt 2019 (D17)



TECHNISCHE
UNIVERSITÄT
DARMSTADT

Vobig, Klaus: Electromagnetic Observables and Open-Shell Nuclei from the In-Medium No-Core Shell Model

Dissertationsort: Darmstadt, Technische Universität Darmstadt

Veröffentlichungsjahr der Dissertation auf TUprints: 2020

URN: urn:nbn:de:tuda-tuprints-113758

Tag der mündlichen Prüfung: 28.10.2019



Veröffentlicht unter CC BY-NC-SA 4.0 International

<http://creativecommons.org/licenses/by-nc-sa/4.0/>

Abstract

We present extensions and new developments of the in-medium no-core shell model (IM-NCSM), which is a novel *ab initio* many-method that merges the multi-reference in-medium similarity renormalization group (MR-IM-SRG) with the no-core shell model (NCSM)—two complementary and successful *ab initio* many-body methods.

Within the IM-NCSM framework, the MR-IM-SRG employs a correlated NCSM reference state and unitarily transforms observables such that the reference state is decoupled. Consequently, the model-space convergence of a subsequent NCSM calculation is substantially accelerated—demonstrating the power of the IM-SRG decoupling scheme—and the IM-NCSM can treat nuclei that are out of reach for traditional NCSM calculations.

In earlier applications we already employed the IM-NCSM for addressing scalar observables w.r.t. ground and excited states in even open-shell nuclei, however, this initial formulation of the IM-NCSM had several restrictions that we eliminate in this work.

Due to the spherical formulation of the IM-SRG equations—which is mandatory from a computational point of view—the total angular momentum of the reference state is required to vanish and, thus, the IM-NCSM was restricted to the treatment of even nuclei. The particle-attached/particle-removed extension overcomes this restriction and makes odd nuclei accessible. Furthermore, the spherical formulation of the IM-SRG equations did not account for non-scalar operators and, therefore, the consistent transformation of electromagnetic observables was not possible. By deriving and implementing the IM-SRG equations corresponding to non-scalar observables, we open up the possibility to calculate electromagnetic observables from the IM-NCSM. These observables are sensitive to different aspects of the wave functions and, therefore, ideal for validating theoretical models and new opportunities for fruitful collaborations with experimentalists are opened up. For the transformation of observables we implemented a Magnus-type transformation, which determines the generator for the IM-SRG transformation and greatly reduces the computational effort.

Considering numerical applications, we employ the IM-NCSM for the calculation of ground-state energies, excitation energies, radii, magnetic dipole moments, electric quadrupole moments, $B(M1)$ transitions, and $B(E2)$ transitions, where we study various medium-mass nuclei up to calcium isotopes. These calculations are already converged at very small model-space

sizes—showing the great advantage of the IM-NCSM—and the results are compatible with large-scale NCSM calculations. These applications demonstrate that the IM-NCSM is now capable of addressing the full range of nuclear structure observables—including spectroscopic and electromagnetic observables—in fully open-shell nuclei.

Zusammenfassung

In dieser Arbeit stellen wir Erweiterungen und Neuentwicklungen des In-Medium No-Core Shell-Modell (IM-NCSM) vor. Das IM-NCSM ist eine neuartige Ab-Initio-Vielteilchenmethode, welche die Multi-Reference In-Medium Similarity Renormalization Group (MR-IM-SRG) mit dem No-Core-Shell-Modell (NCSM) vereint, wobei ein wesentlicher Aspekt des IM-NCSM die Komplementarität dieser beiden Methoden ist.

Im Rahmen des IM-NCSM verwendet die MR-IM-SRG einen korrelierten NCSM-Referenzzustand und transformiert Observablen derart, dass eine Entkopplung des Referenzzustands erreicht wird. Folglich ist die Modellraumkonvergenz einer nachfolgenden NCSM-Berechnung wesentlich beschleunigt und das IM-NCSM kann Kerne behandeln, die für traditionelle NCSM-Berechnungen unerreichbar sind.

In früheren Anwendungen wurde das IM-NCSM bereits zur Berechnung von skalaren Observablen bezüglich des Grundzustands und angeregten Zustände in Kernen mit offenen Schalen eingesetzt. Diese erste Formulierung des IM-NCSM hatte jedoch mehrere Einschränkungen, welche durch diese Arbeit beseitigt werden.

Aufgrund der sphärischen Formulierung der IM-SRG-Gleichungen – welche unerlässlich für eine rechen technisch effiziente Implementierung ist – muss der Gesamtdrehimpuls des Referenzzustandes verschwinden, woraus folgt, dass das IM-NCSM auf die Behandlung von geraden Kernen beschränkt war. Die Particle-Attached/Particle-Removed Erweiterung des IM-NCSM überwindet diese Einschränkung und macht die Behandlung von ungerade Kernen möglich. Darüber hinaus war die sphärische Formulierung der IM-SRG-Gleichungen eingeschränkt auf skalare Observablen. Folglich war eine Transformation von elektromagnetischen Observablen nicht möglich. Mittels einer Herleitung und Implementierung von IM-SRG-Gleichungen, welche den sphärischen Tensorrang der zu transformierenden Observable variabel hält, eröffnen wir die Möglichkeit elektromagnetische Observablen mittels des IM-NCSM zu berechnen. Diese Observablen sprechen auf andere Aspekte der Wellenfunktion an und sind daher von großem Nutzen für die Validierung von theoretischen Modellen und bieten neuen Möglichkeiten für Kollaborationen mit Experimentatoren. Für die Transformation von Observablen haben wir eine Magnus-artige Transformation implementiert, welche den Generator der IM-SRG Transformation bestimmt und den Rechenaufwand erheblich reduziert.

In numerischen Anwendungen verwenden wir das IM-NCSM für die Berechnung von Grundzustandsenergien, Anregungsenergien, Radien, magnetischen Dipolmomenten, elektrischen Quadrupolmomenten, $B(M1)$ Übergängen und $B(E2)$ Übergängen, bei denen wir verschiedene mittelschwere Kerne bis zu Kalziumisotopen untersuchen. Diese Berechnungen sind bereits bei sehr geringem Modellraumgrößen konvergiert – was den großen Vorteil des IM-NCSM zeigt – und die Ergebnisse sind kompatibel mit großskaligen NCSM-Berechnungen. Diese Anwendungen zeigen, dass das IM-NCSM nun in der Lage ist, die gesamte Fülle von Kernstrukturobservablen zu berechnen – einschließlich spektroskopischer und elektromagnetischer Observablen – in Kernen mit vollständig offenen Schalen.

Acronyms and Abbreviations

| | |
|-------------------|--|
| 3N | three-nucleon |
| BLAS | basic linear algebra subprograms |
| CC | coupled cluster |
| CCSD | coupled cluster with singles and doubles |
| CI | configuration interaction |
| EFT | effective field theory |
| HF | Hartree-Fock |
| HFB | Hartree-Fock-Bogoliubov |
| HO | harmonic oscillator |
| IM-SRG | in-medium similarity renormalization group |
| IT-NCSM | importance-truncated no-core shell model |
| LO | leading order |
| MCPT | multi-configurational perturbation theory |
| NCSM | no-core shell model |
| NLO | next-to-leading order |
| N ² LO | next-to-next-to-leading order |
| NN | nucleon-nucleon |
| NO2B | normal-ordered two-body |
| nph | <i>n</i> -particle <i>n</i> -hole |
| ODE | ordinary differential equation |
| PA/PR | particle-attached/particle-removed |
| QCD | quantum chromodynamics |
| RKF | Runge Kutta Fehlberg |
| SRG | similarity renormalization group |
| VSSM | valence-space shell model |

Contents

| | |
|---|-----------|
| 1. Introduction | 1 |
| 2. No-Core Shell Model | 7 |
| 2.1. Basic Concepts | 8 |
| 2.2. Symmetries | 11 |
| 2.3. Importance Truncation | 12 |
| 2.4. Single-Particle Basis Optimizations | 14 |
| 3. Normal Order | 17 |
| 3.1. Second Quantization | 18 |
| 3.2. Single-Reference Normal Order | 19 |
| 3.3. Multi-Reference Normal Order | 22 |
| 3.4. Representation Changes | 25 |
| 3.5. Normal-Ordered Two-Body Approximation | 26 |
| 4. Multi-Reference IM-SRG—Basics | 29 |
| 4.1. Similarity Renormalization Group | 29 |
| 4.1.1. Free-Space SRG | 32 |
| 4.2. In-Medium SRG—Motivation and General Concepts | 33 |
| 4.3. Reference States | 37 |
| 4.4. IM-SRG(2) | 38 |
| 4.5. Magnus Expansion—General Concepts | 40 |
| 4.6. Magnus(2) | 43 |
| 4.7. Generators for the IM-SRG | 49 |
| 4.8. Applications—Single-Reference IM-SRG | 52 |
| 5. Multi-Reference IM-SRG—Commutator Evaluation | 57 |
| 5.1. Spherical Natural Orbitals and m -Scheme Equations | 58 |
| 5.2. Angular Momentum Theory | 63 |
| 5.3. m -Scheme Equations—Revisited | 70 |
| 5.4. Diagrammatic Approach | 73 |
| 5.5. Coupled and Reduced Matrix Elements—Conventions and Formulas | 77 |

| | | |
|-----------|--|------------|
| 5.6. | Spherical Equations | 81 |
| 5.6.1. | Derivation Zero-Body Part | 81 |
| 5.6.2. | Derivation One-Body Part | 83 |
| 5.6.3. | Derivation Two-Body Part | 95 |
| 5.6.4. | Remarks | 101 |
| 6. | In-Medium No-Core Shell Model | 103 |
| 6.1. | Complementarity and Correlations | 103 |
| 6.2. | Remarks on Hamiltonians | 105 |
| 6.3. | Stages of the IM-NCSM | 106 |
| 6.4. | The IM-NCSM: An Illustration | 108 |
| 6.5. | Generator Optimizations | 112 |
| 6.5.1. | Generalized Particle-Hole Excitations | 112 |
| 6.5.2. | Decoupling pattern—Conventional | 113 |
| 6.5.3. | Decoupling pattern—IM-NCSM | 115 |
| 6.5.4. | Construction of Generator Matrix Elements | 117 |
| 6.5.5. | Numerical Applications | 118 |
| 6.6. | Oxygen Chain and Impact of Reference Space | 122 |
| 6.7. | Particle-Attached/Particle-Removed | 128 |
| 6.7.1. | Outline of Approach | 128 |
| 6.7.2. | Numerical Applications—A simple Example | 129 |
| 6.7.3. | Numerical Applications—Shell-Closure Effects | 131 |
| 6.7.4. | Conclusion | 135 |
| 6.8. | Importance Truncation and Reference States | 135 |
| 6.9. | Evolution of Observables—Concepts | 140 |
| 6.9.1. | Theoretical Foundation of the Radius Operator | 141 |
| 6.9.2. | Theoretical foundation of Electromagnetic Observables | 142 |
| 6.10. | Evolution of Observables—Applications | 145 |
| 6.10.1. | Hierarchy Inversion | 154 |
| 6.10.2. | Observables and Particle-Attached/Particle-Removed | 158 |
| 7. | In-Medium No-Core Shell Model—Applications and Outlook | 161 |
| 7.1. | Oxygen and Fluorine Chain | 161 |
| 7.2. | New Generations of Chiral Interactions | 167 |
| 7.2.1. | Regulator Effects: Local vs. Non-Local Regulators | 169 |
| 7.2.2. | Study of Energy-Radius Correlations | 170 |
| 7.3. | Oxygen Chain—Revisited | 172 |
| 7.4. | Neutron-Rich Fluorine Isotopes | 174 |
| 7.5. | Neon Chain | 176 |
| 8. | Summary and Outlook | 181 |
| A. | Effective Valence-Space Interactions from the In-Medium SRG | 185 |

| | |
|--|------------|
| B. Details on the Implementation of the In-Medium SRG | 191 |
| B.1. Spherical Equations for Representation Change | 192 |
| B.2. Numerical Solution of ODEs | 192 |
| B.3. Commutator Equations and Matrix Products | 193 |
| C. Experimental Data | 197 |
| Bibliography | 199 |

Introduction

Theoretical nuclear physics aims for an understanding of the structure and dynamics of nuclei from first principles. To this end, two intertwined problems have to be addressed: The construction of a nuclear Hamiltonian and the solution of the many-body Schrödinger equation—both tasks are far from trivial.

For the construction of a nuclear Hamiltonian, we face the problem that the protons and neutrons a nucleus consists of are no fundamental particles—they are compounds of quarks and gluons—and, therefore, the nuclear interaction is not fundamental. Instead, the underlying theory is quantum chromodynamics (QCD)—the theory of the strong interaction between the colored quarks and gluons.

Directly deriving a nucleon-nucleon interaction from the underlying theory is not possible since QCD is highly non-perturbative in the relevant low-energy regime—which is also known as the confinement of quarks and gluons into color-neutral hadrons.

However, one may construct a chiral effective field theory (χ EFT) for low-energy QCD, where one usually follows the suggestion of Weinberg [Wei79] and writes down the most general Lagrangian that is consistent with the general symmetries of QCD—especially including the broken chiral symmetry. As we are aiming for an effective theory describing the low-energy regime of nuclear physics, it is the nucleons and pions—instead of quarks and gluons—that are the relevant degrees of freedom. In this context, pions are the Goldstone bosons of the spontaneously broken chiral symmetry, which are not massless as chiral symmetry is also *explicitly* broken. Heavier mesons and nucleon resonances, however, are “integrated out” and the effects of high-energy physics are taken into account by the so-called low-energy constants (LECs), which have to be determined through a fit to experimental data.

A problem that arises within such an χ EFT is that the Lagrangian still contains an infinite number of terms. For that purpose, chiral perturbation theory (χ PT) allows for ordering these infinitely many terms w.r.t. their respective importance via an expansion in powers of $(\frac{Q}{\Lambda_\chi})^\nu$, where Q is the characteristic momentum or pion mass, $\Lambda_\chi \approx 1 \text{ GeV}$ is the chiral symmetry

breaking scale, and ν is the chiral order. As a consequence, each order ν only contains a finite number of contributions [Wei90]. The first orders arising within this power counting scheme are referred to as leading order (LO, $\nu = 0$), next-to-leading order (NLO, $\nu = 2$), next-to-next-to-leading order (N²LO, $\nu = 3$) and so forth, where contributions at $\nu = 1$ vanish due to parity and time-reversal symmetry. The great advantage of χ PT is that it allows for a consistent and systematic choice of interaction terms and explains the empirically observed hierarchy of nuclear forces like, e.g., two-nucleon (NN) interactions are more important than three-nucleon (3N) interactions. Another advantage of interactions derived from χ EFT is their direct connection to the underlying theory of QCD and the natural appearance of particular many-body forces at a specific order. Therefore, interactions derived from χ EFT are systematically improvable and, thus, in accordance with the *ab initio* spirit. In contrast, realistic phenomenological potentials like, e.g., the CD-Bonn [Mac01] and Argonne V18 [WSS95] lack this connection to an underlying fundamental theory and the inclusion of 3N forces—which has been shown to be mandatory for an adequate description of nuclei—is less systematic. For years, there was only a very limited selection of chiral interactions available such that we usually employed the NN interactions at N³LO by Entem and Machleidt [EM03] and 3N interactions at N²LO by Navratil [Nav07]. However, applying these interactions for nuclei beyond the lower *sd*-shell revealed their shortcomings as ground-state energies and radii significantly deviate from experimental data [Bin+14].

During the recent past, there is a new dynamic in developments of interactions derived from χ EFT. To give a few examples, there are interactions by Ekström et al. [Eks+15], which use NN and 3N interactions at N²LO and include many-body observables for the determination of its LECs—in contrast to the traditional approach, where only few-body data is employed. Furthermore, there is the family of interactions from Entem, Machleidt, and Nosyk [EMN17], which consist of NN interactions up to N⁴LO, together with a non-local 3N interaction at N³LO [Heb+15]—allowing for a study of the chiral convergence. Lastly, there is yet another family of interactions that is developed within the LENPIC collaboration. For the construction of these interactions, semi-local regulators are employed and one of the goals is to study the convergence of the chiral expansion and to quantify theoretical uncertainties due to truncations of the chiral expansion through an order-by-order analysis [Bin+16; Bin+18; Epe+19]. This demonstrates that there is a remarkable effort for developing the newest generations of chiral interactions, which eventually paves the way for a new era of high-precision theoretical nuclear physics in the medium-mass regime.

The nuclear Hamiltonian, however, is not the only aspect in the context of calculations of nuclear structure observables: We still have to solve the Schrödinger equation, which cannot be solved exactly and we have to employ controllable approximations. However, a well-known property of realistic nuclear interactions are strong tensor forces and strong short-range repulsions leading to strong couplings of high and low-momentum modes. Many-body calculations with these “bare” interactions pose a major challenge as the convergence of many-body methods that rely on a basis expansion is slowed down—or even inhibited. The free-space similarity renormalization group (SRG) [BFP07; BFS10; RNF10] tries to remedy this problem by aiming for a *generic* decoupling of low and high momenta. As the SRG is usually carried out

in two and three-body space [Rot+14], the improved convergence behavior is accompanied by an error due to the neglect of SRG-induced higher-order contributions.

In recent years ab initio approaches for the solution of the nuclear many-body problem were developed at an exciting pace and tremendous progress has been made in this area. Broadly speaking, the many-body approaches we will be mostly dealing with can be separated into three classes: shell-model-type approaches, medium-mass methods, and hybrid methods.

Two important representatives of shell-model-type approaches are the valence-space shell model [KB66; Cau+05; Cor+14] as well as the ab initio no-core shell model (NCSM) [Nav+07; Nav+09; Bro01; BNV13], which numerically solve a large-scale matrix eigenvalue problem within a model space spanned by a set of many-body states. Thereby, they give direct access to the eigenstates of the Hamiltonian such that we are able to obtain ground and excited-state observables on equal footing. Aiming at an *exact* ab initio solution of the nuclear many-body problem, the NCSM is one of the most successful methods available, however, it is limited by its factorial scaling w.r.t. particle number of the nucleus considered and, therefore, its range of applicability is restricted to p -shell—or lower sd -shell nuclei in the case of the importance-truncated NCSM (IT-NCSM) [RN07; Rot09].

The in-medium similarity renormalization group (IM-SRG) [TBS11; TBS12; Her+13a], the coupled cluster method [Wlo+05; Hag+07; Hag+08; Bin+13b; Bin+13a], and the self-consistent Green's functions approach [CBN13; Som+14] are representatives of the class of ab initio medium-mass methods. These methods employ fundamentally different truncation patterns than shell-model-like approaches and scale much more mildly w.r.t. particle numbers making medium-mass nuclei accessible. However, in their basic formulation they are restricted to the description of ground-state observables of nuclei with shell or sub-shell closures.

It is the IM-SRG, which this work will be mostly dealing with, and that distinguishes itself by the simplicity of its basic concept and flexibility. The IM-SRG is a rather new many-body method employing the SRG framework for the unitary transformation of the Hamiltonian such that a particular many-body reference state is decoupled from particle-hole excitations, where the reference state is usually chosen as an approximation for the ground state of the nucleus under consideration. The single-reference version of the IM-SRG—being restricted to single Slater determinant reference states and, therefore, the calculation of ground states in closed-shell nuclei—was first proposed by Tsukiyama et al. in [TBS11]. However, in [Her+13a] Hergert et al. introduced the multi-reference IM-SRG (MR-IM-SRG), which generalizes the IM-SRG framework to correlated reference states and, therefore, open-shell nuclei are becoming accessible. Using a particle-number projected Hartree-Fock-Bogoliubov (HFB) reference state, the multi-reference IM-SRG was then successfully employed for even-mass isotopes in semi-magic chains in [Her+13a; Her+14].

Lastly, there is also the class of hybrid methods, which merge shell-model-like approaches with medium-mass methods with the aim to merge the individual advantages, while overcoming most of the shortcomings. Over the past few years, many hybrid methods have entered the stage of ab initio many-body methods showing their great potential. The valence-space

shell model relies on effective valence-space interactions, which, traditionally, are constructed phenomenologically [KB66; Cau+05; Cor+09]. However, both the IM-SRG [TBS12; Bog+14; Str+16; Str+17] and the coupled cluster method [Jan+16] open up the possibility to derive non-perturbative effective valence-space interactions within an *ab-initio* framework. Apart from hybrid methods that are based on the valence-space shell model, various innovative NCSM-based hybrid methods were developed like, e.g., the NCSM-PT [Tic+18], which consists of an NCSM calculation in a small model space together with a low-order many-body perturbation theory correction for capturing residual correlations.

Finally, we merged the MR-IM-SRG with the NCSM—which we refer to as IM-NCSM. Within the IM-NCSM framework, the MR-IM-SRG employs a correlated NCSM reference state and transforms the Hamiltonian and other observables in such a way that the model-space convergence of a subsequent NCSM calculation is substantially accelerated. Through a consistent evolution of observables, we gain direct access to observables w.r.t. ground and excited states.

In earlier applications [Geb+16; Geb17], we employed the IM-NCSM for addressing ground and excited-state observables in even open-shell nuclei. However, there were two major restrictions that are eliminated through this work: Firstly, only scalar observables could be consistently evolved due to the spherical formulation of the IM-SRG equations—which is mandatory from a computational point of view. However, in order to meet the requirements for modern many-body methods, the possibility to treat non-scalar observables is essential: Electromagnetic decay processes usually correspond to such non-scalar operators and—being sensitive to different aspects of the wave functions—these processes may substantially contribute to the validation of our theoretical models. To this end, we overcome this restriction of the IM-SRG by explicitly accounting for eventual non-scalar contributions during the angular momentum coupling of the IM-SRG commutator equations. Secondly, our implementation of the IM-SRG is restricted to reference states with vanishing total angular momentum so that only even nuclei may be treated. While this restriction is hard to overcome in practical applications, we established an extension of the IM-NCSM that allows a treatment of odd nuclei after all. With these and other developments and investigations that are presented in this work, the IM-NCSM is now able to study the full range of nuclear structure observables in fully open-shell medium-mass nuclei.

This work is organized as follows: In chapter 2 we discuss the most important aspects of the NCSM, which includes the IT-NCSM and single-particle bases other than the harmonic oscillator. The basic concepts of single and multi-reference normal order and related approximation schemes—which are a fundamental ingredient for the formulation of the IM-SRG—are addressed in chapter 3. Throughout chapter 4 we cover the basic concepts of the IM-SRG: After a brief summary of the general SRG framework and the free-space SRG, we discuss possible choices for the reference states, the IM-SRG(2), the Magnus formulation, the construction of adequate generators, and an illustrative application of the single-reference IM-SRG. In chapter 5 we present the more involved details of commutator evaluations—which are the computationally most time-consuming part of the IM-SRG. After discussing the *m*-scheme

commutator equations, we give a summary of angular momentum theory and spherical tensor operators, followed by a derivation of the spherical commutator equations via diagrammatic angular momentum coupling techniques. In chapter 6 the IM-NCSM and most of our new developments are discussed. After illustrative applications of the IM-NCSM and an explanation of the details of the IM-NCSM framework, we will address several methodical improvements, extensions, and investigations: the optimization of generators, studies of the dependence on the reference state, the particle-attached/particle-removed extension for the treatment of odd nuclei, and the calculation of observables—including electromagnetic transitions. After having studied the characteristics of the IM-NCSM, we apply this many-body method for an investigation of oxygen, fluorine, and neon isotopes and explore the dependence on the chiral interaction in chapter 7. Finally, a summary and an outlook is given in chapter 8.

No-Core Shell Model

Aiming at an *exact ab initio* solution of the nuclear many-body problem employing state-of-the-art realistic nuclear interactions, the no-core shell model (NCSM) is one of the most successful methods available [Nav+09; BNV13]. Formally, the NCSM belongs to the class of configuration interaction (CI) approaches which numerically solve a large-scale matrix eigenvalue problem within a model space spanned by a set of many-body states and, thereby, give access to the eigenstates of the Hamiltonian. Conceptionally, the NCSM is a rather simple approach from which we are able to obtain ground and excited-state observables on equal footing. However, the NCSM is limited by its factorial scaling w.r.t. particle numbers of the nuclei considered and, therefore, its range of applicability is restricted to p -shell and lower sd -shell nuclei. Even though it may not be applied to nuclei beyond the lower sd shell in its standard formulation, the NCSM is a many-body method of greatest importance within theoretical nuclear physics. In the context of other many-body methods with more involved truncation patterns, due to its exact nature the NCSM sets a standard that other methods have to compete against and which allows us to quantify the effects of inherent truncations on numerical results.

Three complementary remedies for the aforementioned limitations of the NCSM, which allow us to significantly extend the reach of the NCSM and which may be used individually or in conjunction with each other are presented throughout this work. Firstly, we will be addressing the so-called importance-truncated NCSM (IT-NCSM) [Rot09] in section 2.3 which employs low-order multiconfigurational perturbation theory for discarding basis states that are irrelevant for the description of specific eigenstates of a Hamiltonian and, thereby, significantly reduces the model-space size. Secondly, we will introduce and motivate the natural orbitals [Tic+19] in section 2.4 as an alternative single-particle basis that exhibits greatly improved convergence properties in NCSM calculations. Lastly, we will address so-called hybrid methods, i.e., combinations of the NCSM with other “traditional” many-body methods. The discussion of this aspect is not confined to this chapter but a large part of this work is dedicated to the in-depth discussion of the foundation, details, and numerical application of such

an hybrid method: the so-called in-medium no-core shell model (IM-NCSM). It combines the multi-reference in-medium SRG (MR-IM-SRG) [Her+13a] with the NCSM in order to overcome most of their individual shortcomings while preserving most of their advantages. Over the past few years, many other NCSM-based hybrid methods have entered the stage of *ab initio* many-body methods and were successfully applied in the context of nuclear structure theory like, e.g., the NCSM-PT [Tic+18], showing the great potential that originates from future developments and advancements of such hybrid methods.

2.1. Basic Concepts

Considering the general quantum properties of a nucleus, it can be described as a fermionic A -body system. As such, it is associated with the antisymmetric A -body Hilbert space $\mathcal{H}_A^{\text{a.s.}}$ which solely consists of antisymmetric many-body states. Therefore, the NCSM employs a model space spanned by a set of Slater determinants $\{|\phi_i\rangle\}$, i.e., antisymmetrized product states, where each Slater determinant $|\phi_i\rangle$ consists of A harmonic oscillator¹ single-particle states $|p_i\rangle$. Therefore, an arbitrary Slater determinant $|\phi\rangle$ may be written as

$$|\phi\rangle = |p_1 p_2 \dots p_A\rangle = \sqrt{A!} \hat{\mathcal{A}}(|p_1\rangle \otimes |p_2\rangle \otimes \dots \otimes |p_A\rangle), \quad (2.1.1)$$

where $\hat{\mathcal{A}}$ denotes the well-known antisymmetrizer. Note that the set of all Slater determinants forms a basis of $\mathcal{H}_A^{\text{a.s.}}$. Each single-particle state $|p\rangle$ can be written as

$$|p\rangle = |n(ls)j m_j t m_t\rangle = |nlj m_j m_t\rangle, \quad (2.1.2)$$

where n denotes the radial quantum number², l denotes the orbital angular momentum, s refers to the spin, j stands for the total ls -coupled angular momentum, m_j refers to the projection quantum number with regard to j , t denotes the isospin, and m_t its associated projection. Note that, for brevity, we usually omit the spin s and isospin t information as both are simply $\frac{1}{2}$ for nucleons. Additionally, the principal quantum number is defined as $e = 2n + l$ such that the harmonic oscillator single-particle energy is given through $\epsilon = (e + \frac{3}{2})\hbar\Omega$.

Without any truncation pattern on either the single-particle basis or the many-body basis, the many-body model-space dimension would be infinite. Considering the NCSM, the model space is solely truncated through an upper limit on the unperturbed excitation energy of each many-body basis state of $N_{\text{max}}\hbar\Omega$. For illustrating this truncation scheme, let us, firstly, define the energy E of a Slater determinant as the sum of the single-particle harmonic oscillator

¹Strictly speaking, the very notion of the NCSM goes hand in hand with the harmonic oscillator basis which has some striking features as we will see in a moment. However, in the context of this work the discussion of this basic formulation of the NCSM is mostly of educational value: It serves as a reasonable starting point for extending the NCSM with regard to other single-particle bases. This extension is straightforward and practical applications throughout this work will usually be based on other single-particle bases than the harmonic oscillator.

²We employ the convention $n = 0, 1, 2, \dots$

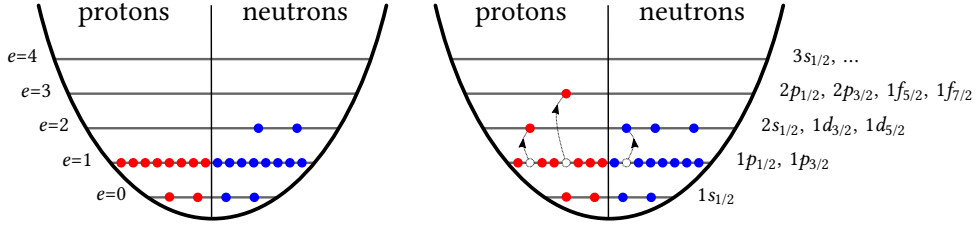


Figure 2.1.: This figure schematically illustrates the truncation scheme that is employed for the construction of an N_{\max} -truncated model space as it is characteristic for the NCSM approach. On the left-hand side one of the base determinants of ^{18}O is depicted: 8 protons and 8 neutrons are filling up the $1s$ and $1p$ shell, respectively, and 2 neutrons are only partially filling up the $2s$ and $1d$ shell. Due to the fact that there are multiple energetically degenerate determinants that only differ by the specific orbitals the two upper neutrons are occupying the $N_{\max} = 0$ model space of ^{18}O is multidimensional. The right-hand side shows an example for a Slater determinant with $N = 4$ harmonic oscillator excitation quanta, i.e., a basis state which would be included within a model space with $N_{\max} \geq 4$.

energies. Secondly, we define the *base determinant* $|\phi_0\rangle$ as a determinant which minimizes this energy. Employing the previous two definitions, the *unperturbed excitation energy* E^* of a determinant $|\phi_i\rangle$ may now be easily defined as the energy difference between itself and the base determinant $|\phi_0\rangle$. Furthermore, the number of harmonic oscillator excitation quanta N of a determinant is given through $N = \frac{E^*}{\hbar\Omega}$. Using this definition, it will prove as useful to employ $|\phi_i^N\rangle$ as a short-hand notation for referring to the i -th NCSM basis state with exactly N harmonic oscillator excitation quanta. Therefore, the N_{\max} -truncated model space can now be written as the span of its many-body basis

$$\mathcal{M}^{N_{\max}} = \text{span}\left(\left\{|\phi_i^N\rangle \mid N \leq N_{\max}\right\}\right). \quad (2.1.3)$$

The corresponding eigenstates obtained from solving the eigenvalue problem are given in terms of superpositions of basis determinants

$$|\psi_i^{N_{\max}}\rangle = \sum_{|\phi_j\rangle \in \mathcal{M}^{N_{\max}}} c_{ij} |\phi_j\rangle, \quad (2.1.4)$$

where c_{ij} may be associated with the overlap between the eigenstate $|\psi_i^{N_{\max}}\rangle$ and the NCSM basis state $|\phi_j\rangle$. The characteristic truncation scheme of the NCSM is further illustrated by means of fig. 2.1: It depicts the base determinant as well as a determinant with four harmonic oscillator excitation quanta with regard to ^{18}O .

Note that, as it is only the N_{\max} truncation scheme of the model space that separates the NCSM approach from an exact treatment of the Schrödinger equation, we have to study the impact of this N_{\max} truncation on numerical results, i.e., assess convergence rates w.r.t. N_{\max} and eventually assign meaningful uncertainties.

A striking advantage of the harmonic oscillator basis within the context of the NCSM is that it leads to a separation of intrinsic and center-of-mass degrees of freedom, whereby the intrinsic part of these eigenstates is translationally invariant.³ In other words, any eigenstate $|\psi\rangle$ factorizes into an intrinsic part $|\psi_{\text{int}}\rangle$ and center-of-mass $|\psi_{\text{cm}}\rangle$ part

$$|\psi\rangle = |\psi_{\text{int}}\rangle \otimes |\psi_{\text{cm}}\rangle, \quad (2.1.5)$$

which only depend on relative and center-of-mass coordinates and momenta, respectively. Furthermore, eigenstates with the same intrinsic component but different center-of-mass components are degenerate. For removing eigenstates with an excited center-of-mass component from our spectrum, we follow the scheme outlined in [RGP09], which eventually goes back to Gloeckner and Lawson in [GL74], and add a center-of-mass Hamiltonian that purely acts on the center-of-mass part of our wavefunction

$$\hat{H}_{\text{tot}} = \hat{H}_{\text{int}} + \lambda_{\text{cm}} \hat{H}_{\text{cm}}. \quad (2.1.6)$$

The center-of-mass Hamiltonian may be constructed as

$$\hat{H}_{\text{cm}} = \frac{\hat{\mathbf{P}}^2}{2Am} + \frac{m\Omega A}{2} \hat{\mathbf{R}}^2 - \frac{3}{2} \hbar\Omega, \quad (2.1.7)$$

where m refers to the nucleon mass and $\hat{\mathbf{P}}^2$ and $\hat{\mathbf{R}}^2$ refer to the center-of-mass momentum and coordinate, respectively. It is noteworthy that the last term within the definition of \hat{H}_{cm} ensures that the center-of-mass ground-state energy is shifted to zero. By using non-zero values for λ_{cm} and solving the eigenvalue problem for \hat{H}_{tot} , we have resolved the aforementioned degeneracy and are shifting eigenstates with an excited center-of-mass component to higher eigenvalues, i.e., removing those eigenstates from the energetically lower part of the spectrum.

We would like to remark that a problem that comes along with any single-particle basis other than the harmonic oscillator basis when employed in the NCSM is that the factorization of intrinsic and center-of-mass degrees of freedoms is not exact anymore and only recovered for $N_{\text{max}} \rightarrow \infty$, i.e., the exact solution. While the diagonalization is still based on a total Hamiltonian given through eqs. (2.1.6) and (2.1.7), we have to be careful regarding the specific choice for the scaling parameter λ_{cm} . This is due to the fact that the factorization of eigenstates is not exact anymore: λ_{cm} has to be chosen large enough such that approximately degenerate eigenstates are shifted upwards in the spectrum and it should be as small as possible such that its action on dominantly intrinsic eigenstates is kept at a minimum. Two common diagnostics for assessing the center-of-mass impact on an eigenstate $|\psi\rangle$ is the calculation and tracking of $\langle \psi | \hat{H}_{\text{cm}} | \psi \rangle$ and the behavior of $\langle \psi | \hat{H}_{\text{tot}} | \psi \rangle$ under variations of λ_{cm} . Considering numerical calculations⁴, we have found that the optimum for λ_{cm} lies in the range of 0.2 to 1.

³We will discuss the case for single-particle bases other than the harmonic oscillator later on.

⁴Within this work the NCSM is usually employed within the context of the IM-NCSM. As a consequence, we do not employ the harmonic oscillator single-particle basis but a more abstract “IM-SRG basis”.

A further advantage of the NCSM approach is its versatility: We are able to calculate ground and low-lying excited states and, as we have direct access to the eigenstates of the Hamiltonian, a large range of nuclear structure observables like, e.g., energies, radii and transitions may be obtained with little effort. Also the extension to three-body or even four-body interactions is straightforward—in contrast to other many-body methods like, e.g., the IM-SRG.

The only limitation of the NCSM is the factorial growth of the model-space size w.r.t. the particle number A and excitation energy $N_{\max}\hbar\Omega$. As we are not aiming at a full diagonalization of the Hamilton matrix but are only interested in a few low-lying eigenstates of the Hamiltonian we are employing a Lanczos-type algorithm, which massively reduces the computational effort and makes calculations with many-body model space sizes up to 10^9 or even 10^{10} [MVS09] possible. However, considering, e.g., ^{16}O even such huge model-space sizes are already reached at around $N_{\max} = 10$ which is usually not sufficient for obtaining converged results w.r.t. N_{\max} . Therefore, such “traditional” NCSM calculations are limited to the description of nuclei with mass numbers $A \leq 16$ [Bin+18].⁵

2.2. Symmetries

For further reducing the model-space size and, as a consequence, extend the reach of NCSM calculations, we may take rotational symmetry and parity conservation into account.

As the Hamiltonian is rotationally invariant it follows that the eigenstates are degenerate w.r.t. the projection quantum number M_J of the associated A -body total angular momentum J . As M_J is an additive quantum number it is simply given through the sum of the single-particle projection quantum numbers

$$M_J = \sum_{i=1}^A m_{j_i}, \quad (2.2.1)$$

and we can project the model space \mathcal{M} onto one specific M_J . Assuming that we do not want to impose any further restrictions on the total angular momenta of the eigenstates contained in the model space, we are usually using the lowest possible absolute value for M_J , i.e., $M_J = 0$ and $M_J = \frac{1}{2}$ for nuclei with even and odd particle numbers, respectively.⁶

Furthermore, the Hamiltonian is parity conserving and, thus, we may even further reduce the model-space size by including positive or negative parity basis states only. The parity of a Slater determinant is given through the product of the parities of the single-particle states it

⁵These numbers already refer to calculations with free-space SRG (see chapter 4) transformed interactions. Calculations with “bare” interactions limit the range of applicability to even lighter nuclei.

⁶Note that a model space restricted to, e.g., $M = 1$ does not contain eigenstates with $J = 0$ anymore.

consists of. As the parity of a single-particle state $|nljm_j m_t\rangle$ is given through $(-)^l$ the parity Π of a determinant can be written as

$$\Pi = \prod_{i=1}^A (-)^{l_i} . \quad (2.2.2)$$

Note that we are usually restricting the model space to states with *natural* parity— the parity of the uncorrelated ground state predicted by the naïve shell model— as opposed to basis states with *unnatural* parity. Due to the opposite parity of two determinants which are associated with consecutive numbers of excitation quanta, N and $N + 1$, respectively, the inclusion of parity conservation implies that the model space exclusively consists of basis states with either an even or odd number of excitation quanta N and, as a consequence, the truncation parameter N_{\max} has to be increased in steps of two.

Summarizing, the N_{\max} -truncated model space $\mathcal{M}_{M_J, \Pi}^{N_{\max}}$ that takes parity conservation and rotational invariance into account and is used for representing the underlying Hamiltonian and for solving the large-scale matrix eigenvalue problem, can now be written as

$$\mathcal{M}_{M_J, \Pi}^{N_{\max}} = \text{span} \left(\left\{ |\phi_i^N\rangle \mid N \leq N_{\max}, |\phi_i^N\rangle \text{ has parity } \Pi \text{ and projection } M_J \right\} \right), \quad (2.2.3)$$

where the parity Π is usually determined through the parity of the $N_{\max} = 0$ ($N_{\max} = 1$) configurations for natural (unnatural) parity eigenstates and for even (odd) total particle numbers we usually use $M_J = 0$ ($M_J = 1$).

2.3. Importance Truncation

One possibility to overcome the limitations of the NCSM due to the growth of its model space to untractable sizes is the so-called importance truncation leading to the importance-truncated NCSM [RN07; Rot09]. It introduces an *a priori* measure for selecting only the physically most relevant basis states necessary for an adequate description of specific eigenstates while taking the properties of the underlying Hamiltonian into account. As shown in [Rot09], a substantial amount of basis states may be discarded without an impact on the quality of the description of certain eigenstates. As a consequence, the size of such an importance-truncated model space is massively reduced compared to the model-space size of an associated *full* NCSM calculation. Thus, this scheme allows us to extend the reach of the NCSM to higher N_{\max} and particle numbers A .

For discussing the principles of the importance-truncation scheme within the NCSM framework, let us begin with a brief summary of multi-configurational many-body perturbation theory (MCPT). For this purpose, let us assume that we are starting from a full model space $\mathcal{M}_{\text{full}}$ spanned by a set of many-body basis states $\{|\phi_i\rangle\}$. Furthermore, \mathcal{M}_{ref} shall be a subspace of $\mathcal{M}_{\text{full}}$ and $|\psi_{\text{ref}}\rangle$ an eigenstate living within \mathcal{M}_{ref} . In the following, we will be using

$|\psi_{\text{ref}}\rangle$ as a first approximation or, in other words, zeroth-order approximation for the corresponding eigenstate we are interested in. Following the general idea of MCPT for estimating low-order corrections to the reference state $|\psi_{\text{ref}}\rangle$, we have to separate the Hamiltonian into an unperturbed part \hat{H}_0 part and a perturbation \hat{W} . Using $|\psi_{\text{ref}}\rangle$ as the unperturbed state, this separation may be performed as follows

$$\hat{H}_0 = \epsilon_{\text{ref}} |\psi_{\text{ref}}\rangle\langle\psi_{\text{ref}}| + \sum_{i \notin \mathcal{M}_{\text{ref}}} \epsilon_i |\phi_i\rangle\langle\phi_i|, \quad (2.3.1)$$

with $\epsilon_{\text{ref}} = \langle\psi_{\text{ref}}|\hat{H}|\psi_{\text{ref}}\rangle$ and the unperturbed energies chosen as $\epsilon_i = \epsilon_{\text{ref}} + \Delta\epsilon_i$, which is associated with the Møller-Plesset-type formulation of MCPT.⁷ Using this approach, the zeroth-order contribution to the eigenstate is the reference state itself and the first-order correction is given through

$$|\psi\rangle^{(1)} = - \sum_{i \notin \mathcal{M}_{\text{ref}}} \frac{\langle\phi_i|\hat{W}|\psi_{\text{ref}}\rangle}{\epsilon_i - \epsilon_{\text{ref}}} |\phi_i\rangle = \sum_{i \notin \mathcal{M}_{\text{ref}}} \underbrace{\frac{-\langle\phi_i|\hat{H}|\psi_{\text{ref}}\rangle}{\epsilon_i - \epsilon_{\text{ref}}}}_{\equiv \kappa_i} |\phi_i\rangle, \quad (2.3.2)$$

where we defined the so-called importance measure κ_i . This *a priori* importance measure κ_i plays a central role: It assesses the significance of a basis state $|\phi_i\rangle$ lying outside of \mathcal{M}_{ref} for the description of an eigenstate of the Hamiltonian, which, in zeroth-order, is described via $|\psi_{\text{ref}}\rangle$. The so-called importance threshold κ_{min} imposes a lower limit on the absolute value of the importance measure $|\kappa_i|$ such that we include only those basis states in our model space with $|\kappa_i| > \kappa_{\text{min}}$ and discard all others.⁸

In the context of the $N_{\text{max}}\hbar\Omega$ truncated space of the NCSM, the general idea of importance truncation may be implemented by means of a *sequential* scheme as will be outlined in the following.⁹ Starting with a full NCSM calculation in a small $N_{\text{max}}\hbar\Omega$ space, we obtain an initial reference state $|\psi_{\text{ref}}\rangle$. Employing this reference state, we then construct an *importance-truncated* $(N_{\text{max}} + 2)\hbar\Omega$ space and perform an NCSM calculation within this space from which we obtain a new, updated, reference state. This updated reference state is then used for the construction of the importance-truncated $(N_{\text{max}} + 4)\hbar\Omega$ space and so on. Compared to the full NCSM the computationally most demanding part of the IT-NCSM is now the construction of the importance-truncated space, whereas the diagonalization itself is computationally much less consuming due to the fact that the importance-truncated model space is much smaller. As the computational cost drastically increases with the number of basis states the reference state $|\psi_{\text{ref}}\rangle$ is composed of, we only take those basis states into account whose contribution to the reference state is larger than c_{min} . Usually, this rather technical c_{min} truncation parameter is of the order 1×10^{-4} and is chosen such that the impact on numerical results is

⁷Employing this definition, the unperturbed reference state is an eigenstate of the unperturbed Hamiltonian and the zeroth-order energy correction is the expectation of the full Hamiltonian w.r.t. the reference state.

⁸Note that the idea of importance truncation is very generic and may also be used in other contexts.

⁹The sequential scheme has been found to be the most efficient scheme.

negligible. For taking the impact of the κ_{\min} truncation on calculated observables into account, we perform calculations at each N_{\max} for a whole sequence of increasing κ_{\min} values, i.e., $\{\kappa_{\min}^0, \kappa_{\min}^1, \kappa_{\min}^2, \dots\}$ from which we obtain a corresponding sequence of observables $\{E(\kappa_{\min}^0), E(\kappa_{\min}^1), E(\kappa_{\min}^2), \dots\}$. As the full NCSM is recovered in the limit $\kappa_{\min} \rightarrow 0$ at each N_{\max} , we perform an *a posteriori* threshold extrapolation to vanishing importance thresholds from which we obtain an approximation for the full NCSM $E(\kappa_{\min} = 0)$ together with an uncertainty estimation $\Delta E(\kappa_{\min} = 0)$.

Note that the scheme for the construction of the importance-truncated model space may be easily extended such that not only one but several eigenstates are taken into account. Having defined a specific importance threshold κ_{\min} , a basis state $|\phi_i\rangle$ is included in the importance-truncated model space if its importance measure w.r.t. *any* reference state is above the importance threshold.

2.4. Single-Particle Basis Optimizations

The convergence of NCSM calculations w.r.t. N_{\max} may be significantly improved through the choice of alternative single-particle bases.¹⁰ Two alternative single-particle bases that play a dominant role within the context of this work are the Hartree-Fock basis and the natural-orbital basis. Note that especially within the context of the IM-NCSM (see chapter 6), other single-particle bases than the harmonic oscillator are particularly valuable for optimizing the NCSM-based reference state.

Hartree-Fock Basis. The simple picture that the eigenstate of an A -body nucleus is represented by a Slater determinant, i.e., an anti-symmetrized product state which consists of A single-particle states where each is occupying a specific orbit is only a crude approximation. Such a mean-field picture would only be true if the nucleons were moving within an external potential with no inter-nucleonic forces. However, the opposite is true: A nucleus is a highly correlated many-body system, i.e., the nucleons are strongly interacting.

Even though a Slater determinant might not be adequate for representing the *exact* ground-state, we may aim for the construction of a Slater determinant that is energetically as close to the ground state as possible—this is the Hartree-Fock approximation. Formally being a Rayleigh-Ritz variational problem of the form

$$\delta \left(\frac{\langle \Phi | \hat{H} | \Phi \rangle}{\langle \Phi | \Phi \rangle} \right) = 0, \quad (2.4.1)$$

¹⁰Note that the notion of the NCSM usually implies the employment of the harmonic oscillator single-particle basis while, strictly speaking, the mere generalization to any other basis would require the notion of an CI approach.

it aims for minimizing the energy of a Slater determinant $|\Phi\rangle$ by conducting a particularly constructed unitary single-particle basis transformation. The variational problem eventually leads to the nonlinear Hartree-Fock equations which can be solved iteratively until self consistency is reached (which means that the single-particle states are not changing anymore from one iteration to the next). Once the iteration is converged, we obtain a self-consistent mean field together with its associated eigenstates and eigenenergies—the Hartree-Fock single-particle states and single-particle energies.

The Hartree-Fock approximation is not only useful as a many-body method on its own, but more importantly a good starting point for more sophisticated many-body methods that explicitly include the effects of correlations. This is due to the fact that the corresponding single-particle basis transformation is conducted with regard to a specific nucleus and, as a consequence, the Hartree-Fock single-particle basis already reflects to a certain extent the fundamental properties of the nucleus under consideration.

The Hartree-Fock approximation is a standard tool of, e.g., nuclear structure physics and quantum chemistry and, therefore, well-covered in the literature and more general information on the construction and details of the Hartree-Fock approximation can be found in, e.g., [SO96; Suh07; RS80].

As successful as the Hartree-Fock basis might be applied within the context of, e.g., the single-reference IM-SRG, or coupled cluster theory [Hag+16; Hag+14] for targeting medium-mass nuclei, it comes along with major problems when employed in NCSM-like approaches, as it has already been pointed out in [Tic+19]. Broadly speaking, this is due to the fact that the Hartree-Fock approximation is eventually aiming for an uncorrelated mean-field and only variationally optimizes occupied single-particle states while unoccupied states are only fixed through orthonormality. The interplay of, firstly, deficiencies of the wavefunctions of unoccupied Hartree-Fock states, and secondly, the fact that the N_{\max} -truncated model space does not fully resolve the single-particle space in which the Hartree-Fock transformation takes place, leads to the fact that the Hartree-Fock basis does not enhance but even impedes the N_{\max} convergence. As a consequence, the Hartree-Fock basis is not an adequate choice for the NCSM.

Natural Orbital Basis. Another alternative single-particle basis with advantageous properties is the natural orbital basis: It does not only enhance the N_{\max} convergence of observables, but also removes the $\hbar\Omega$ dependency [Tic+19]. Generally, the natural-orbital basis is the eigenbasis of the one-body density matrix. While there exist several approaches for the construction of this one-body density matrix, which differ by the amount of correlations they are taking into consideration, we found that it is sufficient to employ a second-order corrected one-body density matrix which originates from many-body perturbation theory. An advantage of this approach—in contrast to approaches, which employ a fully correlated ground-state from, e.g., a previous NCSM calculation, for the construction of the density matrix—is computational simplicity.

Due to the fact that all single-particle states—including those that are not occupied within the Hartree-Fock Slater determinant—are contributing to the correlated ground-state and to the one-body density matrix it follows that also all single-particle states are eventually optimized.

For more details on the natural orbitals like, e.g., their construction and a comparison of NCSM calculations employing the harmonic oscillator, Hartree-Fock, and natural orbital basis can be found in [Tic+19] and references therein. Due to their advantageous properties, the natural orbitals are most commonly employed within the IM-NCSM framework as will be discussed in more detail in chapter 6.

Normal Order

In this chapter we discuss one of the cornerstones of this work: The concept of normal order, which is employed in this work for the truncation of operators at a specific particle rank in a systematic and controllable manner. This truncation is necessary as analytic complexity as well as computational effort increase dramatically for higher particle ranks. Furthermore, normal order is a fundamental ingredient of the IM-SRG framework, reflected by the fact that operators within the IM-SRG are entering in normal-ordered form up to a specific particle rank. More specifically, we are usually employing the normal-ordered two-body (NO2B) approximation [Rot+12; GCR16], i.e., operators are included up to the normal-ordered two-body rank. Additionally, normal ordering also lays the foundation for the evaluation of many-body matrix elements by means of an application of Wick's theorem.

Broadly speaking, normal ordering reassigns specific parts of an operator to lower particle ranks based on a so-called reference state $|\psi_{\text{ref}}\rangle$. This reference state should already capture the main structure of an eigenstate of the quantum system under consideration to a certain degree, such that correlations represented by the reference state are already absorbed into the normal-ordered Hamiltonian. Usually, an approximation for the ground state is chosen as the reference state.

Often, normal order is only defined w.r.t. a single Slater determinant reference state $|\psi_{\text{ref}}\rangle$, which is referred to as *single-reference normal ordering*. This approach is only applicable to closed-shell systems as only here a Slater determinant may represent an adequate approximation for the ground state and can, therefore, be used as a reference state. In the context of single-reference normal ordering, the reference state is interpreted as a physical vacuum and defines occupied and unoccupied single-particle states as hole and particle states, respectively. Furthermore, a particle-hole picture is employed for redefining specific creation and annihilation operators to quasiparticle creators and annihilators. Single-reference normal order is then nothing but a particular order of a product of annihilation and creation operators such

that its expectation value w.r.t. $|\psi_{\text{ref}}\rangle$ vanishes. For more information on the topic of single-reference normal order that goes well beyond the following introductory discussion see, e.g., [BS09].

For open-shell nuclei it is not sufficient to use a single Slater determinant as a reference state due to the fact that there are usually many energetically degenerate Slater determinants. Therefore, we may resort to a multi-determinantal approach, i.e., an approach in which the reference state can be represented by superposition of single Slater determinants. Obviously, in this case the single-reference normal order approach, which is based on a particle-hole picture, breaks down. For that purpose, Kutzelnigg and Mukherjee generalized the concept of normal order to multi-configurational reference states [KM97] and we will mainly follow their line of thought here. However, we will employ a slightly different notation, which was first introduced by Kong, Nooijen, and Mukherjee in [KNM10]. Note that, besides both of the aforementioned references, an educationally valuable introduction into the topic of multi-reference normal order can also be found in [Geb17; Her17].

3.1. Second Quantization

Considering the antisymmetric Fock space \mathcal{F}^a , the so-called basic creation and annihilation operators written as \hat{a}^p and \hat{a}_q , respectively, are formally defined by their action on a Slater determinant as follows

$$\hat{a}^p |p_1 \dots p_A\rangle = \begin{cases} |pp_1 \dots p_A\rangle & \text{if } p \notin \{p_1, \dots, p_A\} \\ 0 & \text{else} \end{cases}, \quad (3.1.1)$$

$$\hat{a}_p |p_1 \dots p_A\rangle = \begin{cases} (-)^{k-1} |p_1 \dots p_{k-1} p_{k+1} \dots p_A\rangle & \text{if } p = p_k \\ 0 & \text{if } p \notin \{p_1, \dots, p_A\} \end{cases}. \quad (3.1.2)$$

From this definition we obtain the well-known anticommutation relations

$$[\hat{a}^p, \hat{a}^q]_+ = [\hat{a}_p, \hat{a}_q]_+ = 0, \quad [\hat{a}^p, \hat{a}_q]_+ = \delta_{pq}. \quad (3.1.3)$$

For convenience, we will employ the following notation for strings of basic creation and annihilation operators

$$\hat{a}_{q_1 \dots q_n}^{p_1 \dots p_n} = \hat{a}^{p_1} \dots \hat{a}^{p_n} \hat{a}_{q_n} \dots \hat{a}_{q_1}, \quad (3.1.4)$$

and exclusively consider particle-number conserving strings, i.e., only those with the same number of basic creation and annihilation operators. Note that we refer to $\hat{a}_{q_1 \dots q_n}^{p_1 \dots p_n}$ as a basic n -body operator. An arbitrary n -body operator \hat{O} can now be written as

$$\hat{O} = \frac{1}{(n!)^2} \sum_{\substack{p_1 \dots p_n \\ q_1 \dots q_n}} O_{q_1 \dots q_n}^{p_1 \dots p_n} \hat{a}_{q_1 \dots q_n}^{p_1 \dots p_n}, \quad (3.1.5)$$

where $O_{q_1 \dots q_n}^{p_1 \dots p_n} \equiv \langle p_1 \dots p_n | \hat{O} | q_1 \dots q_n \rangle$ depicts an n -body matrix element.

Let us now introduce an *index convention* that is most commonly used throughout this work. We employ either letters of the Latin alphabet p, q, \dots or plain numbers $1, 2, \dots$ as single-particle state indices such that a two-body matrix elements may be written, e.g., as O_{2q}^{1p} . In contrast, letters of the Greek alphabet ϕ, ψ, \dots are usually used as many-body state indices such that many-body states are usually expressed as, e.g., $|\phi\rangle, |\psi\rangle, \dots$

3.2. Single-Reference Normal Order

Let us begin with the more simple case of normal order w.r.t. a single Slater determinant reference state $|\psi_{\text{ref}}\rangle = |p_1 \dots p_A\rangle$. The single-particle states $|p_1\rangle, \dots, |p_A\rangle$ occupied in this reference state are called hole states, whereas states that are unoccupied are called particle states. Furthermore, let us assume that together the occupied and unoccupied single-particle states form an orthonormal basis set. We may interpret the reference state $|\psi_{\text{ref}}\rangle$ as a *physical vacuum* by taking the following relations into account

$$\hat{a}^i |\psi_{\text{ref}}\rangle = 0, \quad \hat{a}_i |\psi_{\text{ref}}\rangle \neq 0, \quad \hat{a}^a |\psi_{\text{ref}}\rangle \neq 0, \quad \hat{a}_a |\psi_{\text{ref}}\rangle = 0, \quad (3.2.1)$$

where the indices i and a refer to a hole and a particle state, respectively. It becomes clear that—employing a particle-hole picture—we may reinterpret \hat{a}^i and \hat{a}_a as quasiparticle annihilator and \hat{a}_i and \hat{a}^a as quasiparticle creator. The term (single-reference) normal order and the associated normal order operator may now be defined as follows.

Definition 3.2.1: Normal Order

An arbitrary string of creation and annihilation operators denoted as $\hat{X}_1 \dots \hat{X}_n$ is said to be in normal order if all quasiparticle annihilators appear right to all quasiparticle creators

Definition 3.2.2: Normal Order Operator

The normal order operator—denoted by means of two curly brackets $\{\hat{X}_1 \dots \hat{X}_n\}$ enclosing their argument—brings an arbitrary sequence of creators and annihilators $\hat{X}_1 \dots \hat{X}_n$ into normal order via applying a permutation π to the order of its arguments and including a phase factor reflecting the sign of the specific permutation π

$$\{\hat{X}_1 \dots \hat{X}_n\} \equiv (-)^{\text{sgn}(\pi)} \hat{X}_{\pi(1)} \dots \hat{X}_{\pi(n)}. \quad (3.2.2)$$

For avoiding ambiguities, the specific reference state $|\psi_{\text{ref}}\rangle$ w.r.t. which a product $\hat{X}_1 \dots \hat{X}_n$ is in normal order may be indicated through a subscript like, e.g., $\{\hat{X}_1 \dots \hat{X}_n\}_{|\psi_{\text{ref}}\rangle}$.

Note that the result of the normal order operator is not unique as there may be several sequences that are all compatible with the definition of normal order, which is illustrated by the following examples

$$\{\hat{a}^{h_1} \hat{a}_{a_1} \hat{a}_{h_2} \hat{a}^{a_2}\} = \hat{a}_{h_2} \hat{a}^{a_2} \hat{a}^{h_1} \hat{a}_{a_1} = -\hat{a}^{a_2} \hat{a}_{h_2} \hat{a}^{h_1} \hat{a}_{a_1} = \dots \quad (3.2.3)$$

An important aspect of normal order is that the expectation value of a normal-ordered product w.r.t. the reference state always vanishes

$$\langle \psi_{\text{ref}} | \{\hat{X}_1 \dots \hat{X}_n\} | \psi_{\text{ref}} \rangle = 0. \quad (3.2.4)$$

This particular property will become a fundamental ingredient for the following definition of multi-reference normal order.

In practical applications we are often interested in expressing a sequence of operators $\hat{X}_1 \dots \hat{X}_n$ in terms of normal-ordered products. In principle this can be achieved via iteratively applying the fermionic anti-commutation relations shown in eq. (3.1.3). However, the direct application of these anti-commutation relations can get very time-consuming and tedious. The remedy for this problem is Wick's theorem which gives us a simple and straightforward formula for expressing a product as a sum of its corresponding normal-ordered products.

Theorem 3.2.1: Wick's Theorem

An arbitrary product of operators is equal to its normal-ordered product plus all possible normal-ordered products with single contractions

$$\hat{X}_1 \dots \hat{X}_n = \{\hat{X}_1 \dots \hat{X}_n\} + \sum_{\text{all contr.}} \{\hat{X}_1 \dots \overbrace{\hat{X}_i \dots \hat{X}_j} \dots \hat{X}_n\}, \quad (3.2.5)$$

where a contraction is a complex number and a normal-ordered product with a single contraction is defined as

$$\begin{aligned} & \{\hat{X}_1 \dots \overbrace{\hat{X}_i \dots \hat{X}_j} \dots \hat{X}_n\} \\ &= \overbrace{\hat{X}_i \hat{X}_j} (-)^{\text{sgn}(\pi)} \{\hat{X}_1 \dots \hat{X}_{i-1} \hat{X}_{i+1} \dots \hat{X}_{j-1} \hat{X}_{j+1} \dots \hat{X}_n\}, \end{aligned} \quad (3.2.6)$$

and π refers to permutation necessary for \hat{X}_i and \hat{X}_j being next to each other without changing their original order.

The question how we can determine the value of a specific contraction is given by Wick's theorem itself. Applying Wick's theorem to the product $\hat{X}_1 \hat{X}_2$ and considering the expectation value of the resulting equation, we obtain

$$\langle \psi_{\text{ref}} | \hat{X}_1 \hat{X}_2 | \psi_{\text{ref}} \rangle = \langle \psi_{\text{ref}} | \left(\{\hat{X}_1 \hat{X}_2\} + \overbrace{\hat{X}_1 \hat{X}_2} \right) | \psi_{\text{ref}} \rangle. \quad (3.2.7)$$

Taking into account that a contraction is defined as a complex number and that the expectation of a product in normal order vanishes yields

$$\overline{\hat{X}_1 \hat{X}_2} = \langle \psi_{\text{ref}} | \hat{X}_1 \hat{X}_2 | \psi_{\text{ref}} \rangle . \quad (3.2.8)$$

As we are using a single Slater determinant as reference state there are only two non-vanishing contractions that we need to consider. The first type is called a hole contraction

$$\overline{\hat{a}^p \hat{a}_q} = \langle \psi_{\text{ref}} | \hat{a}^p \hat{a}_q | \psi_{\text{ref}} \rangle = \gamma_q^p , \quad (3.2.9)$$

where γ refers to the one-particle density matrix of the reference state. The second type of non-vanishing contraction is also called particle contraction

$$\overline{\hat{a}_p \hat{a}^q} = \langle \psi_{\text{ref}} | \hat{a}_p \hat{a}^q | \psi_{\text{ref}} \rangle = \bar{\gamma}_q^p = \delta_q^p - \gamma_p^q , \quad (3.2.10)$$

where we used $\bar{\gamma}$ for referring to the one-hole density matrix. For the single-reference case the aforementioned density matrices simplify as follows

$$\gamma_q^p = n_p \delta_q^p , \quad (3.2.11)$$

$$\bar{\gamma}_q^p = (1 - n_p) \delta_q^p , \quad (3.2.12)$$

where n_p indicates a so-called occupation number, formally defined as follows

$$n_p = \begin{cases} 1 & \text{if } p \text{ is hole state} \\ 0 & \text{if } p \text{ is particle state} \end{cases} , \quad (3.2.13)$$

which refers to the eigenvalues of the diagonal one-body density matrix whose value is—in the single-reference case—either zero or one.

Finally, the generalized Wick's theorem deals with products of normal-ordered products.

Theorem 3.2.2: Generalized Wick's Theorem

A product of two normal-ordered products evaluates to

$$\begin{aligned} \{\hat{X}_1 \cdots \hat{X}_n\} \{\hat{Y}_1 \cdots \hat{Y}_m\} &= \{\hat{X}_1 \cdots \hat{X}_n \hat{Y}_1 \cdots \hat{Y}_m\} \\ &+ \sum_{\text{ext. contr.}} \{\hat{X}_1 \cdots \overbrace{\hat{X}_i \cdots \hat{X}_n} \hat{Y}_1 \cdots \hat{Y}_j \cdots \hat{Y}_m\} , \end{aligned} \quad (3.2.14)$$

where only external contractions have to be taken into consideration, i.e., contractions between different original normal-ordered products like, e.g., $\overline{\hat{X}_i \hat{Y}_j}$.

Therefore, Wick's theorem gives a formula for the efficient evaluation of products of normal-ordered products.

3.3. Multi-Reference Normal Order

For the case of a multi-determinantal reference state, which can be written as a superposition of single Slater determinants

$$|\psi_{\text{ref}}\rangle = \sum_i c_i |\phi_i\rangle, \quad (3.3.1)$$

it is not directly clear how to define normal order in a traditional particle-hole sense. This is due to the fact that for a multi-determinantal reference state there is no clear distinction anymore between occupied hole and unoccupied particle states and as a consequence a reordering that is primarily based on such an assignment is not applicable anymore. However, in [KM97] Kutzelnigg and Mukherjee generalized normal ordering such that it becomes well-defined and applicable within the context of multiconfigurational reference states, which we will refer to as *multi-reference normal ordering*. In the following we will outline the guiding principles of this generalization, even though we will use a slightly different notation introduced by Kong, Nooijen, and Mukherjee in [KNM10].

The generalization of normal ordering w.r.t. multi-determinantal reference states is based on the following three guiding principles.

1. Normal-ordered operators w.r.t. any reference state must be linear combinations of normal-ordered operators w.r.t. the vacuum.
2. The expectation value of a normal-ordered product w.r.t. the reference state $|\psi_{\text{ref}}\rangle$ must vanish.
3. If the reference state $|\psi_{\text{ref}}\rangle$ is a single Slater determinant, the single-reference normal order must be reproduced.

Within the context of multi-reference normal order, k -body density matrices $\gamma^{[k]}$ are a fundamental ingredient. The matrix elements of $\gamma^{[k]}$ are given through the relation

$$\gamma_{q_1 \dots q_k}^{p_1 \dots p_k} = \langle \psi_{\text{ref}} | \hat{a}_{q_1 \dots q_k}^{p_1 \dots p_k} | \psi_{\text{ref}} \rangle. \quad (3.3.2)$$

Furthermore, we will be employing the antisymmetrizer $\hat{\mathcal{A}}$, which fully antisymmetrizes an object w.r.t. index transpositions within its upper and lower row as depicted through the example

$$\hat{\mathcal{A}}(\lambda_q^p \lambda_s^r) = \lambda_q^p \lambda_s^r - \lambda_s^p \lambda_q^r. \quad (3.3.3)$$

We can now introduce the irreducible k -body density matrices $\lambda^{[k]}$ for $1 \leq k \leq A$, which

encode genuine k -body correlations, and are given via the following recursive relation¹

$$\lambda_q^p = \gamma_q^p, \quad (3.3.4)$$

$$\lambda_{rs}^{pq} = \gamma_{rs}^{pq} - \hat{\mathcal{A}}(\lambda_r^p \lambda_s^q), \quad (3.3.5)$$

$$\lambda_{stuv}^{pqrs} = \gamma_{stuv}^{pqrs} - \hat{\mathcal{A}}(\lambda_s^p \lambda_t^q \lambda_u^r + \lambda_{st}^{pq} \lambda_u^r), \quad (3.3.6)$$

where we omitted the superscript k in $\lambda^{[k]}$ for brevity as the particle rank is implicitly given by the number of indices. Before we state the multi-reference version of Wick's theorem, let us define the notion of a multi-reference contraction.

Definition 3.3.1: Multi-Reference Contraction

A contraction of rank m is a number taking over m upper $p_1 \dots p_m$ and m lower indices $q_1 \dots q_m$ from an operator \hat{a}_{\dots} . The set $p_1 \dots p_m q_1 \dots q_m$ is referred to as contracted indices. For $m = 1$ we call this a one-one contraction, otherwise an m - m or multiple contraction. A rank- m contraction is given by the corresponding irreducible m -body density matrix $\lambda^{[m]}$.

Theorem 3.3.1: Multi-Reference Wick-like Theorem

An operator can be expressed in terms of multi-reference normal-ordered terms via

$$\hat{a}_{y_1 \dots y_A}^{x_1 \dots x_A} = \{\hat{a}_{y_1 \dots y_A}^{x_1 \dots x_A}\} + \sum_{\text{all unique contractions}} \{\hat{a}_{y_1 \dots y_A}^{x_1 \dots x_A}\}. \quad (3.3.7)$$

Each contraction leads to a contribution of a λ tensor of the form

$$(-)^{\text{sgn}(\pi)} \lambda_{y_2}^{x_1} \lambda_{y_3 y_A}^{x_3 x_i} \{\hat{a}_{y_1 y_3 \dots y_{j-1} y_{j+1} \dots y_{A-1}}^{x_2 x_4 \dots x_{i-1} x_{i+1} \dots x_A}\}, \quad (3.3.8)$$

where π is the permutation to bring the indices back to their original order.

Let us illustrate the multi-reference normal ordering procedure by the following examples. For a one-body operator we obtain

$$\hat{a}_q^p = \{\hat{a}_q^p\} + \lambda_q^p. \quad (3.3.9)$$

Taking the expectation value w.r.t. the reference state $|\psi_{\text{ref}}\rangle$ and using the definition of the irreducible density matrix $\lambda^{[1]}$ shows that the expectation value of a normal-ordered one-body operator vanishes

$$\langle \psi_{\text{ref}} | \{\hat{a}_q^p\} | \psi_{\text{ref}} \rangle = 0. \quad (3.3.10)$$

¹Strictly speaking, $\lambda^{[k]}$ are k -body cumulants of the, w.r.t. the particle rank of the full A -body density matrix $\gamma^{[A]}$, reduced density matrix $\gamma^{[k]}$.

Applying the normal ordering procedure to a two-body operator gives

$$\begin{aligned} \hat{a}_{rs}^{pq} &= \{\hat{a}_{rs}^{pq}\} + \lambda_r^p \{\hat{a}_s^q\} - \lambda_s^p \{\hat{a}_r^q\} - \lambda_r^q \{\hat{a}_s^p\} + \lambda_s^q \{\hat{a}_r^p\} \\ &\quad + \lambda_r^p \lambda_s^q - \lambda_s^p \lambda_r^q + \lambda_{rs}^{pq} \end{aligned} \quad (3.3.11)$$

$$= \{\hat{a}_{rs}^{pq}\} + \hat{\mathcal{A}} \left(\lambda_r^p \{\hat{a}_s^q\} + \lambda_r^p \lambda_s^q + \lambda_{rs}^{pq} \right) . \quad (3.3.12)$$

By taking the expectation value of the equation above w.r.t. the reference state $|\psi_{\text{ref}}\rangle$ and using $\langle \psi_{\text{ref}} | \{\hat{a}_q^p\} | \psi_{\text{ref}} \rangle = 0$, we obtain

$$\begin{aligned} \langle \psi_{\text{ref}} | \{\hat{a}_{rs}^{pq}\} | \psi_{\text{ref}} \rangle &= \langle \psi_{\text{ref}} | \hat{a}_{rs}^{pq} | \psi_{\text{ref}} \rangle - \lambda_r^p \lambda_s^q + \lambda_s^p \lambda_r^q - \lambda_{rs}^{pq} = 0 . \\ &= \lambda_{rs}^{pq} + \hat{\mathcal{A}}(\lambda_r^p \lambda_s^q) \end{aligned} \quad (3.3.13)$$

Consequently, the multi-reference normal order fulfills the condition that expectation values of normal-ordered products vanish.

Let us now address the multi-reference version of the generalized Wick's theorem which gives us a formula for evaluating the product of two operators in normal order in a fast and efficient manner.

Theorem 3.3.2: Generalized Wick's Theorem

- The product of two normal-ordered products yields

$$\{\hat{a}_{q_1 \dots q_m}^{p_1 \dots p_m}\} \{\hat{a}_{s_1 \dots s_n}^{r_1 \dots r_n}\} = \{\hat{a}_{q_1 \dots q_m s_1 \dots s_n}^{p_1 \dots p_m r_1 \dots r_n}\} + \sum_{\text{all ext. contr.}} \{\hat{a}_{q_1 \dots q_m s_1 \dots s_n}^{p_1 \dots p_m r_1 \dots r_n}\} , \quad (3.3.14)$$

where only external contractions are contributing, i.e., internal contractions with contracted indices coming only from one of the normal-ordered products are excluded. Every contraction pattern must contribute only once and is, thus, unique.

- Every term with its unique contraction pattern involves, firstly, a specific set of contracted indices which appear in one or more contractions, and secondly, a set of uncontracted indices that appear in the corresponding normal-ordered operator.
- Every contraction is given by the associated irreducible density matrix λ . There is, however, an exception for one-one contractions between a lower index q_i of the first normal-ordered product and an upper index of the second normal-ordered product r_j which is given through

$$\xi_q^p \equiv \lambda_q^p - \delta_q^p = -\bar{\gamma}_q^p , \quad (3.3.15)$$

where $\bar{\gamma}_q^p$ refers to a one-hole density matrix element.

- Every unique term carries a phase factor which is determined by the parity of the permutation needed to bring the indices back into the initial order.

For illustrating the application of the generalized Wick's theorem, let us consider a product of two normal-ordered one-body operators which may be evaluated as follows

$$\{\hat{a}_q^p\}\{\hat{a}_s^r\} = \{\hat{a}_{qs}^{pr}\} - \gamma_s^p \{\hat{a}_q^r\} + \bar{\gamma}_q^r \{\hat{a}_s^p\} + \gamma_s^p \bar{\gamma}_q^r + \lambda_{qs}^{pr} . \quad (3.3.16)$$

Considering the context of this work, the generalized Wick's theorem plays a central role for the IM-SRG as it is being employed for evaluating commutators of normal-ordered products.

3.4. Representation Changes

As we will see during the following discussion in chapter 4 and chapter 5, all operators entering the IM-SRG framework are in non-vacuum normal order, i.e., they are expressed in terms of basic operators that are in normal order w.r.t. a specific reference state $|\psi_{\text{ref}}\rangle$. Thus, starting from an arbitrary operator in vacuum normal order containing up to three-body operators

$$\hat{X} = V_0 + \sum_{pq} V_q^p \{\hat{a}_q^p\}_{|0\rangle} + \frac{1}{4} \sum_{pqrs} V_{rs}^{pq} \{\hat{a}_{rs}^{pq}\}_{|0\rangle} + \frac{1}{36} \sum_{pqrstu} V_{stu}^{pqr} \{\hat{a}_{stu}^{pqr}\}_{|0\rangle} . \quad (3.4.1)$$

We apply Wick's theorem to all basic operators of all particle ranks, classify every resulting term w.r.t. the particle rank of its normal-ordered basic operator, and eventually obtain an operator that is in normal order w.r.t. a reference state $|\psi_{\text{ref}}\rangle$

$$\hat{X} = R_0 + \sum_{pq} R_q^p \{\hat{a}_q^p\}_{|\psi_{\text{ref}}\rangle} + \frac{1}{4} \sum_{pqrs} R_{rs}^{pq} \{\hat{a}_{rs}^{pq}\}_{|\psi_{\text{ref}}\rangle} + \frac{1}{36} \sum_{pqrstu} R_{stu}^{pqr} \{\hat{a}_{stu}^{pqr}\}_{|\psi_{\text{ref}}\rangle} . \quad (3.4.2)$$

Note that we will occasionally refer to the form given in eq. (3.4.1) as the vacuum representation of \hat{X} while eq. (3.4.2) shows the reference-state representation. Likewise, the matrix elements associated with the vacuum and reference-state representation are conveniently referred to as vacuum and reference-state matrix elements, respectively.

The change between the vacuum and reference-state representation is referred to as a representation change and the corresponding expressions relating the associated matrix elements with each other may be obtained through the application of Wick's theorem. Following this approach, reference-state matrix elements are given in terms of vacuum matrix elements as follows

$$R_0 = V_0 + \sum_{pq} V_q^p \gamma_q^p + \frac{1}{4} \sum_{pqrs} V_{rs}^{pq} \gamma_{rs}^{pq} + \frac{1}{36} \sum_{pqrstu} V_{stu}^{pqr} \gamma_{stu}^{pqr} , \quad (3.4.3)$$

$$R_2^1 = V_2^1 + \sum_{pq} V_{2q}^{1p} \gamma_q^p + \frac{1}{4} \sum_{pqrs} V_{2rs}^{1pq} \gamma_{rs}^{pq} , \quad (3.4.4)$$

$$R_{34}^{12} = V_{34}^{12} + \sum_{pq} V_{34q}^{12p} \gamma_q^p , \quad (3.4.5)$$

$$R_{456}^{123} = V_{456}^{123} . \quad (3.4.6)$$

The inverse of these relations can be written as

$$V_0 = R_0 - \sum_{pq} R_q^p Y_q^p - \frac{1}{4} \sum_{pqrs} R_{rs}^{pq} (Y_{rs}^{pq} - 4Y_r^p Y_s^q) - \frac{1}{36} \sum_{pqrst} R_{st}^{pqr} (Y_{st}^{pqr} - 18Y_s^p Y_{tu}^{qr} + 36Y_s^p Y_t^q Y_u^r), \quad (3.4.7)$$

$$V_2^1 = R_2^1 - \sum_{pq} R_{2q}^{1p} Y_q^p - \frac{1}{4} \sum_{pqrs} R_{2rs}^{1pq} (Y_{rs}^{pq} - 4Y_r^p Y_s^q), \quad (3.4.8)$$

$$V_{34}^{12} = R_{34}^{12} - \sum_{pq} R_{34q}^{12p} Y_q^p, \quad (3.4.9)$$

$$V_{456}^{123} = R_{456}^{123}. \quad (3.4.10)$$

Note that a derivation of these relations can be found in [Geb17].

Usually, the operator \hat{X} is a spherical tensor operator with a particular tensor rank.² Taking spherical symmetry into account, eqs. (3.4.3) to (3.4.6) and eqs. (3.4.7) to (3.4.10) can be transformed into their spherical counterpart, i.e., equations in terms of *reduced* matrix elements that do not exhibit any dependence on projection quantum numbers anymore. The result of this transformation can be found in appendix B.1.

Taking spherical symmetry into consideration and assuming that \hat{X} is a spherical tensor operator of rank L , we make an essential observation: The individual particle ranks of the normal-ordered representation of \hat{X} are only exhibiting the original spherical tensor rank L if the density matrices are scalars. This would not only increase the complexity of our theory but also give rise to various fundamental and conceptional questions. For that purpose, we will exclusively perform normal ordering w.r.t. reference states with vanishing total angular momentum—as only those lead to density matrices whose decomposition consists of scalars only.

3.5. Normal-Ordered Two-Body Approximation

A prominent example for the application of normal ordering is the NO2B approximation. Starting from a three-body operator in vacuum normal order

$$\hat{X}^{[3]} = + \frac{1}{36} \sum_{pqrst} V_{st}^{pqr} \{\hat{a}_{stu}^{pqr}\}_{|0\rangle}, \quad (3.5.1)$$

where V_{st}^{pqr} refer to three-body matrix elements with regard to the vacuum normal order, we express the basic operators in terms of (multi-reference) normal-ordered operators via

²See section 5.2 for more information on the topic of spherical tensor operators.

Wick's theorem, i.e., perform a representation change of \hat{X} from vacuum to reference-state representation and obtain

$$\hat{X}^{[3]} = R_0 + \sum_{pq} R_q^p \{ \hat{a}_q^p \}_{|\Psi\rangle} + \frac{1}{4} \sum_{pqrs} R_{rs}^{pq} \{ \hat{a}_{rs}^{pq} \}_{|\Psi\rangle} + \frac{1}{36} \sum_{pqrstu} R_{stuv}^{pqr} \{ \hat{a}_{stuv}^{pqr} \}_{|\Psi\rangle}. \quad (3.5.2)$$

The NO2B approximation omits the normal-ordered three-body part in the equation above such that we obtain the following operator

$$\hat{X}_{\text{NO2B}}^{[3]} \equiv R_0 + \sum_{pq} R_q^p \{ \hat{a}_q^p \}_{|\Psi\rangle} + \frac{1}{4} \sum_{pqrs} R_{rs}^{pq} \{ \hat{a}_{rs}^{pq} \}_{|\Psi\rangle}, \quad (3.5.3)$$

where the matrix elements of this NO2B-approximated operator are directly given through eqs. (3.4.3) to (3.4.6) by setting all initial vacuum matrix elements other than the three-body matrix elements elements to zero. Eventually, we obtain the following result for the matrix elements of the reference-state representation of $\hat{X}_{\text{NO2B}}^{[3]}$

$$R_0 = \frac{1}{36} \sum_{pqrstu} V_{stuv}^{pqr} \gamma_{stuv}^{pqr}, \quad R_2^1 = \frac{1}{4} \sum_{pqrs} V_{2rs}^{1pq} \gamma_{rs}^{pq}, \quad R_{34}^{12} = \sum_{pq} V_{34q}^{12p} \gamma_q^p. \quad (3.5.4)$$

Note that some many-body methods like, e.g., the NCSM are only taking vacuum matrix elements as their input in which case $\hat{X}_{\text{NO2B}}^{[3]}$ has to be of the form

$$\hat{X}_{\text{NO2B}}^{[3]} \equiv \check{V}_0 + \sum_{pq} \check{V}_q^p \{ \hat{a}_q^p \}_{|0\rangle} + \frac{1}{4} \sum_{pqrs} \check{V}_{rs}^{pq} \{ \hat{a}_{rs}^{pq} \}_{|0\rangle}, \quad (3.5.5)$$

where the corresponding vacuum matrix elements \check{V}_0 , \check{V}_q^p , and \check{V}_{rs}^{pq} of the vacuum representation of $\hat{X}_{\text{NO2B}}^{[3]}$ may be obtained by employing eqs. (3.4.7) and (3.4.10).

The fact that $\hat{X}_{\text{NO2B}}^{[3]}$ is now an effective two-body operator demonstrates that the NO2B approximation allows the approximate inclusion of genuine three-body effects embedded into the matrix elements of lower particle ranks while only two-body machinery has to be employed. It has been empirically shown in several publications [GCR16; Bin+13a; Rot+12] that, relative to a full inclusion of 3N forces, this neglect has an impact of 1 – 2% on ground and excited state energies.

Multi-Reference IM-SRG—Basics

This chapter aims at discussing the general concepts of the IM-SRG and the approach it is based on: the similarity renormalization group. We will begin with a brief discussion of the general SRG framework and outline the idea of the so-called *free-space* SRG as an example for a commonly used SRG-based approach other than the *in-medium* SRG. After that, we will address the fundamental elements of the IM-SRG like, e.g., the IM-SRG(2), the Magnus expansion, and generators. We would like to emphasize at this point that—even if usually denoted as IM-SRG for brevity—our studies and developments explicitly refer to a *multi-reference* version of the IM-SRG. Compared with the single-reference IM-SRG, the multi-reference IM-SRG is the more general case regarding the allowed structure of the reference state and eventually reduces to the single-reference IM-SRG if the reference is chosen as a Slater determinant. Thus, the single-reference IM-SRG is merely a special case of the multi-reference IM-SRG. Note that we will not get too involved into the details of commutator evaluations—one of the pillars of the IM-SRG—but moved all of the associated derivations and discussions to chapter 5 instead.

4.1. Similarity Renormalization Group

In this section we are discussing the general idea of the SRG framework, which is the foundation of, both, the free-space SRG and the in-medium SRG. We would like to note that more information on the SRG in general and its utilization in the context of the free-space SRG can be found in, e.g., [RRH08; RNF10; BFS10].

The general idea of the SRG in the formulation of Wegner [Weg94; Weg00] is to transform the Hamiltonian to a more diagonal form w.r.t. a specific basis. For that purpose, we apply an unitary transformation $\hat{U}(\alpha)$, which is continuous w.r.t. a so-called flow parameter α , to a

Hamiltonian \hat{H} yielding a transformed, α -dependent Hamiltonian

$$\hat{H}(\alpha) = \hat{U}^\dagger(\alpha)\hat{H}\hat{U}(\alpha), \quad \hat{H}(0) \equiv \hat{H}, \quad (4.1.1)$$

where, due to the unitary nature of this transformation, the eigenvalue spectrum of the transformed Hamiltonian $\hat{H}(\alpha)$ is independent of α . The unitary transformation can be reformulated through an operator flow equation by taking the derivative w.r.t. α

$$\frac{d}{d\alpha}\hat{H}(\alpha) = \frac{d\hat{U}^\dagger(\alpha)}{d\alpha}\hat{H}(0)\hat{U}(\alpha) + \hat{U}^\dagger(\alpha)\hat{H}(0)\frac{d\hat{U}(\alpha)}{d\alpha}. \quad (4.1.2)$$

Due to the unitarity of $\hat{U}(\alpha)$ it follows that $\hat{U}(\alpha)\hat{U}^\dagger(\alpha) = \hat{1}$ holds. The derivative of this relation w.r.t. α can then be written as

$$\frac{d}{d\alpha}\hat{U}^\dagger(\alpha) = -\hat{U}^\dagger(\alpha)\frac{d\hat{U}(\alpha)}{d\alpha}\hat{U}^\dagger(\alpha). \quad (4.1.3)$$

By defining the anti-Hermitian generator of the unitary transformation as follows

$$\hat{\eta}(\alpha) \equiv -\hat{U}^\dagger(\alpha)\frac{d\hat{U}(\alpha)}{d\alpha}, \quad (4.1.4)$$

we eventually obtain a first-order operator differential equations for the Hamiltonian and the unitary transformation, respectively,

$$\frac{d}{d\alpha}\hat{H}(\alpha) = [\hat{\eta}(\alpha), \hat{H}(\alpha)], \quad \hat{H}(0) = \hat{H}, \quad (4.1.5)$$

$$\frac{d}{d\alpha}\hat{U}^\dagger(\alpha) = \hat{\eta}(\alpha)\hat{U}^\dagger(\alpha), \quad \hat{U}^\dagger(0) = \hat{1}. \quad (4.1.6)$$

The flexibility of the SRG framework is rooted in the fact that we are free to choose the specific form of the generator $\hat{\eta}(\alpha)$. Thus, the behavior of the associated transformation can be tailored to specific needs via an appropriate construction of the generator $\hat{\eta}(\alpha)$.

Consistent Evolution of Observables. It is important to bear in mind that, once we are transforming the Hamiltonian, we have to transform the operators of other observables accordingly. This fact may be illustrated as follows: Starting from the general eigenvalue problem for the Hamiltonian

$$\hat{H}|\Psi^i\rangle = E^i|\Psi^i\rangle, \quad (4.1.7)$$

where $|\Psi^i\rangle$ and E^i refer to the i -th eigenstate and eigenvalue, respectively, we may transform this equation to

$$\hat{U}^\dagger(\alpha)\hat{H}\hat{U}(\alpha)\hat{U}^\dagger(\alpha)|\Psi^i\rangle = E^i\hat{U}^\dagger(\alpha)|\Psi^i\rangle. \quad (4.1.8)$$

Now, we are facing an alternative eigenvalue problem namely w.r.t. the unitarily transformed Hamiltonian $\hat{H}(\alpha) = \hat{U}^\dagger(\alpha)\hat{H}\hat{U}(\alpha)$ whose eigenvectors $|\Psi^i(\alpha)\rangle$ are formally related to the

eigenvectors of the initial Hamiltonian through $|\Psi^i(\alpha)\rangle = \hat{U}^\dagger(\alpha)|\Psi^i\rangle$ and whose eigenvalues are obviously invariant under this transformation

$$\hat{H}(\alpha)|\Psi^i(\alpha)\rangle = E^i|\Psi^i(\alpha)\rangle . \quad (4.1.9)$$

Assuming that we are solving the eigenvalue problem for $\hat{H}(\alpha)$ now, it follows that we naturally obtain the eigenstates $|\Psi^i(\alpha)\rangle$. Expressing a general matrix element of an observable \hat{O} with regard to the *untransformed* i -th and j -th eigenstate in terms of a matrix element with regard to the corresponding *transformed* i -th and j -th eigenstate

$$\langle\Psi^j|\hat{O}|\Psi^i\rangle = \langle\Psi^j|\hat{U}(\alpha)\hat{U}^\dagger(\alpha)\hat{O}\hat{U}(\alpha)\hat{U}^\dagger(\alpha)|\Psi^i\rangle = \langle\Psi^j(\alpha)|\hat{O}(\alpha)|\Psi^i(\alpha)\rangle , \quad (4.1.10)$$

demonstrates that we have to unitarily transform the observable via $\hat{O}(\alpha) = \hat{U}^\dagger(\alpha)\hat{O}\hat{U}(\alpha)$ such that the matrix element is invariant.¹ This unitary transformation of observables can be reformulated by means of a first-order differential equation

$$\frac{d}{d\alpha}\hat{O}(\alpha) = [\hat{\eta}(\alpha), \hat{O}(\alpha)] . \quad (4.1.11)$$

For cases in which the generator $\hat{\eta}(\alpha)$ explicitly depends on the evolved Hamiltonian—as it is most commonly the case for the IM-SRG—the operator differential equations for observables have to be solved *simultaneously* with the one for the Hamiltonian.

Induced Many-Body Interactions. An important aspect that comes along with the SRG framework are induced many-body interactions up to the A -body particle rank. This fact becomes directly evident when considering the operator flow equation given through eq. (4.1.11) for an arbitrary \hat{O} . Assuming that at $\alpha = 0$ the generator $\hat{\eta}(0)$ is an x -body operator and the observable $\hat{O}(0)$ is a y -body operator, the evaluation of the commutator on the right-hand side of the flow equation produces operators up to the particle rank of $x + y - 1$.² Thus, integrating the differential equation for $\hat{O}(\alpha)$ one infinitesimal step $\delta\alpha$ forward from $\alpha = 0$ to $\alpha = \delta\alpha$ gives a set of operators of the following form

$$\left\{ \dots, \hat{O}^{[x+y]}(\delta\alpha), \hat{O}^{[x+y-1]}(\delta\alpha) \right\} . \quad (4.1.12)$$

Given that $x > 1$, it follows from $x+y-1 > y$ that the maximum particle rank of the transformed components of \hat{Y} is increasing, and after a finite number of integrations the particle rank of one of those components reaches A . As the unitary transformation is not carried out in A -body space but confined to lower particle ranks through truncating all operators involved at, e.g., the three-body level, we are neglecting induced higher-order interactions and, as a consequence, we are formally violating the unitarity of our transformation. Therefore, we

¹From another point of view, we are performing a generic unitary transformation of the many-body basis of the A -body Hilbert space through which it also becomes directly evident that *all* observables have to be consistently transformed.

²Note that this is a direct consequence of Wick's theorem.

have to assess the impact of those omitted induced interactions through a study of the α dependence of calculated observables.

Generators & Decoupling Pattern. A simple choice for the generator, originally proposed by Wegner [Weg94; Weg00], consists of a commutator between the diagonal part of the Hamiltonian $\hat{H}^d(\alpha)$ and the Hamiltonian itself

$$\hat{\eta}(\alpha) = \left[\hat{H}^d(\alpha), \hat{H}(\alpha) \right], \quad (4.1.13)$$

$$\hat{H}^d(\alpha) = \sum_{\{\beta_i\}} \langle \beta_i | \hat{H}(\alpha) | \beta_i \rangle | \beta_i \rangle \langle \beta_i |. \quad (4.1.14)$$

Obviously, the definition of $\hat{H}^d(\alpha)$ presumes a choice for the many-body basis $\{|\beta_i\rangle\}$ which is the basis w.r.t. which the Hamiltonian shall be diagonalized. Considering the flow equation in a matrix representation with regard to the eigenbasis of $\hat{H}^d(\alpha)$, two things can be shown: Firstly, the diagonal form $\hat{H}^d(\alpha)$ is a trivial *fixed point*. This can easily be verified by assuming that the Hamiltonian is equal to the proposed diagonal form, i.e., $\hat{H}(\alpha) = \hat{H}^d(\alpha)$ from which it follows that the generator and therefore also the derivative $\frac{d}{d\alpha} \hat{H}(\alpha)$ vanish. Secondly, the off-diagonal matrix elements of the Hamiltonian are continuously suppressed throughout the evolution and, consequently, the diagonal form is an *attractive* fixed point of the evolution to which the Hamiltonian is being driven [RNF10; Weg94].

Considering a more general choice for the generator

$$\hat{\eta}(\alpha) = \left[\hat{G}(\alpha), \hat{H}(\alpha) \right], \quad (4.1.15)$$

and studying the associated flow equation through its matrix representation w.r.t. the eigenbasis of $\hat{G}(\alpha)$, the previous statement—where $\hat{G}(\alpha)$ was chosen as $\hat{H}^d(\alpha)$ —can be generalized to the statement that the Hamiltonian is being driven to a form that is diagonal in the eigenbasis of $\hat{G}(\alpha)$. Through such a choice we are departing from the original choice of Wegner, which aims at a full diagonalization for $\alpha \rightarrow \infty$, and instead aim at a prediagonalization of the Hamiltonian w.r.t. a specific basis, i.e., the eigenbasis of $\hat{G}(\alpha)$. This demonstrates that through a specific choice of our generator we can drive the Hamiltonian to a certain extent to any desired band or block-diagonal form [BFS10].

4.1.1. Free-Space SRG

A well-known characteristic of realistic nuclear interactions is that they exhibit strong tensor forces and strong short-range repulsions. As a consequence, those interactions lead to a strong coupling of high and low momentum modes and strong short-range correlations. Performing many-body calculations with these so-called “bare” interactions poses a major challenge for many-body methods like, e.g., the NCSM. Considering the NCSM approach, the many-body model space consists of Slater determinants which, in principle, can capture any interaction, provided that the model space truncation parameter N_{\max} is chosen large enough. However,

Slater determinants are not an adequate basis for representing strong short-range correlations as this requires energetically very high lying basis states, i.e., very high N_{\max} and it is difficult to obtain converged NCSM results beyond the lightest nuclei. The so-called free-space SRG tries to remedy this problem by aiming for a *generic* decoupling of low and high momenta. For that purpose, the generator of the free-space SRG is usually chosen as follows

$$\hat{\eta}(\alpha) = (2\mu)^2 \left[\hat{T}_{\text{int}}, \hat{H}(\alpha) \right], \quad (4.1.16)$$

where we have used the intrinsic kinetic energy operator \hat{T}_{int} and the reduced nucleon mass μ . Note that this choice leads to a flow parameter having the dimension fm^4 . As discussed previously, this choice for the generator drives the Hamiltonian to a diagonal form w.r.t. the eigenbasis of \hat{T}_{int} , i.e., leads to a band-diagonal form w.r.t. momentum eigenstates. Through this prediagonalization in momentum space we obtain a “softer” and unitary-equivalent interaction with improved convergence properties in subsequent many-body calculations. Furthermore, interactions transformed by means of the free-space SRG are model-space and nucleus independent so that the same transformed Hamiltonian can be used as input for many different calculations.

For more information regarding our current implementation of the free-space SRG and the consistent evolution of chiral three-nucleon interactions see [Rot+14]. An educationally valuable overview over the topic of the (free-space) SRG, background information, and comparisons with other alternative approaches for tackling the impact of strong short-range correlations can be found in [BFP07; BFS10; RNF10].

4.2. In-Medium SRG—Motivation and General Concepts

Generally speaking, the IM-SRG aims at suppressing a specific, so-called off-diagonal part of the Hamiltonian. To that end, let us partition the Hamiltonian as follows

$$\hat{H} \equiv \hat{H}^{\text{d}} + \hat{H}^{\text{od}}, \quad (4.2.1)$$

where \hat{H}^{d} and \hat{H}^{od} indicate the diagonal and off-diagonal parts of the Hamiltonian. It is important to note that the diagonal and off-diagonal parts do not have to coincide with the actual diagonal and off-diagonal part w.r.t. a matrix representation. Instead, they may be freely chosen to a certain extent.

However, common to all cases considered throughout this work is that the off-diagonal part is chosen such that the Hamiltonian becomes block-diagonal w.r.t. a specific *many-body* basis \mathcal{B} . Partitioning the many-body basis \mathcal{B} into \mathcal{V} and \mathcal{W} , i.e., $\mathcal{B} = \mathcal{V} \cup \mathcal{W}$ and $\mathcal{V} \cap \mathcal{W} = \emptyset$, the off-diagonal part is usually chosen as the part of the Hamiltonian that couples \mathcal{V} and \mathcal{W} with each other. Formally, the off-diagonal Hamiltonian may, therefore, be written as

$$\hat{H}^{\text{od}} = \sum_{v \in \mathcal{V}} \sum_{w \in \mathcal{W}} \langle v | \hat{H} | w \rangle |v\rangle \langle w| + \text{herm. conj.} \quad (4.2.2)$$

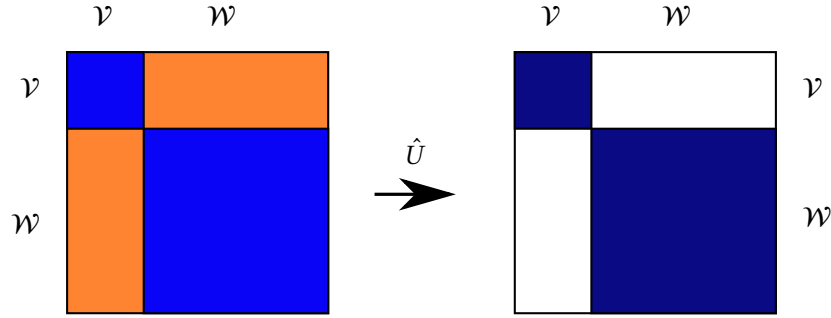


Figure 4.1.: This figure depicts a schematic matrix representation of the initial (left) and final (right) Hamiltonian and illustrates the common decoupling pattern which the IM-SRG is in all of its applications usually aiming for. While the initial Hamiltonian couples elements from \mathcal{V} and \mathcal{W} with each other, the unitary transformation \hat{U} is decoupling these two spaces from each other such that, finally, the span of \mathcal{V} becomes an invariant subspace of \hat{H} , i.e., the matrix representation of \hat{H} is block-diagonalized.

Once the off-diagonal Hamiltonian \hat{H}^{od} is suppressed, the matrix representation of \hat{H} w.r.t. \mathcal{B} becomes block-diagonal and the span of \mathcal{V} is an invariant subspace of \hat{H} , which is further illustrated in fig. 4.1. An obvious advantage of such a block-diagonalization is that we do not have to solve the eigenvalue problem within a model space spanned by \mathcal{B} anymore, but may as well solve the eigenvalue within the smaller model space spanned by \mathcal{V} .

As already indicated by its name, the IM-SRG is an SRG-based method and achieves the suppression of a specific off-diagonal part of an initial Hamiltonian \hat{H} through an unitary transformation

$$\hat{H}(s) \equiv \hat{U}^\dagger(s)\hat{H}(0)\hat{U}(s), \quad \hat{H}(0) \equiv \hat{H}, \quad (4.2.3)$$

where s is a continuous flow parameter. As already shown in the previous section, this unitary transformation can be rewritten as an operator differential equation or flow equation

$$\frac{d}{ds}\hat{H}(s) = \left[\hat{\eta}(s), \hat{H}(s) \right], \quad \hat{H}(0) = \hat{H}, \quad (4.2.4)$$

where $\hat{\eta}(s)$ refers to the anti-Hermitian generator of the unitary transformation. Evidently, the generator has to take the specific choice for the off-diagonal part into account and has to be constructed accordingly. Other observables \hat{O} obey a very similar operator differential equation

$$\frac{d}{ds}\hat{O}(s) = \left[\hat{\eta}(s), \hat{O}(s) \right], \quad \hat{O}(0) = \hat{O}. \quad (4.2.5)$$

As already noted previously, observables have to be evolved simultaneously with the Hamiltonian if—as it is most commonly the case—the generator explicitly depends on the evolved Hamiltonian.

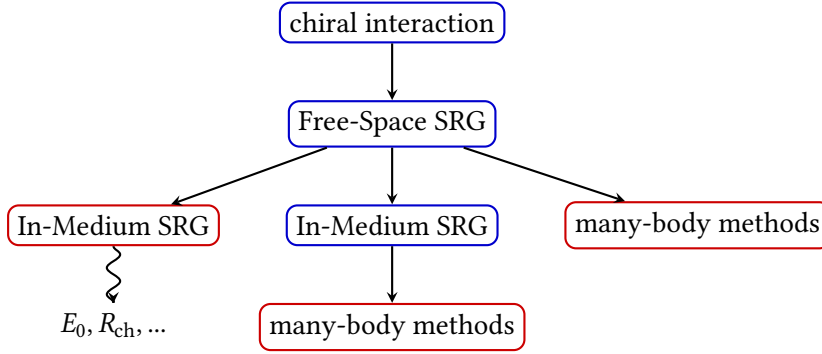


Figure 4.2.: Illustration of the flexibility of SRG approaches. Starting from a chiral interaction and performing a free-space SRG, the IM-SRG may be employed as a stand-alone many-body method directly giving access to nuclear structure observables or, alternatively, it may be employed for preprocessing operators associated with nuclear structure observables which are then passed on to subsequent many-body methods.

A great advantage of the IM-SRG is its flexibility and simplicity. Especially through different choices of generator types and off-diagonal parts, we can tailor this method for specific applications and control its numerical efficiency and behavior. As it is also illustrated in fig. 4.2, we can either directly calculate nuclear structure observables using the IM-SRG framework as it is routinely performed within the single-reference IM-SRG (see section 4.8) or, alternatively, construct effective interactions and use IM-SRG evolved operators as input for subsequent many-body methods, as it is being done within the IM-NCSM framework (see chapter 6). Furthermore, there are new opportunities emerging like the construction of valence-space interactions from an IM-SRG treatment (see appendix A).

IM-SRG(k). Characteristic for the IM-SRG approach—and the main difference to the free-space SRG approach—is that it is being formulated “in medium”, i.e., all operators are normal-ordered w.r.t. a specific reference state³ $|\psi_{\text{ref}}\rangle$ and, for practical reasons, truncated consistently at a specific particle rank k initially ($s = 0$) and throughout the evolution ($s > 0$). Such a truncation pattern—denoted as IM-SRG(k)—can also be formally expressed as follows

$$\hat{H}(s) = \hat{H}^{[0]}(s) + \hat{H}^{[1]}(s) + \dots + \hat{H}^{[k]}(s) = \sum_{i=0}^k \hat{H}^{[i]}(s), \quad (4.2.6)$$

$$\hat{O}(s) = \hat{O}^{[0]}(s) + \hat{O}^{[1]}(s) + \dots + \hat{O}^{[k]}(s) = \sum_{i=0}^k \hat{O}^{[i]}(s), \quad (4.2.7)$$

³The reference state $|\psi_{\text{ref}}\rangle$ is a first approximation for (usually) the ground state obtained from, e.g., a HF, NCSM or HFB calculation

$$\hat{\eta}(s) = \hat{\eta}^{[1]}(s) + \dots + \hat{\eta}^{[k]}(s) = \sum_{i=1}^k \hat{\eta}^{[i]}(s). \quad (4.2.8)$$

where $\hat{X}^{[i]}(s)$ indicates the normal-ordered i -body part of a generic operator $\hat{X}(s)$ whose general operator structure may be written as

$$\hat{X}^{[i]}(s) = \frac{1}{(i!)^2} \sum_{\substack{p_1 \dots p_i \\ q_1 \dots q_i}} X_{q_1 \dots q_i}^{p_1 \dots p_i}(s) \{ \hat{a}_{q_1 \dots q_i}^{p_1 \dots p_i} \}, \quad (4.2.9)$$

where it is important to note that the dependence on the flow parameter s is carried by the matrix elements. Considering the differential equation for the Hamiltonian for demonstration purposes, the Hamiltonian and the generator—both truncated at the k -body level—may now be plugged into the operator differential equation for the Hamiltonian which yields

$$\frac{d}{ds} \hat{H}^{[x]}(s) = \hat{\Pi}^{[x]} \sum_{i=1}^k \sum_{j=0}^k \left[\hat{\eta}^{[i]}(s), \hat{H}^{[j]}(s) \right], \quad (4.2.10)$$

where $\hat{\Pi}^{[x]}$ refers to the projector on the x -body space and $0 \leq x \leq k$ for closing the system of equations. Each commutator within the sum on the right-hand side may also be written as

$$\left[\hat{\eta}^{[i]}(s), \hat{H}^{[j]}(s) \right] = \left(\frac{1}{(i!)(j!)} \right)^2 \sum_{\substack{p_1 \dots p_i \\ q_1 \dots q_i \\ r_1 \dots r_j \\ s_1 \dots s_j}} \eta_{q_1 \dots q_i}^{p_1 \dots p_i}(s) h_{s_1 \dots s_j}^{r_1 \dots r_j}(s) \left[\{ \hat{a}_{q_1 \dots q_i}^{p_1 \dots p_i} \}, \{ \hat{a}_{s_1 \dots s_j}^{r_1 \dots r_j} \} \right]. \quad (4.2.11)$$

The right-hand side of the equation above can then be conveniently evaluated by employing the generalized Wick's theorem (see chapter 3). Obviously, each commutator between an i and j -body operator eventually contributes to various particle ranks of the derivative, which demonstrates that different particle ranks are coupled with each other throughout the evolution in a highly non-trivial way.

Eventually, the evaluation of eq. (4.2.10) yields a coupled system of first-order ordinary differential equations in terms of the matrix elements of the involved operators, which may formally be expressed as follows

$$\frac{d}{ds} \vec{h}(s) = \vec{F} \left(\vec{\eta}(s), \vec{h}(s) \right), \quad (4.2.12)$$

where $\vec{h}(s)$ and $\vec{\eta}(s)$ indicate the entirety of all matrix elements up to the k -body rank of the Hamiltonian and the generator, respectively, and the function \vec{F} represents the matrix-element-based commutator evaluation, i.e., it defines the system of ODEs. This system of differential equations may then be numerically solved until \hat{H}^{od} is “sufficiently” suppressed.

Furthermore, from the generalized Wick's theorem it is evident that evaluating eq. (4.2.10) produces induced many-body interactions up to the A -body rank. More specifically, the commutator between two i -body and j -body operators $\hat{X}^{[i]}$ and $\hat{Y}^{[j]}$, respectively, produces operators up to the $(i + j - 1)$ -body rank from which it becomes evident that after each integration

step of the ODE the maximum particle rank is eventually increasing. As a consequence, the IM-SRG is exact except for initially and intermediately discarded normal-ordered many-body interactions beyond the particle rank k .

4.3. Reference States

Information about the reference state $|\psi_{\text{ref}}\rangle$ is entering the IM-SRG framework solely through the k -body irreducible density matrices $\lambda^{[k]}$, which encode genuine k -body correlations and naturally emerge when evaluating commutators via Wick's theorem. As already noted previously, it is solely the type of the reference state, which sets the single-reference and the more general multi-reference version of the IM-SRG apart.

On the one hand, within the context of the multi-reference IM-SRG the reference state may be multi-determinantal and obtained, e.g., from a Hartree-Fock-Bogoliubov calculation [Her+13a; Her+14] or an NCSM calculation [Geb+16]. As a consequence of its multi-determinantal nature, the multi-reference version is applicable to open-shell nuclei and the naturally arising higher-order irreducible density matrices are explicitly taken into account. However, as an arbitrary correlated reference state may produce irreducible density matrices up to the A -body level, we have to impose some kind of truncations on the particle-rank of these density matrices as otherwise the computational effort would increase dramatically and eventually beyond feasibility. The stages at which irreducible density matrices are emerging and which eventually are subject to truncations with regard to their particle rank are, firstly, the commutator evaluation (see chapter 5), and secondly, the generator construction (see section 4.7). Even though we will discuss both of these topics in more detail later on, it is worth noting that throughout this work we did not include any irreducible density matrices beyond the two-body rank.

On the other hand, the single-reference version of the IM-SRG requires the reference state to be a single Slater determinant which may be, e.g., obtained from a previous Hartree-Fock calculation (see section 2.4). As a consequence, all irreducible density matrices beyond the one-body rank are naturally vanishing and the matrix elements of the one-body density matrix are either zero or one. The single-reference IM-SRG may, therefore, be considered as a special case of the more general multi-reference IM-SRG, as employing a Slater determinant within the framework of the multi-reference IM-SRG leads to the simple single-reference IM-SRG. An obvious downside of the single-reference IM-SRG is that it is only applicable to closed-shell nuclei as only for those a Slater determinant is an adequate first approximation for the ground-state. Furthermore, it is restricted to the description of ground-state observables. However, even though the capabilities of the single-reference version are a subset of those of the multi-reference version, it remains a standard tool for nuclear structure theory and eventually is favored over the multi-reference version in specific applications due to its conceptual simplicity and the fact that it yields reliable nuclear structure observables at a fraction of the computational cost.

Furthermore, it is important to note that we restrict ourselves to reference states $|\psi_{\text{ref}}\rangle$ with total angular momentum $J_{\text{ref}} = 0$ and, as a consequence, to the description of even nuclei only. This is due to the fact that we only want to include scalar density matrices and, given a reference state $|\psi_{\text{ref}}\rangle$ with a specific J_{ref} , the spherical tensor rank L of the associated irreducible density matrices obeys $0 \leq L \leq 2J_{\text{ref}}$ such that L is only restricted to zero if and only if $J_{\text{ref}} = 0$. There are two main problems that would arise with non-scalar density matrices: Firstly, there is a significant increase in computational effort, and secondly, the IM-SRG transformation would begin to break the conservation of the spherical tensor rank of a specific observable \hat{O} so that an initially scalar operator would transform into a non-scalar operator.

4.4. IM-SRG(2)

As noted previously, we have to truncate our operators at a specific particle rank for both analytical and computational reasons. In this work, we are going to discuss and employ the IM-SRG(2)⁴, which is mainly due to the fact that already the IM-SRG(3) shows a tremendous increase in complexity of its flow equations and computational effort inhibiting a “full” IM-SRG(3) up to now. Nevertheless, we are in the process of developing approaches that approximate the impact of induced three-body interactions.

However, within the context of the IM-SRG(2) we are consistently truncating our operators at the normal-ordered two-body level

$$\hat{H}(s) = E(s) + \sum_{pq} f_q^p(s) \{\hat{a}_q^p\} + \frac{1}{4} \sum_{pqrs} \Gamma_{rs}^{pq}(s) \{\hat{a}_{rs}^{pq}\}, \quad (4.4.1)$$

$$\hat{\eta}(s) = \sum_{pq} \eta_q^p(s) \{\hat{a}_q^p\} + \frac{1}{4} \sum_{pqrs} \eta_{rs}^{pq}(s) \{\hat{a}_{rs}^{pq}\}, \quad (4.4.2)$$

where all operators are normal-ordered w.r.t. a reference state $|\psi_{\text{ref}}\rangle$ and we adopted the common convention to employ f and Γ for referring to one and two-body matrix elements, respectively, of the Hamiltonian. Let us now assume that we are starting with a Hamiltonian \hat{H}_{full} that contains a two-body kinetic-energy part $\hat{T}^{[2]}$, a two-body interaction $\hat{V}^{[2]}$ and a three-body interaction $\hat{V}^{[3]}$ and may, therefore, be written as

$$\hat{H} = \hat{T}^{[2]} + \hat{V}^{[2]} + \hat{V}^{[3]}. \quad (4.4.3)$$

The operator for the kinetic energy may be written as $\hat{T}^{[2]} = \sum_{i<j} \frac{(\hat{\mathbf{p}}_i - \hat{\mathbf{p}}_j)^2}{2Am}$ [HR09], where $\hat{\mathbf{p}}_i$ indicates the momentum operator for the i -th particle, A is the mass number, and m is the nucleon mass. The three-body interaction, whose operator form is given through

$$\hat{V}^{[3]} = \frac{1}{36} \sum_{pqrst} V_{stu}^{pqr} \hat{a}_{stu}^{pqr}, \quad (4.4.4)$$

⁴Strictly speaking, we will employ either IM-SRG(2) or Magnus(2).

is now approximated by means of its NO2B approximation $\hat{V}_{\text{NO2B}}^{3\text{N}}$, i.e., the normal-ordered three-body part in the reference-state representation of $\hat{V}^{[3]}$ is neglected such that we obtain

$$\hat{V}^{[3]} \approx \hat{V}_{\text{NO2B}}^{3\text{N}} = X(s) + \sum_{pq} X_q^p(s) \{ \hat{a}_q^p \} + \frac{1}{4} \sum_{pqrs} X_{rs}^{pq}(s) \{ \hat{a}_{rs}^{pq} \}. \quad (4.4.5)$$

The zero, one and two-body matrix elements of this NO2B-approximated three-body interaction $\hat{V}_{\text{NO2B}}^{[3]}$ are essentially given through eq. (3.5.4). It is worth noting that through this NO2B approximation information on the three-body force is partially embedded within the matrix elements of lower particle-ranks. The initial Hamiltonian at $s = 0$ can now be written as

$$\hat{H}(0) = \hat{T}^{[2]} + \hat{V}^{[2]} + \hat{V}_{\text{NO2B}}^{3\text{N}}. \quad (4.4.6)$$

By Inserting the Hamiltonian and the generator given through eq. (4.4.1) and eq. (4.4.2), respectively, into the corresponding operator differential equation for $\hat{H}(s)$, we obtain

$$\frac{d}{ds} \hat{H}(s) = \left[\hat{\eta}(s), \hat{H}(s) \right] \quad (4.4.7)$$

$$= \left[\hat{\eta}^{[1]}(s), \hat{H}^{[1]}(s) \right] + \left[\hat{\eta}^{[1]}(s), \hat{H}^{[2]}(s) \right] \\ + \left[\hat{\eta}^{[2]}(s), \hat{H}^{[1]}(s) \right] + \left[\hat{\eta}^{[2]}(s), \hat{H}^{[2]}(s) \right], \quad (4.4.8)$$

where, e.g., $\hat{H}^{[i]}$ indicates the i -body part of the Hamiltonian. By Evaluating the commutator on the right-hand side of this equation via Wick's theorem,⁵ we eventually obtain a coupled system of first-order ordinary differential equations in terms of the matrix elements of the Hamiltonian and the generator. Schematically, this ODE can be expressed as follows

$$\frac{d}{ds} \vec{h}(s) = \vec{\mathcal{F}}_{\lambda} \left(\vec{\eta}(s), \vec{h}(s) \right), \quad (4.4.9)$$

where we denoted the entirety of all matrix elements of the Hamiltonian and the generator at the flow parameter s as $\vec{h}(s)$ and $\vec{\eta}(s)$, respectively. Additionally, the irreducible density matrices are a parameter to this ODE which is why they are indicated as a subscript of \mathcal{F} . As the generator itself is merely a function of the Hamilton operator, we may also write the ODE as

$$\frac{d}{ds} \vec{h}(s) = \vec{\mathcal{F}}_{\lambda, \eta} \left(\vec{h}(s) \right), \quad (4.4.10)$$

where the generator or, more specifically, the function that constructs generator matrix elements $\vec{\eta}(s)$ taking $\vec{h}(s)$ as input is now added to the parameter list of $\vec{\mathcal{F}}$. In practical applications the ODE system is then solved numerically (see appendix B for more information).

⁵Note that the derivation as-well-as an in-depth discussion of the equations associated with commutator evaluations is contained in chapter 5

4.5. Magnus Expansion—General Concepts

Up to now, we were discussing a formulation of the IM-SRG in which the unitary transformation of observables

$$\hat{H}(s) = \hat{U}^\dagger(s)\hat{H}(0)\hat{U}(s), \quad \hat{H}(0) = \hat{H}, \quad (4.5.1)$$

$$\hat{O}(s) = \hat{U}^\dagger(s)\hat{O}(0)\hat{U}(s), \quad \hat{O}(0) = \hat{O}, \quad (4.5.2)$$

was carried out via *directly* solving the associated operator differential equations

$$\frac{d}{ds}\hat{H}(s) = [\hat{\eta}(s), \hat{H}(s)], \quad \hat{H}(0) = \hat{H}, \quad (4.5.3)$$

$$\frac{d}{ds}\hat{O}(s) = [\hat{\eta}(s), \hat{O}(s)], \quad \hat{O}(0) = \hat{O}. \quad (4.5.4)$$

Let us now refer to solving these kinds of operator differential equations as the *direct evolution* of observables. Since the generator may explicitly depend on the evolved Hamiltonian a major drawback of this direct evolution is that the differential equations for observables eventually have to be solved simultaneously with the one for the Hamiltonian. Resorting to directly solving the differential equation of the unitary transformation itself

$$\frac{d}{ds}\hat{U}^\dagger(s) = \hat{\eta}(s)\hat{U}^\dagger(s), \quad \hat{U}^\dagger(0) = \hat{1}, \quad (4.5.5)$$

is not feasible as $\hat{U}(s)$ is an A -body operator. However, directly related to finding a solution for the unitary transformation is an approach which was first proposed by the mathematician Wilhelm Magnus [Mag54] in the 1950s: the so-called Magnus expansion. Since then, it has been successfully applied in many different contexts, however, it was only recently that it has been applied within the context of the IM-SRG by Morris et al. in [MPB15].

Definition 4.5.1: Magnus Expansion

A unitary transformation $\hat{U}(s)$ may be written as an exponential

$$\hat{U}^\dagger(s) = \exp(\hat{\Omega}(s)), \quad \hat{\Omega}(0) = 0, \quad (4.5.6)$$

where $\hat{\Omega}(s)$ denotes the an anti-Hermitian Magnus operator. As rigorously discussed in [Bla+09], it follows that the Magnus operator $\hat{\Omega}(s)$ obeys the differential equation

$$\frac{d}{ds}\hat{\Omega}(s) = \sum_{k=0}^{\infty} \frac{B_k}{k!} [\hat{\Omega}(s), \hat{\eta}(s)]_k, \quad \hat{\Omega}(0) = \hat{0}, \quad (4.5.7)$$

where B_k refers to the Bernoulli numbers.

For writing the differential equation for $\hat{\Omega}(s)$ in a compact form, we introduced $[\hat{X}, \hat{Y}]_k$ as a short-hand notation for nested commutators w.r.t. to two arbitrary operators \hat{X} and \hat{Y} . Formally, the recursive definition of those nested commutators may be stated as follows

$$[\hat{X}, \hat{Y}]_k = [\hat{X}, [\hat{X}, \hat{Y}]_{k-1}], \quad [\hat{X}, \hat{Y}]_0 = \hat{Y}. \quad (4.5.8)$$

Note that a derivation for the differential equation for $\hat{\Omega}(s)$ given through eq. (4.5.7) as well as a thorough mathematical review addressing, e.g., the important questions of the existence and convergence of the Magnus expansion can be found in [Bla+09].

An appealing feature of the Magnus expansion becomes particularly evident when studied within the context of Lie groups and Lie algebras: Interpreting the unitary transformation $\hat{U}(s)$ as an element of an abstract Lie group G , the anti-Hermitian generator $\hat{\eta}(s)$ is element of the corresponding Lie algebra \mathfrak{g} . Due to the fact that the commutator maps two elements of \mathfrak{g} back into \mathfrak{g} and $\hat{\Omega}(s)$ is constructed from multiple nested commutators of the form $[\hat{\Omega}(s), \hat{\eta}(s)]_k$, the operator $\hat{\Omega}(s)$ always stays within the vector space of the Lie algebra \mathfrak{g} . As a consequence, the corresponding exponential of $\hat{\Omega}(s)$ is always unitary and certain symmetries are automatically conserved throughout the evolution. Therefore, the Magnus expansion may be seen as an approach with which we have implicit access to the unitary transformation $\hat{U}(s)$ by directly obtaining the corresponding Lie algebra element $\hat{\Omega}(s)$.

Construction of the Magnus Operator I. The straightforward way for obtaining a solution for $\hat{\Omega}(s)$ is the direct integration of the ODE for $\hat{\Omega}(s)$ given through eq. (4.5.7). Thus, instead of explicitly solving the differential equations for observables, we may instead solve the associated differential equation for $\hat{\Omega}(s)$. This ODE for $\hat{\Omega}(s)$ may schematically written as follows

$$\frac{d}{ds} \vec{\Omega}(s) = \vec{F}_\eta \left(\vec{\Omega}(s), \vec{h}(s) \right), \quad (4.5.9)$$

where, similar to previous considerations, $\vec{\Omega}(s)$ and $\vec{h}(s)$ indicate the entirety of all matrix elements of the Magnus operator and the Hamiltonian, respectively, and \vec{F} defines the actual system of ODEs.

Compared to the direct evolution of, e.g., the Hamiltonian, a practical advantage of the Magnus expansion stems from the observation that the numerical solution of this differential equation for $\hat{\Omega}(s)$ is more robust with regard to numerical errors such that the numerical integration of the ODE can be carried out at larger stepsizes.

Construction of the Magnus Operator II. For completeness, we want to present another possibility for obtaining a solution for the Magnus operator $\hat{\Omega}(s)$. It is given through the

application of the so-called Picard iteration which yields [Bla+09]

$$\hat{\Omega}_1(s) = \int_0^s ds \hat{\eta} \left(s, \hat{H}(0) \right), \quad (4.5.10)$$

$$\hat{\theta}_{m-1}(s) = \sum_{l=0}^{m-1} \frac{1}{l!} \left[\hat{\Omega}_{m-1}(s), \hat{H}(0) \right]_l, \quad (4.5.11)$$

$$\hat{\Omega}_m(s) = \sum_{k=0}^{m-2} \frac{B_k}{k!} \int_0^s ds \left[\hat{\Omega}_{m-1}(s), \hat{\eta} \left(s, \hat{\theta}_{m-1}(s) \right) \right]_k. \quad (4.5.12)$$

The object $\hat{\Omega}_m(s)$ may be interpreted as follows: Assuming that $\hat{\Omega}(s)$ may be written as an expansion w.r.t. the parameter ϵ

$$\hat{\Omega}(s) = \sum_{n=1}^{\infty} \epsilon^n \hat{X}_n(s), \quad (4.5.13)$$

the solution $\hat{\Omega}_m(s)$ recovers the first m terms of this expansion. Additionally, it can be shown that the associated unitary transformation $\hat{U}^\dagger(s) = \exp \left(\hat{\Omega}_m(s) \right)$ is exact up to orders $\mathcal{O}(s^{m+1})$. From a mathematical point of view it might be interesting to construct a solution for $\hat{\Omega}(s)$ through eqs. (4.5.10) to (4.5.12). In contrast to the previous approach—where $\hat{\Omega}(s)$ was obtained by solving a differential equation—we would now construct the solution for $\hat{\Omega}(s)$ by solving integral equations. However, even though these equations can be simplified due to the fact that the generator does not explicitly depend on the flow parameter s , they are not applicable in practical applications as, e.g., we would have to store many copies of the evolved operators at various values for the flow parameter s for evaluating the integrals. We performed an exploratory study, where we included terms of up to $m = 3$, which showed that higher order terms are necessary for obtaining an adequate solution. This would imply a significant increase in complexity w.r.t., both, analytical derivation and computational implementation.

Observable Transformation. Assuming that we are able to construct the Magnus operator $\hat{\Omega}(s)$, a vital question is how we can carry out the unitary transformation of an initial observable $\hat{O}(0)$ such that we obtain its transformed counterpart $\hat{O}(s)$. For that purpose, let us consider eq. (4.5.6) showing the original Ansatz for the unitary transformation in terms of an exponential of the Magnus operator. This illustrates that, in principle, we have access to the unitary transformation through exponentiation. However, we are never calculating the unitary transformation explicitly but employ the Baker-Campbell-Hausdorff (BCH) series for the unitary transformation of arbitrary observables

$$\hat{O}(s) = \hat{U}^\dagger(s) \hat{O}(0) \hat{U}(s) = e^{+\hat{\Omega}(s)} \hat{O}(0) e^{-\hat{\Omega}(s)} \stackrel{\text{BCH}}{=} \sum_{k=0}^{\infty} \frac{1}{k!} \left[\hat{\Omega}(s), \hat{O}(0) \right]_k. \quad (4.5.14)$$

Opposed to the *direct evolution* of observables, this kind of evolution of observables is now referred to as *Magnus-type* evolution of observables.

Let us now take the opportunity and briefly compare the two different kinds of evolutions, i.e., the Magnus-type evolution and direct evolution, with each other. On the one hand, the direct integration of the ODE for an operator $\hat{O}(s)$ by an infinitesimal step forward such that we obtain $\hat{O}(s + \delta s)$ may be interpreted as the application of an infinitesimal unitary transformation $\delta\hat{U}(s)$. The complete unitary transformation giving $\hat{O}(s)$ from $\hat{O}(0)$ may then be interpreted as a consecutive application of infinitesimal unitary transformations.

However, while the transformation associated with directly solving the ODE for an observable is guaranteed to be unitary through the very structure of the associated ODE, we never gain any direct access to the underlying unitary transformations. On the other hand, the big advantage of the Magnus expansion is that it combines all of these tiny, consecutive transformations and casts them into the Magnus operator $\hat{\Omega}(s)$ such that we gain access to the complete unitary transformation.

It is important to keep in mind that a transformation of observables is not only necessary *after* we have found a solution for $\hat{\Omega}(s)$ but also during the construction of $\hat{\Omega}(s)$ as $\frac{d}{ds}\hat{\Omega}(s)$ may implicitly depend on the Hamiltonian $\hat{H}(s)$. For obtaining $\hat{H}(s)$, we may either directly evolve $\hat{H}(s)$ simultaneously with $\hat{\Omega}(s)$ or perform a Magnus evolution of $\hat{H}(s)$ and evaluate the BCH series. At the moment, we employ the Magnus evolution of $\hat{H}(s)$ for reducing the memory requirements of our implementation.

4.6. Magnus(2)

Similarly to the IM-SRG(2), we have to truncate our operators at a specific particle rank for keeping analytical and computational efforts within certain limits. Therefore, we use the following Ansatz for the Magnus operator $\hat{\Omega}(s)$

$$\hat{\Omega}(s) = \sum_{pq} \Omega_q^p \{ \hat{a}_q^p \} + \frac{1}{4} \sum_{pqrs} \Omega_{rs}^{pq} \{ \hat{a}_{rs}^{pq} \}, \quad (4.6.1)$$

i.e., we are truncating this operator at the NO2B level. Furthermore, the evaluation of each of the convoluted commutators in the derivative for $\hat{\Omega}(s)$

$$\hat{\Omega}'(s) \equiv \frac{d}{ds} \hat{\Omega}(s) = \sum_{k=0}^{\infty} \frac{B_k}{k!} \left[\hat{\Omega}(s), \hat{\eta}(s) \right]_k, \quad (4.6.2)$$

and the BCH series for observables

$$\hat{O}(s) = \sum_{k=0}^{\infty} \frac{1}{k!} \left[\hat{\Omega}(s), \hat{O}(0) \right]_k, \quad (4.6.3)$$

is also truncated at the NO2B level. This truncation scheme is referred to as Magnus(2). Taking into account that the series $\hat{\Omega}'(s)$ as well as the BCH series are infinite, it follows that both

have to be subject to some kind of truncation scheme in practical applications, which will be addressed throughout this section.

We would like to emphasize that the transformation $\hat{U}^\dagger(s) = \exp(\hat{\Omega}(s))$ associated with the Magnus operator $\hat{\Omega}(s)$ is always unitary—even if the calculation of $\hat{\Omega}(s)$ or $\hat{\Omega}'(s)$ is subject to truncations and approximations. The only departure from an exact unitary transformation of an observable \hat{O} , however, arises due to truncations of the BCH series for \hat{O} , where especially the NO2B approximation introduces a theoretical uncertainty.

As both the derivative for $\hat{\Omega}(s)$ and the BCH series rest upon the evaluation of nested commutators, we would like to remark that the *numerical* computation of a nested commutator of depth k is generally performed iteratively by means of k sequential commutator evaluations: Always evaluating only one simple commutator at a time, the numerical result is stored and inserted into the commutator of the next higher order. As a consequence, the numerical calculation of those nested commutators breaks down to the calculation of simple commutators similar to the ones we have already encountered in view of the operator ODEs for observables. This emphasizes the importance of an efficient, general purpose commutator evaluation machinery, which will be discussed in chapter 5.

Construction and Convergence of the Magnus Operator. Algorithmically, the Magnus expansion or, more specifically, the derivative for the Magnus operator is constructed iteratively. Considering the formula for the derivative

$$\frac{d}{ds} \hat{\Omega}(s) = \sum_{k=0}^{\infty} \frac{B_k}{k!} [\hat{\Omega}(s), \hat{\eta}(s)]_k, \quad (4.6.4)$$

and expressing the k -th term in this series as follows

$$\frac{B_k}{k!} [\hat{\Omega}(s), \hat{\eta}(s)]_k = \frac{B_k}{k!} \left[\hat{\Omega}(s), [\hat{\Omega}(s), \hat{\eta}(s)]_{k-1} \right], \quad (4.6.5)$$

illustrates that the depth- k commutator appearing at order k of the series only requires the computation of only one additional commutator as the commutator already calculated at order $k - 1$ is reappearing again and may therefore be reused. Furthermore, we established a specific convergence criterion for the calculation of the derivative of the Magnus operator by truncating the associated series at a specific order x

$$\hat{\Omega}'_x(s) \equiv \sum_{k=0}^x \frac{B_k}{k!} [\hat{\Omega}(s), \hat{\eta}(s)]_k. \quad (4.6.6)$$

Formally, the order x at which the series is considered as converged fulfills the criterion

$$\frac{\|\hat{\Omega}'_x(s) - \hat{\Omega}'_{x-1}(s)\|}{\|\hat{\Omega}'_x(s)\|} < \epsilon \equiv 1 \times 10^{-2} \quad \text{and} \quad B_x \neq 0, \quad (4.6.7)$$

where only orders with non-vanishing Bernoulli numbers are taken into account. Note that we generally employ a simple two-norm $\|\hat{X}\| \equiv \sqrt{X^2 + \sum_{ij}(X_j^i)^2 + \sum_{ijkl}(X_{kl}^{ij})^2}$. The particular value for ϵ in this case has to be chosen small enough such that a further decrease has no additional impact on numerical results. Taking numerical efficiency into consideration, it should also not be chosen too small. As the evaluation of commutators is the driving force regarding computational effort the total number of commutator evaluations should always be kept at a minimum. For practical applications, we are using $\epsilon = 1 \times 10^{-2}$ as a further decrease of this value has no impact on our numerical results and the series is usually converged at orders k of 2 to 4.

However, employing only the convergence criterion given through eq. (4.6.7), there may be occasional problems with divergencies for the series of $\hat{\Omega}'(s)$ due to too large stepsizes during the numerical integration of the ODE for $\hat{\Omega}(s)$. We made the observation that the series seemed to converge taking only lower order terms ($k \approx 2$) into account, but at intermediate orders of the series ($k \approx 10$) the norm of corresponding terms began to increase exponentially. One possible solution is to require a certain lower bound for the order at which the series for $\hat{\Omega}'(s)$ may be truncated like, e.g., always calculate the series up to at least the tenth order. However, as we want our implementation to be as computationally efficient as possible and as the commutator evaluation is the computationally most expensive part, we prefer a solution with which we can diagnose eventual divergencies of the Magnus series already at relatively low orders of the series. As the explosive increase is rooted in the fact that the norm of the commutator itself is not decreasing but rapidly increasing with regard to k , we require, additionally to eq. (4.6.7), the following heuristically motivated condition to be fulfilled

$$\frac{\|[\hat{\Omega}(s), \hat{\eta}(s)]_k\|}{\|[\hat{\Omega}(s), \hat{\eta}(s)]_{k-1}\|} \stackrel{!}{<} 1 \quad \text{for all } k \text{ with } 1 \leq k \leq k_{\max}, \quad (4.6.8)$$

where k_{\max} is the order at which the series is converged according to eq. (4.6.7). We choose this condition due to the observation that once the norm of commutator part is sufficiently decreasing w.r.t. the order k , it is keeping this behavior also at higher orders and, as a consequence, $\hat{\Omega}'(s)$ converges. However, if during the evolution of $\hat{\Omega}(s)$ eq. (4.6.8) is not fulfilled at any order k , the series for $\hat{\Omega}'(s)$ is considered as divergent and the current integration step is restarted with a decreased stepsize—as a too large stepsize is the root of the problem after all.

As already mentioned previously, the numerical integration of the ODE for $\hat{\Omega}(s)$ is numerically much more robust than a corresponding integration of the ODE for the Hamiltonian. This might be partially rooted in the fact that, considering the direct integration of the ODE for the Hamiltonian, numerical errors may lead to a break of unitarity. In contrast, during the integration of the ODE for $\hat{\Omega}(s)$ eventual numerical errors only have an impact on the Magnus operator. Even if these numerical errors lead to a deviation from the decoupling pattern we were originally aiming for, the associated transformation will always remain unitary. It is this conservation of unitarity, which leads to the fact that we could even solve the ODE for $\hat{\Omega}(s)$ via

a simple Euler method. However, we are employing a more involved approach as described in appendix B.

Construction and Convergence of the BCH Series. Similarly to the construction of the series for $\hat{\Omega}'(s)$, also the BCH series is constructed iteratively. Considering the BCH series,

$$\hat{O}(s) = \sum_{k=0}^{\infty} \frac{1}{k!} \left[\hat{\Omega}(s), \hat{O}(0) \right]_k \equiv \sum_{k=0}^{\infty} \hat{O}_k, \quad (4.6.9)$$

the k -th order contribution of the series, denoted as \hat{O}_k , may also be written as follows⁶

$$\hat{O}_k(s) = \frac{1}{k} \left[\hat{\Omega}(s), \hat{O}_{k-1}(s) \right]. \quad (4.6.10)$$

This shows that the k -th order term may be constructed by reusing the result of the order $k - 1$ such that at each order only one additional commutator has to be computed. As the BCH series has to be truncated at a specific order in practical applications, we are choosing a convergence criterion similar to the one for the derivative of the Magnus operator which may be written as follows

$$\delta_{\text{norm}}^{[x]} \equiv \frac{\|\hat{O}_x(s)\|}{\left\| \sum_{k=0}^x \hat{O}_k(s) \right\|} < \epsilon \ll 1. \quad (4.6.11)$$

The particular choice for the value of ϵ obviously has a significant impact on both computational effort and precision of our numerical results as the transformation is, formally, only unitary for $\epsilon \rightarrow 0$. Therefore, the choice for ϵ may vary depending on the particular context.

For finding an adequate choice for the threshold ϵ , let us first consider fig. 4.3. It depicts the evolution of the expectation value of a Magnus-evolved Hamiltonian

$$\langle \psi_{\text{ref}} | \sum_{k=0}^{k_{\text{max}}^{\text{BCH}}} \hat{H}_k(s) | \psi_{\text{ref}} \rangle, \quad (4.6.12)$$

where several different orders $k_{\text{max}}^{\text{BCH}}$ are shown. Additionally, it depicts the evolution of the expectation of a directly evolved Hamiltonian. Evidently, the inclusion of the first three orders is most important for obtaining a ground-state energy that agrees with the direct integration of the ODE for the Hamiltonian.

Furthermore, the individual contributions at each order to the expectation value may have different signs: While the first-order contribution is strongly attractive, the second order contribution is repulsive. Note that we only show $k_{\text{max}}^{\text{BCH}} \leq 4$ as higher orders lie practically on top of each other, i.e., the series is rapidly converging.

⁶Note the difference between \hat{O}_k and $\hat{\Omega}'_k$: The former refers to the k -th order term, while the latter indicates the partial sum up to the k -th order term.

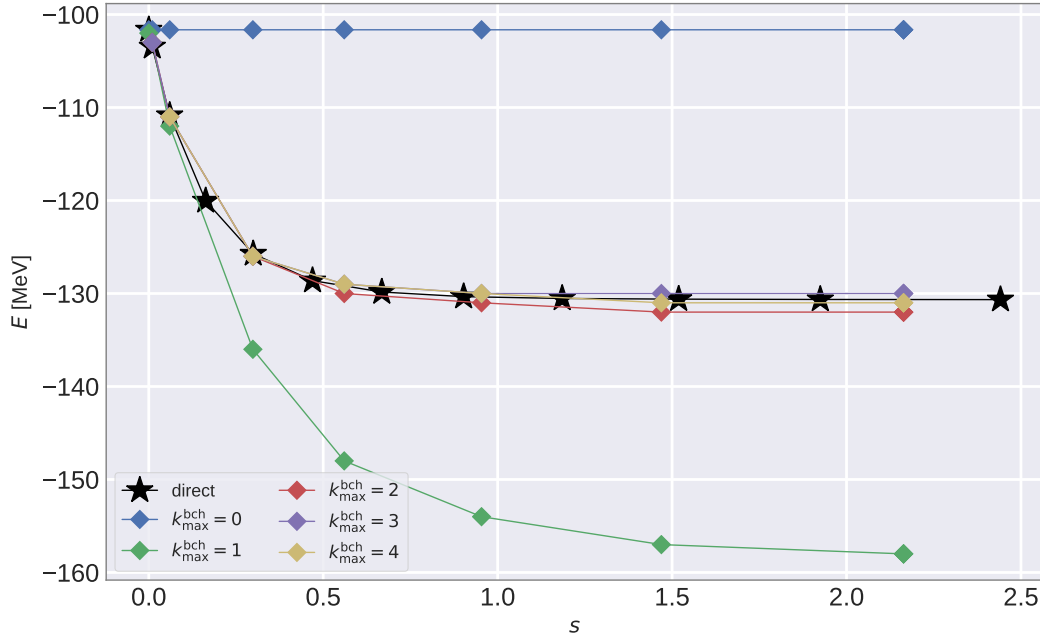


Figure 4.3.: Ground-state energy for ^{16}O . Solving the ODE for the Magnus operator, we employed the solution for $\hat{\Omega}(s)$ for obtaining the transformed Hamiltonian $\hat{H}(s)$ by means of the BCH series. The figure depicts the expectation value of this Magnus-evolved Hamiltonian for several orders k_{\max}^{bch} at which the BCH series was truncated (also depicted through eq. (4.6.12)). Additionally, the figure shows the expectation value of a directly evolved Hamiltonian $\hat{H}(s)$. The calculation was performed with the White generator and the $\text{N}^3\text{LO}_{\text{EM}} + \text{N}^2\text{LO}_{400\text{L}}$ interaction (see chapter 6 for more information on commonly used interactions).

Another interesting feature of the Magnus evolution of observables becomes obvious when comparing the stepsizes of the the Magnus and the direct evolution of $\hat{H}(s)$ with each other. As each symbol corresponds to an ODE integration step for either $\hat{\Omega}(s)$ or $\hat{H}(s)$, it becomes apparent that—given a specific numerical error threshold which should be chosen such that there is no impact on calculated observables⁷—the automatic stepsize control allows the ODE for the Magnus operator to be integrated at slightly larger stepsizes than it is the case for the ODE for the Hamiltonian. The potentially larger stepsizes illustrate another advantage of the Magnus evolution.

For studying the impact of a truncation of the BCH series at the k -th order, the left-hand side of fig. 4.4 shows the evolution of the relative expectation value of the k -th order term defined

⁷See appendix B for for more information and specific values for the error thresholds.

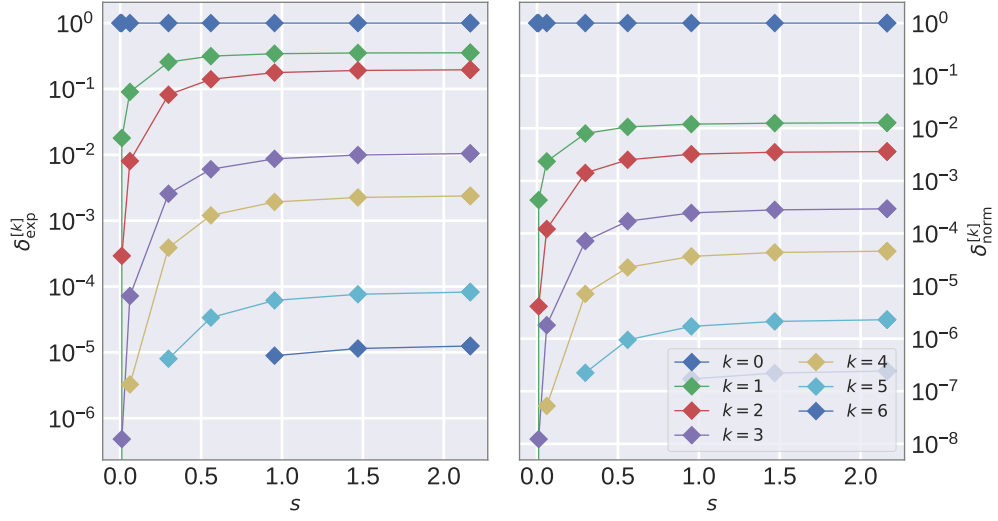


Figure 4.4.: Similarly to fig. 4.3, we solved the ODE for the Magnus operator such that we obtained $\hat{\Omega}(s)$ at several values for the flow parameter s and which was employed for the evaluation of the BCH series for the Hamiltonian. The left-hand side depicts the relative expectation value of the k -th order contribution of the BCH series $\delta_{\text{exp}}^{[k]}$ (see eq. (4.6.11)) and the right-hand side shows the relative norm of the k -th order contribution $\delta_{\text{norm}}^{[k]}$ (see eq. (4.6.13)). Calculations were performed for ^{16}O .

as

$$\delta_{\text{exp}}^{[k]} \equiv \frac{\left\| \langle \psi_{\text{ref}} | \hat{H}_k(s) | \psi_{\text{ref}} \rangle \right\|}{\left\| \langle \psi_{\text{ref}} | \sum_{x=0}^k \hat{H}_x(s) | \psi_{\text{ref}} \rangle \right\|}. \quad (4.6.13)$$

Furthermore, the right-hand side depicts the relative norm of the k -th order term defined in eq. (4.6.11). Considering the values for $\delta_{\text{exp}}^{[k]}$, a rather strict precision goal of about $\delta_{\text{exp}}^{[k]} \leq 1 \times 10^{-4}$ is obtained at $k \approx 5$ which corresponds to $\delta_{\text{norm}}^{[k]} \approx 1 \times 10^{-6}$. Therefore, we choose $\epsilon = 1 \times 10^{-6}$ for all observables that are transformed *after* $\hat{\Omega}(s)$ has been successfully evolved. However, during the evolution of $\hat{\Omega}(s)$ we have to transform the Hamiltonian multiple times. We have found that it is usually sufficient to transform the Hamiltonian in a rather approximate manner by employing a threshold of about $\epsilon = 1 \times 10^{-2}$ which is usually reached at the first or second order of the BCH series. While this is obviously not adequate for obtaining sufficiently precise values for the expectation value of the Hamiltonian, we have found that it is usually sufficient to let the generator only “see” the lowest order contributions of the BCH series to $\hat{H}(s)$. This indicates that these parts are already containing the relevant off-diagonal part which we wish to suppress. The great advantage of this approximate approach is that we are able to significantly boost the numerical efficiency as the number of necessary commuta-

tor evaluations is greatly reduced while—as we have verified in numerical applications—the choice of $\epsilon \approx 1 \times 10^{-2}$ has no significant impact on our numerical results.

Furthermore, we would like to emphasize that this kind of approximation for $\hat{H}(s)$ only introduces another approximation for the series of $\hat{\Omega}'(s)$ —additionally to the truncation of the series at specific order. Even if any of these two kinds of approximations leads to a solution $\hat{\Omega}(s)$ with which we depart from the originally intended decoupling pattern, the associated transformation is still unitary.

4.7. Generators for the IM-SRG

As mentioned before, the IM-SRG aims at suppressing a specific off-diagonal part of the Hamiltonian such that a particular *decoupling pattern* is achieved. Which part of the Hamiltonian we would like to suppress depends on the nature of our problem and can vary significantly. However, all problems discussed in this work define the off-diagonal part as the part of the Hamiltonian that couples a reference-state $|\psi_{\text{ref}}\rangle$ to particle-hole excitations. The question that arises is how to construct a generator $\hat{\eta}(s)$ that suppresses a specific off-diagonal part during the IM-SRG evolution. As it turns out, there are several choices—so-called generator types—available which we discuss in this chapter. In contrast to the *decoupling pattern*, the generator type governs the *decoupling behavior*, i.e., it controls the numerical efficiency and stability of the evolution. The off-diagonal part and the generator type are two independent degrees of freedom that serve as the main ingredients for the construction of a specific generator $\hat{\eta}(s)$ and its matrix elements.

Pictorially, the generator type defines the path within the operator space of unitary equivalent Hamiltonians from an initial to a final Hamiltonian $\hat{H}(0)$ and $\hat{H}(\infty)$, respectively. Eventually, it even defines which particular $\hat{H}(\infty)$ the Hamiltonian is driven to, since there are infinitely many unitarily equivalent operators that are compatible with a decoupling pattern that contains invariant subspaces. However, we are not using an IM-SRG(A) but an IM-SRG(k) framework. As a consequence, unitarity is formally broken and a variation of the path from $\hat{H}(s)$ to $\hat{H}(s + \delta s)$ potentially has an impact on the induced many-body terms beyond the k -particle rank. Hence, the generator type not only defines the *decoupling behavior* but it also controls the error of the IM-SRG(k).

In this work we will employ three different generators types: White [Whi02], imaginary-time, and Wegner [Weg94]. In what follows, we will discuss their operator structure in A -body space and, if possible, give formulas for the construction of their matrix elements. Note that an in-depth analysis of the properties and behavior of generators that goes well beyond our brief discussion can be found in [Her+16; Her17].

Another generator that is commonly employed in the context of the MR-IM-SRG with HFB reference states is the Brillouin generator [Her17]. This generator employs the irreducible

Brillouin conditions [KM04] such that the energy is variationally minimized under the corresponding unitary transformations. While this generator has not been employed in this work, we might reconsider this generator type in future applications—especially in view of the newest generator optimizations that we recently implemented (see chapter 6).

Wegner Generator. From a conceptional point of view, the Wegner generator, first proposed by Wegner in [Weg94], is the most simple choice. As already discussed in section 4.1, it is defined as the commutator between the diagonal part of the Hamiltonian $\hat{H}^d(s)$ and the Hamiltonian itself

$$\hat{\eta}(s) = \left[\hat{H}^d(s), \hat{H}(s) \right] = \left[\hat{H}^d(s), \hat{H}^{\text{od}}(s) \right]. \quad (4.7.1)$$

It can be shown that $\hat{H}^d(s)$ is a trivial, attractive fixed point of an associated evolution of $\hat{H}(s)$

$$\frac{d}{ds} \hat{H}(s) = \left[\hat{\eta}(s), \hat{H}(s) \right], \quad (4.7.2)$$

which is reached for $s \rightarrow \infty$ as $\hat{H}^{\text{od}}(\infty)$ vanishes. Note that for cases in which $\hat{H}^d(s)$ and $\hat{H}^{\text{od}}(s)$ commute with each other due to degeneracies in the spectrum of $\hat{H}(s)$, we may observe fixed points already at finite values of s [Her+16]. In practical calculations, however, the Wegner generator is a very inefficient choice, since the resulting system of ODEs becomes stiff.

It is worth noting that the Wegner generator leads to a true renormalization-group transformation, i.e., it preferably suppresses off-diagonal matrix elements with large energy differences of the corresponding diagonal elements. This property can be nicely demonstrated by analyzing the asymptotic suppression behavior of off-diagonal matrix elements, which yields [Her+16]

$$\langle i | \hat{H}^{\text{od}}(s) | j \rangle = \langle i | \hat{H}^{\text{od}}(s_0) | j \rangle e^{-(E_i - E_j)^2 (s - s_0)}, \quad s > s_0, \quad (4.7.3)$$

where s_0 has to be sufficiently large. Here, we chose the eigenbasis of $\hat{H}^d(s)$ for the representation of $\hat{H}^{\text{od}}(s)$ and E_i refers to the eigenvalues of $\hat{H}^d(s)$.

As the definition of the Wegner generator is based on a commutator, its matrix elements may be constructed by utilizing the general purpose commutator-evaluation machinery, which will be addressed in chapter 5.

In second quantization, the off-diagonal Hamiltonian takes the form

$$\hat{H}^{\text{od}} = \sum_{pq} (f^{\text{od}})_q^p \{ \hat{a}_q^p \} + \frac{1}{4} \sum_{pqrs} (\Gamma^{\text{od}})_{rs}^{pq} \{ \hat{a}_{rs}^{pq} \}, \quad (4.7.4)$$

where the off-diagonal matrix elements are given through

$$(f^{\text{od}})_2^1 = \langle \psi_{\text{ref}} | \hat{H} \{ \hat{a}_2^1 \} | \psi_{\text{ref}} \rangle + [1 \leftrightarrow 2], \quad (4.7.5)$$

$$(\Gamma^{\text{od}})_{34}^{12} = \langle \psi_{\text{ref}} | \hat{H} \{ \hat{a}_{34}^{12} \} | \psi_{\text{ref}} \rangle + [(1, 2) \leftrightarrow (3, 4)]. \quad (4.7.6)$$

White & Imaginary-Time Generator. In this work, we will be mostly dealing with two generator types: Firstly, the White generator, which was first proposed by White in [Whi02] in the context of quantum chemistry, and secondly, the imaginary-time generator, which is originally inspired by Quantum Monte Carlo methods [Car+15]. Both of these generators show an improved decoupling behavior and the associated ODE systems are less stiff than for the Wegner generator. Furthermore, their construction is computationally less demanding than the Wegner generator.

Let us assume that we are aiming to decouple two subspaces $\mathcal{M}, \mathcal{M}' \subset \mathcal{H}^{\text{a.s.}}$ from each other with the properties $\mathcal{M} \cup \mathcal{M}' = \mathcal{H}^{\text{a.s.}}$ and $\mathcal{M} \cap \mathcal{M}' = \emptyset$. The decoupling condition, therefore, reads

$$\langle \Psi | \hat{H} | \Psi' \rangle \stackrel{!}{=} 0 \quad \forall |\Psi\rangle \in \mathcal{B}, |\Psi'\rangle \in \mathcal{B}', \quad (4.7.7)$$

where \mathcal{B} and \mathcal{B}' denote the basis of \mathcal{M} and \mathcal{M}' , respectively. We may now write down the definition of both generators in A -body space as follows

$$\hat{\eta} = \sum_{\substack{\Psi \in \mathcal{B} \\ \Psi' \in \mathcal{B}'}} \langle \Psi | \hat{H} | \Psi' \rangle \mathcal{F} \left(\langle \Psi | \hat{H} | \Psi \rangle - \langle \Psi' | \hat{H} | \Psi' \rangle \right) |\Psi\rangle \langle \Psi'| - \text{h.c.}, \quad (4.7.8)$$

where the argument of the function \mathcal{F} are differences of the diagonal part and varies with the specific generator type

$$\mathcal{F}(x) = \begin{cases} x^{-1} & \text{for White} \\ \text{sgn}(x) & \text{for imaginary-time} \end{cases}. \quad (4.7.9)$$

Note that we suppressed any dependency on the flow parameter s for brevity. Similar to previous considerations with regard to the Wegner generator, an analysis of the asymptotic suppression behavior of the matrix elements of the off-diagonal part $\hat{H}^{\text{od}}(s)$ for $s > s_0$ yields [Her+16; Her17]

$$\langle i | \hat{H}^{\text{od}}(s) | j \rangle = \langle i | \hat{H}^{\text{od}}(s_0) | j \rangle e^{-(s-s_0)}, \quad (4.7.10)$$

$$\langle i | \hat{H}^{\text{od}}(s) | j \rangle = \langle i | \hat{H}^{\text{od}}(s_0) | j \rangle e^{-|E_i - E_j|(s-s_0)}, \quad (4.7.11)$$

for the White and imaginary-time generator, respectively, where $|i\rangle$ and E_i refer to eigenstates and eigenvalues of $\hat{H}^{\text{d}}(s)$, respectively. It is the approximate suppression behavior that treats all matrix elements equally regardless of any energy differences that makes the White generator the numerically most efficient choice. However, in some cases we might encounter divergencies of generator matrix elements due to vanishing denominators. As a resort the numerically less efficient but more stable imaginary-time generator may be employed.

However, as the IM-SRG is formulated in terms of operators in second quantization, we have to cast the definition above into the form

$$\hat{\eta}(s) = \sum_{pq} \eta_q^p \{ \hat{a}_q^p \}_{|\psi_{\text{ref}}\rangle} + \frac{1}{4} \sum_{pqrs} \eta_{rs}^{pq} \{ \hat{a}_{rs}^{pq} \}_{|\psi_{\text{ref}}\rangle}. \quad (4.7.12)$$

For that purpose, let us now assume that \mathbb{B} only has one element denoted as $|\Psi\rangle$, which is also employed as the reference state, i.e., $|\psi_{\text{ref}}\rangle \equiv |\Psi\rangle$. Furthermore, we employ that any $|\Psi'\rangle \in \mathbb{B}'$ can be expressed as a (generalized) k -particle k -hole excitation w.r.t. $|\Psi\rangle$, i.e.,

$$|\Psi'\rangle = \{ \hat{a}_{q_1 \dots q_k}^{p_1 \dots p_k} \} |\Psi\rangle . \quad (4.7.13)$$

Inspired by the definition of the generator matrix elements in A -body space, we obtain the following definition for a general k -body generator matrix element.

Definition 4.7.1: Generator Matrix Elements

A general k -body matrix element of the White or imaginary-time generator in reference-state representation w.r.t. $|\Psi\rangle$

$$\hat{\eta}(s) = \sum_{pq} \eta_q^p \{ \hat{a}_q^p \}_{|\Psi\rangle} + \frac{1}{4} \sum_{pqrs} \eta_{rs}^{pq} \{ \hat{a}_{rs}^{pq} \}_{|\Psi\rangle} + \dots , \quad (4.7.14)$$

may be written as follows

$$\eta_{q_1 \dots q_k}^{p_1 \dots p_k} = \langle \Psi | \hat{H} \{ \hat{a}_{q_1 \dots q_k}^{p_1 \dots p_k} \} | \Psi \rangle \mathcal{F}(\Delta_{p_1 \dots p_k q_1 \dots q_k}) - [p_1 \dots p_k \leftrightarrow q_1 \dots q_k] , \quad (4.7.15)$$

where we use a short-hand notation for the difference of diagonal elements

$$\Delta_{p_1 \dots p_k q_1 \dots q_k} \equiv \langle \Psi_0 | \hat{H} | \Psi_0 \rangle - \langle \Psi_0 | \{ \hat{a}_{q_1 \dots q_k}^{p_1 \dots p_k} \}^\dagger \hat{H} \{ \hat{a}_{q_1 \dots q_k}^{p_1 \dots p_k} \} | \Psi_0 \rangle , \quad (4.7.16)$$

and employ the definition

$$\mathcal{F}(x) = \begin{cases} x^{-1} & \text{for White} \\ \text{sgn}(x) & \text{for imaginary-time} \end{cases} . \quad (4.7.17)$$

This definition naturally leads to a vanishing generator, once the decoupling condition is fulfilled, i.e., the off-diagonal part of the Hamiltonian is suppressed. As a consequence, any $\hat{H}(s)$ that is compatible with the decoupling pattern is a fixed point of the operator differential equation $\frac{d}{ds} \hat{H}(s) = [\hat{\eta}(s), \hat{H}(s)]$ and the flow stops. It is important to note that the general definition of White and imaginary-time matrix elements given through definition 4.7.1 is employed in several contexts throughout this work: the single-reference IM-SRG, the multi-reference IM-SRG within the context of the IM-NCSM, the construction of effective valence-space interactions via the single-reference IM-SRG.

4.8. Applications—Single-Reference IM-SRG

A straightforward and conceptionally rather simple application of the general framework that gives us useful insights into its essential concepts is the single-reference IM-SRG. It utilizes

the IM-SRG framework for the decoupling of a reference state $|\psi_{\text{ref}}\rangle$ from its ph-excitations $\{\hat{a}_{q_1}^{p_1}\}|\psi_{\text{ref}}\rangle$, $\{\hat{a}_{q_1 q_2}^{p_1 p_2}\}|\psi_{\text{ref}}\rangle$. The single-reference IM-SRG is characterized by the choice of a single Slater determinant as reference state. As a first step, we have to define the off-diagonal part of the Hamiltonian that we are aiming to suppress, i.e., partition the Hamiltonian into a diagonal and an off-diagonal part $\hat{H} = \hat{H}^{\text{d}} + \hat{H}^{\text{od}}$. To that end, we have to examine which matrix elements of the Hamiltonian are coupling the reference state to its excitations. Using Wick's theorem, it is straightforward to obtain

$$\langle \psi_{\text{ref}} | \hat{H} \{ \hat{a}_{q_1}^{p_1} \} | \psi_{\text{ref}} \rangle = f_{q_1}^{p_1} \bar{n}_{p_1} n_{q_1} , \quad (4.8.1)$$

$$\langle \psi_{\text{ref}} | \hat{H} \{ \hat{a}_{q_1 q_2}^{p_1 p_2} \} | \psi_{\text{ref}} \rangle = \Gamma_{q_1 q_2}^{p_1 p_2} \bar{n}_{p_1} \bar{n}_{p_2} n_{q_1} n_{q_2} , \quad (4.8.2)$$

where \hat{H} refers to the Hamiltonian in reference-state representation given in eq. (4.4.1). It is these matrix elements that form the off-diagonal part \hat{H}^{od} . The only thing that is left before we are able to construct specific generator matrix elements is a specification of a particular generator type. Considering the White and imaginary-time generator and employing definition 4.7.1, their matrix elements may be written as

$$\eta_2^1 = f_2^1 \bar{n}_1 n_2 \mathcal{F}(\Delta_{12}) , \quad (4.8.3)$$

$$\Delta_{12} = f_1^1 - f_2^2 - \Gamma_{12}^{12} , \quad (4.8.4)$$

$$\eta_{34}^{12} = \Gamma_{34}^{12} \bar{n}_1 \bar{n}_2 n_3 n_4 \mathcal{F}(\Delta_{1234}) , \quad (4.8.5)$$

$$\Delta_{1234} = f_1^1 + f_2^2 - f_3^3 - f_4^4 + \Gamma_{12}^{12} + \Gamma_{34}^{34} - \Gamma_{13}^{13} - \Gamma_{14}^{14} - \Gamma_{23}^{23} - \Gamma_{24}^{24} \quad (4.8.6)$$

where the definition for the function \mathcal{F} depends on the generator type. It is an interesting observation that the argument to \mathcal{F} clearly resembles the energy denominator found within the analytical expression for the second-order energy correction from perturbation theory employing an Epstein-Nesbet partitioning [BS09; SO96]. Furthermore, by omitting the two-body matrix elements, we would obtain the energy denominator of the second-order energy correction in a Møller-Plesset partitioning. All in all, the particular analytical expressions for the generator matrix elements in the single-reference case demonstrate that there is a connection between the IM-SRG and perturbation theory.

Once the off-diagonal part of the Hamiltonian $\hat{H}^{\text{od}}(s)$ is sufficiently suppressed, the reference state becomes an eigenstate of $\hat{H}(s)$ where the corresponding eigenvalue is the zero-body part of the evolved Hamiltonian

$$E_0 \equiv \langle \psi_{\text{ref}} | \hat{H}(s) | \psi_{\text{ref}} \rangle . \quad (4.8.7)$$

As we are numerically solving a system of ODEs, we have to define a particular convergence criterion for the evolution of $\hat{H}(s)$. For that purpose, we are employing second-order perturbation theory for a simple and computationally very cheap way for monitoring the progress of the suppression of the off-diagonal part. We are calculating the second-order energy correction $E^{(2)}$ at each integration step of the ODE and take its ratio with the current zero-body

part of the Hamiltonian into consideration. Once this ratio becomes sufficiently small, i.e.,

$$\frac{E^{(2)}}{\langle \psi_{\text{ref}} | \hat{H} | \psi_{\text{ref}} \rangle} < \epsilon \ll 1, \quad (4.8.8)$$

we consider the evolution as converged. The convergence threshold ϵ is usually chosen as 1×10^{-4} to 1×10^{-3} for obtaining reliable results.

Figure 4.5 shows a single-reference evolution for ${}^4\text{He}$ depicting E_0 and $E_0 + E^{(2)}$ (left-hand side) and the suppression of the norm of the one and two-body off-diagonal part of the Hamiltonian (right-hand side). Evidently, the second-order correction is rapidly absorbed into the zero-body part of the Hamiltonian such that, finally, both lines lie on top each other and the convergence criterion is fulfilled. Likewise, the norm of the two-body off-diagonal part of the Hamiltonian is suppressed by several orders of magnitude. The norm of the one-body off-diagonal part—initially zero as we are employing the Hartree-Fock basis for which the Brillouin condition holds—slightly increases at the beginning of the evolution and begins to decrease again at the end of the evolution.

A matrix plot of the initial and evolved Hamilton matrix in a particle-hole basis is shown in fig. 4.6. We can observe that strong initial couplings of the reference state to two-particle two-hole excitations are suppressed in the evolved Hamiltonian. Note that there are no initial couplings to one-particle one-hole excitations due to the use of the Hartree-Fock single-particle basis and the associated Brillouin condition. Furthermore, it becomes apparent that the transformation does not only affect the blocks corresponding to couplings of the reference state to $npnh$ excitations, but also makes the Hamilton matrix more band-diagonal by also suppressing, e.g., the block that is associated with a coupling of 1p1h excitations to 3p3h excitations.

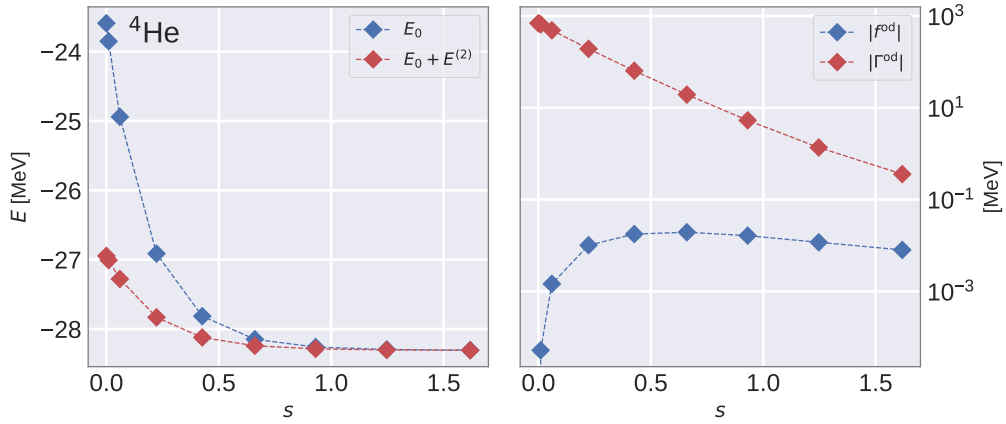


Figure 4.5.: Results of a single-reference IM-SRG calculation for ${}^4\text{He}$. The left-hand side shows an evolution with regard to the flow parameter s of both the IM-SRG energy $E_0 \equiv \langle \psi_{\text{ref}} | \hat{H} | \psi_{\text{ref}} \rangle$ and $E_0 + E^{(2)}$. In this context $E^{(2)}$ refers to the second-order energy correction obtained from perturbation theory. The right-hand side depicts the evolution of the norm of the one and two-body off-diagonal part. Considering the one-body off-diagonal part as an example, the norm is calculated through $|f^{\text{od}}| \equiv \sqrt{\sum_{pq} (f_p^q n_q \bar{n}_p)^2}$. Calculations were performed at $e_{\text{max}} = 12$ and are based on the $\text{N}^3\text{LO}_{\text{EM}} + \text{N}^2\text{LO}_{400\text{L}}$ interaction (see chapter 6 for more information on commonly employed interactions).

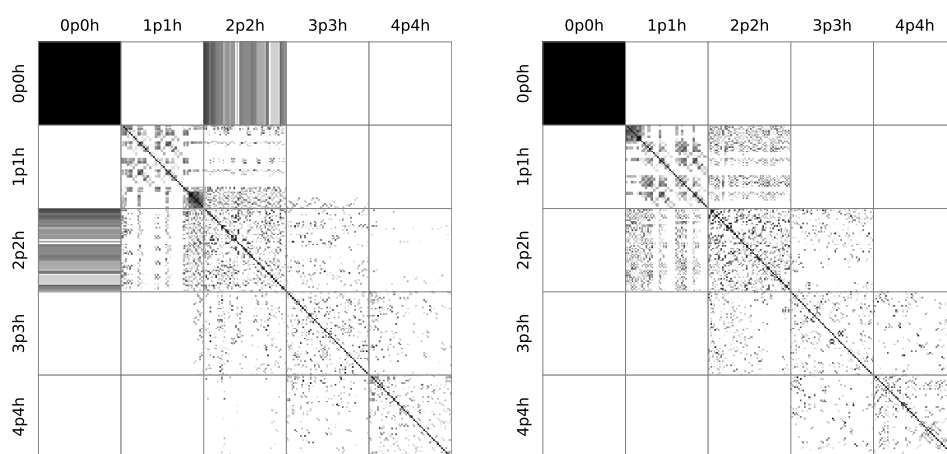


Figure 4.6.: Matrix representations of the initial and final, i.e., transformed Hamiltonian on the left and right-hand side, respectively. The basis chosen for the representation consists of n -particle n -hole excitations of the reference state $|\psi_{\text{ref}}\rangle$ ($0p0h$) which is a simple Slater determinant. Note that we include only a certain subset of determinants in each set of n -particle n -hole excitations used for the representation where the subset consists only of those excitations $|\psi'\rangle$ with the largest absolute values for the overlap with the reference state $|\langle \psi_{\text{ref}} | \hat{H} | \psi' \rangle|$.

Multi-Reference IM-SRG—Commutator Evaluation

In this chapter we cover one of the central aspects of the IM-SRG framework: the evaluation of commutators. The need for commutator evaluations appears in the following different contexts:

- the direct evolution of an observable \hat{O} through

$$\frac{d}{ds}\hat{O}(s) = \left[\hat{\eta}(s), \hat{O}(s) \right], \quad (5.0.1)$$

- the derivative for the Magnus operator $\hat{\Omega}(s)$

$$\frac{d}{ds}\hat{\Omega}(s) = \sum_{k=0}^{\infty} \frac{B_k}{k!} \left[\hat{\Omega}(s), \hat{\eta}(s) \right]_k, \quad (5.0.2)$$

- the construction of the Wegner generator

$$\hat{\eta}(s) = \left[\hat{H}^d(s), \hat{H}(s) \right], \quad (5.0.3)$$

- the unitary transformation of an observable \hat{O} by means of the BCH series

$$\hat{O}(s) = e^{+\hat{\Omega}(s)} \hat{O}(0) e^{-\hat{\Omega}(s)} = \sum_{k=0}^{\infty} \frac{1}{k!} \left[\hat{\Omega}(s), \hat{O}(0) \right]_k. \quad (5.0.4)$$

Taking all of these cases into account, this chapter is dedicated to the evaluation of the general commutator

$$\hat{C}_M^L = \left[\hat{A}_0^0, \hat{B}_M^L \right], \quad (5.0.5)$$

where \hat{C}_M^L and \hat{B}_M^L denote spherical tensor operators of rank L and projection M and \hat{A}_0^0 denotes a scalar operator. We will be commonly referring to the resulting equations in terms of the matrix elements of the operators as *commutator equations*. Note that, if not stated otherwise, we will omit the tensor rank and projection information for \hat{A}_0^0 , \hat{B}_M^L and \hat{C}_M^L and use \hat{A} , \hat{B} , and \hat{C} , respectively, for brevity. Commutators with a non-scalar second argument arise in the context of the consistent evolution of electromagnetic observables as, in general, those observables are associated with non-scalar operators.

This chapter is outlined as follows: Firstly, we present the so-called m -scheme commutator equations, which may be obtained by an application of Wick's theorem and a subsequent transformation into the so-called spherical natural orbitals. Secondly, we briefly review the theory of irreducible spherical tensor operators and the Wigner-Eckart theorem. Thirdly, we use fundamental symmetry properties of the operators and of fermionic many-body states for writing the m -scheme equations in a more compact form. Finally, we derive *spherical* commutator equations in terms of reduced matrix elements by performing angular momentum coupling.

5.1. Spherical Natural Orbitals and m -Scheme Equations

Spherical Natural Orbitals. A central aspect of the commutator equations is that they are formulated in terms of the so-called spherical natural orbitals, which is the eigenbasis of the one-body density matrix $\gamma^{[1]}$. Under the corresponding unitary single-particle transformation the one-body density matrix transforms like

$$\gamma_q^p \rightarrow n_p \delta_q^p, \quad (5.1.1)$$

$$\bar{\gamma}_q^p = \delta_q^p - \gamma_q^p \rightarrow \delta_q^p - n_p \delta_q^p = (1 - n_p) \delta_q^p \equiv \bar{n}_p \delta_q^p, \quad (5.1.2)$$

where we introduced the *fractional* occupation numbers n_p with $0 \leq n_p \leq 1$ as eigenvalues of $\gamma^{[1]}$ and defined $\bar{n}_p \equiv 1 - n_p$. It is noteworthy that this single-particle transformation is unitary and that it only mixes radial quantum numbers.

The main reason for using the natural orbital basis is simple: It reduces the computational effort drastically due to the collapse of summation indices. In practical applications it has proven useful to partition the natural-orbital single-particle basis into a *core* space \mathcal{C} , an *active* space \mathcal{A} , and a *virtual* space \mathcal{V} . For that purpose, let us express the reference state $|\psi_{\text{ref}}\rangle$ as a superposition of Slater determinants $|\phi_i\rangle$

$$|\psi_{\text{ref}}\rangle = \sum_i c_i |\phi_i\rangle. \quad (5.1.3)$$

As the unique assignment of any single-particle state p to one of the aforementioned subspaces is governed by the numerical value of its occupation number n_p , we obtain the definition:

$$p \in \mathcal{C} \Leftrightarrow n_p = 1 \quad \Leftrightarrow p \in |\phi_i\rangle \text{ for all } i \quad \Rightarrow \hat{a}^p |\psi_{\text{ref}}\rangle = 0, \quad (5.1.4)$$

$$p \in \mathcal{A} \Leftrightarrow 0 < n_p < 1 \Leftrightarrow p \in |\phi_i\rangle \text{ for at least one but not all } i, \quad (5.1.5)$$

$$p \in \mathcal{V} \Leftrightarrow n_p = 0 \quad \Leftrightarrow p \notin |\phi_i\rangle \text{ for all } i \quad \Rightarrow \hat{a}_p |\psi_{\text{ref}}\rangle = 0. \quad (5.1.6)$$

The usefulness of this classification is rooted in the fact that particular occupation numbers and two-body irreducible density matrix elements vanish for certain natural orbital single-particle combinations.

For demonstration purposes let us consider a general n -body density matrix element $\gamma_{q_1 \dots q_n}^{p_1 \dots p_n}$. It is easy to verify that such a matrix element is only non-vanishing if none of its indices is associated with a virtual state. As a consequence, the computational impact of particular analytical expression may be further reduced by, e.g., letting specific summation indices only run over core states. For more information see [Geb17].

m -Scheme Equations. In the following we are going to present the result of the evaluation of the general commutator equation

$$\hat{C} = [\hat{A}, \hat{B}], \quad (5.1.7)$$

where each of the three operators is in reference-state representation w.r.t. $|\psi_{\text{ref}}\rangle$, consistently truncated at the NO2B level, and can, therefore, be written as

$$\hat{A} = A_0 + \sum_{pq} A_q^p \{ \hat{a}_q^p \}_{|\psi_{\text{ref}}\rangle} + \frac{1}{4} \sum_{pqrs} A_{rs}^{pq} \{ \hat{a}_{rs}^{pq} \}_{|\psi_{\text{ref}}\rangle}. \quad (5.1.8)$$

For better readability, we split up the commutator evaluation w.r.t. the particle ranks of the operators involved which yields

$$\hat{C} = [\hat{A}, \hat{B}] = [\hat{A}^{[0]} + \hat{A}^{[1]} + \hat{A}^{[2]}, \hat{B}^{[0]} + \hat{B}^{[1]} + \hat{B}^{[2]}] \quad (5.1.9)$$

$$= [\hat{A}^{[1]}, \hat{B}^{[1]}] + [\hat{A}^{[1]}, \hat{B}^{[2]}] + [\hat{A}^{[2]}, \hat{B}^{[1]}] + [\hat{A}^{[2]}, \hat{B}^{[2]}]. \quad (5.1.10)$$

For evaluating each of these commutators we employ Wick's theorem (see chapter 3), which naturally leads to terms involving one-body, irreducible two-body, and irreducible three-body density matrices.

As an example, let us now evaluate the commutator between the two one-body parts $\hat{A}^{[1]}$ and $\hat{B}^{[1]}$ and denote the resulting operator of this operation as $\hat{\kappa}$

$$\hat{\kappa} \equiv \left[\sum_{pq} A_q^p \{ \hat{a}_q^p \}, \sum_{pq} B_q^p \{ \hat{a}_q^p \} \right] \quad (5.1.11)$$

$$= \sum_{pqrs} A_q^p B_s^r \{ \hat{a}_q^p \} \{ \hat{a}_s^r \} - \sum_{pqrs} B_q^p A_s^r \{ \hat{a}_q^p \} \{ \hat{a}_s^r \}, \quad (5.1.12)$$

relabeling of summation indices gives

$$= \sum_{pqrs} A_q^p B_s^r \left(\{\hat{a}_q^p\} \{\hat{a}_s^r\} - \{\hat{a}_s^r\} \{\hat{a}_q^p\} \right), \quad (5.1.13)$$

applying the generalized Wick's theorem to both normal-ordered products yields

$$= \sum_{pqrs} A_q^p B_s^r \left(-\gamma_s^p \{\hat{a}_q^r\} + \bar{\gamma}_q^r \{\hat{a}_s^p\} + \gamma_s^p \bar{\gamma}_q^r + \gamma_{qs}^{pr} \right. \quad (5.1.14)$$

$$\left. + \gamma_q^r \{\hat{a}_s^p\} - \bar{\gamma}_s^p \{\hat{a}_q^r\} - \gamma_q^r \bar{\gamma}_s^p - \gamma_{sq}^{rp} \right), \quad (5.1.15)$$

combining terms with the same normal-ordered product produces

$$= \sum_{pqrs} A_q^p B_s^r \left(-(\gamma_s^p + \bar{\gamma}_s^p) \{\hat{a}_q^r\} + (\bar{\gamma}_q^r + \gamma_q^r) \{\hat{a}_s^p\} \right. \quad (5.1.16)$$

$$\left. + \gamma_s^p \bar{\gamma}_q^r - \gamma_q^r \bar{\gamma}_s^p + \gamma_{qs}^{pr} - \gamma_{sq}^{rp} \right). \quad (5.1.17)$$

By employing the relations

$$\gamma_2^1 + \bar{\gamma}_2^1 = \delta_2^1, \quad \gamma_{qs}^{pr} - \gamma_{sq}^{rp} = \gamma_{qs}^{pr} - \gamma_{qs}^{pr} = 0, \quad (5.1.18)$$

$$\gamma_2^1 \bar{\gamma}_4^3 - \gamma_4^3 \bar{\gamma}_2^1 = \gamma_2^1 \delta_4^3 - \gamma_4^3 \delta_2^1, \quad (5.1.19)$$

we further obtain

$$\hat{\kappa} = \sum_{pqrs} A_q^p B_s^r \left(-\delta_s^p \{\hat{a}_q^r\} + \delta_q^r \{\hat{a}_s^p\} + \gamma_s^p \delta_q^r - \gamma_q^r \delta_s^p \right) \quad (5.1.20)$$

$$= -\sum_{pqrs} A_q^p B_s^r \delta_s^p \{\hat{a}_q^r\} + \sum_{pqrs} A_q^p B_s^r \delta_q^r \{\hat{a}_s^p\} \quad (5.1.21)$$

$$+ \sum_{pqrs} A_q^p B_s^r \gamma_s^p \delta_q^r - \sum_{pqrs} A_q^p B_s^r \gamma_q^r \delta_s^p, \quad (5.1.22)$$

evaluating delta terms and subsequently relabeling summation indices yields

$$= -\sum_{pqr} A_q^p B_p^r \{\hat{a}_q^r\} + \sum_{pqs} A_q^p B_s^q \{\hat{a}_s^p\} + \sum_{pqs} A_q^p B_s^q \gamma_s^p - \sum_{pqr} A_q^p B_p^r \gamma_q^r \quad (5.1.23)$$

$$= -\sum_{p_1 p_2} \sum_q A_{p_2}^q B_q^{p_1} \{\hat{a}_{p_2}^{p_1}\} + \sum_{p_1 p_2} \sum_q A_q^{p_1} B_{p_2}^q \{\hat{a}_{p_2}^{p_1}\} \quad (5.1.24)$$

$$+ \sum_{pqr} \left(A_q^p B_r^q \gamma_r^p - A_r^q B_q^p \gamma_r^p \right), \quad (5.1.25)$$

combining the two one-body parts again gives

$$= \sum_{p_1 p_2} \sum_q \left(A_q^{p_1} B_{p_2}^q - B_q^{p_1} A_{p_2}^q \right) \{\hat{a}_{p_2}^{p_1}\} + \sum_{pqr} \left(A_q^p B_r^q - B_q^p A_r^q \right) \gamma_r^p \quad (5.1.26)$$

$$\stackrel{!}{=} \kappa_0 + \sum_{pq} \kappa_q^p \{\hat{a}_q^p\} + \frac{1}{4} \sum_{pqrs} \kappa_{rs}^{pq} \{\hat{a}_{sr}^{pq}\}. \quad (5.1.27)$$

By comparing each particle rank of the result with the general form of $\hat{\kappa}$, we obtain the following expressions for the zero-body and one-body matrix elements of $\hat{\kappa}$, respectively,

$$\kappa_0 = \sum_{pqr} (A_q^p B_r^q - B_q^p A_r^q) \gamma_r^p, \quad (5.1.28)$$

$$\kappa_2^1 = \sum_q (A_q^1 B_2^q - B_q^1 A_2^q). \quad (5.1.29)$$

A subsequent single-particle basis transformation of the zero-body part into the spherical natural orbitals yields

$$\kappa_0 = \sum_{pqr} (A_q^p B_r^q - B_q^p A_r^q) \gamma_r^p \rightarrow \sum_{pq} (A_q^p B_p^q - B_q^p A_p^q) n_q, \quad (5.1.30)$$

Apparently, κ_2^1 is invariant under this transformation as it does not contain any density matrices.

Applying this approach outlined through this exemplary evaluation of $[\hat{A}^{[1]}, \hat{B}^{[1]}]$ to the remaining terms $[\hat{A}^{[1]}, \hat{B}^{[2]}]$, $[\hat{A}^{[2]}, \hat{B}^{[1]}]$ and $[\hat{A}^{[2]}, \hat{B}^{[2]}]$, including the transformation of all terms into the spherical natural orbital basis, we obtain the m -scheme equations

| Zero-Body m -Scheme | |
|---|----------|
| $C_0 = + \sum_{pq} (n_p - n_q) A_q^p B_p^q$ | (5.1.31) |
| $+ \frac{1}{4} \sum_{pqrs} n_p n_q \bar{n}_r \bar{n}_s (A_{rs}^{pq} B_{pq}^{rs} - [A \leftrightarrow B])$ | (5.1.32) |
| $+ \frac{1}{4} \sum_{pqrs} C_{rs}^{pq} \lambda_{rs}^{pq} + \mathcal{O}(\lambda^{[3]})$ | (5.1.33) |

One-Body m -Scheme

$$C_2^1 = + \sum_p A_p^1 B_2^p - [A \leftrightarrow B] \quad (5.1.34)$$

$$+ \sum_{pq} (n_p - n_q) \left(A_q^p B_{p2}^{q1} - [A \leftrightarrow B] \right) \quad (5.1.35)$$

$$+ \frac{1}{2} \sum_{pqr} (n_p \bar{n}_q \bar{n}_r + \bar{n}_p n_q n_r) \left(A_{qr}^{1p} B_{2p}^{qr} - [A \leftrightarrow B] \right) \quad (5.1.36)$$

$$+ \sum_{rtvsw} \left(\frac{1}{4} A_{sw}^{1t} B_{2t}^{rv} - [A \leftrightarrow B] \right) \lambda_{sw}^{rv}, \quad (5.1.37)$$

$$+ \sum_{rtvsw} \left(A_{ts}^{1r} B_{2w}^{tv} - [A \leftrightarrow B] \right) \lambda_{sw}^{rv}, \quad (5.1.38)$$

$$+ \sum_{rtvsw} \left(\frac{1}{2} A_{2t}^{1r} B_{sw}^{tv} - \frac{1}{2} A_{2s}^{1t} B_{tw}^{rv} - [A \leftrightarrow B] \right) \lambda_{sw}^{rv}, \quad (5.1.39)$$

 Two-Body m -Scheme

$$C_{34}^{12} = + \sum_p \left(\left(A_p^1 B_{34}^{p2} - [1 \leftrightarrow 2] \right) - \left(A_3^p B_{p4}^{12} - [3 \leftrightarrow 4] \right) \right) - [A \leftrightarrow B] \quad (5.1.40)$$

$$+ \frac{1}{2} \sum_{pq} (1 - n_p - n_q) \left(A_{pq}^{12} B_{34}^{pq} - [A \leftrightarrow B] \right) \quad (5.1.41)$$

$$+ \sum_{pq} (n_p - n_q) \left(\left(A_{3q}^{1p} B_{4p}^{2q} - [A \leftrightarrow B] \right) - [1 \leftrightarrow 2] \right). \quad (5.1.42)$$

These equations are commonly referred to as m -scheme equations due to the fact that they still depend on projection quantum numbers—in contrast to the so-called *spherical* equations, which will be derived later on. It becomes evident that the zero-body part is the only part which, in principle, contains an irreducible three-body density matrix. However, this term will be neglected in this work as it has been shown that its impact is negligible [Geb17]. Furthermore, it is noteworthy that the subset of the equations above not containing any two-body irreducible density matrices $\hat{\lambda}^{[2]}$ is equal to the set of single-reference equations. Assuming the reference state is a Slater determinant, all terms containing higher-order irreducible density matrices $\hat{\lambda}^{[2]}$ vanish which shows that the multi-reference equations reduce to the single-reference equations. Additionally, we would like to note that during the derivation of the m -scheme equations presented here, no symmetries of the operators were exploited, in particular, we did not assume any symmetry under Hermitian conjugation. For more information

and details on the derivation of the single-reference and multi-reference equations see [Vob14] and [Geb17], respectively.

5.2. Angular Momentum Theory

Taking rotational symmetry into account is not only educationally valuable but is also an essential cornerstone for the following derivation of the spherical commutator equations which—compared to the m -scheme commutator equations—significantly reduce the computational effort. Furthermore, it will allow us to write the m -scheme equations in a much more compact manner, making them much easier to handle. To that end, we are going to briefly discuss angular momentum theory, introduce spherical tensor operators and address the Wigner-Eckart theorem in this section. For educationally highly valuable information on this topic beyond our following considerations see [Suh07; VMK88].

Angular Momentum Coupling. A (vector) operator $\hat{\mathbf{J}}$ is said to be an angular momentum operator if its three Cartesian components \hat{J}_x , \hat{J}_y , and \hat{J}_z are Hermitian and, additionally, satisfy the commutation relations

$$\left[\hat{J}_x, \hat{J}_y\right] = i\hbar\hat{J}_z, \quad \left[\hat{J}_y, \hat{J}_z\right] = i\hbar\hat{J}_x, \quad \left[\hat{J}_z, \hat{J}_x\right] = i\hbar\hat{J}_y. \quad (5.2.1)$$

Starting from this abstract definition of an angular momentum operator $\hat{\mathbf{J}}$, it can be shown that the orthonormal eigenstates of $\hat{\mathbf{J}}$ fulfill the following eigenvalue relations

$$\hat{\mathbf{J}}^2 |jm\rangle = j(j+1)\hbar^2 |jm\rangle, \quad (5.2.2)$$

$$\hat{J}_z |jm\rangle = m\hbar |jm\rangle, \quad (5.2.3)$$

where $-j \leq m \leq j$. We would like to note that the notion of angular momentum arises naturally within the context of rotational symmetry. This is rooted in the fact that an angular momentum operator is closely related to the rotation group—its components are the three infinitesimal generators of the rotation group.

Having defined the notion of an angular momentum operator, we are now prepared to address the *coupling* of angular momenta. Generally, the sum $\hat{\mathbf{J}} = \hat{\mathbf{J}}_1 + \hat{\mathbf{J}}_2$ of two commuting angular momentum operators $\hat{\mathbf{J}}_1$ and $\hat{\mathbf{J}}_2$ again forms an angular momentum operator, where $\hat{\mathbf{J}}_1$ and $\hat{\mathbf{J}}_2$ may be, e.g., the angular momenta of two different particles or those of the orbital and spin angular momentum. The complete set of basis states $\{|j_1 m_1, j_2 m_2\rangle\}$ is called the *uncoupled* basis w.r.t. the operator set $\{\hat{\mathbf{J}}_1^2, \hat{J}_{1z}, \hat{\mathbf{J}}_2^2, \hat{J}_{2z}\}$. However, as $\hat{\mathbf{J}} = \hat{\mathbf{J}}_1 + \hat{\mathbf{J}}_2$ is also an angular momentum operator the complete set of basis states $\{|(j_1 j_2) jm\rangle\}$ is called the *coupled* basis w.r.t. the operator set $\{\hat{\mathbf{J}}_1^2, \hat{\mathbf{J}}_2^2, \hat{\mathbf{J}}^2, \hat{J}_z\}$. The transformation between the coupled and uncoupled basis is unitary and a basis state of the coupled basis can be expressed in terms of basis states of the

uncoupled basis as follows

$$|(j_1 j_2) j m\rangle = \sum_{m_1 m_2} |j_1 m_2 j_2 m_2\rangle \langle j_1 m_2 j_2 m_2 | (j_1 j_2) j m\rangle \quad (5.2.4)$$

$$\equiv \sum_{m_1 m_2} \begin{pmatrix} j_1 & j_2 & j \\ m_1 & m_2 & m \end{pmatrix} |j_1 m_1 j_2 m_2\rangle, \quad (5.2.5)$$

where we defined the overlap between a coupled and an uncoupled basis state as the Clebsch Gordan coefficient. Closely related to Clebsch-Gordan coefficients are the so-called $3j$ symbols¹ which can be expressed in terms of each other as follows

$$\begin{pmatrix} j_1 & j_2 & J \\ m_1 & m_2 & M \end{pmatrix} = (-)^{j_1 - j_2 - M} \Pi_J^{-1} \begin{pmatrix} j_1 & j_2 & J \\ m_1 & m_2 & -M \end{pmatrix}, \quad (5.2.6)$$

$$\begin{pmatrix} j_1 & j_2 & J \\ m_1 & m_2 & M \end{pmatrix} = (-)^{j_1 - j_2 + M} \Pi_J \begin{pmatrix} j_1 & j_2 & J \\ m_1 & m_2 & -M \end{pmatrix} = (-)^{2j_2} \Pi_J (-)^{J-M} \begin{pmatrix} J & j_2 & j_1 \\ -M & m_2 & m_1 \end{pmatrix}, \quad (5.2.7)$$

where the so-called hatfactor is defined via

$$\Pi_J \equiv \sqrt{2J+1}, \quad \Pi_{J_1 J_2 \dots J_x} \equiv \Pi_{J_1} \cdot \Pi_{J_2} \cdots \Pi_{J_x}. \quad (5.2.8)$$

We will usually employ $3j$ symbols instead of Clebsch-Gordan coefficients as these are accompanied by very convenient symmetry properties: Firstly, a $3j$ symbol is invariant under cyclic permutations of its columns, whereas an anti-cyclic permutation produces merely an additional phase factor of $(-)^{j_1 + j_2 + J}$. Secondly, an inversion of all of its projection quantum numbers in the bottom row produces the same phase factor as in the context of anti-cyclic permutation

$$\begin{pmatrix} j_1 & j_2 & j_3 \\ m_1 & m_2 & m_3 \end{pmatrix} = \begin{pmatrix} j_3 & j_1 & j_2 \\ m_3 & m_1 & m_2 \end{pmatrix} = (-)^{j_1 + j_2 + j_3} \begin{pmatrix} j_2 & j_1 & j_3 \\ m_2 & m_1 & m_3 \end{pmatrix}, \quad (5.2.9)$$

$$\begin{pmatrix} j_1 & j_2 & j_3 \\ m_1 & m_2 & m_3 \end{pmatrix} = (-)^{j_1 + j_2 + j_3} \begin{pmatrix} j_1 & j_2 & j_3 \\ -m_1 & -m_2 & -m_3 \end{pmatrix}. \quad (5.2.10)$$

Another useful property of the $3j$ symbol involves the case where one of the angular momenta vanishes

$$\begin{pmatrix} j_1 & j_2 & 0 \\ m_1 & m_2 & 0 \end{pmatrix} = (-)^{j_1 - m_1} \Pi_{j_1}^{-1} \delta_{j_1 j_2} \delta_{m_1, -m_2}. \quad (5.2.11)$$

Considering the case of coupling three angular momenta, there is, compared to the case of two angular momenta, a slight complication as there are three possible coupling orders in which the three angular momenta may be coupled and the coupled states associated with each coupling scheme are different from each other. However, each of the three sets forms a

¹Note that in the literature the object we are referring to as a $3j$ symbol it sometimes referred to as $3jm$ symbol.

complete basis and the $6j$ symbol arises within the context of the unitary basis transformations between two different coupling schemes. Note that, formally, the $6j$ symbol may be written in terms of $3j$ symbols as follows

$$\left\{ \begin{matrix} j_1 & j_2 & j_3 \\ J_1 & J_2 & J_3 \end{matrix} \right\} = \sum_{M_1 M_2 M_3 m_1 m_2 m_3} (-)^{J_1 - M_1 + J_2 - M_2 + J_3 - M_3} \begin{pmatrix} j_1 & j_2 & j_3 \\ m_1 & m_2 & m_3 \end{pmatrix} \begin{pmatrix} j_1 & J_2 & J_3 \\ -m_1 & -M_2 & M_3 \end{pmatrix} \begin{pmatrix} J_1 & j_2 & J_3 \\ M_1 & m_2 & -M_3 \end{pmatrix} \begin{pmatrix} J_1 & J_2 & j_3 \\ -M_1 & M_2 & m_3 \end{pmatrix}. \quad (5.2.12)$$

The basic symmetry properties of the $6j$ symbol are: invariance under permutations of its columns and invariance under *simultaneous* exchange of lower and upper arguments in any two of its columns.

Similarly to the $6j$ symbol, the $9j$ symbol arises within the context of transformations between coupling schemes w.r.t. four angular momenta and is denoted as

$$\left\{ \begin{matrix} j_{11} & j_{12} & j_{13} \\ j_{21} & j_{22} & j_{23} \\ j_{31} & j_{32} & j_{33} \end{matrix} \right\}. \quad (5.2.13)$$

Again, there are several ways in which the four angular momenta may be coupled to a total angular momentum, states associated with different coupling schemes are not equal to each other, and each set of basis states associated with each of the different coupling schemes forms a complete basis. Considering the basic symmetry properties, the $9j$ symbol is invariant under reflection w.r.t. to either of its two diagonals, it is invariant under even permutations of its rows and columns, and for odd permutations of its rows or columns a phase factor of $\prod_{x,y}^3 (-)^{j_{xy}}$ emerges.

Spherical Tensor Operators. Generally, a Cartesian tensor operator can be reduced to spherical tensor operators of several spherical ranks. As the definition of spherical tensor operators is closely connected to their behavior under rotations in coordinate space, let us briefly recapitulate the most important implications arising within the context of those rotations.

Under a rotation, represented by the rotation operator \hat{R} with matrix elements R_j^i , the three components V^i of a Cartesian vector and the nine components T^{ij} of a second-rank Cartesian tensor are transforming as follows

$$V'^i = \sum_{j=1}^3 R_j^i V^j \quad \longrightarrow \quad \mathbf{V}' = \mathbf{R} \mathbf{V}, \quad (5.2.14)$$

$$T'^{ij} = \sum_{k,l=1}^3 R_k^i R_l^j T^{kl} \quad \longrightarrow \quad \mathbf{T}' = \mathbf{R} \mathbf{T} \mathbf{R}^{-1}, \quad (5.2.15)$$

where both rotations were additionally written as matrix equations with the orthogonal matrix R . A rotation R in three-dimensional Cartesian space leads to a unitary transformation \hat{U}

of angular momentum eigenstates $|jm\rangle$ in a $(2j + 1)$ -dimensional Hilbert space. The so-called Wigner D functions are the matrix representation of these unitary transformations in a basis consisting of angular momentum eigenstates

$$D_{m,m'}^j \equiv \langle jm' | \hat{U} | jm \rangle . \quad (5.2.16)$$

Rewriting the previous definition to the form

$$\hat{U} | jm \rangle = \sum_{m'=-j}^j D_{m,m'}^j | jm' \rangle , \quad (5.2.17)$$

illustrates how an eigenstate $|jm\rangle$ transforms under rotations induced by \hat{U} .

Employing the definition of the Wigner D functions, a spherical tensor operator \hat{T}^L with rank L consists of $(2L + 1)$ components $\{ \hat{T}_M^L \mid -L \leq M \leq +L \}$ which transform under rotations as follows

$$\hat{U} \hat{T}_M^L \hat{U}^\dagger = \sum_{M'=-L}^L D_{M,M'}^L \hat{T}_{M'}^L . \quad (5.2.18)$$

Put differently, the components \hat{T}_M^L of a spherical tensor operator are transforming just like angular momentum eigenstates $|jm\rangle$. Equivalently, spherical tensor operators can formally be defined through the following commutation relations

$$[\hat{J}_z, \hat{T}_M^L] = M\hbar \hat{T}_M^L , \quad (5.2.19)$$

$$[\hat{J}_\pm, \hat{T}_M^L] = \hbar \sqrt{(J \pm M + 1)(J \mp M)} \hat{T}_{M\pm 1}^L , \quad (5.2.20)$$

where $\hat{J}_\pm = \hat{J}_x \pm i\hat{J}_y$ are the ladder operators. These commutation relations are especially useful for testing whether or not a set of objects forms a spherical tensor operator.

As noted previously, Cartesian tensor operators of a specific Cartesian rank can be reduced to spherical tensors of several spherical ranks. A special case are Cartesian scalars and vectors as their spherical counterparts have the same rank, i.e., a Cartesian scalar is a spherical scalar and a Cartesian vector is a spherical vector. However, a rank-two Cartesian tensor can be decomposed into spherical tensors of rank zero, one, and two. In other words, Cartesian tensors are *reducible* whereas spherical tensors are *irreducible*. This is why they are commonly referred to as *irreducible* spherical tensor operators.² As an example for the decomposition of Cartesian tensors into spherical tensors, let us consider a vector \hat{V} with the Cartesian components \hat{V}_x , \hat{V}_y and \hat{V}_z . The associated spherical components can now be written as follows

$$\hat{V}_\pm = \mp \frac{1}{\sqrt{2}} \left(\hat{V}_x \pm i\hat{V}_y \right) , \quad \hat{V}_0 = \hat{V}_z . \quad (5.2.21)$$

²Mathematically speaking, an irreducible spherical tensor operator corresponds to an irreducible representation of the rotation group, i.e., a group representation with no further invariant subspaces.

Note that, if not stated otherwise, we will assume to deal with *Hermitian* tensor operators in this work, which obey

$$(\hat{T}_M^L)^\dagger = (-)^M \hat{T}_{-M}^L, \quad (5.2.22)$$

where the $M = 0$ component of such tensor operators fulfills the well-known criterion for being Hermitian $(\hat{T}_0^L)^\dagger = \hat{T}_0^L$.

Wigner-Eckart Theorem. We are now ready to discuss the Wigner-Eckart theorem [Wig31; Eck30]. It simplifies the calculation of matrix elements of nuclear observables by expanding observables in terms of spherical tensor operators which then allows to exploit their special transformation properties. Using the notation $|\psi; JM\rangle$ for referring to states with angular momentum J and projection M the Wigner-Eckart theorem can be stated as follows.

Theorem 5.2.1: Wigner-Eckart Theorem

A matrix element of a component $\hat{T}_{M_L}^L$ of a spherical tensor operator \hat{T}^L can be rewritten as

$$\langle \psi; JM | \hat{T}_{M_L}^L | \psi'; J' M' \rangle = (-)^{J-M} \begin{pmatrix} J & L & J' \\ -M & M_L & M' \end{pmatrix} \langle \psi; J || \hat{T}^L || \psi'; J' \rangle, \quad (5.2.23)$$

where $\langle \psi; J || \hat{T}^L || \psi'; J' \rangle$ denotes the so-called *reduced* matrix element which does not depend on any projection quantum numbers anymore.

Therefore, the Wigner-Eckart theorem states that it is possible to separate matrix elements of spherical tensor operators into a part that still contains projection quantum numbers from the rest, i.e., the reduced matrix element. This reduced matrix element is rotationally invariant and contains the “physics” of the initial and final state and that of the tensor operator. The inverse relation of the Wigner-Eckart theorem will prove very useful and can be written as

$$\langle \psi; J || \hat{T}^L || \psi'; J' \rangle = \sum_{MM'M_L} (-)^{J-M} \begin{pmatrix} J & L & J' \\ -M & M_L & M' \end{pmatrix} \langle \psi; JM | \hat{T}_{M_L}^L | \psi'; J' M' \rangle. \quad (5.2.24)$$

From the Wigner-Eckart theorem given through eq. (5.2.23) and the general properties of $3j$ symbols it becomes evident that the matrix element of a spherical tensor operator vanishes if either the triangular condition or the projection quantum number conservation is violated. Formally, this can be expressed as

$$\langle \psi; JM | \hat{T}_{M_L}^L | \psi'; J' M' \rangle = 0 \quad \text{if } !\Delta(JLJ') \text{ or } (-M + M_L + M') \neq 0, \quad (5.2.25)$$

where $\Delta(JLJ')$ indicates the triangular condition.

Let us consider a matrix element and its complex conjugate counterpart

$$\langle \psi; JM | \hat{T}_{M_L}^L | \psi'; J' M' \rangle = \langle \psi'; J' M' | (\hat{T}_{M_L}^L)^\dagger | \psi; JM \rangle^* , \quad (5.2.26)$$

where we used the definition of the Hermitian conjugation of operators. Assuming from now on that we are dealing with *Hermitian* spherical tensor operators, we apply the Wigner-Eckart theorem to both sides of the previous equation and obtain

$$\langle \psi; J_\psi | \hat{T}^L | \psi'; J' \rangle = (-)^{J-J'} \langle \psi'; J' | \hat{T}^L | \psi; J \rangle^* , \quad (5.2.27)$$

which is an important symmetry property of reduced matrix elements.

An interesting special case is the Wigner-Eckart theorem for scalar operators: As both L and M_L are vanishing in this case we obtain the simplified equation

$$\langle \psi; JM | \hat{T}_0^0 | \psi'; J' M' \rangle = \Pi_J^{-1} \langle \psi; J | \hat{T}^0 | \psi'; J' \rangle \delta_{JJ'} \delta_{MM'} . \quad (5.2.28)$$

Two things become evident here: Firstly, coupled matrix elements of scalar operators are only non-zero if both the total angular momentum and its projection are equal in bra and ket, respectively. Secondly, the matrix element is independent of the specific value of the projection. Therefore, we may replace reduced with coupled matrix elements with each other, even though one has to take the hatfactor both are differing by into account.

Tensor Product. The tensor product of rank L and projection M of two spherical tensor operators \hat{X}^{L_X} and \hat{Y}^{L_Y} of rank L_X and L_Y , respectively, is defined through

$$[\hat{X}^{L_X} \otimes \hat{Y}^{L_Y}]_M^L = \sum_{M_1 M_2} \begin{pmatrix} L_X & L_Y & L \\ M_1 & M_2 & M \end{pmatrix} \hat{X}_{M_1}^{L_X} \hat{Y}_{M_2}^{L_Y} . \quad (5.2.29)$$

Considering the special case where one of the two spherical tensor operators involved in the tensor product is a scalar, we obtain the relation

$$[\hat{X}^{L_X} \otimes \hat{Y}^0]_M^L = \sum_{M_1} \begin{pmatrix} L_X & 0 & L \\ M_1 & 0 & M \end{pmatrix} \hat{X}_{M_1}^{L_X} \hat{Y}_0^0 = \delta_{L_X L} \delta_{M_1 M} \hat{X}_{M_1}^{L_X} \hat{Y}_0^0 , \quad (5.2.30)$$

from which it follows that any product of a spherical tensor operator of rank L and projection M with a scalar operator is equivalent to a tensor product of rank L and projection M . As a consequence, also the commutator of a non-scalar operator with a scalar operator is again a tensor operator with rank and projection equal to the ones of the non-scalar operator which in turn justifies our previous assumption given through eq. (5.0.5).

During the following process of angular momentum coupling, matrix elements of two types of tensor products will appear naturally. Therefore, let us consider these two cases such that we may directly identify specific terms as tensor products.

Matrix Elements of Tensor Products I. In the first case we assume that \hat{X}^{L_X} and \hat{Y}^{L_Y} are two spherical tensor operators, where each depends exclusively on variables of its own subsystem. The matrix elements of such a tensor product, which can be written as

$$\hat{Z}_{M_Z}^{L_Z} = [\hat{X}^{L_X} \otimes \hat{Y}^{L_Y}]_{M_Z}^{L_Z}, \quad (5.2.31)$$

are then given through [VMK88]

$$\langle (j_1 j_2) J \parallel \hat{Z}^{L_Z} \parallel (j_3 j_4) J' \rangle = \Pi_{L_Z} \Pi_{J'} \Pi_J \begin{Bmatrix} j_1 & j_2 & J \\ j_3 & j_4 & J' \\ L_X & L_Y & L_Z \end{Bmatrix} \langle j_1 \parallel \hat{X}^{L_X} \parallel j_3 \rangle \langle j_2 \parallel \hat{Y}^{L_Y} \parallel j_4 \rangle. \quad (5.2.32)$$

There are two important special cases:

1. $L_Y = 0$ which leads to the following matrix elements

$$\begin{aligned} \langle (j_1 j_2) J \parallel \hat{Z}^L \parallel (j_3 j_4) J' \rangle &= \Pi_L \Pi_{J'} \Pi_J (-)^{j_1 + j_4 + J' + L} \begin{Bmatrix} j_1 & J & j_2 \\ J' & j_3 & L \end{Bmatrix} \\ &\langle j_1 \parallel \hat{X}^L \parallel j_3 \rangle \langle j_2 \parallel \hat{Y}^0 \parallel j_4 \rangle, \end{aligned} \quad (5.2.33)$$

2. $L_X = L_Y = 0$ which gives

$$\langle (j_1 j_2) J \parallel \hat{Z}^0 \parallel (j_3 j_4) J' \rangle = \frac{\Pi_J}{\Pi_{j_2 j_1}} \langle j_1 \parallel \hat{X}^0 \parallel j_3 \rangle \langle j_2 \parallel \hat{Y}^0 \parallel j_4 \rangle. \quad (5.2.34)$$

Matrix Elements of Tensor Products II. Another possibility for coupling two tensor operators deals with the case, where both are acting on the same Hilbert space [Suh07, p. 34]. This leads to

$$\begin{aligned} \langle J_1 \parallel \hat{Z}^{L_Z} \parallel J_2 \rangle &= (-)^{J_1 + L + J_2} \Pi_{L_Z} \sum_{J_p} \begin{Bmatrix} L_X & L_Y & L_Z \\ J_2 & J_1 & J_p \end{Bmatrix} \\ &\langle J_1 \parallel \hat{X}^{L_X} \parallel J_p \rangle \langle J_p \parallel \hat{Y}^{L_Y} \parallel J_2 \rangle, \end{aligned} \quad (5.2.35)$$

where J_i refers to the total angular momentum of the ‘‘spherical’’ many-body state ψ_i . We will commonly face a special case of this relation, where one of the two operators involved in the tensor product is a scalar which leads to

$$\langle J_1 \parallel \hat{Z}^L \parallel J_2 \rangle = \Pi_{J_2} \sum_{J_p} \langle J_1 \parallel \hat{X}^L \parallel J_p \rangle \langle J_p \parallel \hat{Y}^0 \parallel J_2 \rangle. \quad (5.2.36)$$

5.3. m -Scheme Equations—Revisited

The m -scheme commutator eqs. (5.1.31) to (5.1.42) are overly complicated. This is due to the fact that they are mixing up the general symmetries of each matrix element of a spherical tensor operator with the structure inherent to the commutator equations. In this section we will separate these general symmetries of matrix elements and the inherent structure of the commutator equations from each other. Apart from gaining aesthetically more attractive equations, the practical advantage of this approach is that we obtain equations that exhibit fewer terms and are easier to handle. As a consequence, the subsequent angular momentum coupling procedure will be significantly simplified and less error-prone.

We will employ a short-hand notation for index transpositions via an index transposition operator

$$\hat{\tau}_2^1 \mathcal{F}_{1,2} \equiv \mathcal{F}_{2,1}, \quad (5.3.1)$$

where \mathcal{F} is an arbitrary object with two indices. Furthermore, we assume that all involved operators have a definite symmetry under Hermitian conjugation of 1 or -1, where the symmetry of \hat{C} is determined through the symmetry of \hat{A} and \hat{B} and denoted as $\xi_C = \pm 1$

$$\left(\hat{C}_M^L\right)^\dagger = \xi_C (-)^M \hat{C}_{-M}^L = \pm (-)^M \hat{C}_{-M}^L. \quad (5.3.2)$$

Choosing the matrix elements to be real it follows that³

$$\langle \psi | \hat{C}_M^L | \psi' \rangle = \pm (-)^M \langle \psi' | \hat{C}_{-M}^L | \psi \rangle. \quad (5.3.3)$$

Symmetrizer. The resulting one-body matrix elements $(C_M^L)_2^1$ should be invariant under the action of the symmetrizer

$$\hat{\Xi}_{12M}^{\mathcal{M}\pm} \equiv \frac{1}{2} \left(1 \pm (-)^M \hat{\tau}_{-M}^M \hat{\tau}_2^1 \right). \quad (5.3.4)$$

Furthermore, two-body matrix elements $(C_M^L)_{34}^{12}$ shall be invariant under the action of

$$-\hat{\tau}_2^1, \quad -\hat{\tau}_4^3, \quad \pm (-)^M \hat{\tau}_{-M}^M \hat{\tau}_3^1 \hat{\tau}_4^2, \quad (5.3.5)$$

giving 8 distinct permutations. Consequently, the symmetrizer for the two-body matrix elements may be written as

$$\hat{\Xi}_{1234M}^{\mathcal{M}\pm} \equiv \frac{1}{8} \left(1 - \hat{\tau}_2^1 \right) \left(1 - \hat{\tau}_4^3 \right) \left(1 \pm (-)^M \hat{\tau}_{-M}^M \hat{\tau}_3^1 \hat{\tau}_4^2 \right). \quad (5.3.6)$$

³Note that in the context of the symmetrizer we will from now on employ \pm for referring to ξ_C .

As an example, let us consider the first term of the two-body equations (see eq. (5.1.40)), which can be rewritten as

$$\begin{aligned} & \sum_p \left(\left((A_p^1 B_{34}^{p2} - B_p^1 A_{34}^{p2}) - [1 \leftrightarrow 2] \right) - \left((A_3^p B_{p4}^{12} - B_3^p A_{p4}^{12}) - [3 \leftrightarrow 4] \right) \right) \\ &= \sum_p (1 - \hat{\tau}_2^1 \pm \hat{\tau}_3^1 \hat{\tau}_4^2 \mp \hat{\tau}_3^4 \hat{\tau}_3^1 \hat{\tau}_4^2) (A_p^1 B_{34}^{p2} - B_p^1 A_{34}^{p2}) \end{aligned} \quad (5.3.7)$$

$$= \sum_p (1 - \hat{\tau}_2^1 \pm \hat{\tau}_3^1 \hat{\tau}_4^2 \mp \hat{\tau}_3^4 \hat{\tau}_3^1 \hat{\tau}_4^2) \frac{1 - \hat{\tau}_4^3}{2} (A_p^1 B_{34}^{p2} - B_p^1 A_{34}^{p2}) \quad (5.3.8)$$

$$= \hat{\Xi}_{1234M}^{\mathcal{M}\pm} 4 \sum_p (A_p^1 B_{34}^{p2} - B_p^1 A_{34}^{p2}) \quad (5.3.9)$$

Evidently, the equation takes on a much simpler form as any two terms that merely differ by an exchange of particles such that basic matrix elements symmetries are satisfied are now broken down to one as any of those redundant “exchange” terms is now recovered through the action of the symmetrizer.

Result. Applying this approach to all the remaining terms is straightforward and results in the following set of equations.

| Zero-Body <i>m</i> -Scheme Enhanced | |
|--|----------|
| $C_0 = + \sum_{pq} (n_p - n_q) A_q^p B_p^q \quad (5.3.10)$ | (5.3.10) |
| $+ \frac{1}{4} \sum_{pqrs} n_p n_q \bar{n}_r \bar{n}_s (A_{rs}^{pq} B_{pq}^{rs} - [A \leftrightarrow B]) \quad (5.3.11)$ | (5.3.11) |
| $+ \frac{1}{4} \sum_{pqrs} C_{rs}^{pq} \lambda_{rs}^{pq} \quad (5.3.12)$ | (5.3.12) |

One-Body m -Scheme Enhanced

$$(C_M^L)_2^1 = + \hat{\Xi}_{12M}^{\mathcal{M}\pm} \sum_p 2 A_p^1 B_2^p \quad (5.3.13)$$

$$+ \hat{\Xi}_{12M}^{\mathcal{M}\pm} \sum_{pq} (n_p - n_q) \left(A_q^p B_{p2}^{q1} \right) \quad (5.3.14)$$

$$- \hat{\Xi}_{12M}^{\mathcal{M}\pm} \sum_{pq} (n_p - n_q) \left(B_q^p A_{p2}^{q1} \right) \quad (5.3.15)$$

$$+ \hat{\Xi}_1^{\mathcal{M}\pm} \sum_{pqr} A_{qr}^{1p} B_{2p}^{qr} (n_p \bar{n}_q \bar{n}_r + \bar{n}_p n_q n_r) \quad (5.3.16)$$

$$+ \hat{\Xi}_{12M}^{\mathcal{M}\pm} \sum_{rtvsw} \frac{1}{2} A_{sw}^{1t} \lambda_{rv}^{sw} B_{2t}^{rv} \quad (5.3.17)$$

$$+ \hat{\Xi}_{12M}^{\mathcal{M}\pm} \sum_{rtvsw} (-2) A_{st}^{1r} \lambda_{vr}^{sw} B_{2w}^{vt} \quad (5.3.18)$$

$$+ \hat{\Xi}_{12M}^{\mathcal{M}\pm} \sum_{rtvsw} A_{t2}^{1r} B_{sw}^{tv} \lambda_{vr}^{sw} \quad (5.3.19)$$

$$- \hat{\Xi}_{12M}^{\mathcal{M}\pm} \sum_{rtvsw} (B_M^L)_{t2}^{1r} (A_0^0)_{sw}^{tv} (\lambda_0^0)_{vr}^{sw} \quad (5.3.20)$$

 Two-Body m -Scheme Enhanced

$$(C_M^L)_{34}^{12} = + \hat{\Xi}_{1234M}^{\mathcal{M}\pm} \sum_p 4 A_p^1 B_{34}^{p2} \quad (5.3.21)$$

$$- \hat{\Xi}_{1234M}^{\mathcal{M}\pm} \sum_p 4 B_p^1 A_{34}^{p2} \quad (5.3.22)$$

$$+ \hat{\Xi}_{1234M}^{\mathcal{M}\pm} \sum_{pq} (1 - n_p - n_q) A_{pq}^{12} B_{34}^{pq} \quad (5.3.23)$$

$$+ \hat{\Xi}_{1234M}^{\mathcal{M}\pm} \sum_{pq} 4 (n_p - n_q) A_{3q}^{1p} B_{4p}^{2q} \quad (5.3.24)$$

Comparing these equations with the previous set of equations given through eqs. (5.1.31) to (5.1.42) demonstrates that they exhibit a simpler structure. As a consequence, they are the ideal starting point of the derivation of the spherical commutator equations.

5.4. Diagrammatic Approach

In the context of angular momentum coupling of the m -scheme commutator equations, we will face expressions containing sums over products of many Clebsch-Gordan coefficient and $3j$ symbols symbols. Such expressions can get extremely complicated and performing manipulations is a very time-consuming process. The reason for this is simple: The expressions contain many arguments and it is very difficult to grasp all of the interrelations and to understand symmetries and invariances of specific terms.

For facilitating the process of angular momentum transformations, we will resort to a graphical representation of those analytical expressions. Such a graphical representation is a much clearer and more compact way for representing the structure inherent to the expressions.

There has to be a unique relationship between any analytic expression and its associated graphical representation. Any transformation of an analytic expression may be translated into an unique transformation of the associated diagrams [VMK88].

Let us briefly recapitulate the basics of a diagrammatic treatment of angular momentum coupling. As we are only using the diagrammatic representation of $3j$ symbols and its associated transformation rules, we are merely employing a subset of the rules presented in [VMK88] on which this section is based on.

As a starting point, bra and ket states with a definite angular momentum j and projection m are represented as follows

$$\Pi_j^{-1} |jm\rangle = \bullet \rightarrow \overset{jm}{}, \quad \Pi_j^{-1} \langle jm| = \overset{jm}{} \rightarrow \bullet, \quad (5.4.1)$$

where the lines coming into or out of a node are referred to as j -lines and the variable above them indicates the state they are associated with.

A $3j$ symbol is represented by a dot which connects three j -lines, where each of the line corresponds to one of the three angular momenta within the $3j$ symbol. The cyclic order of the arguments of the $3j$ symbol is determined through the sign of the node which may either be positive or negative determining if the j -lines around the node have to be interpreted anticlockwise or a clockwise, respectively. Note that the sign of a node is indicated through a solid edge (positive sign, anticlockwise) or a dashed edge (negative sign, clockwise).⁴⁵

$$\begin{pmatrix} j_1 & j_2 & j_3 \\ m_1 & m_2 & m_3 \end{pmatrix} = \begin{array}{c} j_1 m_1 \\ \uparrow \\ \bullet \\ \swarrow \quad \searrow \\ j_2 m_2 \quad j_3 m_3 \end{array} = \begin{array}{c} j_3 m_3 \\ \uparrow \\ \bullet \\ \swarrow \quad \searrow \\ j_2 m_2 \quad j_1 m_1 \end{array}, \quad (5.4.2)$$

⁴Note that the introduction of solid or dashed edges instead of simply noting “+” or “-” next to each node is the only deviation from the original notation given in [VMK88].

⁵This reflects the invariance of the $3j$ under cyclic permutations of its columns as only the order in its diagrammatic representation counts.

Furthermore, a j -line associated with $\langle jm|$ may come into a node in which case the $3j$ symbol carries an additional phase factor of $(-)^{j-m}$ and its projection quantum number m is inverted

$$\begin{array}{c} j_1 m_1 \\ \downarrow \\ \bullet \\ \swarrow \quad \searrow \\ j_2 m_2 \quad j_3 m_3 \end{array} = (-)^{j_1 - m_1} \begin{pmatrix} j_1 & j_2 & j_3 \\ -m_1 & m_2 & m_3 \end{pmatrix}. \quad (5.4.3)$$

In the following, we will summarize the most important rules for the transformation of diagrams, however, this treatment is far from exhaustive and for further reading and background information we refer to [VMK88].

1. **Invariant summation over projection quantum numbers:** Two j -lines with compatible direction, i.e., one is going into its node and the other out of its node may be linked together producing an *internal* j -line

$$\sum_{m_x, m_y} \begin{array}{c} j_x m_x \\ \swarrow \\ \bullet \\ \searrow \\ j_y m_y \end{array} \begin{array}{c} j_1 m_1 \\ \rightarrow \\ \bullet \\ \rightarrow \\ j_2 m_2 \end{array} = \begin{array}{c} j_x \\ \swarrow \quad \searrow \\ \bullet \quad \bullet \\ \rightarrow \quad \rightarrow \\ j_y \end{array} \begin{array}{c} j_1 m_1 \\ \rightarrow \\ \bullet \\ \rightarrow \\ j_2 m_2 \end{array}, \quad (5.4.4)$$

where the linked j -line has the same direction as the two original ones. Such an internal j -line implies the summation over the associated projection quantum number. Note that each internal line is corresponding to a scalar product of the two irreducible tensors the line is linking and, as a consequence, internal variables are invariant under rotations. Another type of lines are *external* lines: Those lines are linked to a node only at one end and the other one is free, i.e., their associated external variables are parameters of the expression under consideration and not involved in any summations.

2. **Summation over angular momentum:** A summation not only of the projection but also over the angular momentum j itself is indicated through a thick j -line

$$\sum_J \Pi_J^2 \begin{array}{c} j_4 m_4 \\ \swarrow \\ \bullet \\ \searrow \\ j_3 m_3 \end{array} \begin{array}{c} j_1 m_1 \\ \swarrow \\ \bullet \\ \searrow \\ j_2 m_2 \end{array} \begin{array}{c} J \\ \leftarrow \quad \rightarrow \\ \bullet \quad \bullet \end{array} = \begin{array}{c} j_4 m_4 \\ \swarrow \\ \bullet \\ \searrow \\ j_3 m_3 \end{array} \begin{array}{c} j_1 m_1 \\ \swarrow \\ \bullet \\ \searrow \\ j_2 m_2 \end{array} \begin{array}{c} J \\ \leftarrow \quad \rightarrow \\ \bullet \quad \bullet \end{array}, \quad (5.4.5)$$

where one has to keep in mind the additional hatfactor involved in the summation.

3. **Change of node sign:** It is very often convenient to exchange two j -lines with each other for example if they are crossing each other. Such an exchange of j -lines corresponds to a change of the momentum coupling order and has to be taken into account either by an inversion of the sign of the associated node or by a phase factor of the form $(-)^{j_1 + j_2 + j_3}$ as already discussed previously (see eq. (5.4.2)).

4. **Change of direction of internal lines:** Inverting the direction of an internal j -line produces a phase factor of $(-)^{2j}$ in the associated analytic expression

$$\begin{array}{c} j_x \\ \circlearrowleft \\ j_1 m_1 \leftarrow \bullet \bullet \rightarrow j_2 m_2 \\ \circlearrowright \\ j_y \end{array} = (-)^{2j_x} \begin{array}{c} j_x \\ \circlearrowright \\ j_1 m_1 \leftarrow \bullet \bullet \rightarrow j_2 m_2 \\ \circlearrowleft \\ j_y \end{array} . \quad (5.4.6)$$

It becomes evident that changing the direction of internal j -lines for integer angular momenta (as opposed to half-integer angular momenta) does not change the associated analytical expression. As a consequence, we will usually omit the direction of integer angular momentum internal lines.

5. **Linking subdiagrams:** Two subdiagrams A and B which have at least one identical node may be linked together by means of the rule

$$\begin{array}{c} j_1 \\ \circlearrowleft \\ A \xrightarrow{j_2} \bullet \bullet \xrightarrow{j_2} B \\ \circlearrowright \\ j_3 \end{array} = \begin{array}{c} j_1 \\ \xrightarrow{\quad} \\ A \xrightarrow{j_2} B \\ \xrightarrow{j_3} \end{array} . \quad (5.4.7)$$

Note that a necessary condition for the validity of this rule is that at least one of the subdiagrams does not have an external line.

6. **Cutting into subdiagrams:** In this work we will only be dealing with cutting one or two lines connecting two subdiagrams A and B and the two corresponding rules may be diagrammatically written as follows

$$\begin{array}{c} j_1 \\ \xrightarrow{\quad} \\ A \xrightarrow{j_1} B \\ \xrightarrow{j_2} \end{array} = \begin{array}{c} A \\ B \end{array} , \quad (5.4.8)$$

$$\begin{array}{c} j_1 \\ \circlearrowleft \\ A \xrightarrow{j_1} B \\ \circlearrowright \\ j_2 \end{array} = \begin{array}{c} j_1 \\ \circlearrowleft \\ A \\ \circlearrowright \\ j_2 \end{array} \frac{\delta_{j_1 j_2}}{\Pi_{j_1}^2} . \quad (5.4.9)$$

Note that a condition for the validity of these rules is that at least one of the two subdiagrams does not exhibit any external lines.

7. **Hermitian conjugation:** Very often it is necessary to invert the direction of all external lines of the diagrammatic representation of the $3j$ symbol. Such a transformation produces a phase factor of $(-)^{2j_1}$, where j_1 corresponds to the j -line whose direction is differing from the other two j -lines. If, however, the directions are all the same, i.e., either out or ingoing, then the diagram is invariant under such an inversion.

8. **Orthonormality relation:** The graphical representation of the orthonormality relation of $3j$ symbols reads

$$\begin{array}{c} j_2 \\ \circlearrowleft \\ j_3 m_3 \rightarrow \bullet \bullet \rightarrow j_3' m_3' \\ \circlearrowright \\ j_1 \end{array} = \frac{\delta_{j_3 j_3'} \delta_{m_3 m_3'}}{\Pi_{j_3}^2} . \quad (5.4.10)$$

9. **Completeness relation:** Diagrammatically, the completeness relation for $3j$ symbols is given through

$$\begin{array}{c}
 \begin{array}{ccc}
 \begin{array}{c} \downarrow j_1 m_1 \\ \bullet \\ \uparrow j_2 m_2 \end{array} & \begin{array}{c} \leftarrow j_3 \\ \bullet \\ \rightarrow j_1 m'_1 \\ \downarrow j_2 m'_2 \end{array} & \\
 \end{array} & = & \delta_{m_1 m'_1} \delta_{m_2 m'_2} .
 \end{array} \tag{5.4.11}$$

10. **Elimination of vanishing j -lines:** A vanishing j -line, defined as a line with $j = 0$, may be removed from the diagram along with its corresponding node

$$\begin{array}{c}
 \begin{array}{ccc}
 \begin{array}{c} \leftarrow j_1 m_1 \\ \bullet \\ \rightarrow j_2 m_2 \\ \downarrow j=0 \end{array} & & \\
 \end{array} & = & \frac{\delta_{j_1 j_2} \delta_{m_1 m_2}}{\Pi_{j_1}} .
 \end{array} \tag{5.4.12}$$

Note that the remaining two j -lines keep their original direction and are involved in a delta term. This rule can be applied to any diagram exhibiting vanishing j -line by means of a reduction to the diagram shown above.

As already noted previously, we will also face the emergence of $6j$ and $9j$ symbols. Diagrammatically, these symbols may be represented via

$$\left\{ \begin{array}{c} j_1 \ j_2 \ j_3 \\ J_1 \ J_2 \ J_3 \end{array} \right\} = \begin{array}{c} \bullet \\ \begin{array}{ccc} \swarrow J_2 & \uparrow j_3 & \searrow J_1 \\ \bullet & & \bullet \\ \nwarrow j_1 & \downarrow j_2 & \nearrow J_3 \end{array} \\ \bullet \end{array} , \tag{5.4.13}$$

$$\left\{ \begin{array}{c} j_{11} \ j_{12} \ j_{13} \\ j_{21} \ j_{22} \ j_{23} \\ j_{31} \ j_{32} \ j_{33} \end{array} \right\} = \begin{array}{c} \bullet \\ \begin{array}{ccc} \swarrow j_{11} & \downarrow j_{12} & \searrow j_{13} \\ \bullet & & \bullet \\ \nwarrow j_{31} & \downarrow j_{33} & \nearrow j_{23} \\ \bullet & & \bullet \\ \swarrow j_{32} & \downarrow j_{21} & \searrow j_{22} \\ \bullet & & \bullet \end{array} \\ \bullet \end{array} . \tag{5.4.14}$$

Note that the diagrammatic representation of the $6j$ ($9j$) symbol elucidates that it may be written in terms of four (six) $3j$ symbols and the aforementioned symmetry properties of both the $6j$ and $9j$ symbol appear naturally within their diagrammatic representation.

Note that diagrams that only differ by some kind of deformation but still represent the same analytical expression will be called *identical*. Furthermore, diagrams that only differ by their node signs or directions of lines are called *topologically similar* as they usually only differ by a phase factor.

5.5. Coupled and Reduced Matrix Elements—Conventions and Formulas

Up to now, a collective index like, e.g., p denoted a full m -scheme collective index, i.e., it fully specified a single-particle state, which could then be written as $|p\rangle$. Instead, from now on p shall denote a *spherical* collective single-particle index that does not depend on the projection quantum number anymore. As a consequence, a single-particle state may now be written as $|pm_p\rangle$ where m_p is the corresponding projection. For expressing all previous m -scheme equations in terms of this new convention, the following transformation with regard to single-particle indices has to be conducted

$$p \rightarrow pm_p, \quad X_q^p \rightarrow X_{qm_q}^{pm_p}, \quad X_{rs}^{pq} \rightarrow X_{rm_rsm_s}^{pm_pqm_q}. \quad (5.5.1)$$

Note that this step is necessary for resolving ambiguities within the context of the transformation from m -scheme equations to spherical equations, where we will encounter expressions in which both m -scheme and reduced matrix elements are occurring.

Two-Body Matrix Elements. Using spherical collective single-particle indices, a general m -scheme two-body matrix element is now written as

$$(X_{M_L}^L)^{1m_1 2m_2}_{3m_3 4m_4} = \langle 1m_1, 2m_2 | \hat{X}_{M_L}^L | 3m_3, 4m_4 \rangle. \quad (5.5.2)$$

Our general approach is to couple the two angular momenta in bra and ket to a total angular momentum $\hat{J} = \hat{j}_1 + \hat{j}_2$ and $\hat{J}' = \hat{j}_3 + \hat{j}_4$, respectively, which gives

$$(X_{M_L}^L)^{1m_1 2m_2}_{3m_3 4m_4} = \langle 1m_1 2m_2 | \hat{X}_{M_L}^L | 3m_3 4m_4 \rangle \quad (5.5.3)$$

$$= \sum_{JM_J J' M_{J'}} \begin{pmatrix} j_1 & j_2 & J \\ m_1 & m_2 & M_J \end{pmatrix} \begin{pmatrix} j_3 & j_4 & J' \\ m_3 & m_4 & M_{J'} \end{pmatrix} \langle 12; JM_J | \hat{T}_{M_L}^L | 34; J' M_{J'} \rangle \quad (5.5.4)$$

$$\equiv \sum_{JJ' M_J M_{J'}} \begin{pmatrix} j_1 & j_2 & J \\ m_1 & m_2 & M_J \end{pmatrix} \begin{pmatrix} j_3 & j_4 & J' \\ m_3 & m_4 & M_{J'} \end{pmatrix} (X_{M_L}^L)^{(12)JM_J}_{(34)J'M_{J'}}, \quad (5.5.5)$$

where we introduced a short-hand notation for a coupled two-body matrix element

$$(X_{M_L}^L)^{(12)JM_J}_{(34)J'M_{J'}} \equiv \langle 12; JM_J | \hat{X}_{M_L}^L | 34; J' M_{J'} \rangle \quad (5.5.6)$$

Additionally, we apply the Wigner-Eckart theorem for obtaining reduced matrix elements

$$(X_{M_L}^L)^{(12)JM_J}_{(34)J'M_{J'}} = \langle 12; JM | \hat{X}_{M_L}^L | 34; J' M' \rangle \quad (5.5.7)$$

$$= (-)^{J-M_J} \begin{pmatrix} J & L & J' \\ -M_J & M_L & M_{J'} \end{pmatrix} \langle 12; J || \hat{X}^L || 34; J' \rangle \quad (5.5.8)$$

$$= (-)^{J-M_J} \begin{pmatrix} J & L & J' \\ -M_J & M_L & M_{J'} \end{pmatrix} (X^L)^{(12)J}_{(34)J'}, \quad (5.5.9)$$

Again, we introduced a new short-hand notation only this time for *reduced* matrix elements of two-body operators

$$\left(X^L\right)_{(34)J'}^{(12)J} \equiv \langle 12; J || \hat{X}^L || 34; J' \rangle, \quad (5.5.10)$$

which are, compared to coupled matrix elements, not depending on projection quantum numbers anymore. Plugging both relations into each other and expressing Clebsch Gordan coefficients in terms of $3j$ symbols yields

$$\begin{aligned} \left(X_{M_L}^L\right)_{3m_3 4m_4}^{1m_1 2m_2} &= \sum_{JJ'} \left(X^L\right)_{(34)J'}^{(12)J} (-)^{J+j_1+j_3-j_2-j_4} \Pi_J \Pi_{J'} \\ &\times \sum_{M_J M_{J'}} (-)^{M_{J'}} \begin{pmatrix} J & L & J' \\ -M_J & M_L & M_{J'} \end{pmatrix} \begin{pmatrix} j_1 & j_2 & J \\ m_1 & m_2 & -M_J \end{pmatrix} \begin{pmatrix} j_3 & j_4 & J' \\ m_3 & m_4 & -M_{J'} \end{pmatrix}, \end{aligned} \quad (5.5.11)$$

whereas the inverse relation is given through

$$\begin{aligned} \left(X^L\right)_{(34)J'}^{(12)J} &= \Pi_J \Pi_{J'} \sum_{\substack{MM_J M_{J'} \\ m_1 m_2 m_3 m_4}} (-)^{j_1-m_1+j_2-m_2+j_3-m_3+j_4-m_4+J'-M_{J'}+L-M} \\ &\times \begin{pmatrix} L & J' & J \\ -M_L & -M_{J'} & M_J \end{pmatrix} \begin{pmatrix} j_1 & j_2 & J \\ m_1 & m_2 & -M_J \end{pmatrix} \begin{pmatrix} j_3 & j_4 & J' \\ m_3 & m_4 & -M_{J'} \end{pmatrix} \left(X_M^L\right)_{3m_3 4m_4}^{1m_1 2m_2}. \end{aligned} \quad (5.5.12)$$

Note that for a scalar ($L = 0$) there is a simple relation between a reduced and a coupled matrix elements

$$\left(X_0^0\right)_{(34)J' M_{J'}}^{(12)J M_J} = \delta_{JJ'} \delta_{M_J M_{J'}} \Pi_J^{-1} \left(X^0\right)_{(34)J'}^{(12)J}, \quad (5.5.13)$$

which is a direct consequence of the Wigner-Eckart theorem. During the course of the following angular momentum coupling, we will commonly switch between reduced and coupled matrix elements like

$$\left(X^0\right)_{(34)J}^{(12)J} \leftrightarrow \Pi_J \left(X_0^0\right)_{(34)J_0}^{(12)J_0} \equiv \Pi_J \left(X^0\right)_{(34)J}^{(12)J}, \quad (5.5.14)$$

where we usually omit the indication of the projection quantum number for the bra and ket state for brevity. Diagrammatically expressing the relations giving m -scheme in terms of reduced matrix elements and vice versa leads to

$$\left(X_{M_L}^L\right)_{3m_3 4m_4}^{1m_1 2m_2} = \sum_{JJ'} \left(X^L\right)_{(34)J'}^{(12)J} \Pi_J \Pi_{J'} \begin{array}{c} \begin{array}{c} j_4 \\ \uparrow \\ \bullet \\ \downarrow \\ j_3 \end{array} \begin{array}{c} L \\ \uparrow \\ \bullet \\ \downarrow \\ j_2 \end{array} \begin{array}{c} j_1 \\ \uparrow \\ \bullet \\ \downarrow \\ j_2 \end{array} \end{array}, \quad (5.5.15)$$

$$\left(X^L\right)_{(34)J'}^{(12)J} = \Pi_J \Pi_{J'} \sum_{\substack{Mm_1 m_2 \\ m_3 m_4}} \left(X_M^L\right)_{3m_3 4m_4}^{1m_1 2m_2} \begin{array}{c} \begin{array}{c} j_4 \\ \uparrow \\ \bullet \\ \downarrow \\ j_3 \end{array} \begin{array}{c} L \\ \uparrow \\ \bullet \\ \downarrow \\ j_2 \end{array} \begin{array}{c} j_1 \\ \uparrow \\ \bullet \\ \downarrow \\ j_2 \end{array} \end{array}. \quad (5.5.16)$$

One-Body Matrix Elements. Considering one-body matrix elements, the angular momentum coupling step is not required, thus, we only apply the Wigner Eckart theorem for obtaining *reduced* matrix elements from *m*-scheme matrix elements

$$(T_M^L)_{qm_q}^{pm_p} = (-)^{j_p - m_p} \begin{pmatrix} j_p & L & j_q \\ -m_p & M & m_q \end{pmatrix} (T^L)_q^p . \quad (5.5.17)$$

Similarly to the two-body case, there is a simple relation between coupled and reduced matrix elements for scalars, which can be written as

$$(X_0^0)_{2m_2}^{1m_1} = \delta_{j_1 j_2} \delta_{m_1 m_2} \Pi_{j_1}^{-1} (X^0)_2^1 , \quad (5.5.18)$$

and which allows us to simply replace one with the other. Diagrammatically expressing the relations giving *m*-scheme in terms of reduced matrix elements and vice versa leads to

$$(T_M^L)_{2m_2}^{1m_1} = (T^L)_2^1 \begin{array}{c} \uparrow LM_L \\ \swarrow j_1 m_1 \quad \searrow j_2 m_2 \\ \bullet \end{array} , \quad (5.5.19)$$

$$(T^L)_2^1 = \sum_{M m_1 m_2} (T_M^L)_{2m_2}^{1m_1} \begin{array}{c} \uparrow LM_L \\ \swarrow j_1 m_1 \quad \searrow j_2 m_2 \\ \bullet \end{array} . \quad (5.5.20)$$

Pandya Transformation. An important, but rather technical aspect of the spherical commutator equations is the Pandya transformation [Suh07]. Formally, the Pandya transformation may be defined for *scalar* spherical tensor operators as

$$\left(\overline{A_0^0}\right)_{(34)\bar{j}}^{(12)\bar{j}} = - \sum_{\bar{j}} \left\{ \begin{array}{c} j_1 \ j_2 \ \bar{j} \\ j_3 \ j_4 \ J \end{array} \right\} (A_0^0)_{(32)J}^{(14)J} , \quad (5.5.21)$$

where the inverse of the relation above is of the exact same form and we usually suppress any indication of the projection quantum number of the bra and ket state for brevity. In this work, the Pandya transformation—closely related to cross-coupled matrix elements [Kuo+81]—is employed for coupling single-particle states in bra and ket with each other. More specifically, it enables us to couple the first single-particle state of the bra with the first single-particle state of the ket. The motivation for this procedure are algebraic terms in which summation indices are distributed over the bra and ket states. Such terms may be transformed by means of the Pandya transformation resulting in an expression in which the summation indices are not scattered across the bra and ket anymore

$$\sum_{pq} (X_0^0)_{(p2)J}^{(1q)J} (Y_0^0)_{(3q)J}^{(p4)J} \rightsquigarrow \sum_{pq} \left(\overline{X_0^0}\right)_{(pq)\bar{j}}^{(12)\bar{j}} \left(\overline{Y_0^0}\right)_{(34)\bar{j}}^{(pq)\bar{j}} . \quad (5.5.22)$$

The reason why we prefer the form which exhibits Pandya-transformed matrix elements is simple: It can be formulated as matrix-matrix product implying a massive increase of computational efficiency even if taking the computational cost of the Pandya transformation into account.

For *non-scalar* operators we have to redefine the Pandya transformation as follows

$$\left(\overline{\mathbf{X}^L}\right)_{(34)\bar{J}'}^{(12)\bar{J}} = - \sum_{JJ'} \Pi_{\bar{J}} \Pi_{\bar{J}'} \Pi_J \Pi_{J'} \left\{ \begin{matrix} j_1 & j_2 & \bar{J} \\ j_4 & j_3 & \bar{J}' \\ J & J' & L \end{matrix} \right\} (-)^{j_2+j_4+\bar{J}'+J'} (\mathbf{X}^L)_{(32)J'}^{(14)J} . \quad (5.5.23)$$

This generalization of the Pandya transformation to non-scalar spherical tensor operators with arbitrary rank L was guided by two principles: Firstly, form invariance under inversion, and secondly, compatibility with the definition for scalar operators. However, it is important to note that the definition for non-scalar operators is *not* equal to the scalar definition for vanishing tensor ranks, but Pandya-transformed matrix elements based on either one or the other definition are related by

$$\left(\overline{\mathbf{X}^0}\right)_{(34)\bar{J}'}^{(12)\bar{J}} = \delta_{\bar{J}\bar{J}'} \Pi_{\bar{J}} \left(\overline{\mathbf{X}^0}\right)_{(34)\bar{J}}^{(12)\bar{J}} . \quad (5.5.24)$$

Evidently, this relation is similar to the relation between reduced and coupled matrix elements for scalars. Therefore, Pandya-transformed matrix elements of non-scalar operators may be considered as “reduced”.

The following relation which diagrammatically gives an m -scheme matrix element in terms of Pandya-transformed matrix elements will prove very useful

$$\left(\mathbf{X}^0\right)_{3m_3 4m_4}^{1m_1 2m_2} = \sum_{\bar{J}} \Pi_{\bar{J}}^2 \left(\overline{\mathbf{X}^0}\right)_{(32)\bar{J}}^{(14)\bar{J}} \begin{array}{c} j_2, m_2 \swarrow \quad \bar{J} \quad \nwarrow j_1, m_1 \\ \bullet \text{---} \bullet \\ j_3, m_3 \swarrow \quad \nwarrow j_4, m_4 \end{array} , \quad (5.5.25)$$

$$\left(\mathbf{X}_M^L\right)_{3m_3 4m_4}^{1m_1 2m_2} = \sum_{\bar{J}\bar{J}'} \Pi_{\bar{J}} \Pi_{\bar{J}'} \left(\overline{\mathbf{X}^L}\right)_{(32)\bar{J}'}^{(14)\bar{J}} \begin{array}{c} \bar{J} \quad \bar{J}' \\ \bullet \quad \bullet \\ \swarrow \quad \downarrow \quad \searrow \\ j_4 m_4 \quad j_1 m_1 \quad j_2 m_2 \quad j_3 m_3 \end{array} . \quad (5.5.26)$$

In the context of angular momentum coupling, this relation will facilitate the treatment of several terms by *directly* inserting Pandya-transformed matrix elements if necessary.

Another relation deals with the case where one of the total angular momenta of the Pandya-transformed matrix element vanishes

$$\left(\overline{\mathbf{X}^L}\right)_{(34)0}^{(12)\bar{J}} = - \sum_{JJ'} \Pi_{\bar{J}} \Pi_0 \Pi_J \Pi_{J'} \left\{ \begin{matrix} j_1 & j_2 & \bar{J} \\ j_4 & j_3 & 0 \\ J & J' & L \end{matrix} \right\} (-)^{j_2+j_4+0+J'} (\mathbf{X}^L)_{(32)J'}^{(14)J} \quad (5.5.27)$$

$$= - \sum_{JJ'} \delta_{j_3 j_4} \delta_{\bar{J} L} \Pi_{J, J'} \Pi_{j_3}^{-1} (-)^{j_1+j_2+L} \left\{ \begin{matrix} j_1 & j_2 & L \\ J' & J & j_3 \end{matrix} \right\} (\mathbf{X}^L)_{(32)J'}^{(14)J} . \quad (5.5.28)$$

This relation will prove its usefulness during the following derivation of the spherical commutator evaluation equations where we will encounter terms resembling the right-hand side of the relation above which can then be directly identified as Pandya-transformed matrix elements. Note that we employed the following relation, whose diagrammatic derivation is

straightforward, for rewriting a $9j$ symbol with a single vanishing angular momentum in terms of a $6j$ symbol

$$\left\{ \begin{matrix} j_1 & j_2 & \bar{J} \\ j_4 & j_3 & 0 \\ J & J' & L \end{matrix} \right\} = \delta_{j_3, j_4} \delta_{JL} \Pi_L^{-1} \Pi_{j_3}^{-1} (-)^{j_1+j_3+L+J'} \left\{ \begin{matrix} j_1 & j_2 & L \\ J' & J & j_3 \end{matrix} \right\}. \quad (5.5.29)$$

5.6. Spherical Equations

Let us now employ the symmetry-optimized m -scheme equations eqs. (5.3.10) to (5.3.24) as a starting point for angular momentum coupling. In this context this means that we get rid of any projection quantum numbers and express our equation in terms of *reduced* matrix elements. The motivation for this endeavor is clear: It greatly reduces the computational effort as all sums that run over single-particle states produce considerably less terms.

5.6.1. Derivation Zero-Body Part

Zero-Body Part, Term 1. Starting from the expression

$$C_0 = \sum_{pqm_p m_q} (n_{pm_p} - n_{qm_q}) (A_0^0)^{pm_p}_{qm_q} (B_M^L)^{qm_q}_{pm_p}, \quad (5.6.1)$$

we may express the m -scheme matrix elements in terms of spherical matrix elements

$$= \sum_{pq} (n_p - n_q) (A^0)_q^p (B^L)_p^q \sum_{m_p m_q} \begin{matrix} 0 \\ j_p \uparrow \downarrow j_q \\ \bullet \end{matrix} \begin{matrix} LM \\ j_q \uparrow \downarrow j_p \\ \bullet \end{matrix}, \quad (5.6.2)$$

merging the two diagrams yields

$$= \sum_{pq} (n_p - n_q) (A^0)_q^p (B^L)_p^q \begin{matrix} j_q \\ 0 \leftarrow \bullet \rightleftarrows \bullet \rightarrow LM \\ \bullet \\ j_p \end{matrix}, \quad (5.6.3)$$

as the diagram evaluates to a delta expression we obtain

$$= \sum_{pq} (n_p - n_q) (A^0)_q^p (B^L)_p^q (-)^{2j_p} (-)^{j_p+j_q+L} \frac{\delta_{L,0} \delta_{M,0} \delta_{j_p j_q}}{\Pi_L^2}. \quad (5.6.4)$$

This equation may then be written as

Zero-Body Part, Term 1

$$C_0 = \sum_{pq} (n_p - n_q) (A^0)_q^p (B^0)_p^q \delta_{L,0} \delta_{M,0} . \quad (5.6.5)$$

Zero-Body Part, Term 2. Starting from the m -scheme expression

$$C_0 = \frac{1}{4} \sum_{pqrs} \sum_{m_p m_q m_r m_s} n_{p m_p} n_{q m_q} \bar{n}_{r m_r} \bar{n}_{s m_s} \left((A_{M_A}^{L_A})_{r m_r s m_s}^{p m_p q m_q} (B_{M_B}^{L_B})_{p m_p q m_q}^{r m_r s m_s} - [A \leftrightarrow B] \right) , \quad (5.6.6)$$

we express the matrix elements in terms of their reduced counterpart, which produces

$$= \frac{1}{4} \sum_{pqrs} n_p n_q \bar{n}_r \bar{n}_s \sum_{J_A J'_A J_B J'_B} \Pi_{J_A J'_A J_B J'_B} (A^{L_A})_{(rs)J'_A}^{(pq)J_A} (B^{L_B})_{(pq)J'_B}^{(rs)J_B} \sum_{m_p m_q m_r m_s} \left(\begin{array}{c} j_s m_s \quad L_A M_A \quad j_p m_p \\ \swarrow \quad \uparrow \quad \swarrow \\ \text{---} J'_A \text{---} J_A \text{---} \\ \searrow \quad \downarrow \quad \searrow \\ j_r m_r \quad j_q m_q \end{array} \right) \left(\begin{array}{c} j_q m_q \quad L_B M_B \quad j_r m_r \\ \swarrow \quad \uparrow \quad \swarrow \\ \text{---} J'_B \text{---} J_B \text{---} \\ \searrow \quad \downarrow \quad \searrow \\ j_p m_p \quad j_s m_s \end{array} \right) - [A \leftrightarrow B] , \quad (5.6.7)$$

putting together the two diagrams results in

$$= \frac{1}{4} \sum_{pqrs} n_p n_q \bar{n}_r \bar{n}_s \sum_{J_A J'_A J_B J'_B} \Pi_{J_A J'_A J_B J'_B} (A^{L_A})_{(rs)J'_A}^{(pq)J_A} (B^{L_B})_{(pq)J'_B}^{(rs)J_B} \left(\begin{array}{c} j_p \\ \swarrow \quad \searrow \\ \text{---} J_A \text{---} \quad \text{---} J'_B \text{---} \\ \swarrow \quad \searrow \\ j_q \quad j_s \\ \swarrow \quad \searrow \\ \text{---} J'_A \text{---} \quad \text{---} J_B \text{---} \\ \swarrow \quad \searrow \\ L_A M_A \quad L_B M_B \\ \downarrow \quad \downarrow \\ j_r \end{array} \right) - [A \leftrightarrow B] , \quad (5.6.8)$$

the diagram evaluates to several delta terms giving the expression

$$= \frac{1}{4} \sum_{pqrs} n_p n_q \bar{n}_r \bar{n}_s \sum_{J_A J'_A J_B J'_B} \Pi_{J_A J'_A J_B J'_B} (A^{L_A})_{(rs)J'_A}^{(pq)J_A} (B^{L_B})_{(pq)J'_B}^{(rs)J_B} \frac{\delta_{J_A J'_B} \delta_{J'_A J_B} \delta_{L_B L_A} \delta_{M_B, -M_A}}{\Pi_{J_A}^2 \Pi_{J'_A}^2 \Pi_{L_A}^2} - [A \leftrightarrow B] \quad (5.6.9)$$

$$= \frac{1}{4} \sum_{pqrs} n_p n_q \bar{n}_r \bar{n}_s \sum_{JJ'} (A^{L_A})_{(rs)J'}^{(pq)J} (B^{L_B})_{(pq)J}^{(rs)J'} \frac{\delta_{L_B L_A} \delta_{M_B, -M_A}}{\Pi_{L_A}^2} - [A \leftrightarrow B] . \quad (5.6.10)$$

Finally, we obtain the result

| Zero-Body Part, Term 2 | |
|--|----------|
| $C_0 = \frac{1}{4} \sum_{pqrs} n_p n_q \bar{n}_r \bar{n}_s \sum_J \left((A^0)_{(rs)J}^{(pq)J} (B^{LB})_{(pq)J}^{(rs)J} - [A \leftrightarrow B] \right) \delta_{L_B, 0} .$ | (5.6.11) |

Zero-Body Part, Term 3. Starting from

$$C_0 = \frac{1}{4} \sum_{pqrs} \sum_{m_p m_q m_r m_s} (C_M^L)_{rm_r sm_s}^{pm_p qm_q} (\lambda_0^0)_{rm_r sm_s}^{pm_q qm_q} \quad (5.6.12)$$

$$= \frac{1}{4} \sum_{pqrs} \sum_{m_p m_q m_r m_s} (C_M^L)_{rm_r sm_s}^{pm_p qm_q} (\lambda_0^0)_{pm_q qm_q}^{rm_r sm_s} , \quad (5.6.13)$$

we obtain similar diagrams as for the previous term, which leads to

| Zero-Body Part, Term 3 | |
|--|----------|
| $C_0 = \frac{1}{4} \sum_{pqrs} \sum_J (C^L)_{(rs)J}^{(pq)J} (\lambda^0)_{(pq)J}^{(rs)J} \delta_{L, 0} .$ | (5.6.14) |

5.6.2. Derivation One-Body Part

All terms contributing to the one-body part can be written as

$$(C_M^L)_{2m_2}^{1m_1} = \hat{\Xi}_{12M}^{M\pm} f(1, m_1, 2, m_2, L, M) \quad (5.6.15)$$

$$= \frac{1 \pm (-)^M \hat{t}_{-M}^M \hat{t}_2^1}{2} f(1, m_1, 2, m_2, L, M) . \quad (5.6.16)$$

This way all the general symmetry properties of one-body matrix elements are absorbed into the symmetrizer $\hat{\Xi}_{12M}^{M\pm}$. However, our goal is to obtain equations in terms of *reduced* matrix elements such that all our equations exhibit the form

$$(C^L)_2^1 = \hat{\Xi}_{12}^{S\pm} \tilde{f}(1, 2, L) , \quad (5.6.17)$$

where we introduced the *spherical* symmetrizer $\hat{\Xi}_{12}^{S\pm}$ and the function \tilde{f} as the spherical counterpart of f . Similarly to the the m -scheme symmetrizer $\hat{\Xi}_{12M}^{M\pm}$, the spherical symmetrizer $\hat{\Xi}_{12}^{S\pm}$ shall, once acting on a reduced one-body matrix element, restore all basic symmetry properties common to those one-body matrix elements. Note that the right-hand side of the equation above does not exhibit any dependence on projection quantum numbers anymore.

Let us now start with deriving the spherical symmetrizer by expressing a reduced one-body matrix element in terms of an m -scheme element

$$(C^L)_2^1 = \sum_{M m_1 m_2} \begin{pmatrix} j_1 & L & j_2 \\ -m_1 & M & m_2 \end{pmatrix} (-)^{j_1 - m_1} (C_M^L)_{2 m_2}^{1 m_1}, \quad (5.6.18)$$

employing eq. (5.6.16) yields

$$= \sum_{M m_1 m_2} \begin{pmatrix} j_1 & L & j_2 \\ -m_1 & M & m_2 \end{pmatrix} (-)^{j_1 - m_1} \frac{1 + \xi_C (-)^M \hat{\tau}_{-M}^M \hat{\tau}_2^1}{2} f(1, m_1, 2, m_2, L, M), \quad (5.6.19)$$

pulling the symmetrizer to the front of the expression and taking into account eventually arising phase factors due to the non-commutativity of this action yields

$$= \frac{1 + \xi_C (-)^{j_1 - j_2} \hat{\tau}_2^1}{2} \sum_{M m_1 m_2} \begin{pmatrix} j_1 & L & j_2 \\ -m_1 & M & m_2 \end{pmatrix} (-)^{j_1 - m_1} f(1, m_1, 2, m_2, L, M). \quad (5.6.20)$$

By comparison, we obtain the following result for the spherical one-body symmetrizer and the spherical function \tilde{f}

$$\hat{\Xi}_{12}^{S^\pm} = \frac{1}{2} (1 \pm (-)^{j_1 - j_2} \hat{\tau}_2^1), \quad (5.6.21)$$

$$\tilde{f}(1, 2, L) = \sum_{M m_1 m_2} \begin{pmatrix} j_1 & L & j_2 \\ -m_1 & M & m_2 \end{pmatrix} (-)^{j_1 - m_1} f(1, m_1, 2, m_2, L, M). \quad (5.6.22)$$

Summarizing, spherical equations may be conveniently obtained through the following diagrammatically formulated formula

$$(C^L)_2^1 = \hat{\Xi}_{12}^{S^\pm} \tilde{f}(1, 2, L) = \hat{\Xi}_{12}^{S^\pm} \sum_{M m_1 m_2} \begin{matrix} LM \\ j_1 m_1 \uparrow j_2 m_2 \\ \bullet \end{matrix} f(1, m_1, 2, m_2, L, M). \quad (5.6.23)$$

Evidently, transforming the m -scheme equations into a spherical form breaks down to the calculation of \tilde{f} .

One-Body Part, Term 1. Starting from the term

$$(C_{M_C}^{L_C})_{2 m_2}^{1 m_1} = \hat{\Xi}_{12 M}^{\mathcal{M}^\pm} \sum_{p m_p} 2 (A_{M_A}^{L_A})_{p m_p}^{1 m_1} (B_{M_B}^{L_B})_{2 m_2}^{p m_p}, \quad (5.6.24)$$

the spherical counterpart of this equation is given through

$$(C^L)_2^1 = \hat{\Xi}_{12}^{S^\pm} \sum_{M_C m_1 m_2} \begin{matrix} L_C M_C \\ j_1 m_1 \uparrow j_2 m_2 \\ \bullet \end{matrix} \sum_{p m_p} 2 (A_{M_A}^{L_A})_{p m_p}^{1 m_1} (B_{M_B}^{L_B})_{2 m_2}^{p m_p}. \quad (5.6.25)$$

Expressing the occurring matrix elements of \hat{A} and \hat{B} in terms of reduced matrix elements yields

$$(C^L)_2^1 = \hat{\Xi}_{12}^{S\pm} \sum_p 2 (A^{L_A})_p^1 (B^{L_B})_2^p \sum_{\substack{M_C m_p \\ m_1 m_2}} j_1 m_2 \begin{array}{c} L_A M_A \\ \uparrow \\ \bullet \\ \downarrow \\ j_p m_p \end{array} \begin{array}{c} L_B M_B \\ \uparrow \\ \bullet \\ \downarrow \\ j_2 m_2 \end{array} \begin{array}{c} L_C M_C \\ \uparrow \\ \bullet \\ \downarrow \\ j_1 m_1 \end{array} . \quad (5.6.26)$$

The three $3j$ symbols may be put together to one big diagram

$$(C^L)_2^1 = \hat{\Xi}_{12}^{S\pm} \sum_p 2 (A^{L_A})_p^1 (B^{L_B})_2^p \sum_{M_C} (-) \begin{array}{c} L_B M_B \\ \uparrow \\ \bullet \\ \downarrow \\ j_2 \\ \swarrow \quad \searrow \\ \bullet \quad \bullet \\ \uparrow \quad \downarrow \\ L_A M_A \quad L_C M_C \\ \swarrow \quad \searrow \\ \bullet \\ \downarrow \\ j_1 \end{array} , \quad (5.6.27)$$

by exploiting that the spherical tensor rank L_A vanishes, we obtain

$$= \hat{\Xi}_{12}^{S\pm} \sum_p 2 (A^0)_p^1 (B^{L_B})_2^p \sum_{M_C} \delta_{j_1 j_p} \Pi_{j_1}^{-1} \begin{array}{c} j_2 \\ \uparrow \\ \bullet \\ \downarrow \\ j_1 \end{array} \begin{array}{c} L_B M_B \\ \uparrow \\ \bullet \\ \downarrow \\ j_1 \end{array} \begin{array}{c} L_C M_C \\ \uparrow \\ \bullet \\ \downarrow \\ j_1 \end{array} , \quad (5.6.28)$$

which can be simplified to the following final expression

| One-Body Part, Term 1 | |
|--|--|
| $(C^L)_2^1 = \hat{\Xi}_{12}^{S\pm} \sum_p 2 (A^0)_p^1 (B^L)_2^p \Pi_{j_1}^{-1} . \quad (5.6.29)$ | |

One-Body Part, Term 2.1. Starting from

$$C_{2m_2}^{1m_1} = \hat{\Xi}_{12M}^{S\pm} \sum_{pq} \sum_{m_p m_q} (n_{pm_p} - n_{qm_q}) (A_0^0)_{qm_q}^{pm_p} (B_M^L)_{pm_p 2m_2}^{qm_q 1m_1} , \quad (5.6.30)$$

the spherical equations are obtained from

$$(C^L)_2^1 = \hat{\Xi}_{12}^{S\pm} \sum_{M j_1 j_2} j_1 m_1 \begin{array}{c} LM \\ \uparrow \\ \bullet \\ \downarrow \\ j_2 m_2 \end{array} \sum_{pq} \sum_{m_p m_q} (n_{pm_p} - n_{qm_q}) (A_0^0)_{qm_q}^{pm_p} (B_M^L)_{pm_p 2m_2}^{qm_q 1m_1} , \quad (5.6.31)$$

expressing the matrix elements in terms of their reduced counterparts gives

$$\begin{aligned}
 &= \hat{\Xi}_{12}^{S\pm} \sum_{pq} (n_p - n_q) \sum_{J_B J'_B} \Pi_{J_B} \Pi_{J'_B} (A^0)_q^p (B^L)_{(p2)J'_B}^{(q1)J_B} \\
 &\sum_{M j_1 j_2} \sum_{m_p m_q} j_1 m_1 \uparrow j_2 m_2 \uparrow \begin{array}{c} 0 \\ j_p m_p \uparrow j_q m_q \end{array} \begin{array}{c} LM \\ j_2 m_2 \uparrow j_1 m_1 \end{array} \begin{array}{c} LM \\ j_q m_q \uparrow j_1 m_1 \end{array} \quad , \quad (5.6.32)
 \end{aligned}$$

putting together all occurring $3j$ symbols produces

$$\begin{aligned}
 &= \hat{\Xi}_{12}^{S\pm} \sum_{pq} (n_p - n_q) \sum_{J_B J'_B} (A^0)_q^p (B^L)_{(p2)J'_B}^{(q1)J_B} \\
 &\Pi_{J_B} \Pi_{J'_B} \Pi_{j_p}^{-1} (-1) \begin{array}{c} \bullet \\ J_B \quad L \\ \quad J'_B \\ j_p \quad j_2 \\ \bullet \\ j_1 \end{array} \quad . \quad (5.6.33)
 \end{aligned}$$

The occurring diagram may be interpreted as a $6j$ symbol, which leads to the intermediate result

$$\begin{aligned}
 (C^L)_2^1 &= \hat{\Xi}_{12}^{S\pm} \sum_{pq} (n_p - n_q) \sum_{J_B J'_B} (A^0)_q^p (B^L)_{(p2)J'_B}^{(q1)J_B} \\
 &\Pi_{J_B} \Pi_{J'_B} \Pi_{j_p}^{-1} (-)^{J_B+L+j_p+j_2} \left\{ \begin{array}{c} j_p \quad j_2 \quad J'_B \\ L \quad J_B \quad j_1 \end{array} \right\} . \quad (5.6.34)
 \end{aligned}$$

Examining this term closely, reveals that it may be simplified by rewriting the $6j$ symbol in terms of a $9j$ symbol, which then allows us to introduce the Pandya transformation of the operator \hat{B}

$$\begin{aligned}
 (C^L)_2^1 &= \hat{\Xi}_{12}^{S\pm} \sum_{pq} (n_p - n_q) (A^0)_q^p \\
 &\sum_{J_B J'_B} (B^L)_{(p2)J'_B}^{(1q)J_B} \Pi_{J_B} \Pi_{J'_B} \Pi_L (-)^{j_q+j_2+J'_B+1} \left\{ \begin{array}{c} j_1 \quad j_2 \quad L \\ j_p \quad j_p \quad 0 \\ J_B \quad J'_B \quad L \end{array} \right\} , \quad (5.6.35)
 \end{aligned}$$

and, finally, we obtain

| One-Body Part, Term 2.1 | |
|---|--|
| $(C^L)_2^1 = \hat{\Xi}_{12}^{S\pm} \sum_{pq} (n_p - n_q) (\overline{B^L})_{(pq)0}^{(12)L} (A^0)_q^p . \quad (5.6.36)$ | |

One-Body Part, Term 2.2. Starting from

$$(C_M^L)^{1m_1}_{2m_2} = - \hat{\Xi}_{12M}^{\mathcal{M}\pm} \sum_{pq} \sum_{m_p m_q} (n_{pm_p} - n_{qm_q}) (B_M^L)^{pm_p}_{qm_q} (A_0^0)^{qm_q 1m_1}_{pm_p 2m_2}, \quad (5.6.37)$$

the spherical equation can be derived by evaluating

$$(C^L)_2^1 = - \hat{\Xi}_{12}^{S\pm} \sum_{pq} \sum_{m_p m_q} (n_{pm_p} - n_{qm_q}) \sum_{M j_1 m_1 j_2 m_2}^{LM} (B_M^L)^{pm_p}_{qm_q} (A_0^0)^{qm_q 1m_1}_{pm_p 2m_2}. \quad (5.6.38)$$

Expressing the matrix elements on the right-hand side in terms of reduced matrix elements produces

$$(C^L)_2^1 = - \hat{\Xi}_{12}^{S\pm} \sum_{pq} (n_p - n_q) \sum_{J_A J'_A} \Pi_{J_A} \Pi_{J'_A} (B^L)_q^p (A^0)^{(q1)J_A}_{(p2)J'_A} \sum_{M j_1 m_1 j_2 m_2}^{LM} \sum_{m_p m_q}^{LM} \begin{array}{c} j_p m_p \uparrow j_q m_q \\ \downarrow \uparrow \\ j_1 m_1 \uparrow j_2 m_2 \\ \downarrow \uparrow \end{array} \begin{array}{c} 0 \\ \uparrow \\ J'_A \quad J_A \\ \downarrow \uparrow \\ j_2 m_2 \quad j_1 m_1 \end{array}. \quad (5.6.39)$$

Merging all diagrams into one yields

$$(C^L)_2^1 = - \hat{\Xi}_{12}^{S\pm} \sum_{pq} (n_p - n_q) \sum_{J_A J'_A} \Pi_{J_A} \Pi_{J'_A} (B^L)_q^p (A^0)^{(q1)J_A}_{(p2)J'_A} (-1) \delta_{J_A J'_A} \Pi_{J_A}^{-1} \begin{array}{c} \bullet \\ \downarrow \\ J_A \quad j_p \quad j_2 \\ \swarrow \downarrow \searrow \\ j_q \quad L \\ \swarrow \downarrow \searrow \\ j_1 \end{array}. \quad (5.6.40)$$

$$= - \hat{\Xi}_{12}^{S\pm} \sum_{pq} (n_p - n_q) \sum_{J_A} \Pi_{J_A} (B^L)_q^p (A^0)^{(q1)J_A}_{(p2)J_A} (-)^{j_q + j_1 + J_A} \times \begin{array}{c} \bullet \\ \downarrow \\ J_A \quad j_p \quad j_2 \\ \swarrow \downarrow \searrow \\ j_q \quad L \\ \swarrow \downarrow \searrow \\ j_1 \end{array}. \quad (5.6.41)$$

Expressing the diagram in terms of a 6j symbol gives

$$(C^L)_2^1 = -\hat{\Xi}_{12}^{S^\pm} \sum_{pq} (n_p - n_q) \sum_{J_A} \Pi_{J_A} (B^L)_q^p (A^0)_{(p2)J_A}^{(q1)J_A} (-)^{j_q+j_1+J_A} \left\{ \begin{matrix} j_q & L & j_p \\ j_2 & J_A & j_1 \end{matrix} \right\} \quad (5.6.42)$$

$$= -\hat{\Xi}_{12}^{S^\pm} \sum_{pq} (n_p - n_q) (B^L)_q^p \sum_{J_A} \Pi_{J_A} (A^0)_{(p2)J_A}^{(1q)J_A} (-1) \left\{ \begin{matrix} j_1 & j_2 & L \\ j_p & j_q & J_A \end{matrix} \right\} \quad (5.6.43)$$

$$= -\hat{\Xi}_{12}^{S^\pm} \sum_{pq} (n_p - n_q) (B^L)_q^p \sum_{J_A} \Pi_{J_A}^2 (A^0)_{(p2)J_A^0}^{(1q)J_A^0} (-1) \left\{ \begin{matrix} j_1 & j_2 & L \\ j_p & j_q & J_A \end{matrix} \right\}. \quad (5.6.44)$$

By exploiting that the rear part of this expression matches the very definition of the Pandya transformation for scalar operators, we obtain

One-Body Part, Term 2.2

$$(C^L)_2^1 = -\hat{\Xi}_{12}^{S^\pm} \sum_{pq} (n_p - n_q) (B^L)_q^p \left(\overline{A^0} \right)_{(pq)L}^{(12)L}. \quad (5.6.45)$$

One-Body Part, Term 3. Starting point is the term

$$(C_{MC}^{LC})_{2m_2}^{1m_1} = \hat{\Xi}_{12M}^{M^\pm} \sum_{pqr} \sum_{m_p m_q m_r} (n_{pm_p} \bar{n}_{qm_q} \bar{n}_{rm_r} + \bar{n}_{pm_q} n_{qm_q} n_{rm_r}) (A_{M_A}^{L_A})_{qm_q rm_r}^{1m_1 pm_p} (B_{M_B}^{L_B})_{2m_2 pm_p}^{qm_q rm_r}, \quad (5.6.46)$$

and the associated spherical term is given through

$$(C^{LC})_2^1 = \hat{\Xi}_{12}^{S^\pm} \sum_{M_C m_1 m_2} j_1 m_1 \begin{matrix} L_C M_C \\ \uparrow \\ j_2 m_2 \end{matrix} \sum_{pqr} \sum_{m_p m_q m_r} (n_{pm_p} \bar{n}_{qm_q} \bar{n}_{rm_r} + \bar{n}_{pm_q} n_{qm_q} n_{rm_r}) (A_{M_A}^{L_A})_{qm_q rm_r}^{1m_1 pm_p} (B_{M_B}^{L_B})_{2m_2 pm_p}^{qm_q rm_r}. \quad (5.6.47)$$

Expressing all matrix elements on the right-hand side in terms of their reduced counterpart and merging all emerging diagrams yields

$$(C^{LC})_2^1 = \hat{\Xi}_{12}^{S^\pm} \sum_{pqr} (n_p \bar{n}_q \bar{n}_r + \bar{n}_p n_q n_r) \sum_{J_A J'_A J_B J'_B} A_{(qr)J'_A}^{(1p)J_A} B_{(2p)J'_B}^{(qr)J_B}$$

$$\Pi_{J_A J'_A J_B J'_B} (-1) \sum_{M_{LC}} \left(\text{Diagram} \right), \quad (5.6.48)$$

the diagram simplifies to

$$\begin{aligned}
 &= \hat{\Xi}_{12}^{S^\pm} \sum_{pqr} (n_p \bar{n}_q \bar{n}_r + \bar{n}_p n_q n_r) \sum_{J_A J'_A J_B J'_B} \mathbf{A}_{(qr)J'_A}^{(1p)J_A} \mathbf{B}_{(2p)J'_B}^{(qr)J_B} \\
 &\Pi_{J_A J'_A J_B J'_B} (-1) \delta_{J_A J'_A} \delta_{J'_A J_B} \delta_{J'_B J_B} \Pi_{J_B}^{-2} \delta_{L_C L_B} \quad \cdot \quad (5.6.49)
 \end{aligned}$$

Finally, we obtain the result

$$\begin{aligned}
 (C^L)_2^1 &= \hat{\Xi}_{12}^{S^\pm} \sum_{pqr} (n_p \bar{n}_q \bar{n}_r + \bar{n}_p n_q n_r) \sum_{J_A J_B} (\mathbf{A}^0)_{(qr)J_A}^{(1p)J_A} (\mathbf{B}^L)_{(2p)J_B}^{(qr)J_A} \\
 &\Pi_{J_B} (-)^{j_1+j_p+J_B+L_B} \left\{ \begin{matrix} j_2 & j_1 & L \\ J_A & J_B & j_p \end{matrix} \right\}. \quad (5.6.50)
 \end{aligned}$$

In principle, we could stop at this point as any dependence on projection quantum numbers has been integrated out. However, the $6j$ symbol occurring in this term resembles the definition of the Pandya transformation and, in fact, we can express this term in terms of a Pandya transformation, which is not only analytically more concise but also advantageous regarding the implementation of this term.

One-Body Part, Term 3

$$(C^L)_2^1 = \hat{\Xi}_{12}^{S^\pm} \sum_p \Pi_{j_p} \left(n_p (\overline{\boldsymbol{\gamma}^L})_{(pp)0}^{(12)L} + \bar{n}_p (\boldsymbol{\gamma}^L)_{(pp)0}^{(12)L} \right), \quad (5.6.51)$$

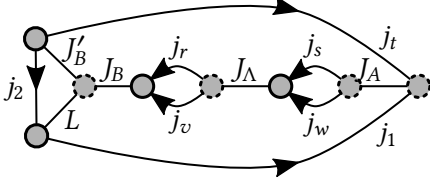
$$(\boldsymbol{\gamma}^L)_{(34)J'}^{(12)J} = \sum_{pq} \frac{\bar{n}_p \bar{n}_q}{\Pi_J} (\mathbf{A}^0)_{(pq)J}^{(12)J} (\mathbf{B}^L)_{(34)J'}^{(pq)J}, \quad (5.6.52)$$

$$(\boldsymbol{\gamma}'^L)_{(34)J'}^{(12)J} = \sum_{pq} \frac{n_p n_q}{\Pi_J} (\mathbf{A}^0)_{(pq)J}^{(12)J} (\mathbf{B}^L)_{(34)J'}^{(pq)J}. \quad (5.6.53)$$

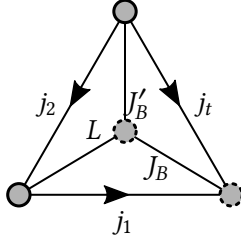
One-Body Part, Term 4. Starting from the m -scheme term

$$(C_{M_L}^L)_{2m_2}^{1m_1} = \frac{\hat{\Xi}_{12M}^{\mathcal{M}^\pm}}{2} \sum_{rtvs} \sum_{\substack{m_r m_r m_v \\ m_s m_w}} (\mathbf{A}_0^0)_{sm_s wm_w}^{1m_1 tm_t} (\lambda_0^0)_{rm_r vm_v}^{sm_s wm_w} (\mathbf{B}_M^L)_{2m_2 tm_t}^{rm_r vm_v}, \quad (5.6.54)$$

we are expressing all matrix elements in terms of reduced matrix elements which yields

$$(C^L)_2^1 = \frac{\hat{\Xi}_{12}^{S^\pm}}{2} \sum_{rtvsw} \sum_{J_A J_\lambda J_B J'_B} (A^0)_{(sw)J_A}^{(1t)J_A} (\lambda^0)_{(rv)J_\lambda}^{(sw)J_\lambda} (B^L)_{(2t)J'_B}^{(rv)J_B}$$


$$(-1)^{\Pi_{J_A J_\lambda J_B J'_B}} \quad (5.65)$$

$$= \frac{\hat{\Xi}_{12}^{S^\pm}}{2} \sum_{rtvsw} \sum_{J_B J'_B} (A^0)_{(sw)J_B}^{(1t)J_B} (\lambda^0)_{(rv)J_B}^{(sw)J_B} (B^L)_{(2t)J'_B}^{(rv)J_B}$$


$$(-1)^{\Pi_{J_B}^{-1} \Pi_{J'_B}} \quad (5.66)$$

Interpreting the last diagram as a $6j$ symbol, we obtain

$$(C^L)_2^1 = \frac{\hat{\Xi}_{12}^{S^\pm}}{2} \sum_{rtvsw} \sum_{JJ'} (A^0)_{(sw)J}^{(1t)J} (\lambda^0)_{(rv)J}^{(sw)J} (B^L)_{(2t)J'}^{(rv)J}$$

$$(-1)^{L+J'+j_1+j_t} \Pi_J^{-1} \Pi_{J'} \left\{ \begin{matrix} L & J & J' \\ j_t & j_2 & j_1 \end{matrix} \right\} . \quad (5.657)$$

A more compact result is obtained by defining

$$(\gamma^L)_{(2t)J'}^{(1t)J} \equiv \sum_{swrv} (A_0^0)_{(sw)J}^{(1t)J} (\lambda_0^0)_{(rv)J}^{(sw)J} (B^L)_{(2t)J'}^{(rv)J} , \quad (5.658)$$

through which the previous result can be written as

$$(C^L)_2^1 = \frac{\hat{\Xi}_{12}^{S^\pm}}{2} \sum_t \sum_{JJ'} (\gamma^L)_{(2t)J'}^{(1t)J} (-1)^{L+J'+j_1+j_t} \Pi_J \Pi_{J'} \left\{ \begin{matrix} L & J & J' \\ j_t & j_2 & j_1 \end{matrix} \right\} . \quad (5.659)$$

Expressing the $6j$ symbol via a $9j$ symbol by employing eq. (5.5.29), interchanging the two single-particle states in the bra of γ (which leads to the emergence of a phase factor) produces an expression, which contains a term that exactly matches the definition of a Pandya transformed matrix element and, finally, we obtain

One-Body Part, Term 4

$$(C^L)_2^1 = \frac{\hat{\Xi}_{12}^{S^\pm}}{2} \sum_t (\overline{\gamma^L})_{(tt)0}^{(12)L}, \quad (5.6.60)$$

$$(\gamma^L)_{(34)J'}^{(12)J} = \sum_{pqrs} (A_0^0)_{(pq)J}^{(12)J} (\lambda_0^0)_{(rs)J}^{(pq)J} (B^L)_{(34)J'}^{(rs)J} \delta_{2,4}. \quad (5.6.61)$$

One-Body Part, Term 5. Starting from

$$(C_M^L)_{2m_2}^{1m_1} = \hat{\Xi}_{12M}^{M^\pm} (-2) \sum_{rtvs} \sum_{\substack{m_r m_t m_v \\ m_s m_w}} (A_0^0)_{sm_s t m_t}^{1m_1 r m_r} (\lambda_0^0)_{vm_v r m_r}^{sm_s w m_w} (B_M^L)_{2m_2 w m_w}^{vm_v t m_t}, \quad (5.6.62)$$

we are now deviating from the usual procedure and express the m -scheme matrix elements on the right-hand side directly in terms of *Pandya-transformed* matrix elements

$$(C^L)_2^1 = \hat{\Xi}_{12}^{S^\pm} (-2) \sum_M \sum_{m_1 m_2} \sum_{rtvs} \sum_{\substack{m_r m_t \\ m_v m_s \\ m_w}} \Pi_{\bar{J}_A}^2 (\overline{A_0^0})_{(sr)\bar{J}_A}^{(1t)\bar{J}_A} \\ \sum_{\bar{J}_\lambda} \Pi_{\bar{J}_\lambda}^2 (\overline{\lambda_0^0})_{(vw)\bar{J}_\lambda}^{(sr)\bar{J}_\lambda} \sum_{\bar{J}_B \bar{J}'_B} \Pi_{\bar{J}_B} \Pi_{\bar{J}'_B} (\overline{B^L})_{(2t)\bar{J}'_B}^{(vw)\bar{J}_B} \\ \begin{array}{c} \begin{array}{ccc} j_r m_r & \xrightarrow{\bar{J}_A} & j_1 m_1 \\ j_s m_s & \searrow & \swarrow j_t m_t \end{array} \\ \begin{array}{ccc} j_w m_w & \xrightarrow{\bar{J}_\Lambda} & j_s m_s \\ j_v m_v & \searrow & \swarrow j_r m_r \end{array} \\ \begin{array}{ccc} LM_L & & \\ j_1 m_1 & \uparrow & j_2 m_2 \end{array} \\ \begin{array}{ccc} \bar{J}_B & & \bar{J}'_B \\ j_w m_w & \swarrow & \searrow j_2 m_2 \\ j_v m_v & \downarrow L & j_t m_t \end{array} \end{array} \quad (5.6.63)$$

Merging all diagrams yields

$$(C^L)_2^1 = \hat{\Xi}_{12}^{S^\pm} (+2) \sum_{rtvs} \sum_{\bar{J}_A \bar{J}_\lambda \bar{J}_B \bar{J}'_B} \Pi_{\bar{J}_A \bar{J}_\lambda}^2 \Pi_{\bar{J}_B \bar{J}'_B} (\overline{A_0^0})_{(sr)\bar{J}_A}^{(1t)\bar{J}_A} \\ (\overline{\lambda_0^0})_{(vw)\bar{J}_\lambda}^{(sr)\bar{J}_\lambda} (\overline{B^L})_{(2t)\bar{J}'_B}^{(vw)\bar{J}_B} \\ \begin{array}{c} \begin{array}{ccccccc} & & j_t & & \bar{J}'_B & & \\ & & \uparrow & & \downarrow & & \\ \bar{J}_A & \xrightarrow{j_s} & j_1 & \xrightarrow{j_2} & \bar{J}_B & \xrightarrow{j_w} & \bar{J}_B \\ & \swarrow & \downarrow L & \swarrow & \downarrow & \swarrow & \\ & j_r & & & j_v & & \end{array} \end{array} \quad (5.6.64)$$

which may be simplified to the expression

$$= \hat{\Xi}_{12}^{S\pm} (+2) \sum_t \sum_{\bar{J}_B \bar{J}'_B} \sum_{r v s w} \underbrace{\left(\overline{A_0^0} \right)_{(sr)\bar{J}_B}^{(1t)\bar{J}_B} \left(\overline{\lambda_0^0} \right)_{(vw)\bar{J}_B}^{(sr)\bar{J}_B} \left(\overline{B^L} \right)_{(2t)\bar{J}'_B}^{(vw)\bar{J}_B}}_{= \left(\overline{\gamma^L} \right)_{(2t)\bar{J}'_B}^{(1t)\bar{J}_B}}$$

$$\Pi_{\bar{J}_B \bar{J}'_B} \begin{array}{c} \bullet \\ \swarrow \quad \downarrow \quad \searrow \\ \bar{J}_B \quad \bar{J}'_B \quad L \\ \swarrow \quad \downarrow \quad \searrow \\ \bullet \quad \bullet \quad \bullet \\ \nearrow \quad \nwarrow \\ j_1 \end{array} \quad (5.6.65)$$

The last diagram is the diagrammatic representation of a $6j$ symbol and we obtain the result

One-Body Part, Term 5

$$\left(C^L \right)_2^1 = \hat{\Xi}_{12}^{S\pm} (+2) \sum_t \sum_{\bar{J}_B \bar{J}'_B} \Pi_{\bar{J}_B \bar{J}'_B} \left(\overline{\gamma^L} \right)_{(2t)\bar{J}'_B}^{(1t)\bar{J}_B} (-)^{j_1+j_t+L+\bar{J}'_B} \left\{ \begin{array}{ccc} j_t & j_2 & \bar{J}'_B \\ L & \bar{J}_B & j_1 \end{array} \right\}, \quad (5.6.66)$$

$$\left(\overline{\gamma^L} \right)_{(2t)\bar{J}'_B}^{(1t)\bar{J}_B} = \sum_{r v s w} \left(\overline{A_0^0} \right)_{(sr)\bar{J}_B}^{(1t)\bar{J}_B} \left(\overline{\lambda_0^0} \right)_{(vw)\bar{J}_B}^{(sr)\bar{J}_B} \left(\overline{B^L} \right)_{(2t)\bar{J}'_B}^{(vw)\bar{J}_B}. \quad (5.6.67)$$

One-Body Part, Term 6.1. Starting from

$$\left(C_M^L \right)_{2m_2}^{1m_1} = \hat{\Xi}_{12M}^{\mathcal{M}\pm} \sum_{r t v s w} \sum_{m_r m_t m_v m_s m_w} \left(A_0^0 \right)_{tm_t 2m_2}^{1m_1 r m_r} \left(B_M^L \right)_{sm_s w m_w}^{tm_t v m_v} \left(\lambda_0^0 \right)_{vm_v r m_r}^{sm_s w m_w}, \quad (5.6.68)$$

the spherical equation is given through

$$\begin{aligned} \left(C^L \right)_2^1 &= \hat{\Xi}_{12}^{S\pm} \sum_{r t v s w} \sum_{m_1 m_2 M} \sum_{m_r m_t m_v m_s m_w} \\ &\sum_{\bar{J}_A} \Pi_{\bar{J}_A}^2 \left(\overline{A_0^0} \right)_{(tr)\bar{J}_A}^{(12)\bar{J}_A} \sum_{\bar{J}_B \bar{J}'_B} \Pi_{\bar{J}_B \bar{J}'_B} \left(\overline{B^L} \right)_{(sv)\bar{J}'_B}^{(tv)\bar{J}_B} \sum_{J_\lambda} \Pi_{J_\lambda} \left(\lambda_0^0 \right)_{(rv)J_\lambda}^{(sw)J_\lambda} \\ &\begin{array}{ccc} \begin{array}{c} j_r m_r \swarrow \quad \nwarrow \\ \bullet \quad \bullet \\ \nearrow \quad \searrow \\ j_t m_t \quad j_1 m_1 \end{array} & \begin{array}{c} j_w m_w \swarrow \quad \nwarrow \\ \bullet \quad \bullet \\ \nearrow \quad \searrow \\ j_s m_s \quad j_v m_v \end{array} & \\ &\begin{array}{c} LM \\ \bullet \\ \nearrow \quad \searrow \\ j_1 m_1 \quad j_2 m_2 \end{array} & \begin{array}{c} L \\ \bullet \quad \bullet \\ \nearrow \quad \searrow \\ j_s m_s \quad j_v m_v \end{array} & \end{array}, \quad (5.6.69) \end{aligned}$$

putting all diagrams together produces

$$\begin{aligned}
 &= \hat{\Xi}_{12}^{S^\pm} \sum_{rtvsw} \sum_{\bar{J}_A J_B J'_B J_\lambda} \left(\overline{A_0^0} \right)_{(tr)\bar{J}_A}^{(12)\bar{J}_A} (\mathbf{B}^L)_{(sw)J'_B}^{(tv)J_B} (\boldsymbol{\lambda}^0)_{(rv)J_\lambda}^{(sw)J'_B} \\
 &\quad \Pi_{\bar{J}_A}^2 \Pi_{J_B J'_B} \Pi_{J_\lambda} \quad \text{Diagram (5.6.70)} \quad , \tag{5.6.70}
 \end{aligned}$$

the diagram may be simplified to the expression

$$\begin{aligned}
 &= \hat{\Xi}_{12}^{S^\pm} \sum_{rtvsw} \sum_{\bar{J}_A J_B J'_B J_\lambda} \left(\overline{A_0^0} \right)_{(tr)\bar{J}_A}^{(12)\bar{J}_A} (\mathbf{B}^L)_{(sw)J'_B}^{(tv)J_B} (\boldsymbol{\lambda}^0)_{(rv)J_\lambda}^{(sw)J'_B} \\
 &\quad \Pi_{\bar{J}_A}^2 \Pi_{J_B J'_B} \Pi_{J_\lambda} \quad \text{Diagram (5.6.71)} \quad . \tag{5.6.71}
 \end{aligned}$$

Evaluating all diagrammatic delta terms and recognizing the diagrammatic representation of the $6j$ symbol within the equation above yields

$$\begin{aligned}
 (C^L)_2^1 &= \hat{\Xi}_{12}^{S^\pm} \sum_{rtvsw} \sum_{J_B J'_B} \left(\overline{A_0^0} \right)_{(tr)L}^{(12)L} (\mathbf{B}^L)_{(sw)J'_B}^{(tv)J_B} (\boldsymbol{\lambda}_0^0)_{(rv)J'_B}^{(sw)J'_B} \\
 &\quad \Pi_{J_B J'_B} (-)^{j_t+j_v+L+J'_B} \left\{ \begin{array}{c} L \quad j_t \quad j_r \\ j_v \quad J'_B \quad J_B \end{array} \right\} , \tag{5.6.72}
 \end{aligned}$$

interchanging the two single-particle states in the ket of $\hat{\lambda}$ and taking into account the emerging phase factor gives

$$\begin{aligned}
 &= \hat{\Xi}_{12}^{S^\pm} \sum_{rtv} \sum_{J_B J'_B} \left(\overline{A_0^0} \right)_{(tr)L}^{(12)L} \sum_{sw} (\mathbf{B}^L)_{(sw)J'_B}^{(tv)J_B} (\boldsymbol{\lambda}_0^0)_{(vr)J'_B}^{(sw)J'_B} \\
 &\quad \Pi_{J_B J'_B} (-)^{j_t+j_r+L} \left\{ \begin{array}{c} L \quad j_t \quad j_r \\ j_v \quad J'_B \quad J_B \end{array} \right\} , \tag{5.6.73}
 \end{aligned}$$

defining $\hat{\gamma}$ as the tensor product of \hat{B} and $\hat{\lambda}$ results in

$$\begin{aligned}
 &= \hat{\Xi}_{12}^{S^\pm} \sum_{rtv} \left(\overline{A_0^0} \right)_{(tr)L}^{(12)L} \sum_{J_B J'_B} (\boldsymbol{\gamma}^L)_{(vr)J'_B}^{(tv)J_B} \Pi_{J_B J'_B} (-)^{j_t+j_r+L} \left\{ \begin{array}{c} L \quad j_t \quad j_r \\ j_v \quad J'_B \quad J_B \end{array} \right\} . \tag{5.6.74}
 \end{aligned}$$

Identifying the rear part of the expression above as a Pandya-transformed matrix element, we obtain the result

One-Body Part, Term 6.1

$$(C^L)_2^1 = \hat{\Xi}_{12}^{S^\pm} \sum_{\nu} \Pi_{j_{\nu}} \sum_{tr} \left(\overline{A_0^0} \right)_{(tr)L}^{(12)L} \left(\overline{\gamma^L} \right)_{(\nu\nu)0}^{(tr)L}, \quad (5.6.75)$$

$$\left(\gamma^L \right)_{(34)J'}^{(12)J} = \sum_{pq} \left(B^L \right)_{(pq)J'}^{(12)J} \left(\lambda_0^0 \right)_{(34)J'}^{(pq)J'}. \quad (5.6.76)$$

One-Body Part, Term 6.2. Starting from

$$(C_M^L)_{2m_2}^{1m_1} = -\hat{\Xi}_{12M}^{M^\pm} \sum_{rtvs} \sum_{m_r m_t m_\nu m_s m_w} \left(B_M^L \right)_{tm_t 2m_2}^{1m_1 r m_r} \left(A_0^0 \right)_{sm_s w m_w}^{tm_t \nu m_\nu} \left(\lambda_0^0 \right)_{\nu m_\nu r m_r}^{sm_s w m_w}, \quad (5.6.77)$$

we obtain the spherical analogue from

$$(C^L)_2^1 = \hat{\Xi}_{12}^{S^\pm} (-1) \sum_{rtv} \sum_{sw} \sum_{m_r m_t m_\nu m_s m_w} \sum_M \sum_{\bar{J}_B \bar{J}'_B} \Pi_{\bar{J}_B \bar{J}'_B} \left(\overline{B^L} \right)_{(tr)\bar{J}'_B}^{(12)\bar{J}_B} \sum_{J_A} \Pi_{J_A}^2 \left(A_0^0 \right)_{(sw)J_A}^{(tv)J_A} \sum_{J_\Lambda} \Pi_{J_\Lambda}^2 \left(\lambda_0^0 \right)_{(\nu r)J_\Lambda}^{(sw)J_\Lambda}$$

$$(5.6.78)$$

Putting the diagrams together produces

$$(C^L)_2^1 = \hat{\Xi}_{12}^{S^\pm} \sum_{rtv} \sum_{sw} \sum_{\bar{J}_B \bar{J}'_B J_A J_\Lambda} \left(\overline{B^L} \right)_{(tr)\bar{J}'_B}^{(12)\bar{J}_B} \left(A_0^0 \right)_{(sw)J_A}^{(tv)J_A} \left(\lambda_0^0 \right)_{(\nu r)J_\Lambda}^{(sw)J_\Lambda}$$

$$\Pi_{\bar{J}_B \bar{J}'_B} \Pi_{J_A}^2 \Pi_{J_\Lambda}^2, \quad (5.6.79)$$

cutting the \bar{J}'_B line gives

$$\begin{aligned}
 &= \hat{\Xi}_{12}^{S\pm} (-1) \sum_{rtv} \sum_{\substack{\bar{J}_B \bar{J}'_B J_A J_\lambda \\ sw}} \left(\bar{\mathbf{B}}^L \right)_{(tr)\bar{J}'_B}^{(12)\bar{J}_B} \left(A_0^0 \right)_{(sw)J_A}^{(tv)J_A} \left(\lambda_0^0 \right)_{(vr)J_\lambda}^{(sw)J_\lambda} \\
 &\quad \Pi_{\bar{J}_B \bar{J}'_B} \Pi_{J_A}^2 \Pi_{J_\lambda}^2 \quad \begin{array}{c} \text{Diagram 1: A node on the left with two outgoing arrows labeled } j_2 \text{ and } j_1 \text{ to two nodes. These two nodes are connected by a curved arrow labeled } L. \text{ A third arrow labeled } \bar{J}_B \text{ points to a node on the right. From this node, an arrow labeled } \bar{J}'_B = 0 \text{ points to the right.} \end{array} \quad \begin{array}{c} \text{Diagram 2: A node on the left with an incoming arrow labeled } \bar{J}'_B. \text{ Two outgoing arrows labeled } j_t \text{ and } j_r \text{ point to two nodes. These two nodes are connected by a curved arrow labeled } J_A. \text{ A third arrow labeled } j_w \text{ points to a node on the right. From this node, an arrow labeled } j_s \text{ points to the right.} \end{array} \quad (5.6.80)
 \end{aligned}$$

$$\begin{aligned}
 &= \hat{\Xi}_{12}^{S\pm} (-1) \sum_{rtv} \sum_{J_A} \Pi_L \Pi_{J_A}^4 \left(\bar{\mathbf{B}}^L \right)_{(tr)0}^{(12)L} \overbrace{\sum_{sw} \left(A_0^0 \right)_{(sw)J_A}^{(tv)J_A} \left(\lambda_0^0 \right)_{(vr)J_A}^{(sw)J_A}}^{\equiv \left(\gamma_0^0 \right)_{(vr)J_A}^{(tv)J_A}} \\
 &\quad (-)^{j_r+j_v+J_A+j_r+j_t} \delta_{j_r j_t} \Pi_{j_t}^{-1} \Pi_{J_A}^{-2} \Pi_L^{-1} \quad (5.6.81)
 \end{aligned}$$

$$= \hat{\Xi}_{12}^{S\pm} \sum_{rtv} \sum_{J_A} \left(\bar{\mathbf{B}}^L \right)_{(tr)0}^{(12)L} \left(\gamma_0^0 \right)_{(vr)J_A}^{(tv)J_A} (-)^{j_t+j_v+J_A} \delta_{j_r j_t} \Pi_{j_t}^{-1} \Pi_{J_A}^2. \quad (5.6.82)$$

The final results may now be written as

| One-Body Part, Term 6.2 | |
|---|--|
| $ \left(C^L \right)_2^1 = \hat{\Xi}_{12}^{S\pm} (-1) \sum_v \Pi_{j_v} \sum_{rt} \left(\bar{\mathbf{B}}^L \right)_{(tr)0}^{(12)L} \left(\gamma_0^0 \right)_{(v)0}^{(tr)0}, \quad (5.6.83) $ | |
| $ \left(\gamma_0^0 \right)_{(34)J}^{(12)J} = \sum_{pq} \left(A_0^0 \right)_{(pq)J}^{(12)J} \left(\lambda_0^0 \right)_{(34)J}^{(pq)J}. \quad (5.6.84) $ | |

5.6.3. Derivation Two-Body Part

Analogously to the one-body part, we can write all terms contributing to the two-body part in the form

$$\left(C_M^L \right)_{3m_3 4m_4}^{1m_1 2m_2} = \hat{\Xi}_{1234M}^{\mathcal{M}\pm} f(1m_1, 2m_2, 3m_3, 4m_4, LM), \quad (5.6.85)$$

from which we are now trying to obtain the corresponding *spherical* equations, i.e., equations in terms of reduced matrix elements and a spherical two-body symmetrizer without any dependencies on the m quantum numbers left

$$\left(C^L \right)_{(34)J'}^{(12)J} = \hat{\Xi}_{1234JJ'}^{S\pm} \tilde{f}(1, 2, 3, 4, L, J, J'). \quad (5.6.86)$$

Following similar steps as taken for the one-body part, the spherical two-body symmetrizer is given through

$$\hat{\Xi}_{1234JJ'}^{\pm S} = \frac{1}{8} \left(1 + (-)^{j_1+j_2+J+1} \hat{\tau}_2^1 \right) \left(1 + (-)^{j_3+j_4+J'+1} \hat{\tau}_4^3 \right) \times \left(1 \pm (-)^{J+J'} \hat{\tau}_3^1 \hat{\tau}_4^2 \hat{\tau}_{J'}^J \right), \quad (5.6.87)$$

whereas the spherical analogue to the function f may be written as

$$\begin{aligned} & \tilde{f}(1, 2, 3, 4, L, J, J') \\ &= \sum_{M_L m_1 m_2 m_3 m_4} \Pi_{JJ'} (-)^{J'-M_{J'}+j_2-m_2+j_1-m_1+J-M_J} \begin{pmatrix} j_4 & j_3 & J' \\ m_4 & m_3 & -M_{J'} \end{pmatrix} \\ & \quad \begin{pmatrix} j_2 & j_1 & J \\ -m_2 & -m_1 & M_J \end{pmatrix} \begin{pmatrix} J & L & J' \\ -M_J & M_L & M_{J'} \end{pmatrix} f(1m_1, 2m_2, 3m_3, 4m_4, LM) \end{aligned} \quad (5.6.88)$$

$$= \sum_{\substack{M_L m_1 \\ m_2 m_3 \\ m_4}} \begin{array}{c} j_4 m_4 \quad LM \quad j_1 m_1 \\ \nearrow \quad \uparrow \quad \searrow \\ \text{---} J' \text{---} J \text{---} \\ \searrow \quad \downarrow \quad \nearrow \\ j_3 m_3 \quad \quad j_2 m_2 \end{array} \Pi_J \Pi_{J'} f(1m_1, 2m_2, 3m_3, 4m_4, LM). \quad (5.6.89)$$

Two-Body Part, Term 1.1. Starting from the equation

$$\left(C_{M_C}^{L_C} \right)_{3m_3 4m_4}^{1m_1 2m_2} = \hat{\Xi}_{1234M}^{\pm \mathcal{M}} 4 \sum_{p m_p} \left(A_{M_A}^{L_A} \right)_{p m_p}^{1m_1} \left(B_{M_B}^{L_B} \right)_{3m_3 4m_4}^{p m_p 2m_2}, \quad (5.6.90)$$

the spherical equation is given through

$$\left(C_{M_C}^{L_C} \right)_{(34)J'}^{(12)J} = \hat{\Xi}_{1234JJ'}^{\pm S} 4 \sum_P \sum_{J_B J'_B} \left(A^{L_A} \right)_P^1 \left(B^{L_B} \right)_{(34)J'_B}^{(p2)J_B} \Pi_{JJ' J_B J'_B} \quad (5.6.91)$$

Employing that the tensor rank L_A vanishes in this case, the diagram above completely collapses producing only phasefactors, Kronecker delta functions, and hatfactors, which leads to

$$\left(C_{M_C}^{L_C} \right)_{(34)J'}^{(12)J} = \hat{\Xi}_{1234JJ'}^{\pm S} 4 \sum_P \left(B^L \right)_{(34)J'}^{(p2)J} \left(A^0 \right)_P^1 \Pi_{J_1}^{-1}. \quad (5.6.92)$$

Employing that $f(y) = \sum_x f(x)\delta_{y,x}$, we may rewrite the previous equation as

$$(\mathbf{C}^{L_C})_{(34)J'}^{(12)J} = \hat{\Xi}_{1234JJ'}^{S_{\pm}} 4 \sum_{px} (\mathbf{B}^L)_{(34)J'}^{(px)J} \underbrace{\Pi_{j_i}^{-1} (A_0^0)_p^1}_{\equiv (\alpha_0^0)_{(px)J}^{(12)J}} \delta_{2,x} \Pi_{j_i}^{+1}. \quad (5.6.93)$$

Finally, we obtain

| Two-Body Part, Term 1.1 | |
|---|--|
| $(\mathbf{C}^{L_C})_{(34)J'}^{(12)J} = \hat{\Xi}_{1234JJ'}^{S_{\pm}} 4 \sum_{px} \Pi_{j_i}^{+1} (\mathbf{B}^L)_{(34)J'}^{(px)J} (\alpha_0^0)_{(px)J}^{(12)J}, \quad (5.6.94)$ | $(\alpha_0^0)_{(px)J}^{(12)J} = \Pi_{j_i}^{-1} (A_0^0)_p^1 \delta_{2,x}. \quad (5.6.95)$ |

Note that, formally, $\hat{\alpha}$ may be interpreted as a tensor product

$$\hat{\alpha}_0^0 \sim \left[\hat{\mathbf{A}}^0 \otimes \hat{\boldsymbol{\delta}}^0 \right]_0^0, \quad (5.6.96)$$

where the delta function itself is a spherical tensor operator of rank zero. The motivation for the definition of α is that an implementation of the resulting equations is computationally much more efficient as they may be expressed as regular matrix-matrix products. (see appendix B for more information).

Two-Body Part, Term 1.2. Starting from

$$(\mathbf{C}_{M_C}^{L_C})_{3m_3 4m_4}^{1m_1 2m_2} = \hat{\Xi}_{1234M}^{M_{\pm}} (-4) \sum_{pm_p} (\mathbf{B}_{M_B}^{L_B})_{pm_p}^{1m_1} (\mathbf{A}_{M_A}^{L_A})_{3m_3 4m_4}^{pm_p 2m_2}, \quad (5.6.97)$$

as this term is similar to the previous term 2B-1.1 but with an interchange $A \leftrightarrow B$ and a minus sign, we may reuse the intermediate diagram from there by simply replacing A with B and vice versa. As a consequence we obtain the diagram

$$(\mathbf{C}^{L_C})_{(34)J'}^{(12)J} = \hat{\Xi}_{1234JJ'}^{S_{\pm}} (-4) \sum_P \sum_{JAJ'_A} (\mathbf{B}^{L_B})_P^1 (\mathbf{A}^{L_A})_{(34)J'_A}^{(p2)J_A} \Pi_{JJ'JAJ'_A} \quad (5.6.98)$$

The diagram above simplifies to a diagram, which may be interpreted as a $6j$ symbol giving the result

$$(C^L)_{(34)J'}^{(12)J} = \hat{\Xi}_{1234JJ'}^{S_{\pm}} (-4) \sum_p \Pi_J (A^0)_{(34)J'}^{(p2)J} (B^{LC})_p^1 (-)^{L+J'+j_1+j_2} \left\{ \begin{matrix} j_1 & J & j_2 \\ J' & j_p & L \end{matrix} \right\}, \quad (5.6.99)$$

which may be further simplified as

$$(C^L)_{(34)J'}^{(12)J} = \hat{\Xi}_{1234JJ'}^{S_{\pm}} (-4) \sum_p \Pi_J (A^0)_{(34)J'}^{(p2)J} (B^L)_p^1 (-)^{L+J'+j_1+j_2} \left\{ \begin{matrix} j_1 & J & j_2 \\ J' & j_p & L \end{matrix} \right\} \quad (5.6.100)$$

$$= \hat{\Xi}_{1234JJ'}^{S_{\pm}} (-4) \sum_{px} (A^0)_{(34)J'}^{(px)J} (B^L)_p^1 \underbrace{\delta_{2,x} \Pi_J (-)^{L+J'+j_1+j_x} \left\{ \begin{matrix} j_1 & J & j_x \\ J' & j_p & L \end{matrix} \right\}}_{\equiv \Pi_{J'}^{-1} \Pi_{j_2} (\beta^L)_{(px)J'}^{(12)J}} \quad (5.6.101)$$

$$= \hat{\Xi}_{1234JJ'}^{S_{\pm}} (-4) \sum_{px} (A^0)_{(34)J'}^{(px)J} \Pi_{J'}^{-1} \Pi_{j_2} (\beta^L)_{(px)J'}^{(12)J}. \quad (5.6.102)$$

Finally, the *optimized* result may be written as

| Two-Body Part, Term 1.2 | |
|---|--|
| $(C^L)_{(34)J'}^{(12)J} = \hat{\Xi}_{1234JJ'}^{S_{\pm}} (-4) \sum_{px} \Pi_{J'}^{-1} \Pi_{j_2} (A^0)_{(34)J'}^{(px)J} (\beta^L)_{(px)J'}^{(12)J}, \quad (5.6.103)$ | |
| $(\beta^L)_{(px)J'}^{(12)J} = (B^L)_p^1 \delta_{2,x} (-)^{L+J'+j_1+j_x} \Pi_{J'}^{-1} \Pi_{j_2}^{-1} \Pi_J \left\{ \begin{matrix} j_1 & J & j_x \\ J' & j_p & L \end{matrix} \right\}. \quad (5.6.104)$ | |

Note that, formally, $\hat{\beta}$ may be interpreted as a tensor product

$$\hat{\beta}_M^L \sim \left[\hat{B}^L \otimes \hat{\delta}^0 \right]_M^L, \quad (5.6.105)$$

where the delta function itself is a scalar spherical tensor operator. Again, The motivation for the definition of β is that an implementation of the resulting equations is computationally much more efficient as they may be expressed as regular matrix-matrix products. (see appendix B for more information).

Two-Body Part, Term 2. Starting from

$$(C_{M_C}^{LC})_{3m_3 4m_4}^{1m_1 2m_2} = \hat{\Xi}_{1234M}^{M_{\pm}} \sum_{\substack{m_p m_q \\ pq}} (1 - n_{pm_p} - n_{qm_q}) (A_{M_A}^{LA})_{pm_p qm_q}^{1m_1 2m_2} (B_M^L)_{3m_3 4m_4}^{pm_p qm_q}, \quad (5.6.106)$$

we are obtaining the spherical equation by evaluating the expression

$$\begin{aligned}
 (C^{L_C})_{(34)J'}^{(12)J} &= \hat{\Xi}_{1234JJ'}^{S_{\pm}} \sum_{pq} (1 - n_p - n_q) \sum_{\substack{M_C m_{j_1} m_{j_2} \\ m_{j_3} m_{j_4} \\ m_p m_q}} (A_{M_A}^{L_A})_{pm_p q m_q}^{1 m_1 2 m_2} (B_{M_B}^{L_B})_{3 m_3 4 m_4}^{p m_p q m_q} \\
 &\quad \Pi_J \Pi_{J'} \quad \begin{array}{c} \text{Diagram: A horizontal chain of three nodes. The middle node is labeled } L_C M_C \text{ with an upward arrow. The left node is labeled } J' \text{ and the right node is labeled } J. \text{ Four arrows point outwards from the nodes: } j_4 m_4 \text{ (up-left), } j_3 m_3 \text{ (down-left), } j_1 m_1 \text{ (up-right), and } j_2 m_2 \text{ (down-right).} \end{array} \quad (5.6.107)
 \end{aligned}$$

Expressing the right-hand side matrix elements in terms of reduced matrix elements yields

$$\begin{aligned}
 &= \hat{\Xi}_{1234JJ'}^{S_{\pm}} \sum_{pq} (1 - n_p - n_q) \sum_{\substack{M_C \\ m_{j_1} m_{j_2} \\ m_{j_3} m_{j_4} \\ m_p m_q}} \sum_{\substack{J_A J'_A \\ J_B J'_B}} (A^{L_A})_{(34)J'_A}^{(12)J_A} (B^{L_B})_{(34)J'_B}^{(pq)J_B} \\
 &\quad \begin{array}{c} \text{Diagram: Three separate diagrams. The top one has nodes } J'_A, J_A, J'_B, J_B \text{ with arrows } j_q m_q, j_p m_p, j_1 m_1, j_2 m_2, j_3 m_3, j_4 m_4 \text{ and labels } L_A M_A, L_B M_B. \text{ The middle one is identical to (5.6.107). The bottom one has nodes } J'_C, J_C \text{ with arrows } j_3 m_3, j_4 m_4, j_1 m_1, j_2 m_2 \text{ and label } L_C M_C. \end{array} \quad (5.6.108)
 \end{aligned}$$

merging all diagrams into one gives

$$\begin{aligned}
 &= \hat{\Xi}_{1234JJ'}^{S_{\pm}} \sum_{pq} (1 - n_p - n_q) \Pi_{J_C} \Pi_{J'_C} \sum_{J_A J'_A} \Pi_{J_A J'_A} (A^{L_A})_{(34)J'_A}^{(12)J_A} \\
 &\quad \sum_{J_B J'_B} \Pi_{J_B J'_B} (B^{L_B})_{(34)J'_B}^{(pq)J_B} \quad \begin{array}{c} \text{Diagram: A complex network of nodes and arrows. Nodes are labeled } J_C, J'_C, J_A, J'_A, J_B, J'_B. \text{ External arrows are } L_C, L_A, L_B. \text{ Internal arrows are labeled } j_1, j_2, j_3, j_4, j_p, j_q. \end{array} \quad (5.6.109)
 \end{aligned}$$

the diagram simplifies to

$$= \hat{\Xi}_{1234JJ'}^{S_{\pm}} \sum_{pq} (1 - n_p - n_q) \Pi_{J_C}^{-1} (A^{L_A})_{(34)J'_C}^{(12)J_C} (B^{L_B})_{(34)J'_C}^{(pq)J_C} \delta_{L_C L_B} \delta_{M_{L_C} M_{L_B}} \quad (5.6.110)$$

Finally, we obtain

Two-Body Part, Term 2

$$(C^L)_{(34)J'}^{(12)J} = \hat{\Xi}_{1234JJ'}^{S_{\pm}} \sum_{pq} (1 - n_p - n_q) \Pi_J^{-1} (A^0)_{(pq)J}^{(12)J} (B^L)_{(34)J'}^{(pq)J} . \quad (5.6.111)$$

Two-Body Part, Term 3. Starting from

$$(C_M^L)_{3m_3 4m_4}^{1m_1 2m_2} = \hat{\Xi}_{1234M}^{M_{\pm}} \sum_{pq} \sum_{m_p m_q} 4(n_{pm_p} - n_{qm_q}) (A_0^0)_{3m_3 4m_4}^{1m_1 2m_2} (B_M^L)_{4m_4 3m_3}^{2m_2 1m_1} \quad (5.6.112)$$

$$= \hat{\Xi}_{1234M}^{M_{\pm}} \sum_{pq} \sum_{m_p m_q} 4(n_{pm_p} - n_{qm_q}) (A_0^0)_{qm_q 3m_3}^{1m_1 2m_2} (B_M^L)_{4m_4 3m_3}^{qm_q 2m_2} , \quad (5.6.113)$$

we are following the usual steps and express the matrix elements of \hat{A} and \hat{B} in terms of their Pandya-transformed analogues

$$(C^L)_{(34)J'}^{(12)J} = \hat{\Xi}_{1234JJ'}^{S_{\pm}} \sum_{pq} 4(n_p - n_q) \sum_{J_A} \Pi_{J_A}^2 (\overline{A_0^0})_{(qp)J_A}^{(13)J_A} \sum_{J_B J'_B} \Pi_{J_B J'_B} (\overline{B^L})_{(42)J'_B}^{(qp)J_B} \sum_{\substack{m_p m_q \\ M m_1 \\ m_2 m_3 \\ m_4}} \Pi_{JJ'} \quad (5.6.114)$$

Merging the diagrams into one diagram yields

$$(C^L)_{(34)J'}^{(12)J} = \hat{\Xi}_{1234JJ'}^{S_{\pm}} \sum_{pq} 4(n_p - n_q) \sum_{J_A J_B J'_B} \Pi_{J_A}^2 \Pi_{J_B J'_B J'_B} (\overline{A_0^0})_{(qp)J_A}^{(13)J_A} (\overline{B^L})_{(42)J'_B}^{(qp)J_B} (-)^{2j_2+2j_1} (-)^{j_2+j_4+J'_B} \quad (5.6.115)$$

simplifying the diagram produces

$$\begin{aligned}
 &= \hat{\Xi}_{1234JJ'}^{\pm} 4 \sum_{J_A J_B J'_B} \Pi_{J_A}^2 \Pi_{J_B J'_B J J'} (-1) \sum_{pq} (n_q - n_p) \underbrace{\left(\overline{A_0^0} \right)_{(qp)J_B}^{(13)J_B} \left(\overline{B^L} \right)_{(42)J'_B}^{(qp)J_B}}_{= (\overline{\gamma^L})_{(42)J'_B}^{(13)J_B}} \\
 & (-)^{j_2+j_4+J'_B} (-)^{2j_p} \delta_{J_A J_B} \Pi_{J_A}^{-2} \left(\begin{array}{ccc} j_1 & & j_2 \\ & J & \\ j_3 & & j_4 \\ & J_B & \\ j' & & j'_B \\ & L & \end{array} \right) , \tag{5.6.116}
 \end{aligned}$$

writing the diagram as a $9j$ symbol gives

$$\begin{aligned}
 &= \hat{\Xi}_{1234JJ'}^{\pm} 4 \sum_{J_B J'_B} \Pi_{J_B J'_B J J'} \left(\overline{\gamma^L} \right)_{(42)J'_B}^{(13)J_B} (-)^{j_2+j_4+J'_B+2j_3+J'+J'} \left\{ \begin{array}{ccc} j_1 & J & j_2 \\ J_B & L & J'_B \\ j_3 & J' & j_4 \end{array} \right\} \tag{5.6.117} \\
 &= \hat{\Xi}_{1234JJ'}^{\pm} 4 (-)^{+j_4+j_3+J'+1} \sum_{J_B J'_B} \Pi_{J_B J'_B J J'} \underbrace{\left(\overline{\gamma^L} \right)_{(42)J'_B}^{(13)J_B} (-)^{j_2+j_3+J'_B+J'+1} \left\{ \begin{array}{ccc} j_1 & J & j_2 \\ J_B & L & J'_B \\ j_3 & J' & j_4 \end{array} \right\}}_{= (\overline{\gamma^L})_{(43)J'}^{(12)J}} , \tag{5.6.118}
 \end{aligned}$$

where we exploited that the previous expression contains a part that matches the definition of the (reversed) Pandya transformation. We obtain the final result

| Two-Body Part, Term 3) | |
|--|--|
| $ \left(C^L \right)_{(34)J'}^{(12)J} = \hat{\Xi}_{1234JJ'}^{\pm} 4 \left(\gamma^L \right)_{(34)J'}^{(12)J} , \tag{5.6.119} $ | |
| $ \left(\overline{\gamma^L} \right)_{(42)J'_B}^{(13)J_A} = \sum_{pq} (n_p - n_q) \left(\overline{A_0^0} \right)_{(pq)J_A}^{(13)J_A} \left(\overline{B^L} \right)_{(42)J'_B}^{(pq)J_B} . \tag{5.6.120} $ | |

5.6.4. Remarks

Let us complete this section with a few remarks and observations regarding the general structure of the spherical commutator equations for non-scalar operators. The right-hand side of these equations is given in terms of sums over one and two-body matrix elements—including

Pandya transformed matrix elements—of the first and second argument \hat{A}^0 and \hat{B}^L , respectively, of the commutator. Accounting for the eventual non-zero tensor rank of \hat{B}^L leads to much more involved equations compared to the scalar case, which is shown in [Geb17]. As a matter of fact, these equations are not only analytically but also computationally more involved: Since the matrix elements of \hat{B}^L are not diagonal in the total angular momentum anymore the computational effort increases substantially. As a consequence, we only employ a Magnus evolution for non-scalar observables since a direct evolution is computationally not feasible.

During the derivation of the spherical equations we were aiming for an analytic form that is not only concise but also computationally easy to handle and efficient. Considering an implementation of the commutator equations, we do not directly implement these equations via simple loops over single-particle indices, but the building blocks of our implementation are matrix-matrix products—allowing an implementation that is employing basic linear algebra subprograms (BLAS) [BLA17]—and the Pandya transformation. For more information on aspects of our implementation, see appendix B.

In-Medium No-Core Shell Model

The IM-NCSM is a hybrid method that combines the NCSM with the IM-SRG. While both of these methods are already very successful on their own, the IM-NCSM aims to overcome each of their individual shortcomings while preserving their benefits. We want to emphasize at this point that we are employing a multi-reference version of the IM-SRG: The reference state $|\psi_{\text{ref}}\rangle$ is multi-determinantal and higher-order irreducible density matrices are explicitly included. In this chapter, we cover the foundations of the IM-NCSM as well as most of the new developments within this research project: generator improvements, the particle-attached/particle-removed framework, studies of the $N_{\text{max}}^{\text{ref}}$ impact, alternative reference-state constructions, and the calculation of electromagnetic observables. Note that each of these discussions consists not only of a theoretical consideration, but also includes a numerical investigation for studying the behavior and validity of our developments.

6.1. Complementarity and Correlations

Before we go into the specific details of this novel many-body method, let us discuss the general idea that the IM-NCSM is built upon: The separation of correlations into two types, which are successively accounted for during the different stages of the IM-NCSM. A striking aspect of the IM-NCSM is the complementarity of the involved inherent truncation schemes such that each stage is able to handle different kind of correlations.

On the one hand, the NCSM is employed for the construction of a reference state $|\psi_{\text{ref}}\rangle$, which already governs the correlations that are stringently required for reproducing fundamental properties and structure of an eigenstate like, e.g., the total angular momentum. The NCSM employs an N_{max} -truncation scheme which limits the unperturbed excitation energy of each determinant contained within the model space. As a consequence, up to $A_p A_h$ excitations of the NCSM base determinant, i.e., many particles, may eventually contribute to the reference state, which captures this first type of correlations. However, as we are usually employing

rather small values of N_{\max}^{ref} due to computational limitations of the NCSM, high-lying single-particle orbitals are not accounted for.

On the other hand, the IM-SRG is employed for targeting residual correlations that are necessary for an accurate description of the nucleus and not captured through the reference state $|\psi_{\text{ref}}\rangle$. These correlations are manifesting themselves through generalized particle-hole excitations on top of the reference state, which are then absorbed into the Hamiltonian during the IM-SRG evolution. The IM-SRG is naturally employing a single-particle energy quantum number truncation such that it takes correlations into account that are represented by determinants with high-lying single-particle state contributions—in contrast to the NCSM. However, the analytical and computational effort increases significantly when considering more than 2p2h excitations of the reference state. This is rooted in the fact that the consideration of higher-order excitations implies an increase of the particle rank of the irreducible density matrices we have to take into account.

Note that a similar picture may be applied to the MR-IM-SRG with HFB reference states, where the reference state is obtained from a symmetry-broken mean-field calculation. However, there is a clear difference between the IM-NCSM and the HFB-based MR-IM-SRG: While the distinction between the two aforementioned types of correlations is clearly defined within the context of the HFB-based MR-IM-SRG, the IM-NCSM allows for a conversion of one into the other through a variation of N_{\max}^{ref} . As a consequence, the IM-NCSM allows for an investigation of the impact of the reference state on our numerical results.

The decoupling of the reference state from its particle-hole excitations by means of the IM-SRG is nicely demonstrated through fig. 6.1: It depicts a representation of the initial (left) and transformed (right) Hamiltonian matrix. It is evident that the IM-SRG transformation leads to the formation of a block-like structure, where the decoupled block in the upper left corner of the matrix representation corresponds to the $N_{\max} = 0$ space.

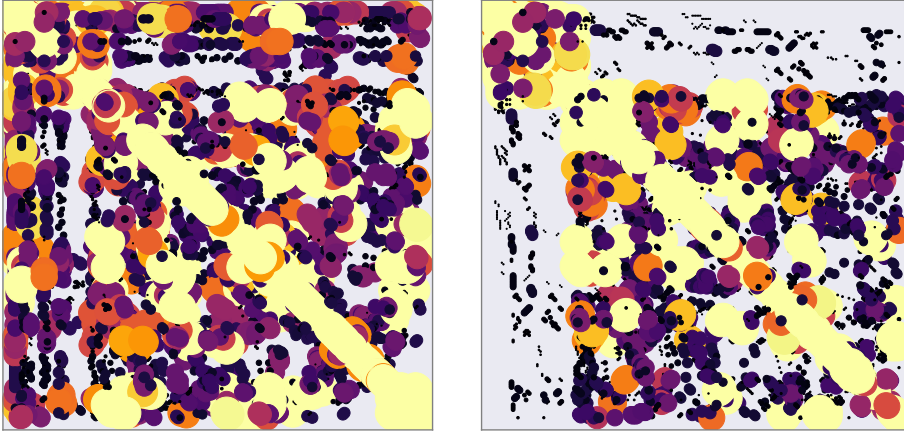


Figure 6.1.: Depiction of the initial (left) and IM-SRG-transformed (right) Hamilton matrix for ^{12}C . Note that the absolute value of each matrix elements is correlated with both the area of its corresponding plot marker and the color. It is strikingly illustrated that the IM-SRG transformation leads to the shaping of a block-diagonal structure, where the block in the upper left corner of the transformed Hamilton matrix refers to the $N_{\text{max}} = 0$ subspace. For more information see fig. 6.4.

6.2. Remarks on Hamiltonians

For all calculations throughout this work, we are employing a chiral interaction as a starting point. In this chapter we employ, if not stated otherwise, an NN interaction by Entem and Machleidt [EM03] with a cutoff of $\Lambda_{\text{NN}} = 500$ MeV together with a local 3N interaction with a reduced cutoff of $\Lambda_{3\text{N}} = 400$ MeV [Rot+12; Nav07]. Employing a short-hand notation, this interaction is now indicated through $\text{N}^3\text{LO}_{\text{EM},500} + \text{N}^2\text{LO}_{400,\text{Local}}$ or, even shorter, $\text{N}^3\text{LO}_{\text{EM}} + \text{N}^2\text{LO}_{400,\text{L}}$. This interaction is then prediagonalized via the *free-space* SRG transformation at the three-body level with a flow parameter $\alpha = 0.08 \text{ fm}^4$ [Rot+11; JNF09; Rot+14; BFP07; Heb12].

The single-particle basis is truncated at $e_{\text{max}} = 12$, i.e., 13 major shells are included, which is sufficient for the mass range we are considering throughout this work.

For controlling the memory requirements of the initial three-body matrix elements, we are employing $E_{3\text{max}} = 14$, where $e_1 + e_2 + e_3 \leq E_{3\text{max}}$ and e_i refers to one of the three single-particle principal quantum numbers of the bra (ket) [Bin+14; Bin+13a; Her+13b; Her+13a; Rot+12]. Furthermore, the initial harmonic oscillator frequency is fixed to $\hbar\Omega = 24$ MeV.

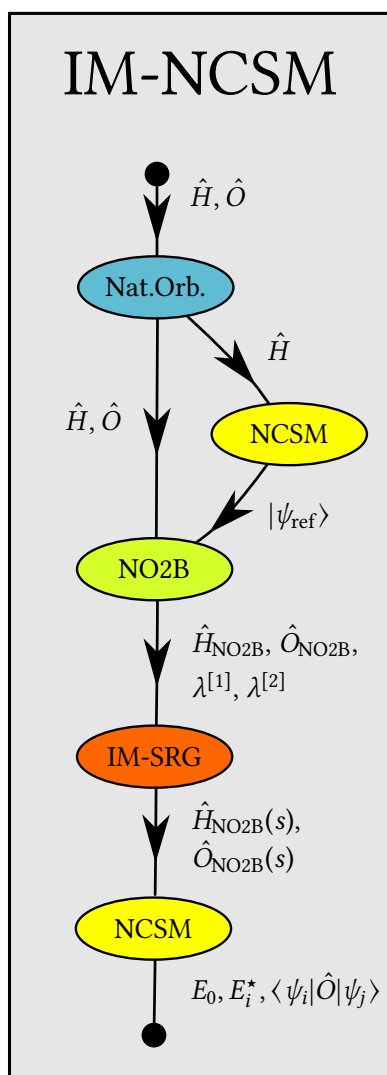


Figure 6.2.: This figure graphically illustrates the IM-NCSM framework. Starting with an initial Hamiltonian and observables, the associated operators are transformed into the single-particle natural orbital basis. The Hamiltonian is then entering the NCSM which gives the reference state $|\psi_{\text{ref}}\rangle$. Based on this reference state the NO2B approximation of \hat{H} and \hat{O} is performed such that all operators are truncated at the normal-ordered two-body level and, additionally, the one and two-body density matrices $\hat{\lambda}^{[1]}$ and $\hat{\lambda}^{[2]}$ are constructed. Next, the NO2B-approximated operators and irreducible density matrices are entering the IM-SRG framework which applies a particularly constructed unitary transformation to all operators. Those IM-SRG-transformed operators $\hat{H}_{\text{NO2B}}(s)$ and $\hat{O}_{\text{NO2B}}(s)$ are then used as input for a subsequent NCSM calculation.

6.3. Stages of the IM-NCSM

Let us now discuss the different stages of IM-NCSM calculations and, if necessary, address important details. Note that the following discussion is accompanied by the illustration given in fig. 6.2

Natural Orbitals. The initial stage of the IM-NCSM consists of a single-particle basis transformation that aims for optimizing the reference state. Especially the dependence on the harmonic oscillator frequency was a problem we were facing in earlier applications of the IM-NCSM and which is a well-known issue within the context of the IM-SRG [Her+16]. The frequency dependence is largely lifted by switching to the Hartree-Fock basis. For applications

of the *single-reference* IM-SRG, the Hartree-Fock basis is already sufficient for the construction of an optimized reference state. However, as we are employing the *multi-reference* IM-SRG the reference state is constructed from an initial NCSM calculation. Therefore, we are employing the natural orbital basis. Starting with an initial Hartree-Fock approximation, we obtain a Slater determinant $|\Phi\rangle$ as a first approximation for the ground state. Due to the fact that we are usually aiming for the description of open-shell systems the original formulation of the Hartree-Fock approximation has to be extended: We are employing the so-called equal-filling approximation (see, e.g., [PR08] for more information), which employs fractional occupation numbers such that all single-particle states within an open shell are equally (fractionally) filled. The Hartree-Fock ground state then serves as starting point for the construction of a second-order corrected one-body density matrix $\gamma^{[1]}$ derived from many-body perturbation theory. Finally, the natural orbitals are defined as the eigenbasis of $\gamma^{[1]}$.

NCSM and NO2B. Next, we perform an NCSM calculation in a small model space, typically $N_{\max}^{\text{ref}} = 0$ or 2, for the construction of a reference state $|\psi_{\text{ref}}\rangle$. Employing this reference state $|\psi_{\text{ref}}\rangle$, we perform an NO2B approximation of the initial three-body interaction. Furthermore, the one and two-body density matrices, $\gamma^{[1]}$ and $\gamma^{[2]}$, respectively, are constructed from $|\psi_{\text{ref}}\rangle$.

In-Medium SRG. The reference state $|\psi_{\text{ref}}\rangle$ is then entering the IM-SRG calculation through its associated one-body and two-body density matrices. These densities encode higher-order correlations of our reference state and are essential for a successful description of open-shell nuclei. Our implementation of the IM-SRG is designed such that a large portion of the N_{\max}^{ref} space, to which $|\psi_{\text{ref}}\rangle$ belongs, gets decoupled. If not stated otherwise, we are using the Magnus evolution of observables. Thus, we are, firstly, solving the ODE for the Magnus operator $\hat{\Omega}(s)$. Secondly, any observable $\hat{O}(s)$ is transformed via the Baker-Campbell-Hausdorff series employing $\hat{\Omega}(s)$. It is a vital aspect that the IM-SRG transformation implies a particular transformation of the single-particle basis. As a consequence, the single-particle basis associated with the IM-SRG-evolved Hamiltonian—denoted as the IM-SRG basis—is different from the initial natural-orbital basis.

Post-NCSM & Observables. Subsequently to the IM-SRG transformation, we use the IM-SRG-evolved Hamiltonian $\hat{H}(s)$ and observables $\hat{O}(s)$ as input of an NCSM calculation. In the limit $s \rightarrow \infty$ the N_{\max}^{ref} space is decoupled and a post-diagonalization at $N_{\max} \geq N_{\max}^{\text{ref}}$ yields converged results not only for the ground state but also for the lowest lying excited eigenstates that are structurally similar to the reference state. The IM-SRG acts as a convergence booster for the NCSM, making the treatment of nuclei possible that are out of reach for the large-scale IT-NCSM.

For removing eigenstates that are dominated by center-of-mass degrees of freedom from the low-lying parts of the spectrum, we add a (transformed) center-of-mass Hamiltonian $\hat{H}_{\text{cm}}(s)$ and eventually solve the eigenvalue problem for $\hat{H}_{\text{tot}} \equiv \hat{H}_{\text{int}} + \lambda_{\text{cm}} \hat{H}_{\text{cm}}$. However, an important issue within the context of the IM-NCSM or, more generally, the NCSM with other single-particle bases than the harmonic oscillator, is that eigenstates do not factorize into an intrinsic and a center-of-mass part anymore and may be center-of-mass contaminated or even spurious

eigenstates. As the IM-SRG-evolved operators are given in terms of the IM-SRG basis, we have to confront this issue. As the factorization is only approximate we have to be careful with the choice for λ_{cm} : It has to be large enough such that center-of-mass dominated eigenstates get sufficiently shifted upwards and small enough such that the effect on intrinsically dominated eigenstates is kept at a minimum. We have found in practical applications that $\lambda_{\text{cm}} = 0.2$ fulfills these two aforementioned requirements and is, therefore, most commonly used throughout our applications of the IM-NCSM.

6.4. The IM-NCSM: An Illustration

This section gives an introduction of most of the protocols that are employed for a concise presentation of numerical results. For this purpose, we performed calculations for ^{20}O employing an $N_{\text{max}}^{\text{ref}} = 0$ reference state. For each value of the IM-SRG flow parameter s contained in a set $\{s, s_1, s_2, \dots, s_N\}$ we calculated the intrinsic Hamiltonian and center-of-mass Hamiltonian $\hat{H}_{\text{int}}(s_i)$ and $\hat{H}_{\text{cm}}(s_i)$, respectively, which were then used as input for a subsequent NCSM calculation at several N_{max} .

Evolution Plots. Figure 6.3 represents an “evolution plot” and shows the IM-SRG flow of the ground-state energy, low-lying excited states, and the expectation value of the center-of-mass Hamiltonian \hat{H}_{cm} . Looking at the upper panel of fig. 6.3, we can study how the IM-SRG energy $E_0(s) = \langle \psi_{\text{ref}} | \hat{H}(s) | \psi_{\text{ref}} \rangle$ and the energy of the 0_1^+ state obtained from an NCSM calculation at $N_{\text{max}} = 0, 2$ are evolving w.r.t the flow parameter s . Two things become evident here: Firstly, the IM-SRG energy and the energy of the ground state at $N_{\text{max}} = 0$ have the same value throughout the evolution. Regarding the flow parameter $s = 0$, this observation should not come as a surprise as we were choosing the reference state $|\psi_{\text{ref}}\rangle$ as the ground state of the $N_{\text{max}} = 0$ space denoted by $|\psi_{\text{g.s.}}^{N_{\text{max}}=0}\rangle$, which is a 0^+ state. However, since the energy of $|\psi_{\text{g.s.}}^{N_{\text{max}}=0}\rangle$ and $E(s)$ are also equal for $s \geq 0$ it follows that the reference state $|\psi_{\text{ref}}\rangle$ remains the lowest eigenstate of the $N_{\text{max}} = 0$ space even for the evolved Hamiltonian. Secondly, the energy gap between the associated energies of $|\psi_{\text{g.s.}}^{N_{\text{max}}=0}\rangle$ and $|\psi_{\text{g.s.}}^{N_{\text{max}}>0}\rangle$ is vanishing throughout the flow and we eventually obtain converged results at $N_{\text{max}} = 0$, which demonstrates that $|\psi_{\text{g.s.}}^{N_{\text{max}}=0}\rangle$ gets decoupled from all basis states $|\phi_i^{N>0}\rangle$. Taking a look at the middle panel of fig. 6.3, the previous statement can even be generalized: Remarkably, it is not only the ground state that gets decoupled from higher lying basis states, but also the N_{max} convergence of excited states gets significantly enhanced such that they are practically converged at $N_{\text{max}} = N_{\text{max}}^{\text{ref}} = 0$ for final values of s . The reason for this behavior lies in the decoupling pattern of the IM-SRG: We are decoupling all 1p1h and 2p2h excitations of the reference, i.e., matrix elements that mediate these couplings of the reference state $|\psi_{\text{ref}}\rangle$ to higher lying basis $|\phi_i^{N=2,4,\dots}\rangle$ are suppressed. However, other eigenstates are also decoupled along with the reference state as long as they are structurally similar. This demonstrates one of the crucial advantages of the IM-NCSM framework, namely ground and excited-state properties may be accessed on equal footing.

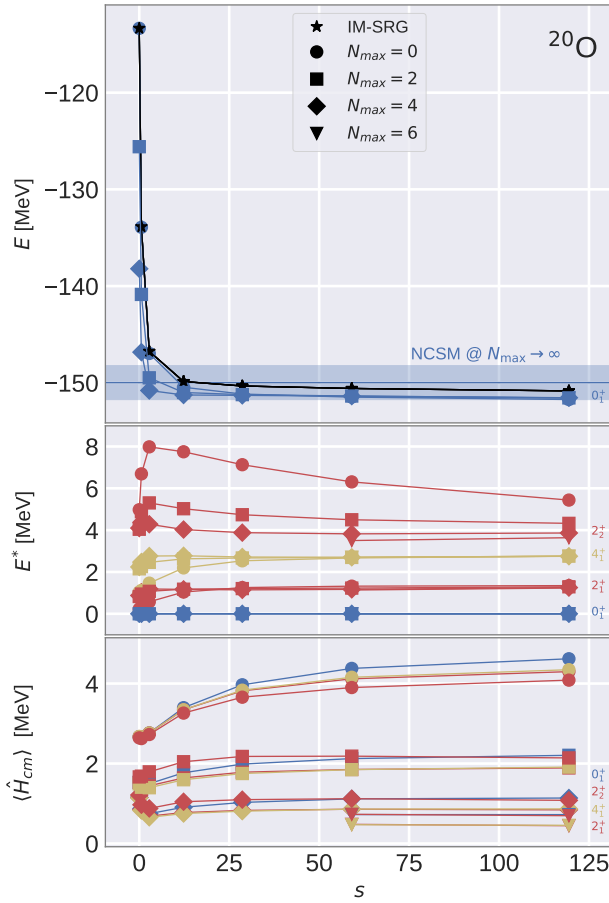


Figure 6.3.: Demonstration of the effects of the IM-SRG evolution on the N_{\max} convergence for the ground state energy (upper row), energies of excited states (middle row), and center-of-mass Hamiltonian expectation values (lower row) for ^{20}O . Note that each symbol refers to a specific N_{\max} and, additionally, we are employing a specific color for each state depending on the total angular momentum J . For assessing the impact of induced interactions beyond the NO2B level during the IM-SRG evolution, a horizontal line within a shaded band indicates the N_{\max} -extrapolated result and corresponding error, respectively, of a large-scale NCSM calculation employing an initial NO2B Hamiltonian. Calculations have been performed at $N_{\max}^{\text{ref}} = 0$.

As shown in Figure 6.3, we are tracking the expectation value of the center-of-mass Hamiltonian $\hat{H}_{\text{cm}}(s)$ of each eigenstate to distinguish intrinsically and center-of-mass dominated eigenstates. For all eigenstates considered here we observe that the expectation value decreases w.r.t. N_{\max} . This observation is in line with the assumption that the factorization into intrinsic and center-of-mass component is restored for $N_{\max} \rightarrow \infty$. However, whenever an eigenstate exhibits a center-of-mass expectation value of more than ~ 20 MeV—corresponding to approximately one harmonic oscillator excitation quantum—this state has an excited center-of-mass component and should be discarded. The fact that all eigenstates shown here exhibit a rather small center-of-mass expectation value indicates that they are intrinsically dominated eigenstates.

Matrix Representation. The decoupling of the whole N_{\max}^{ref} space is also demonstrated by fig. 6.4. It depicts a matrix representation of the Hamiltonian at $s = 0$ (left) and at $s \sim 120$ (right). Initially, the $N_{\max} = 0$ space exhibits a sizeable coupling to the $N_{\max} = 2$ space and, finally, this coupling is greatly reduced. Another noticeable observation is that, along with

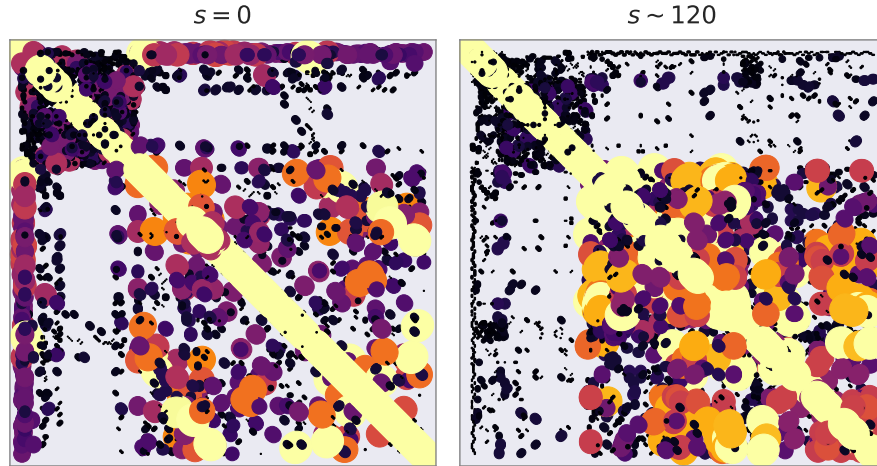


Figure 6.4.: Hamilton matrix representation for ^{20}O at $N_{\max}^{\text{ref}} = 0$ w.r.t. a many-body basis consisting of Slater determinants $|\phi_i^N\rangle$ employing the initial Hamiltonian at $s = 0$ (left) and the evolved Hamiltonian at $s \sim 120$ (right). The basis used for this representation is sorted such that the excitation quanta N associated with each basis state are ascending. In this case, we are using a basis consisting of Slater determinants with up to $N = 2$. Furthermore, we are only including those basis states $|\phi_i^{N=0,2}\rangle$ whose importance measure κ_i is above the importance threshold of $\kappa_{\min} = 3 \times 10^{-5}$. There is a linear relation between the absolute size of each matrix element and the area of each plot marker used for its representation. However, note that we were limiting the area for each matrix element to the area associated with a matrix element with a value of 1. Otherwise, the perception of our representation would be dominated by huge matrix element of the order 100 which are located on the diagonal of the matrix. For further facilitating the interpretation of this matrix representation, the color and the area of each marker are also correlated with each other. An interpretation of this figure can be found in the text.

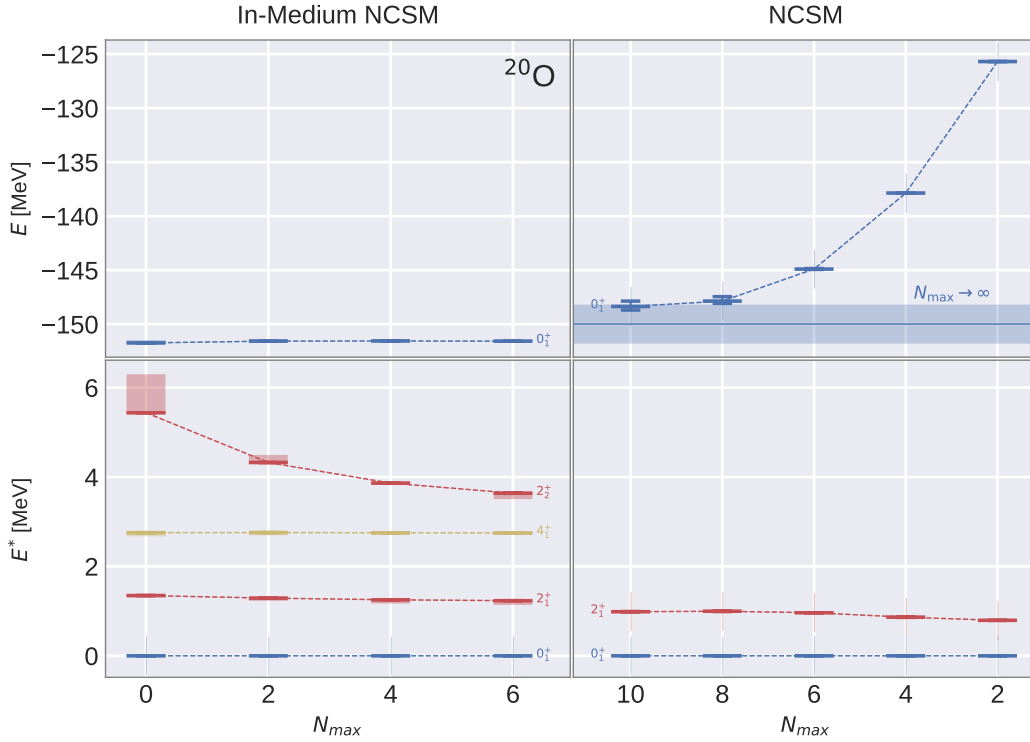


Figure 6.5.: Comparison of the N_{\max} convergence for the the IM-NCSM at $s \sim 120$ (left panel) and the regular NCSM (right panel) for ^{20}O . The figure depicts both ground state energies (upper panel) and the lowest-lying excited states (lower panel). Both methods are employing a NO2B Hamiltonian as input such that eventual discrepancies are purely related to induced interactions of the IM-SRG. The IM-NCSM calculations shown here have been performed at $N_{\max}^{\text{ref}} = 0$. We introduced several graphical representations of theoretical uncertainties (for details see text).

the suppression of the off-diagonal couplings, also the $N_{\max} = 0$ and $N_{\max} = 2$ blocks itself are changing.

NCSM Model-Space Convergence. Another point of view on the effects of the IM-SRG evolution is given through fig. 6.5, which is an “ N_{\max} -convergence plot”. It shows a comparison of the N_{\max} convergence of the IM-NCSM (left panels) and the regular NCSM (right panels), for the ground-state energy (upper panels) and excited-state energies (lower panels). Note that this figure introduces several graphical representations of theoretical uncertainties that will be employed in these kind of figures from now on.

- In the context of the IM-NCSM, we are using little shaded boxes directly attached to a plot marker for indicating the associated value at $s/2$ as can be seen, e.g., for the second

2^+ state at $N_{\max} = 0$.

- Shaded horizontal rectangles with a vertically centered solid line that both are covering the full horizontal width of plot are employed for indicating a specific value and its corresponding uncertainty, respectively. Most commonly, this kind of representation is employed for depicting the N_{\max} -extrapolated value and the associated uncertainty with regard to a specific observable.
- We are employing “usual” error bars, i.e., vertical lines with small horizontal caps for indicating uncertainties w.r.t. the κ_{\min} extrapolation. Such an error bar can be, e.g., clearly seen for the ground state at $N_{\max} = 10$ obtained from an NCSM calculation.

The improved convergence of IM-NCSM calculations is clearly demonstrated: At $N_{\max} = 0$ the IM-NCSM yields converged results that are compatible with NCSM calculations at $N_{\max} = 10$. Possible differences between converged results of the IM-NCSM and the NCSM are solely due to neglected operators beyond the NO2B rank that are induced throughout the IM-SRG evolution. Another interesting observation can be deduced from the lower panel, where the N_{\max} convergence of excited states is shown. In the NCSM the 2_1^+ state is slowly moving into a direction that is compatible with the N_{\max} -converged results given of the IM-NCSM. In the IM-NCSM also the 4_1^+ is practically converged at $N_{\max} = 0$, however, the 2_2^+ state shows a very slow N_{\max} convergence indicating that its structure is dominated by basis states beyond the reference space.

6.5. Generator Optimizations

In this section we want to address a generator modification that is specifically tailored to the IM-NCSM framework—and eventually resolves the issue of non-convergent IM-SRG evolutions. In this context, we will discuss the general decoupling pattern we used previously [Geb17] and alter this pattern. After discussing the construction of generator matrix elements, we will perform a numerical investigation.

6.5.1. Generalized Particle-Hole Excitations

A central aspect for this discussion are generalized kph excitations w.r.t. the reference state $|\psi_{\text{ref}}\rangle$ denoted as $\{\hat{a}_{q_1 \dots q_k}^{p_1 \dots p_k}\} |\psi_{\text{ref}}\rangle$. First, we discuss the question: What makes a generalized particle-hole excitation w.r.t. a correlated reference state special, i.e., what sets it apart from particle-hole excitations with regard to Slater determinants? For the single-reference case things are rather simple: Arbitrary particle-hole excitations on top of the reference state are orthogonal to each other, which is a direct consequence of the single-reference version of the generalized Wick’s theorem. Considering the multi-reference case, only the reference state

$|\psi_{\text{ref}}\rangle$ itself—by means of the very definition of multi-reference normal order—is orthogonal to any rank- k excitation

$$\langle \psi_{\text{ref}} | \{ \hat{a}_{q_1 \dots q_k}^{p_1 \dots p_k} \} | \psi_{\text{ref}} \rangle = 0. \quad (6.5.1)$$

In contrast to the single-reference case, two different particle-hole excitations may have an overlap with each other as can easily be seen by the overlap between the following two 1p1h excitations

$$\langle \psi_{\text{ref}} | \{ \hat{a}_2^1 \} \{ \hat{a}_4^3 \} | \psi_{\text{ref}} \rangle = -n_1 \bar{n}_2 \delta_4^1 \delta_3^2 + \lambda_{24}^{13}, \quad (6.5.2)$$

which is a direct consequence of the generalized Wick's theorem for correlated reference states. Note that under certain circumstances the basis consisting of all generalized particle-hole excitations of the reference state is overcomplete [Geb17], which, fortunately, is not a problem for the IM-SRG—in stark contrast to other many-body methods, where this poses a major challenge [Her17].

For our considerations, the two most important cases are generalized 1p1h and 2p2h excitations defined as

$$\{ \hat{a}_q^p \} | \psi_{\text{ref}} \rangle = \hat{a}_q^p | \psi_{\text{ref}} \rangle - \delta_q^p n_p | \psi_{\text{ref}} \rangle \quad (6.5.3)$$

$$\begin{aligned} \{ \hat{a}_{q_1 q_2}^{p_1 p_2} \} | \psi_{\text{ref}} \rangle &= \hat{a}_{q_1 q_2}^{p_1 p_2} | \psi_{\text{ref}} \rangle - \mathcal{A}(\lambda_{q_1}^{p_1} \{ \hat{a}_{q_2}^{p_2} \}) | \psi_{\text{ref}} \rangle \\ &\quad - \mathcal{A}(\lambda_{q_1}^{p_1} \lambda_{q_2}^{p_2}) | \psi_{\text{ref}} \rangle - \mathcal{A}(\lambda_{q_1 q_2}^{p_1 p_2}) | \psi_{\text{ref}} \rangle \\ &= \hat{a}_{q_1 q_2}^{p_1 p_2} | \psi_{\text{ref}} \rangle - \mathcal{A}(\lambda_{q_1}^{p_1} \hat{a}_{q_2}^{p_2}) | \psi_{\text{ref}} \rangle - \mathcal{A}(\lambda_{q_1 q_2}^{p_1 p_2}) | \psi_{\text{ref}} \rangle \end{aligned} \quad (6.5.4)$$

where we directly applied the inverse Wick's theorem for rewriting the normal-ordered operators acting on the reference state.

6.5.2. Decoupling pattern—Conventional

Conventionally, e.g., in the context of the MR-IM-SRG with HFB reference states [Her+13a], the transformation is aiming at decoupling the reference state $|\psi_{\text{ref}}\rangle$ from its generalized particle-hole excitations

$$\langle \psi_{\text{ref}} | \hat{H} \{ \hat{a}_q^p \} | \psi_{\text{ref}} \rangle \stackrel{!}{=} 0, \quad (6.5.5)$$

$$\langle \psi_{\text{ref}} | \hat{H} \{ \hat{a}_{r_s}^{p_q} \} | \psi_{\text{ref}} \rangle \stackrel{!}{=} 0, \quad (6.5.6)$$

⋮

$$\langle \psi_{\text{ref}} | \hat{H} \{ \hat{a}_{q_1 \dots q_A}^{p_1 \dots p_A} \} | \psi_{\text{ref}} \rangle \stackrel{!}{=} 0. \quad (6.5.7)$$

These decoupling conditions implicitly define the off-diagonal part of the Hamiltonian, referred to via $\hat{H}^{\text{od}}(s)$, which shall be suppressed in the limit $s \rightarrow \infty$. This traditional MR-IM-SRG decoupling pattern is rather strict, as it aims at a full decoupling of the reference state $|\psi_{\text{ref}}\rangle$, which then becomes a true eigenstate of the fully evolved Hamiltonian $\hat{H}(\infty)$.

Usually, we are aiming for a decoupling of the reference state from all 1p1h and 2p2h excitations, i.e., only the many-body states contained within the following set are taken into consideration

$$E_{1\text{p}1\text{h}} = \left\{ \{ \hat{a}_q^p \} | \psi_{\text{ref}} \rangle \right\}, \quad E_{2\text{p}2\text{h}} = \left\{ \{ \hat{a}_{rs}^{pq} \} | \psi_{\text{ref}} \rangle \right\}. \quad (6.5.8)$$

Therefore, let us now evaluate the decoupling conditions w.r.t. rank-1 and rank-2 excitations of the reference state via Wick's theorem. The results of this evaluation for a 1p1h excitation reads [Her17; Geb17]

$$\begin{aligned} 0 &\stackrel{!}{=} \mathcal{D}_1(1, 2) \equiv \langle \psi_{\text{ref}} | \hat{H} \{ \hat{a}_2^1 \} | \psi_{\text{ref}} \rangle \\ &= n_1 \bar{n}_2 f_2^1 + \sum_{pq} f_q^p \lambda_{q2}^{p1} \\ &\quad + \frac{1}{2} \sum_{pqr} (\bar{n}_1 \lambda_{2p}^{qr} \Gamma_{1p}^{qr} - n_2 \Gamma_{qr}^{2p} \lambda_{qr}^{1p}) + \mathcal{O}(\lambda^{[3]}), \end{aligned} \quad (6.5.9)$$

whereas the result for 2p2h excitations is given through

$$\begin{aligned} 0 &\stackrel{!}{=} \mathcal{D}_2(1, 2, 3, 4) \equiv \langle \psi_{\text{ref}} | \hat{H} \{ \hat{a}_{34}^{12} \} | \psi_{\text{ref}} \rangle \\ &= + \bar{n}_1 \bar{n}_2 n_3 n_4 \Gamma_{12}^{34} \\ &\quad + (1 - \hat{\tau}_4^3) n_4 \sum_p f_p^4 \lambda_{p3}^{12} - (1 - \hat{\tau}_2^1) \bar{n}_2 \sum_p f_2^p \lambda_{34}^{p1} \\ &\quad + \frac{1}{2} \bar{n}_1 \bar{n}_2 \sum_{pq} \Gamma_{12}^{pq} \lambda_{34}^{pq} + \frac{1}{2} n_3 n_4 \sum_{pq} \Gamma_{pq}^{34} \lambda_{pq}^{12} \\ &\quad - (1 - \hat{\tau}_2^1)(1 - \hat{\tau}_4^3) n_3 \bar{n}_1 \sum_{pq} \Gamma_{1q}^{p3} \lambda_{q4}^{p2} + \mathcal{O}(\dots). \end{aligned} \quad (6.5.10)$$

Note that, for convenience, we defined the functions \mathcal{D}_1 and \mathcal{D}_2 giving the Hamilton matrix element that couples the reference state and a particular particle-hole excitation. It is important to note that we neglected all contributions of n -body irreducible density matrices beyond two-body rank as well as higher-order, e.g., quadratic contributions of the two-body irreducible density matrix. Through the emergence of higher-order contributions of irreducible density matrix it becomes obvious that the reference state is coupled to excitations in a highly non-trivial way.

6.5.3. Decoupling pattern—IM-NCSM

Considering the IM-NCSM framework, we can relax the rather strict decoupling condition described in section 6.5.2. For that purpose, let us briefly summarize the model-space construction of the NCSM. The N_{\max} -truncated model space \mathcal{M} of the NCSM is spanned by all Slater determinants with up to N_{\max} excitation quanta and may, therefore, be written as

$$\mathcal{M}^{N_{\max}} = \text{span} \left(\{ |\phi_i^N\rangle \mid N \leq N_{\max} \} \right). \quad (6.5.11)$$

The model space in which the reference state lives may now be defined as $\mathcal{M}^{\text{ref}} \equiv \mathcal{M}^{N_{\max}^{\text{ref}}}$. Furthermore, it will prove useful to employ $\overline{\mathcal{M}}^{\text{ref}}$ for indicating the complement of \mathcal{M}^{ref} in $\mathcal{H}_A^{a.s.}$. Lastly, The reference state can be written as a superposition of Slater determinants

$$|\psi_{\text{ref}}\rangle = \sum_N \sum_i^{N_{\max}^{\text{ref}}} c_i^N |\phi_i^N\rangle, \quad (6.5.12)$$

where c_i^N is a real coefficient.

Relaxation of the Decoupling Pattern. It is not necessary that the reference state $|\psi_{\text{ref}}\rangle$ gets decoupled from *all* excitations, but it is already sufficient if $|\psi_{\text{ref}}\rangle$ gets decoupled from basis states lying within $\overline{\mathcal{M}}^{\text{ref}}$, since the final NCSM calculation in the IM-NCSM framework is always performed at $N_{\max} \geq N_{\max}^{\text{ref}}$. Therefore, we do not care whether the reference state is coupling to other basis states within \mathcal{M}^{ref} or not—the diagonalization within this model space is performed anyway. As a consequence, we may alter the decoupling pattern such that we allow a coupling of $|\psi_{\text{ref}}\rangle$ to basis states contained in \mathcal{M}^{ref} , which eventually implies that the reference state may not be an eigenstate of \mathcal{M}^{ref} anymore.

This relaxation of the decoupling pattern may be achieved by only decoupling those particle hole excitations in which the sum of the single-particle energy quantum numbers e of the created and annihilated states is not equal. Formally, these 1p1h and 2p2h excitations are then contained in either of the two sets

$$\mathbb{E}'_{1p1h} \equiv \left\{ \{ \hat{a}_q^p \} |\psi_{\text{ref}}\rangle \mid e(p) \neq e(q) \right\} \subset \mathbb{E}_{1p1h}, \quad (6.5.13)$$

$$\mathbb{E}'_{2p2h} \equiv \left\{ \{ \hat{a}_{q_1 q_2}^{p_1 p_2} \} |\psi_{\text{ref}}\rangle \mid e(p_1) + e(p_2) \neq e(q_1) + e(q_2) \right\} \subset \mathbb{E}_{2p2h}, \quad (6.5.14)$$

However, the excitations contained in

$$\overline{\mathbb{E}}'_{1p1h} \equiv \mathbb{E}_{1p1h} \setminus \mathbb{E}'_{1p1h} = \left\{ \{ \hat{a}_q^p \} |\psi_{\text{ref}}\rangle \mid e(p) = e(q) \right\}, \quad (6.5.15)$$

$$\overline{\mathbb{E}}'_{2p2h} \equiv \mathbb{E}_{2p2h} \setminus \mathbb{E}'_{2p2h} = \left\{ \{ \hat{a}_{q_1 q_2}^{p_1 p_2} \} |\psi_{\text{ref}}\rangle \mid e(p_1) + e(p_2) = e(q_1) + e(q_2) \right\}, \quad (6.5.16)$$

are excluded and not decoupled from the reference state.

For proving that it is sufficient to only decouple particle-hole excitations contained in E'_{1p1h} and E'_{2p2h} , let us examine the overlap of particle-hole excitations contained within the corresponding complements \bar{E}'_{1p1h} and \bar{E}'_{2p2h} with an arbitrary determinant $|\phi_j^{N'}\rangle$. If this overlap vanishes for $N' > N_{\max}^{\text{ref}}$, it is clear that such excitations are contained within the model space \mathcal{M}^{ref} and, therefore, do not have to be accounted for when setting up the decoupling pattern. It is important to note that we will employ the spherical natural orbital basis for our following considerations, i.e., $\lambda_{\frac{1}{2}}^1 = \delta_{\frac{1}{2}}^1 n_1$ holds.

Let us begin with the overlap of an 1p1h excitation $\{\hat{a}_q^p\}|\psi_{\text{ref}}\rangle \in E_{1p1h}$ with any Slater determinant $|\phi_j^{N'}\rangle$

$$\langle \phi_j^{N'} | \{\hat{a}_q^p\} | \psi_{\text{ref}} \rangle = \langle \phi_j^{N'} | \sum_N \sum_i^{N_{\max}^{\text{ref}}} c_i^N \{\hat{a}_q^p\} | \phi_i^N \rangle, \quad (6.5.17)$$

rewriting the normal-ordered product gives

$$= \langle \phi_j^{N'} | \sum_N \sum_i^{N_{\max}^{\text{ref}}} c_i^N (\hat{a}_q^p - \lambda_q^p) | \phi_i^N \rangle \quad (6.5.18)$$

$$= \sum_N \sum_i^{N_{\max}^{\text{ref}}} c_i^N \langle \phi_j^{N'} | \hat{a}_q^p | \phi_i^N \rangle - \sum_N \sum_i^{N_{\max}^{\text{ref}}} c_i^N \lambda_q^p \langle \phi_j^{N'} | \phi_i^N \rangle, \quad (6.5.19)$$

employing the orthonormality of Slater determinants yields

$$= \sum_N \sum_i^{N_{\max}^{\text{ref}}} c_i^N \langle \phi_j^{N'} | \hat{a}_q^p | \phi_i^N \rangle - c_j^{N'} \lambda_q^p. \quad (6.5.20)$$

Assuming now that $\{\hat{a}_q^p\}|\psi_{\text{ref}}\rangle \in \bar{E}'_{1p1h}$ and $N' > N_{\max}^{\text{ref}}$, we obtain

$$\langle \phi_j^{N'} | \{\hat{a}_q^p\} | \psi_{\text{ref}} \rangle = \sum_N \sum_i^{N_{\max}^{\text{ref}}} c_i^N \underbrace{\langle \phi_j^{N'} | \hat{a}_q^p | \phi_i^N \rangle}_{\sim \delta_{N'}^N} - c_j^{N'} \lambda_q^p \quad (6.5.21)$$

$$= \sum_i c_i^{N'} \langle \phi_j^{N'} | \hat{a}_q^p | \phi_i^{N'} \rangle - c_j^{N'} \lambda_q^p = 0 \quad (6.5.22)$$

where we used that $c_i^N = 0$ for all $N' > N_{\max}^{\text{ref}}$.

Analogously, the overlap of a general 2p2h excitation with an arbitrary basis state $|\phi_j^{N'}\rangle$ may

be rewritten as

$$\langle \phi_j^{N'} | \{ \hat{a}_{q_1 q_2}^{p_1 p_2} \} | \psi_{\text{ref}} \rangle = \langle \phi_j^{N'} | \sum_N \sum_i^{N_{\text{max}}} c_i^N \{ \hat{a}_{q_1 q_2}^{p_1 p_2} \} | \phi_i^N \rangle \quad (6.5.23)$$

$$= \langle \phi_j^{N'} | \sum_N \sum_i^{N_{\text{max}}} c_i^N \left(\hat{a}_{q_1 q_2}^{p_1 p_2} - \mathcal{A}(\lambda_{q_1}^{p_1} \hat{a}_{q_2}^{p_2}) - \mathcal{A}(\lambda_{q_1 q_2}^{p_1 p_2}) \right) | \phi_i^N \rangle \quad (6.5.24)$$

$$\begin{aligned} &= \sum_N \sum_i^{N_{\text{max}}} c_i^N \langle \phi_j^{N'} | \hat{a}_{q_1 q_2}^{p_1 p_2} | \phi_i^N \rangle - \sum_N \sum_i^{N_{\text{max}}} c_i^N \langle \phi_j^{N'} | \mathcal{A}(\lambda_{q_1}^{p_1} \hat{a}_{q_2}^{p_2}) | \phi_i^N \rangle \\ &\quad - \sum_N \sum_i^{N_{\text{max}}} c_i^N \mathcal{A}(\lambda_{q_1 q_2}^{p_1 p_2}) \langle \phi_j^{N'} | \phi_i^N \rangle = 0, \end{aligned} \quad (6.5.25)$$

where we assumed in the last step that $\{ \hat{a}_{r's}^{p'q} \} | \psi_{\text{ref}} \rangle \in \bar{\mathbb{E}}'_{2p2h}$ and $N' > N_{\text{max}}^{\text{ref}}$ holds.

Employing \mathcal{D}_1 and \mathcal{D}_2 given through eqs. (6.5.9) and (6.5.10) as a starting point, we now obtain the following slightly altered decoupling conditions

$$0 \stackrel{!}{=} \tilde{\mathcal{D}}_1(p_1, p_2) = \begin{cases} \mathcal{D}_1(p_1, p_2) & \text{if } e(p_1) \neq e(p_2) \\ 0 & \text{else} \end{cases}, \quad (6.5.26)$$

$$0 \stackrel{!}{=} \tilde{\mathcal{D}}_1(p_1, p_2, p_3, p_4) = \begin{cases} \mathcal{D}_1(p_1, p_2, p_3, p_4) & \text{if } e(p_1) + e(p_2) \neq e(p_3) + e(p_4) \\ 0 & \text{else} \end{cases}, \quad (6.5.27)$$

where we defined $\tilde{\mathcal{D}}_1(p_1, p_2)$ and $\tilde{\mathcal{D}}_2(p_1, p_2, p_3, p_4)$ for convenience and later reference.

6.5.4. Construction of Generator Matrix Elements

As discussed in section 4.7 the White and imaginary-time generator matrix elements can be constructed via

$$\eta_{q_1}^{p_1} = \left(1 - \hat{\tau}_{q_1}^{p_1} \right) \langle \psi_{\text{ref}} | \hat{H} \{ \hat{a}_{q_1}^{p_1} \} | \psi_{\text{ref}} \rangle \mathcal{F}(\Delta_{p_1 q_1}), \quad (6.5.28)$$

$$\eta_{q_1 q_2}^{p_1 p_2} = \left(1 - \hat{\tau}_{q_1}^{p_1} \hat{\tau}_{q_2}^{p_2} \right) \langle \psi_{\text{ref}} | \hat{H} \{ \hat{a}_{q_1 q_2}^{p_1 p_2} \} | \psi_{\text{ref}} \rangle \mathcal{F}(\Delta_{p_1 p_2 q_1 q_2}). \quad (6.5.29)$$

One ingredient for the construction of these matrix elements are Hamiltonian matrix elements between the reference state and 1p1h or 2p2h excitations. We may either employ \mathcal{D}_1 and \mathcal{D}_2 given through eqs. (6.5.9) and (6.5.10) or, alternatively, we use the modified decoupling pattern and employ $\tilde{\mathcal{D}}_1$ and $\tilde{\mathcal{D}}_2$ given by eqs. (6.5.26) and (6.5.27). Another ingredient are differences

between expectation values w.r.t. the reference state and excitations

$$\Delta_{12} \equiv \langle \psi_{\text{ref}} | \{ \hat{a}_2^1 \}^\dagger \hat{H} \{ \hat{a}_2^1 \} | \psi_{\text{ref}} \rangle - \langle \psi_{\text{ref}} | \hat{H} | \psi_{\text{ref}} \rangle \quad (6.5.30)$$

$$= -\bar{n}_1^2 \bar{n}_2^2 \Gamma_{12}^{12} + \bar{n}_1^2 n_2 f_1^1 - \bar{n}_1 n_2^2 f_2^2 + (\bar{n}_1 n_2 - 1) E_0 + \mathcal{O}(\lambda^{[2]}) \quad (6.5.31)$$

$$\Delta_{1234} \equiv \langle \psi_{\text{ref}} | \{ \hat{a}_{34}^{12} \}^\dagger \hat{H} \{ \hat{a}_{34}^{12} \} | \psi_{\text{ref}} \rangle - \langle \psi_{\text{ref}} | \hat{H} | \psi_{\text{ref}} \rangle, \quad (6.5.32)$$

$$= \left(1 + \hat{\tau}_2^1 \hat{\tau}_4^3 \right) \left(\bar{n}_1 \bar{n}_2 n_3 n_4 \left(\frac{1}{2} \bar{n}_1 \bar{n}_2 \Gamma_{12}^{12} + \frac{1}{2} n_3 n_4 \Gamma_{34}^{34} - \bar{n}_1 n_4 \Gamma_{14}^{14} - \bar{n}_1 n_3 \Gamma_{13}^{13} \right) \right. \quad (6.5.33)$$

$$\left. + \bar{n}_1 \bar{n}_2 n_3 n_4 (\bar{n}_1 f_1^1 - n_3 f_3^3) + \frac{1}{2} (\bar{n}_1 \bar{n}_2 n_3 n_4 - 1) E_0 + \mathcal{O}(\lambda^{[2]}) \right). \quad (6.5.34)$$

At this point we have several choices for the construction of specific generator matrix elements. Firstly, we can choose the generator type through the function \mathcal{F} . Secondly, we can choose the decoupling pattern, i.e., we can either aim to decouple *all* 1p1h and 2p2h excitations from the reference state and employ \mathcal{D}_1 and \mathcal{D}_2 , or we can choose a simplified decoupling pattern and use $\tilde{\mathcal{D}}_1$ and $\tilde{\mathcal{D}}_2$. Finally, we may truncate the resulting expressions for a generator matrix element at a specific order in the irreducible density matrices.

We set up the following naming scheme to identify different combinations of generator types, decoupling patterns, and truncation schemes:

1. “White” employs the White generator type and aims for a decoupling of *all* 1p1h and 2p2h excitations. All terms involving $\lambda^{[2,3,\dots]}$ are neglected.
2. “White-NCSM” is equal to “White” but excitations that purely lie within the $N_{\text{max}}^{\text{ref}}$ -space are left out.
3. “Imaginary-time” employs the Imaginary-time generator type and aims for a decoupling of *all* 1p1h and 2p2h excitations. All terms involving $\lambda^{[2,3,\dots]}$ are neglected.
4. “Imaginary-time-NCSM” is equal to “Imaginary-time” but excitations that purely lie within the $N_{\text{max}}^{\text{ref}}$ -space are left out.

6.5.5. Numerical Applications

In fig. 6.6a we see the IM-SRG evolution of the energies of the ground and low-lying excited states employing the traditional White and imaginary-time generator. Obviously, the energies seem to converge w.r.t. the flow parameter s and we do not observe any instabilities. Furthermore, both generators are giving compatible results, even though on different scales of the flow parameter s .

However, while a large portion of the nuclear systems we were treating so far is behaving very similar to ^{20}O , there are few systems that show a different behavior. A prime example for such a differently behaving system is ^{12}C whose associated IM-SRG flow of the ground

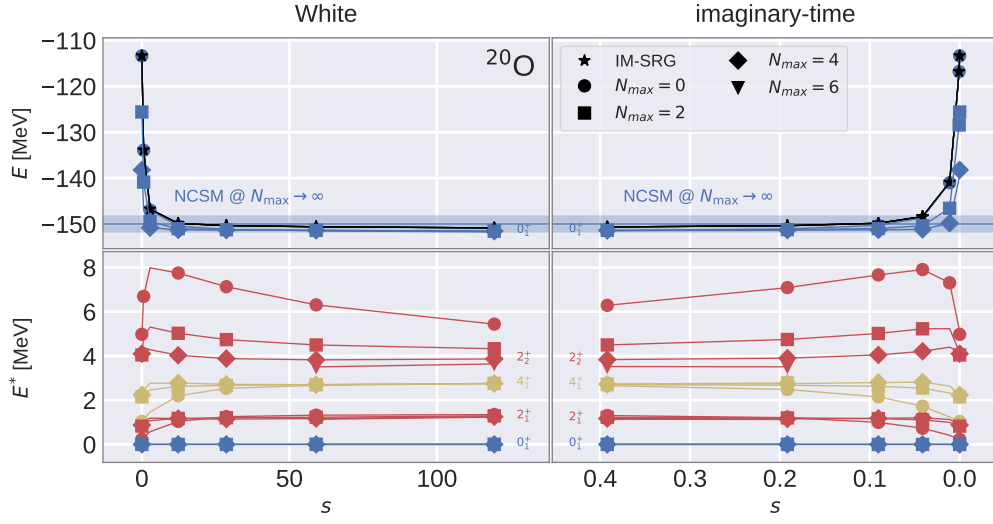
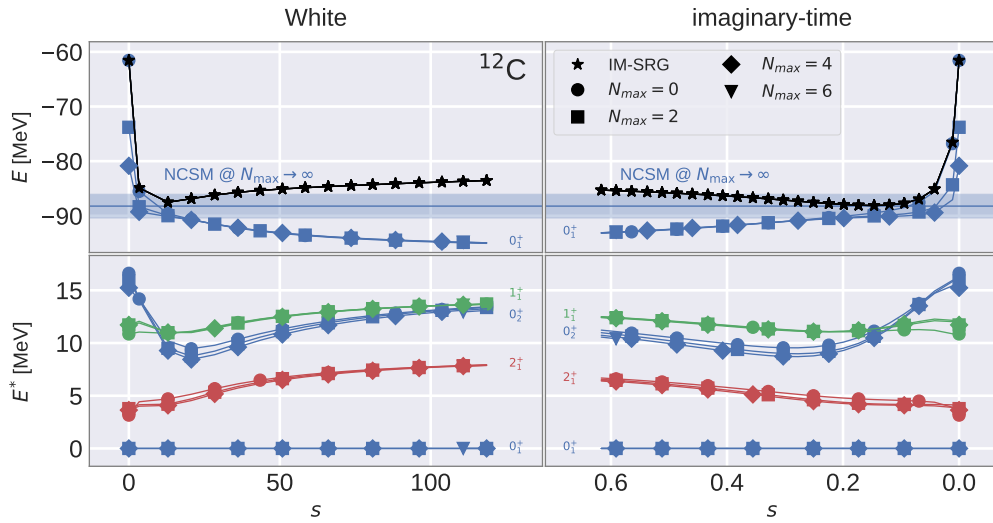
(a) Generator comparison for ^{20}O (b) Generator comparison for ^{12}C

Figure 6.6.: Evolution for ^{20}O and ^{12}C employing either the generator White (left panels) or the imaginary-time (right panels). Different symbols indicate different N_{max} values for the IM-NCSM and horizontal lines and shaded bands indicate N_{max} -extrapolated results and uncertainties, respectively, obtained from the NCSM. In order to reduce cluttering, only for a subset of the available data points plot markers are shown.

state is shown in fig. 6.6b. Here, for both generators White and imaginary-time the ground-state energy drops below the energy obtained from an IT-NCSM calculation and does not seem to stabilize. Another problem is raised by the energy of the first excited state, i.e., the 2_1^+ state: Compared with the NCSM result, which lies at about 4 MeV, the IM-NCSM lies much too high. Furthermore, the IM-SRG energy $E(s)$ and the energy of $|\psi_{g.s.}^{N_{\max}=0}\rangle$ are drifting apart throughout the evolution. This behavior is a clear indication that the reference state $|\psi_{\text{ref}}\rangle$ is not an eigenstate of the $N_{\max} = 0$ space anymore, i.e., $|\psi_{\text{ref}}\rangle$ begins to couple to other basis states $|\phi_i^{N=0}\rangle$. All in all, these observations leads us to the conclusion that the IM-SRG evolution for ^{12}C is suffering from a significant amount of induced interactions beyond the NO2B level. In previous publications [Geb+16] we have tackled this problem by employing a rather complicated protocol: We identified a flow parameter range at intermediate values for s in which the N_{\max} convergence of the ground-state energy is already sufficiently enhanced, but the induced interactions were supposedly still under control. For the imaginary-time generator such a “plateau” is observed approximately between $s = 0.1$ and $s = 0.2$. Once we move beyond this plateau, the energy begins to drop again. For the White generator, however, there is no plateau at all.

A solution to this problem are the modified generators White-NCSM and imaginary-time-NCSM, whose numerical applications for ^{12}C are shown in fig. 6.7b. We observe that the flow stabilizes and the converged ground-state energy is now much closer to the NCSM result. Additionally, the IM-NCSM energy we obtain through these modified generators is much more consistent with the result obtained from an MR-IM-SRG calculation with a Hartree-Fock-Bogoliubov reference state as can be seen in [Geb+16]. A similar picture emerges for excited states: the flow stabilizes very early and the energies obtained from our IM-NCSM calculation is now compatible with the NCSM results. Furthermore, we do not see the first 0^+ excitation at lower energies around 7.7 MeV but at much higher energies (which we do not show here) showing that the IM-NCSM framework does not adequately describe the Hoyle state—as to be expected.

Thus, by relaxing the decoupling condition, i.e, allowing the reference state $|\psi_{\text{ref}}\rangle$ to couple with other basis states of its own reference space, we stabilize the IM-SRG evolution and resolve the issue of substantial amounts of induced interactions beyond the NO2B level.¹ Figure 6.7a shows that the evolution for ^{20}O and both generators White-NCSM and imaginary-time-NCSM is approximately the same as for White and imaginary-time depicted in fig. 6.6a. This demonstrates that our modified generators do not introduce any complications.

Comparing White-NCSM and imaginary-time-NCSM with each other, both generators yield similar results once the evolution is converged. However, White-NCSM is numerically much more efficient and needs fewer integration steps for obtaining converged results, which reduces the computational effort of the IM-SRG calculation. Therefore, we will use the White-NCSM generator by default except noted otherwise. In the rare event of a numerically unstable IM-SRG evolution, however, we employ the more stable imaginary-time generator.

¹This solution is by far much more simple than the eventual alternative, where higher irreducible density matrices for the generator construction are included.

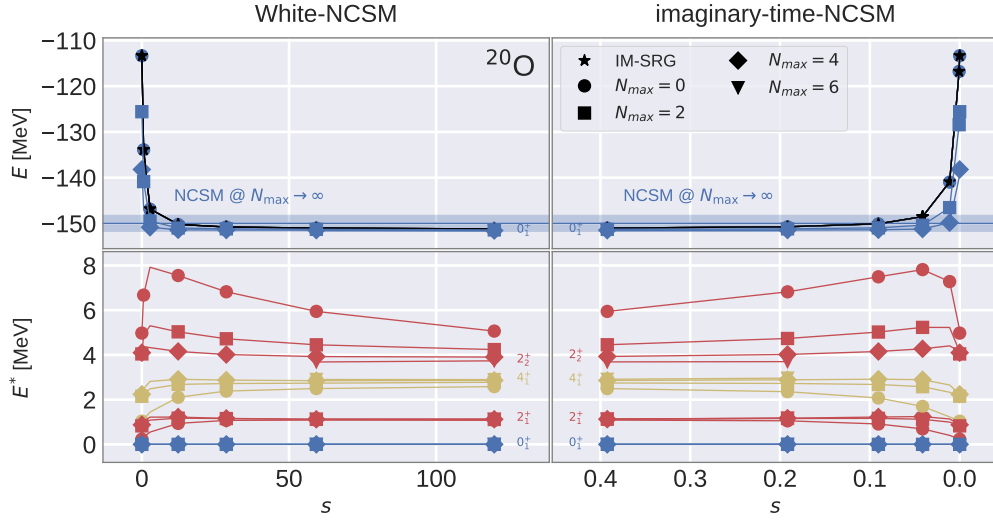
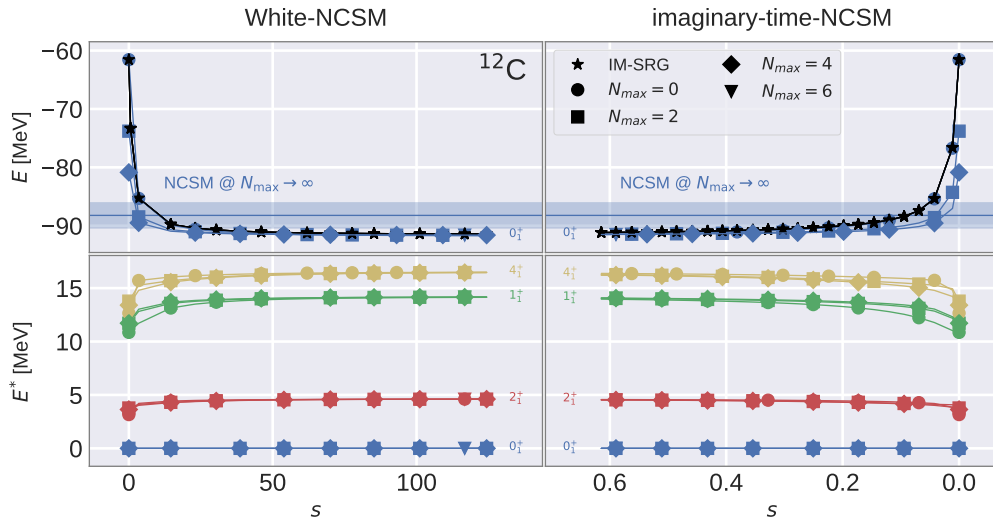
(a) Generator comparison for ^{20}O (b) Generator comparison for ^{12}C

Figure 6.7.: IM-SRG evolution for ^{20}O and ^{12}C employing the updated generators White-NCSM (left panels) and imaginary-time-NCSM (right panels). Different symbols indicate different N_{max} values for the IM-NCSM and horizontal lines and shaded bands again indicate N_{max} -extrapolated results and uncertainties, respectively, obtained from the NCSM.

6.6. Oxygen Chain and Impact of Reference Space

Let us now turn to the investigation of the impact of the size of the reference space, which is governed by the choice for N_{\max}^{ref} . Since it is not only the reference state that gets decoupled, but also a large portion of the reference space, the parameter N_{\max}^{ref} specifies the size of the “box” in which we are forcing the part of the Hamiltonian governing the lowest eigenstates into. In any case, the reference-space size should be large enough such that fundamental properties and symmetries of a specific eigenstate are captured by the reference state $|\psi_{\text{ref}}\rangle$.

The structure of the reference state has an impact at two different stages: Firstly, the initial NO2B approximation of the three-body interaction and the normal ordering. Secondly, it enters the IM-SRG through its associated one and two-body irreducible density matrices. As the IM-SRG also employs a NO2B throughout the evolution, it will eventually suffer from induced many-body interactions beyond the two-body rank. Through a variation of the model-space size, i.e., N_{\max}^{ref} , we are able to control which correlations are already captured at the level of the reference state and which are left for the IM-SRG to deal with.

In the limit $N_{\max}^{\text{ref}} \rightarrow \infty$ the difference between the exact result and a result obtained from the IM-NCSM is only governed by the quality of the (initial) NO2B approximation. Assuming that the NO2B approximation itself improves with increasing N_{\max}^{ref} this shows that we expect the IM-NCSM framework to yield more precise results with increasing N_{\max}^{ref} .

Oxygen Isotopic Chain. The question that arises at this point is whether and to which extent the reference space size N_{\max}^{ref} is affecting our numerical results. We performed calculations for nuclei within the oxygen chain at several N_{\max}^{ref} and compared the results to NCSM calculations and experimental values as shown by fig. 6.8 and fig. 6.9, where the former shows ground-state energies and the latter energies of the lowest-lying excited states. The influence of N_{\max}^{ref} on ground-state energies depicted by fig. 6.8 is manifesting itself in two different ways. Firstly, it leads to different N_{\max} -convergence behaviors, while still converging to approximately the same value for large N_{\max} values. Such a behavior can, e.g., be seen for the 2_2^+ state in ^{18}O . Secondly, calculations at different N_{\max}^{ref} lead to different results for sufficiently large values for N_{\max} —a signal for different amounts of induced interactions beyond the NO2B rank. Take, for example, the ground-state energy of ^{20}O shown in fig. 6.8: the result at $N_{\max} = 6$ deviates between $N_{\max}^{\text{ref}} = 0$ and $N_{\max}^{\text{ref}} = 4$ by about 1.5 MeV or 1%. However, a comparison of the different N_{\max}^{ref} shows that the largest deviation appears between $N_{\max}^{\text{ref}} = 0$ and $N_{\max}^{\text{ref}} = 2$ whereas the difference between $N_{\max}^{\text{ref}} = 2$ and $N_{\max}^{\text{ref}} = 4$ is negligible, which indicates that it is sufficient to employ $N_{\max}^{\text{ref}} = 2$ for oxygen chain isotopes.

Another representation of the data contained in the previous figures is given through fig. 6.10a which exclusively addresses the effects of an increase of N_{\max}^{ref} from 0 to 2 by showing relative changes of the corresponding results. It becomes evident that for all oxygen isotopes considered here the relative difference of calculation with $N_{\max}^{\text{ref}} = 0$ and $N_{\max}^{\text{ref}} = 2$, respectively, are below 1%, where ^{20}O is showing the most pronounced differences of about 0.7%.

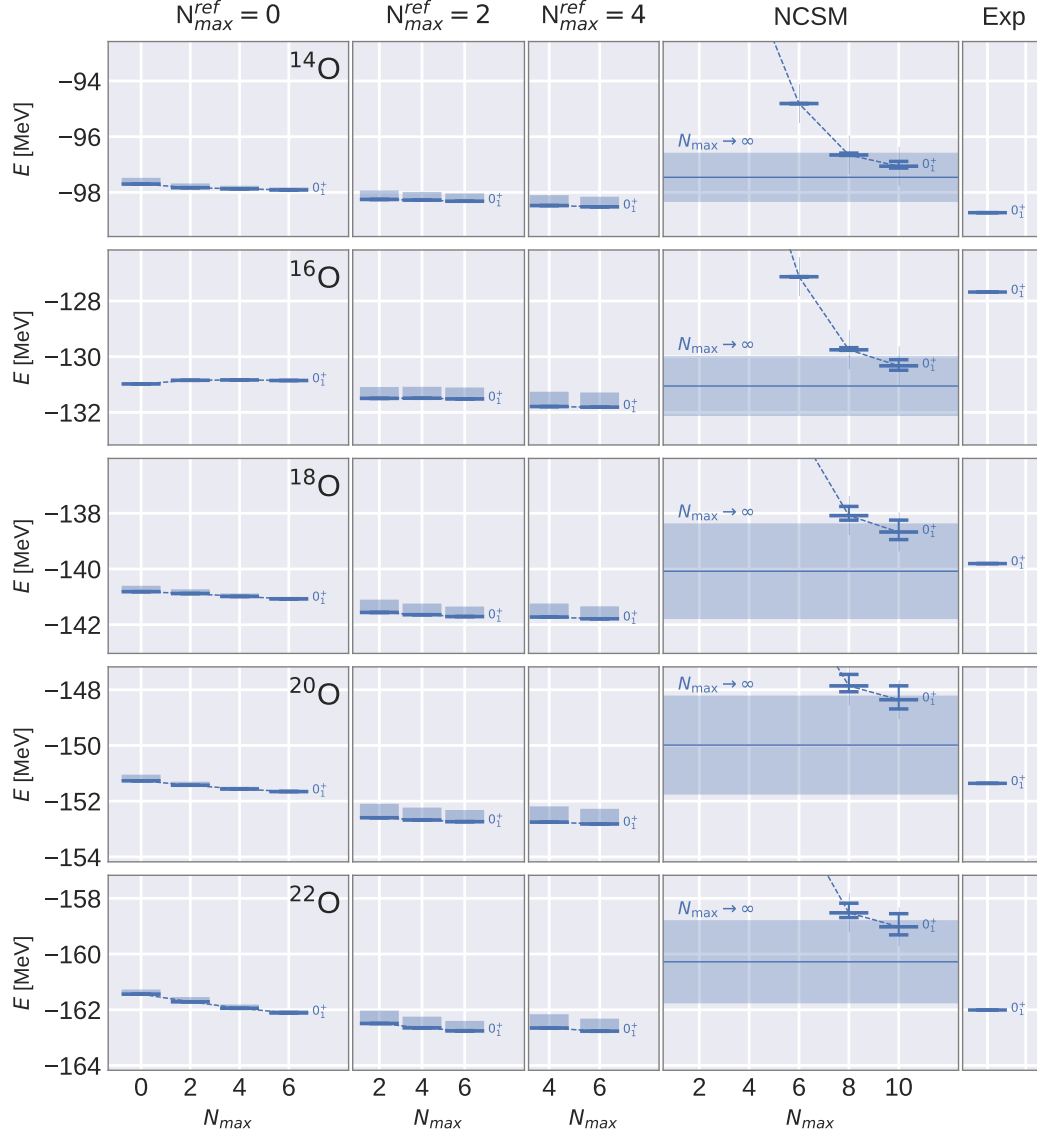


Figure 6.8.: Depiction of ground-state energies. Each column refers to IM-NCSM calculations at $N_{max}^{ref}=0, 2,$ and 4 (column 1-3), NCSM calculations employing an initial NO2B Hamiltonian (fourth column) and associated experimental values (fifth column) and each row refers to one of the even oxygen isotopes between ^{14}O and ^{22}O . Additionally, N_{max} -extrapolated NCSM results are shown as shaded bands (within the column depicting NCSM results). For details on experimental data see appendix C.

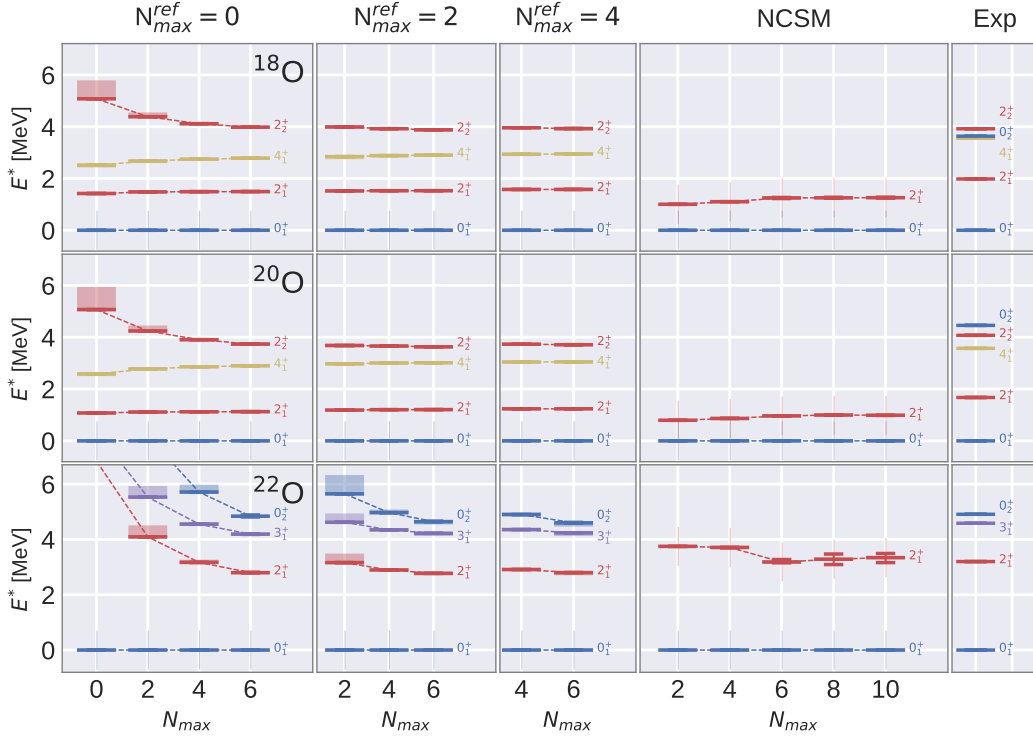
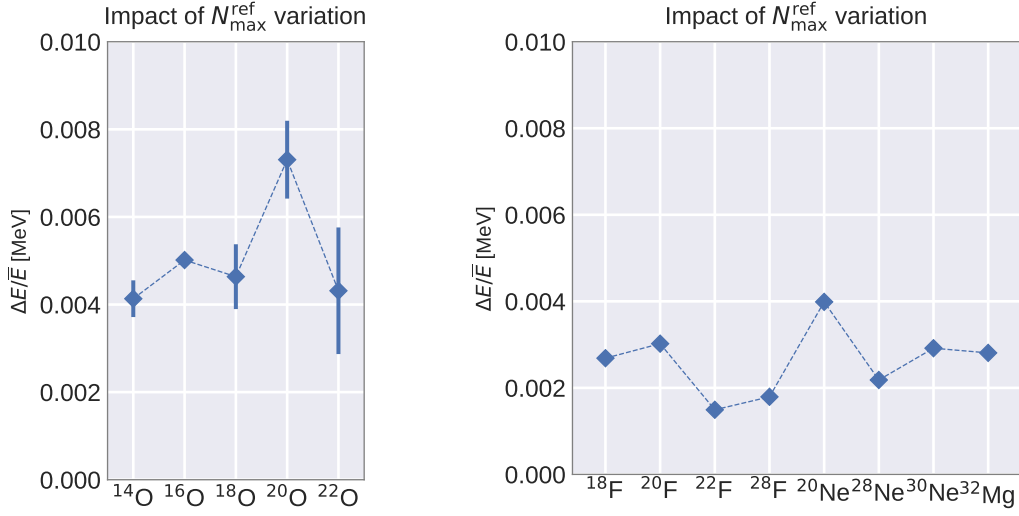


Figure 6.9.: Similarly to fig. 6.8, this figure shows excitation energies of the lowest lying states.

Dominant Source of Impact. Looking at fig. 6.11, we are able to inspect the source of the N_{\max}^{ref} dependence, which is either the initial NO2B approximation or the IM-SRG evolution. For that purpose, we were deviating from the standard procedure and allowed the N_{\max}^{ref} employed within the NO2B approximation and the IM-SRG evolution denoted via $N_{\max}^{\text{ref,no}}$ and $N_{\max}^{\text{ref,ims}}$, respectively, to be different. It becomes obvious that: An increase of $N_{\max}^{\text{ref,no}}$ has a slight repulsive effect, an increase of $N_{\max}^{\text{ref,ims}}$ has an attractive effect, and, comparing the absolute size of both effects with each other, the impact of the $N_{\max}^{\text{ref,ims}}$ parameter seems to be the more dominant one. Note that the behavior for increasing $N_{\max}^{\text{ref,no}}$ may be intuitively expected: We know that the NO2B approximation has the tendency to lead to a slight overbinding of about 1% in medium-mass systems [Rot+12; GCR16] and, assuming that the quality of this approximation improves with N_{\max}^{ref} , we expect less binding for higher N_{\max}^{ref} .

Beyond the Oxygen Chain. Up to now, we were only considering oxygen isotopes. For completing the picture, let us consider ^{22}Ne . Depicted in fig. 6.12a is the evolution of the ground and low-lying excited states energies and fig. 6.12b illustrates the N_{\max} convergence w.r.t. different N_{\max}^{ref} and a comparison with experimental values. Through this exemplary study of the fully open-shell nucleus ^{22}Ne , it becomes evident that the IM-NCSM framework works equally well and has a similar characteristics for isotopes beyond the oxygen chain: The



- (a) Using E^x for denoting the ground-state energy that is obtained from an IM-NCSM calculation at $N_{\max}^{\text{ref}} = x$, this figure shows the *relative* difference of E^0 and E^2 through $\frac{\Delta E}{\bar{E}} \equiv \frac{|E^2 - E^0|}{2(E^2 + E^0)}$ for selected oxygen isotopes with even mass numbers. Note that calculations were performed at $N_{\max} = 2$ and 4 and error bars indicate the difference between these two values for N_{\max} .
- (b) Similarly to fig. 6.10a, this figure depicts the relative impact of different values for N_{\max}^{ref} on results obtained from the IM-NCSM for selected fluorine, neon, and magnesium isotopes. Note that the results shown in this figure are based on the chiral interaction $N^4\text{LO}_{\text{EMN}} + N^2\text{LO}_{500,\text{NL}}$ (see chapter 7 for more information). Note that, in contrast to fig. 6.10a, no error bars indicating uncertainties in regard to different N_{\max} are shown here.

Figure 6.10.: Depiction of relative N_{\max}^{ref} impact on IM-NCSM ground-state energies.

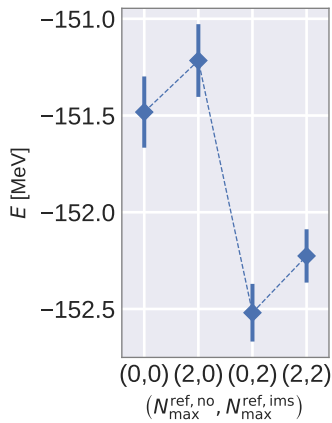
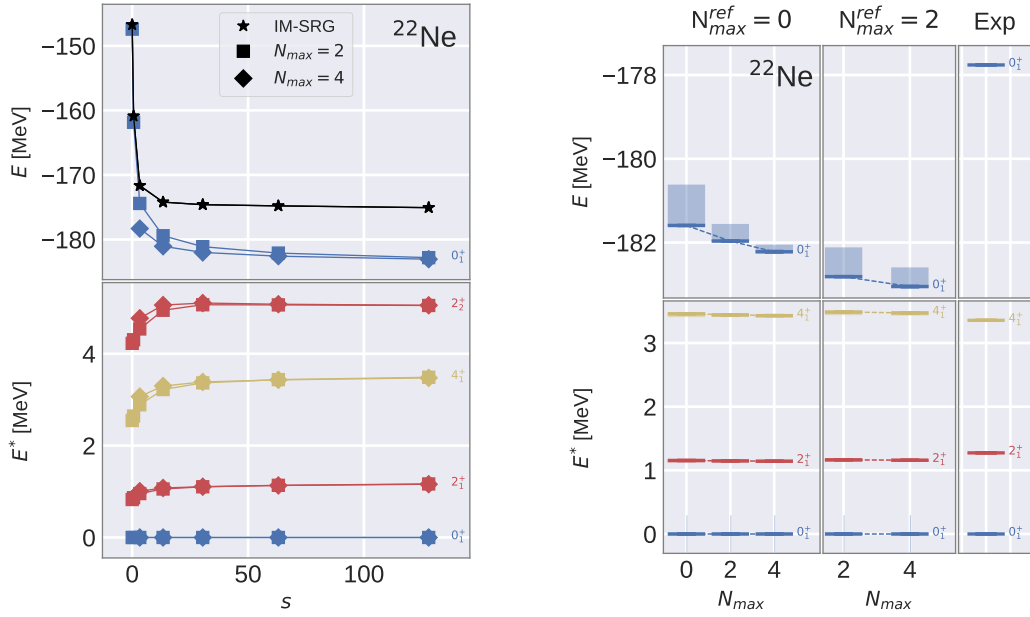


Figure 6.11.: Depiction of ground-state energies obtained from the IM-NCSM employing $N_{\max}^{\text{ref,no}} = 0$ and $N_{\max}^{\text{ref,no}} = 2$ for the NO2B approximation and $N_{\max}^{\text{ref,ims}} = 2$ and $N_{\max}^{\text{ref,ims}} = 2$ for the IM-SRG evolution. Note that, in contrast to the usual procedure, we allowed the two specific N_{\max}^{ref} employed within these two stages of the IM-NCSM to be different such that we may study the individual N_{\max}^{ref} impact on our numerical results. Additionally, error bars indicate the difference between the results obtained from $N_{\max} = 0$ and 2.



(a) Evolution of the ground-state and the lowest-lying excited states for ^{22}Ne at $N_{\max}^{\text{ref}} = 2$. (b) N_{\max} convergence of IM-NCSM calculations at $N_{\max}^{\text{ref}} = 0$ and 2 and experimental values for ^{22}Ne . For details on experimental data see appendix C.

Figure 6.12.: Evolution and N_{\max} convergence for ^{22}Ne .

N_{\max} convergence is significantly enhanced such that we practically obtain converged results for $N_{\max} \approx N_{\max}^{\text{ref}}$. Regarding the N_{\max}^{ref} dependence, it seems that there is a less pronounced dependency. This is confirmed by fig. 6.10b, which shows the relative difference of results at $N_{\max}^{\text{ref}} = 0$ and 2 for selected fluorine, neon, and magnesium isotopes. All values lie in the region of 0.2% to 0.4%, where ^{20}Ne shows the largest deviation with 0.4%. Note that the calculations shown in fig. 6.10b employed the $N^4\text{LO}_{\text{EMN}} + N^2\text{LO}_{500,\text{NL}}$ interaction. However, we do not expect the interaction to have a significant impact on the behavior of the IM-NCSM under N_{\max}^{ref} variation and, therefore, conclusions drawn with regard to the N_{\max}^{ref} behavior should be largely interaction independent.

Employing this interaction, fig. 6.13 shows calculations for ^{32}Mg and ^{34}Mg . While for both isotopes the ground-state energy differs noticeably from experiment—due to deficiencies of the chiral interaction employed in this case—the excited states show only a slight dependence on N_{\max}^{ref} and N_{\max} and are in agreement with experimental values.

IM-NCSM, NCSM, Experiment. Let us now look a bit closer at differences between results obtained from the IM-NCSM and the NCSM. As shown in fig. 6.8, it becomes evident that IM-NCSM results—which are already converged at small values for N_{\max} —are compatible with

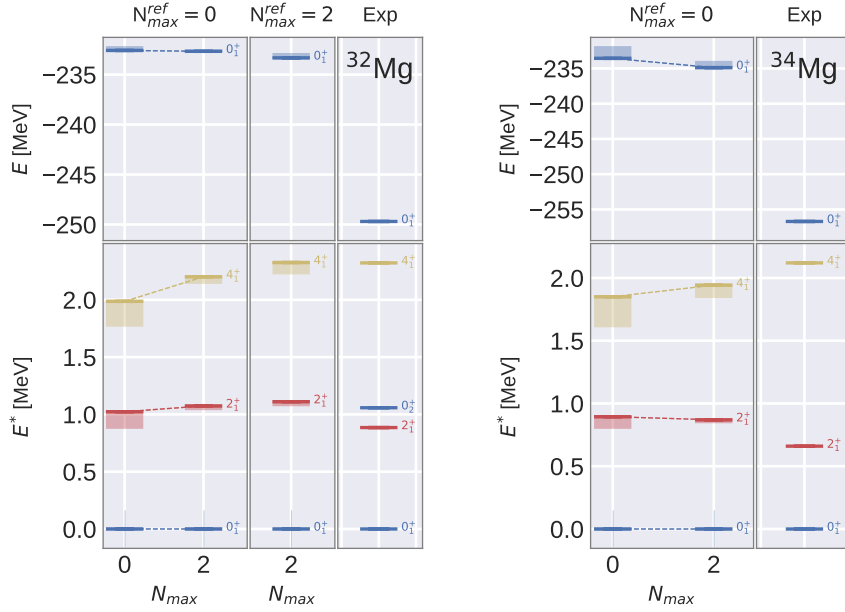


Figure 6.13.: Ground and lowest-lying excited states of ^{32}Mg (left) and ^{34}Mg (right) from the IM-NCSM. Calculations are based on the chiral interaction $\text{N}^4\text{LO}_{\text{EMN}}+\text{N}^2\text{LO}_{500,\text{NL}}$ (see chapter 7 for more information). For details on experimental data see appendix C.

N_{max} -extrapolated NCSM results. The fact that huge N_{max} are necessary for getting close to the region of convergence again demonstrates the benefit of the IM-NCSM.

Considering differences with experimental ground-state energies, we observe an overall good agreement, where the largest deviation can be found for ^{16}O by about 4 MeV. Furthermore, fig. 6.9 illustrates that also the low-lying excited states obtained from the IM-NCSM and NCSM are in good agreement with each other. A comparison with experimental values remarkably shows that the IM-NCSM yields a good prediction of the lowest-lying states, which can also be observed in fig. 6.12b.

Recommendation. Considering the choice for $N_{\text{max}}^{\text{ref}}$ for nuclei within the oxygen chain, we come to the conclusion that it is sufficient to use $N_{\text{max}}^{\text{ref}} = 2$. It is worth noting that oxygen chain isotopes might be a special case: Employing a $N_{\text{max}}^{\text{ref}} = 0$ reference space, the proton shell is closed and there are no correlations contained by the associated reference state.

This assumption is further supported by investigations of fully open-shell nuclei which exhibit a much smaller dependency on $N_{\text{max}}^{\text{ref}}$ and for which we, therefore, consider $N_{\text{max}}^{\text{ref}} = 0$ as sufficient.

6.7. Particle-Attached/Particle-Removed

In this section we are going to address the basic concepts of one of the major advancements of the IM-NCSM framework that allows for a treatment of odd nuclei: the particle-attached/particle-removed (PA/PR) extension.

6.7.1. Outline of Approach

A problem that emerges for odd mass numbers like, e.g., ^{21}O is that the eigenstates exhibit half-integer total angular momenta. As a consequence, the angular momentum coupled IM-SRG equations that rely on scalar density matrices do not apply. Note that an inclusion of non-scalar density matrices would imply that the spherical tensor rank of operators would not be conserved anymore leading not only to analytically but also computationally severe implications.

The general approach of the PA/PR extension to overcome the restriction of the IM-NCSM framework to even- A nuclei is simple: We differentiate between the odd- A target nucleus we want to treat eventually and an even- A *parent* nucleus lying in the close vicinity of the target nucleus. The reference state construction and IM-SRG evolution is carried out for the parent nucleus, whereas the post-diagonalization is performed for the target nucleus.

Ultimately, the IM-SRG transformation aims for decoupling a specific eigenstate of the parent nucleus—the reference state—from its excitations or, equivalently, higher-lying NCSM basis states. This decoupling is achieved through a suppression of particular matrix elements and, as a consequence, also excited states or even complete model spaces get decoupled in this process. Similarly, also eigenstates of the target nucleus get partially decoupled as long as these eigenstates are structurally similar to the reference state such that similar matrix elements are mediating the coupling to higher-lying determinants. In this case, we also expect a significant acceleration of the N_{\max} convergence of an NCSM calculation w.r.t. the target nucleus—not unlike the acceleration of the N_{\max} convergence we previously observed for excited states of the parent nucleus.

The extension relies on the specification of a parent nucleus with Z_{parent} protons, N_{parent} neutrons, and A_{parent} nucleons and a target nucleus with A_{target} nucleons, Z_{target} protons, and N_{target} neutrons, where $|Z_{\text{target}} - Z_{\text{parent}}| + |N_{\text{target}} - N_{\text{parent}}| \approx 1$ shall hold. Particle-attachment in regards to a specific nucleon species may now be defined as either $Z_{\text{target}} > Z_{\text{parent}}$ or $N_{\text{target}} > N_{\text{parent}}$ and particle removal refers to either $Z_{\text{target}} < Z_{\text{parent}}$ or $N_{\text{target}} < N_{\text{parent}}$.

In a nutshell, the even parent nucleus defines the system w.r.t. which any transformation or approximation is performed: the unitary transformation into the natural orbitals, the reference state, the NO2B approximation, and the IM-SRG transformation. The final NCSM calculation, however, is performed with regard to the target nucleus. Thus, the target nucleus and its associated Z_{target} , N_{target} and A_{target} come into play whenever an initial operator that is plugged into the IM-NCSM framework explicitly carries information on the proton, neutron

or total nucleon number. Therefore, let us consider the initial intrinsic Hamiltonian, which generally consists of the kinetic energy, a NN interaction and a 3N interaction part

$$\hat{H}_{\text{int}} = \hat{T}_{\text{int}} + \hat{V}_{\text{NN}} + \hat{V}_{\text{3N}}. \quad (6.7.1)$$

The kinetic energy operator can be written as [HR09]

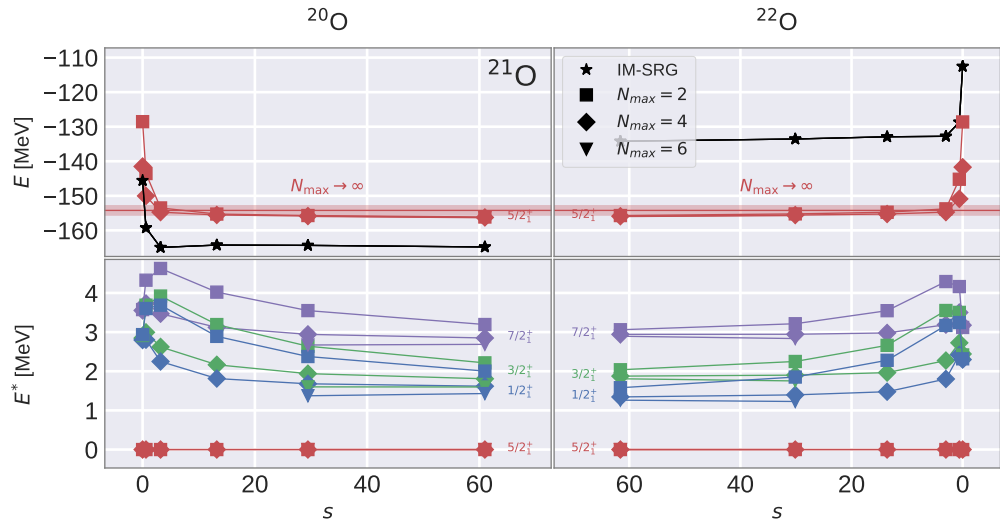
$$\hat{T}_{\text{int}} = \sum_{i < j} \frac{(\hat{\mathbf{p}}_i - \hat{\mathbf{p}}_j)^2}{2m_{A_{\text{target}}}}. \quad (6.7.2)$$

As, ultimately, we are aiming for calculating nuclear structure observables in an Hilbert space $\mathcal{H}_{A_{\text{target}}}$, the kinetic energy part has to employ the total nucleon number of the target nucleus. The initial NN and 3N interaction, however, do not have any explicit dependence on the nucleon number and are, therefore, independent. Note that the kinetic energy is embedded into the Hamiltonian at the very beginning of the IM-NCSM framework and, therefore, cannot be rescaled after the transformation, but has to carry the information for which nucleus the final NCSM calculation is performed from the start.

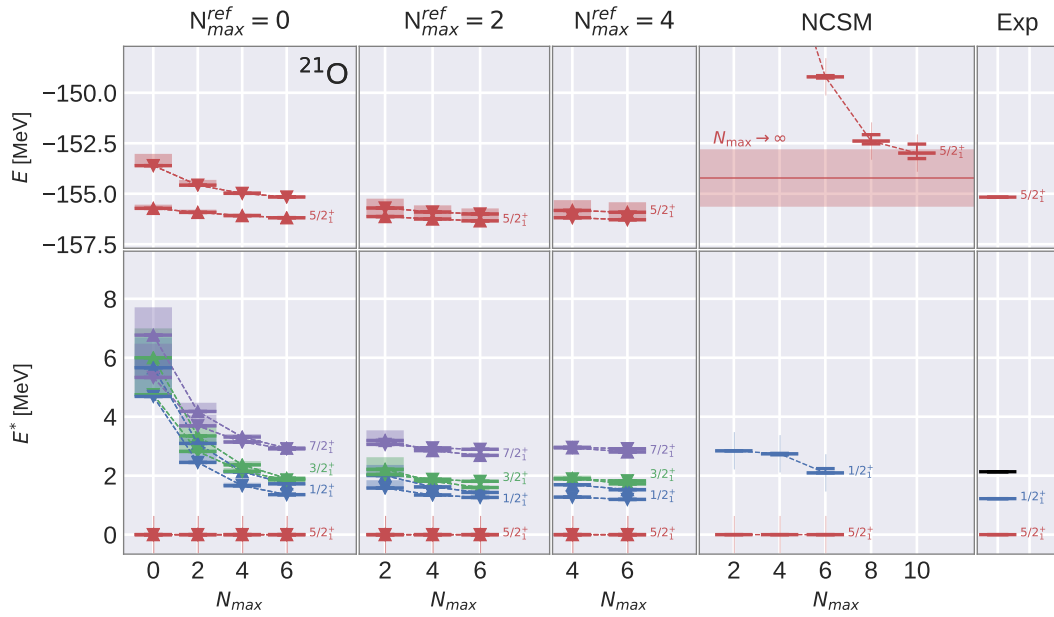
6.7.2. Numerical Applications—A simple Example

Let us now discuss numerical applications of the PA/PR extension. To begin with, we present calculations targeting ^{21}O from the parent nuclei ^{20}O and ^{22}O in fig. 6.14. Considering the evolution depicted in fig. 6.14a, we observe that, firstly, the ground-state energy is rapidly stabilizing in the flow parameter s , secondly, we obtain results that are converged at $N_{\text{max}} = 2$ already at an early stage of the evolution, and lastly, both parent nuclei yield similar results for large values of s . This demonstrates that calculations employing the PA/PR extension of the IM-NCSM are behaving very similar to “regular” IM-NCSM calculations: The IM-SRG substantially boosts the N_{max} convergence of the subsequent NCSM calculation and we obtain converged results at small values for N_{max} .

We investigate the N_{max} convergence and the dependence on $N_{\text{max}}^{\text{ref}}$ of the PA/PR extension in more detail in fig. 6.14b. For all $N_{\text{max}}^{\text{ref}}$ and both parents the N_{max} convergence patterns are fairly compatible with each other—for both ground and excited states. However, similar to previous investigations of even nuclei, we observe that there is an effect of $N_{\text{max}}^{\text{ref}}$ on the N_{max} convergence, especially when comparing the convergence of excitation energies at $N_{\text{max}}^{\text{ref}} = 0$ and $N_{\text{max}}^{\text{ref}} = 2$ with each other. Considering the ground-state energy obtained from the IM-NCSM, it is compatible with the N_{max} -extrapolated result from the NCSM as well as the experimental value. However, the first $1/2^+$ state obtained from the IM-NCSM is closer to the experimental value than to the NCSM result. Note that we only show NCSM results for $N_{\text{max}} \leq 6$ for the 2_1^+ as the κ_{min} threshold extrapolation becomes unreliable for higher N_{max} .



(a) Evolution of ground and excited state energies for the target nucleus ^{21}O . We employed the parent nuclei ^{20}O (left panel) and ^{22}O (right panel). The calculations shown here were performed at $N_{\text{max}}^{\text{ref}} = 2$. The IM-SRG energy refers to the expectation value w.r.t. the reference state of the parent nucleus.



(b) Ground and excited-state energies for ^{21}O obtained from the IM-NCSM at several $N_{\text{max}}^{\text{ref}}$, the NCSM and experiment. We employed the parent nuclei ^{20}O (triangle up) and ^{22}O (triangle down). For details on experimental data see appendix C.

Figure 6.14.: Evolution and N_{max} convergence for ^{21}O .

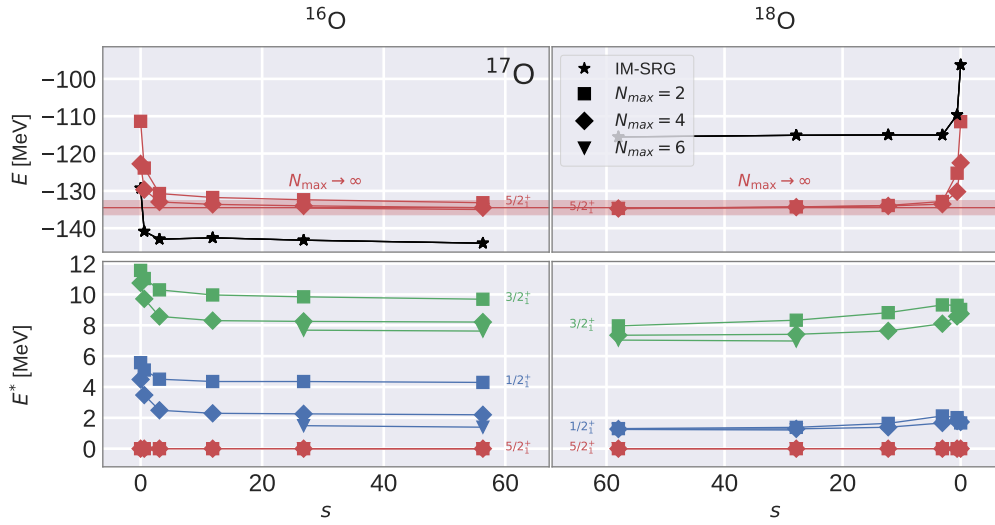
6.7.3. Numerical Applications—Shell-Closure Effects

Now that we have studied a case where the PA/PR extension works very well, let us proceed to a more interesting case, which, at least at first glance, seems to be problematic and raises questions about the adequateness of certain nuclei as parent nuclei. However, we will see that there is a reason why calculations w.r.t. specific parent nuclei behave fundamentally different than others and we will be able to establish a rule which parent and target nucleus combinations are reasonable and which are not.

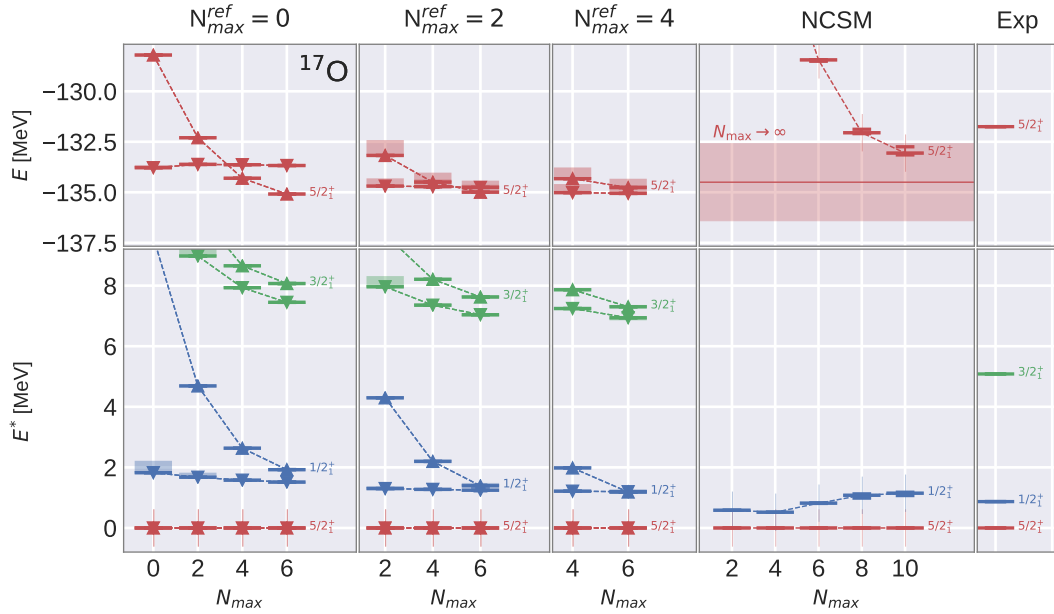
Neutron Shell Closure. Figure 6.15a shows the evolution of ground and excited-states energies of ^{17}O employing the two parents ^{16}O and ^{18}O , respectively. Unlike to the case for ^{21}O , we observe that the two parent nuclei lead to significantly different N_{max} convergence rates even at large values for the flow parameter s . Calculations based on ^{16}O as parent nucleus exhibit a much slower convergence. This is especially clear in fig. 6.15b, where we show IM-NCSM calculations for several $N_{\text{max}}^{\text{ref}}$. While calculations based on ^{18}O are practically converged for $N_{\text{max}} \geq N_{\text{max}}^{\text{ref}}$, there is a substantial N_{max} dependence for calculations based on ^{16}O and large N_{max} are necessary such that both parent nuclei yield similar results for all $N_{\text{max}}^{\text{ref}}$.

The reason for this difference between the two parent nuclei lies in their shell structure. In the context of the NCSM, the notion of a closed or open-shell nucleus refers to a one or multi-dimensional $N_{\text{max}} = 0$ space, respectively. Additionally, it may be further specified whether an open-shell nucleus exhibits a closed shell w.r.t. either of the two particle species. Considering $N_{\text{max}}^{\text{ref}} = 0$ space, all three nuclei have closed proton shells, but the parent nucleus ^{16}O also has a closed neutron shell while ^{18}O and ^{17}O do not. As a consequence, the $N_{\text{max}} = 0$ spaces of ^{16}O and ^{17}O have a fundamentally different structure while the associated spaces for ^{18}O and ^{17}O are very similar. This difference is relevant during the IM-SRG transformation, which aims at decoupling a specific reference state $|\psi_{\text{ref}}\rangle$ from particle-hole excitations. This decoupling is governed by the partitioning of the single-particle basis into a core ($n = 1$), active ($0 < n < 1$) and virtual space ($n = 0$), where n refers to the corresponding occupation number. Considering ^{16}O and ^{17}O at $N_{\text{max}} = 0$, they may have the same core states, but differ w.r.t. their active states. Thus, the decoupling patterns of these two nuclei are—already at a single-particle level—not compatible with each other as all determinants within the $N_{\text{max}}^{\text{ref}}$ space of ^{17}O with a dominant contribution of single-particle states belonging to the active space are not accounted for by an IM-SRG transformation w.r.t. ^{16}O and, therefore, not decoupled from higher-lying determinants. Thus, we do not expect a significant N_{max} -convergence acceleration when performing an IM-NCSM calculation w.r.t. the parent nucleus ^{16}O and the target nucleus ^{17}O —a fact that is strikingly demonstrated by fig. 6.15.

Comparing the IM-NCSM with the NCSM in fig. 6.15b, we observe that for both the ground state as well as the first excited $1/2^+$ state the two methods agree very well with each other. Furthermore, the IM-NCSM calculations employing ^{18}O as parent nucleus yield converged results for the ground state and the first excited state $1/2^+$ at $N_{\text{max}} = 0$ to 2 which again demonstrates the greatly improved N_{max} convergence. The convergence of the $3/2^+$ state w.r.t. N_{max} , however, is rather slow such that it is necessary to perform calculations at $N_{\text{max}} = 4$ to 6 for



(a) Similarly to fig. 6.14a, this figure depicts the evolution of ground and excited-state energies for ^{17}O w.r.t. the two parent nuclei ^{16}O (left panel) and ^{18}O (right panel).



(b) Similarly to fig. 6.14b, this figure depicts IM-NCSM, NCSM and experimental values for ^{17}O , where we employed the parent nuclei ^{16}O (triangle up) and ^{18}O (triangle down). For details on experimental data see appendix C.

Figure 6.15.: Evolution and N_{max} convergence for ^{17}O .

obtaining reliable results. Taking experimental values into our considerations, the experimentally observed ground-state energy is overestimated by about 2.5 MeV and the theoretically predicted and experimentally observed energy of the $1/2^+$ are in good agreement with each other. The $3/2^+$ state, however, lies too high by about 2 MeV at $N_{\max} = 6$, but may still move down at higher N_{\max} due to an incomplete convergence.

Proton Shell Closure. Up to now, we were only applying the PA/PR for adding or removing neutrons to oxygen isotopes, i.e., we stay within the oxygen chain. Figure 6.16 depicts calculations where we employed the PA/PR scheme for targeting ^{21}F by attaching or removing a proton from the parent nuclei ^{20}O or ^{22}Ne , respectively.

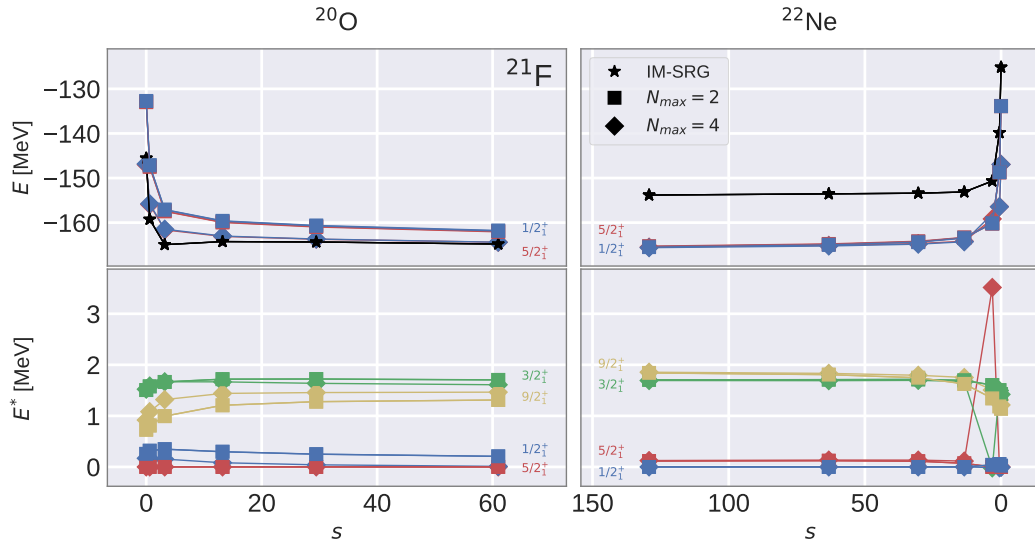
The evolution depicted in fig. 6.16a shows the well-known convergence pattern w.r.t. the flow parameter s . The energies obtained from both parents are similar to each other, but they exhibit a different N_{\max} -convergence behavior. The order of the two lowest-lying and nearly degenerate states, a $5/2^+$ and $1/2^+$ state, differs between the two parent nuclei.

Considering fig. 6.16b, it is once more clearly demonstrated that the N_{\max} convergence is different for both parent nuclei, especially for the ground-state energies shown in the upper panel. However, the behavior observed here is to be expected: Targeting ^{21}F from ^{20}O is similar to the previous case with ^{17}O from ^{16}O , respectively, as ^{20}O has a closed proton shell while ^{21}F does not.

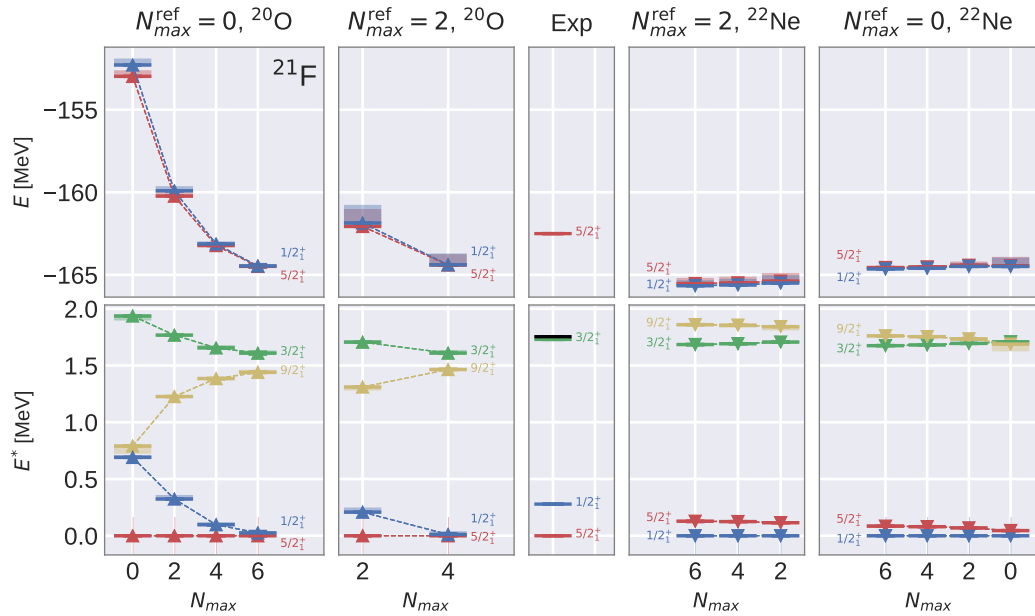
The ground-state energy obtained from the IM-NCSM is about 3 MeV below the experimental value. The two lowest-lying states obtained from the IM-NCSM are nearly degenerate and only the calculation based on the parent nucleus ^{20}O yields the experimentally observed $5/2^+$ as ground state, while ^{22}Ne predicts a $1/2^+$ state. However, as the IM-NCSM results obtained from calculation based on ^{20}O as parent nucleus are not fully converged, also here the $1/2^+$ state may turn out to be the ground state. Note that also experimentally the two $5/2^+$ and $1/2^+$ states are energetically very close to each other and the incorrect theoretical prediction of the ground-state may very well be a deficiency of the interaction.

Similarly to the ground-state and the first excited state, also the second pair of states, i.e., the $3/2^+$ and $9/2^+$ states are nearly degenerate—both theoretically and experimentally—and different orders are obtained for the two parent nuclei. However, the excitation energies of these two states are in good agreement with the experimental values and the state that lies experimentally slightly above the $3/2^+$ is predicted to be a $9/2^+$ state.

Calculations at $N_{\max}^{\text{ref}} = 2$ and $N_{\max} = 6$ with ^{20}O as parent nucleus are not shown in fig. 6.16b as several eigenstates becomes degenerate here leading to problems with the κ_{\min} threshold extrapolation—which is eventually due to the fact that the Hamiltonian and the total angular momentum operator do not commute within an importance-truncated model space. However, we verified that the energies are well converged.



(a) Similarly to fig. 6.14a, this figure shows the evolution of the ground and excited state energies for the target nucleus ^{21}F . We employed the parent nuclei ^{20}O (left panel) and ^{22}Ne (right panel).



(b) Similarly to fig. 6.14b, this figure depicts IM-NCSM, NCSM and experimental results for ground and excited state energies of the target nucleus ^{21}F . We employed the parent nuclei ^{20}O (first and second column) and ^{22}Ne (fourth and fifth column). For details on experimental data see appendix C.

Figure 6.16.: Evolution and N_{\max} convergence for ^{21}F .

6.7.4. Conclusion

The PA/PR extension works very well and leads to similar effects than for the regular case in which parent and target nucleus are equal: The N_{\max} convergence is substantially accelerated and we basically obtain converged results for $N_{\max} \gtrsim N_{\max}^{\text{ref}}$. However, as we saw through the calculations targeting ^{17}O and ^{21}F it is not advisable to perform a particle attachment if the parent nucleus exhibits a closed shell w.r.t. the particle species that is attached. Note that a similar observation can be made for a particle removal for nuclei that exhibit a closed shell w.r.t. the particle species that shall be removed. Both of these cases are problematic since the structure of the reference state—which is an eigenstate of the parent nucleus—is fundamentally different from the structure of the lowest lying eigenstates of the target nucleus and, as a consequence, couplings of these eigenstates of the target nucleus to higher-lying NCSM basis states are not suppressed through the IM-SRG transformation.

Apart from the fact that a closed-shell nucleus is not an adequate choice for a parent nucleus within the context of the PA/PR extension, we observed that a particle removal is usually the more robust choice. Thus, in cases of doubt the particle removal is our favored scheme.

6.8. Importance Truncation and Reference States

Let us now discuss an extension of the scheme for the construction of reference states, where the necessity is motivated through fig. 6.17: Employing a nuclear-chart-like representation, it shows the model-space dimensions of NCSM calculations. For each isotope, specified through its associated neutron and proton numbers, the corresponding model-space dimension D is given through its logarithm $\log(D)$. In our current implementation the NO2B approximation is the computational bottleneck of the IM-NCSM framework. Here, the computational effort scales drastically with the number of configurations such that we are restricted to approximately $D \leq D_{\max} \equiv 5 \times 10^6$.² Considering isotopes in the sd shell and lower pf shell, calculations with $N_{\max}^{\text{ref}} = 0$ are still feasible, however, performing calculations at $N_{\max}^{\text{ref}} = 2$ is only possible for nuclei lying either directly on or in the vicinity of shell-closure lines. Calculations far away from shell closures, however, are out of the question due to model-space dimensions of up to 1×10^8 or even beyond. Going to $N_{\max}^{\text{ref}} = 4$, it becomes evident that there are no sd -shell nuclei left that we could treat employing the IM-NCSM framework.

As simple and straightforward approach for extending the reach of the IM-NCSM is an importance truncation within the context of the IT-NCSM (see chapter 2). The initial NCSM calculation is replaced by an IT-NCSM calculation employing a specific value for the importance threshold κ_{\min} . As a consequence, the associated importance-truncated model space, which contains the reference state as one of its eigenstates, has a greatly reduced dimension. Other than that, the details of the IM-NCSM framework remain unchanged. In the following,

²Note that this is not a hard limit and there may be future improvements of our implementation that eventually increase D_{\max} .

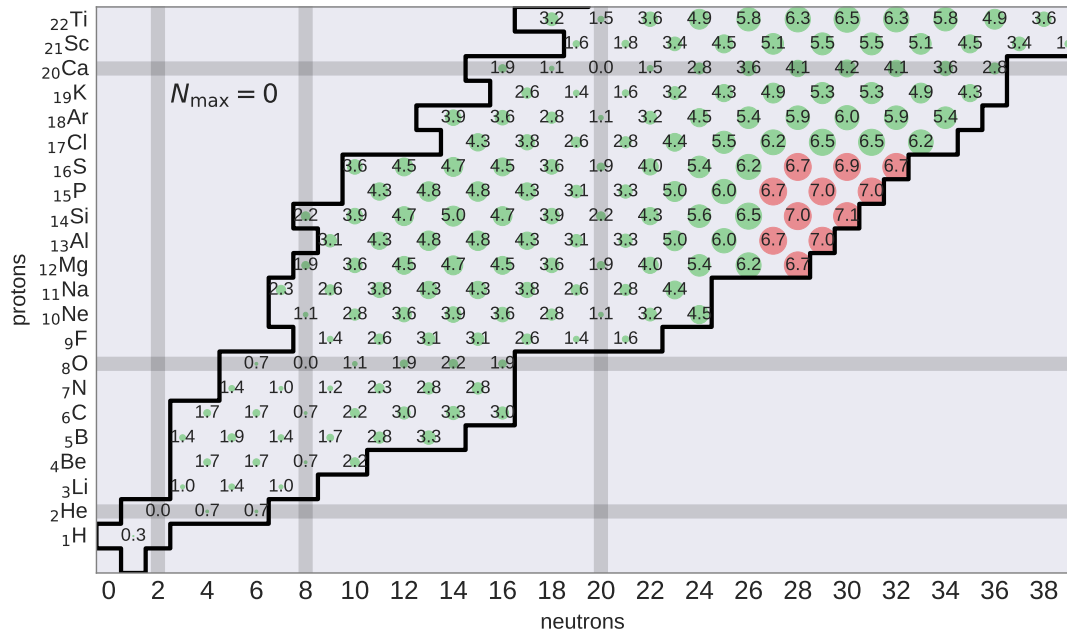


Figure 6.17.: Illustration of the NCSM model-space dimension D for $N_{\max} = 0$ (see fig. 6.18 for $N_{\max} = 0$ and 2). We choose a nuclear-chart-like format such that proton and neutron numbers vary vertically and horizontally, respectively. Model-space dimensions are depicted for all even isotopes of hydrogen up to titan that do not lie beyond either the proton or neutron drip line (indicated through solid black lines). There are three ways in which we indicated the model-space dimensions: Firstly, a number indicating $\log(D)$, where, if non-existent, $D \gtrsim 1 \times 10^9$, which lies far beyond the computational capacities of the IM-NCSM. Secondly, the area of each plot marker linearly correlates with $\log(D)$, where the maximum area is capped at $D_{\max} \equiv 5 \times 10^6$, which corresponds to the maximally feasible dimension of our current implementation (with reasonable computational effort). Lastly, we employ two different colors for indicating if $D \leq D_{\max}$ (green) or $D > D_{\max}$ (red). Furthermore, shaded gray bands indicate shell closures.

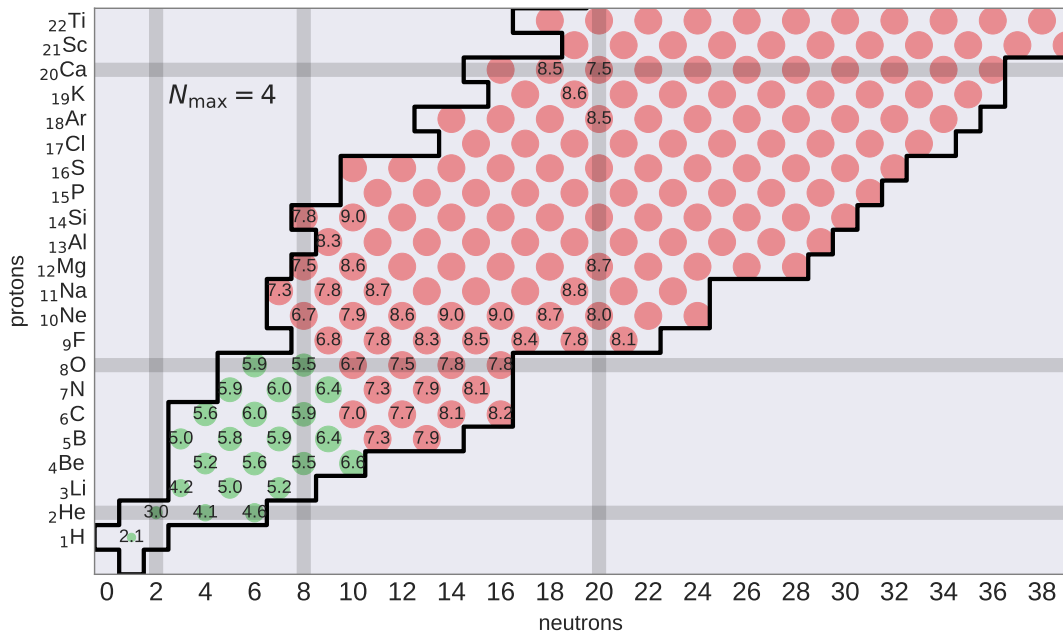
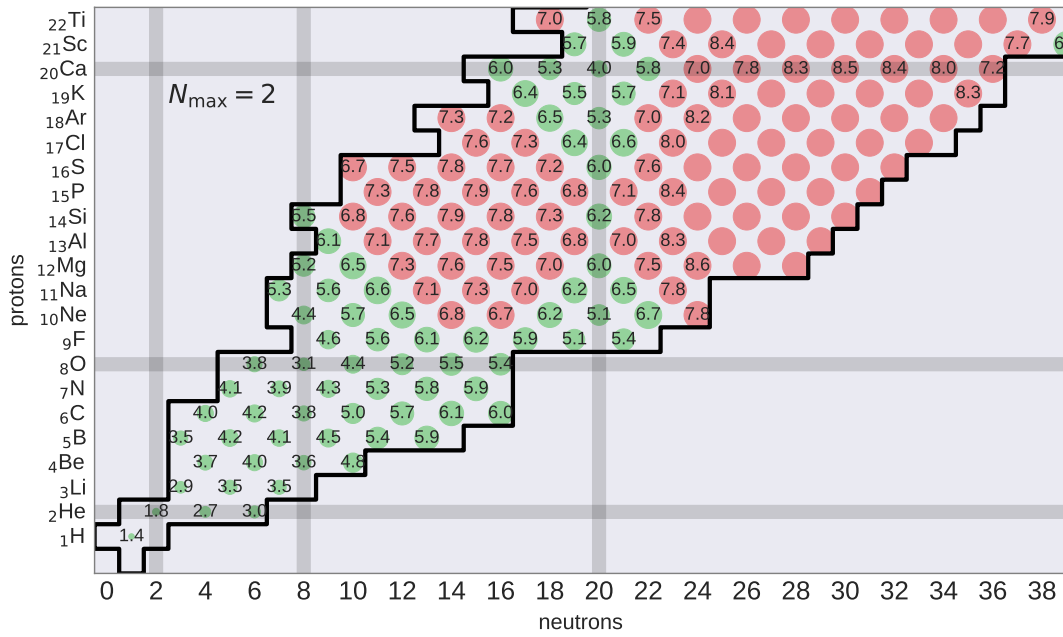


Figure 6.18.: Illustration of NCSM model-space dimensions (see fig. 6.17 for details).

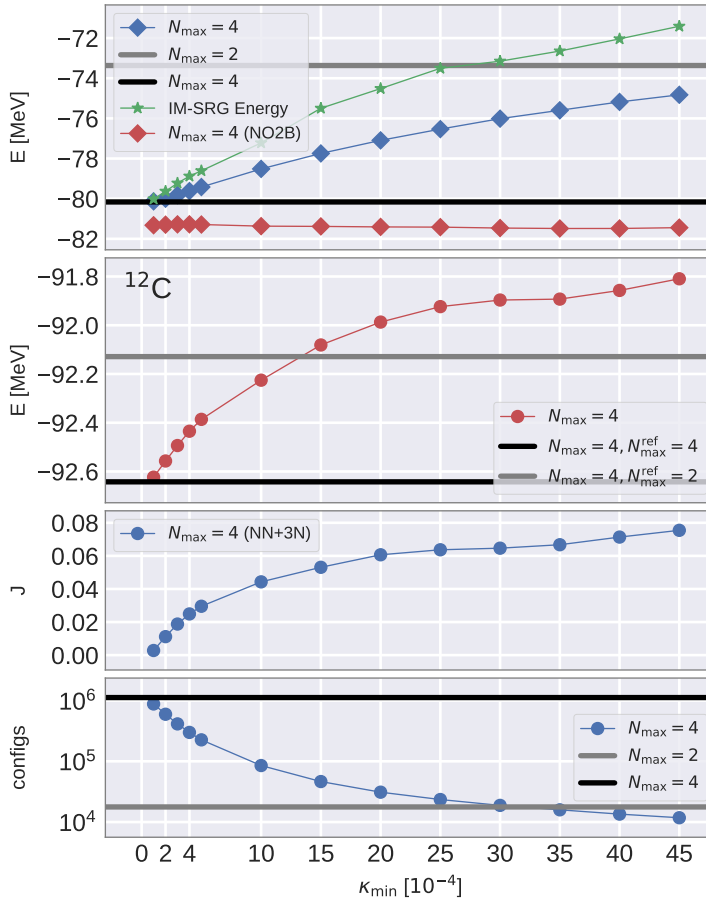


Figure 6.19.: Using a specific importance threshold κ_{\min} for the construction of the reference state, this figure illustrates how several aspects of an IM-NCSM calculation are depending on the choice for κ_{\min} . See text for more information.

let us investigate an eigenstate of an importance-truncated model space as a reference state. Additionally, such an importance-truncated reference state will be denoted as $|\psi_{\text{ref}}^{N_{\max}}(\kappa_{\min})\rangle$, where κ_{\min} refers to the importance threshold of the corresponding importance-truncated model space.

For investigating the properties of an importance-truncated reference state, let us consider fig. 6.19. Starting from an initial Hamiltonian including 3N interactions, we perform an initial IT-NCSM calculations at $N_{\max} = 4$ using several values for κ_{\min} from which we obtain individual reference states $|\psi_{\text{ref}}^{N_{\max}=4}(\kappa_{\min})\rangle$. The corresponding eigenenergies are shown by the curve labeled “ $N_{\max} = 4$ ” in the upper panel. Additionally, the results of $N_{\max} = 2$ and $N_{\max} = 4$ calculations without importance truncation are shown as horizontal lines. We observe that the result of a full $N_{\max} = 4$ calculation is reproduced for $\kappa_{\min} \rightarrow 0$, and that the curve is approaching the $N_{\max} = 2$ result for increasing values of κ_{\min} .

The bottom panel in fig. 6.19 depicts the corresponding model-space sizes: A full $N_{\max} = 4$ cal-

ulation needs roughly 1×10^6 configurations whereas the $N_{\max} = 2$ model-space dimension is reduced by several orders of magnitude. As the model-space size varies significantly with the choice for κ_{\min} we might ask: Can we choose a κ_{\min} such that the importance-truncated model space is of significantly reduced size and, simultaneously, obtain a proper approximation for the full reference state?

For that purpose, let us proceed by looking at the steps which follow the initial IT-NCSM calculation for the construction of the reference state. The operator \hat{H} and its corresponding reference state $|\psi_{\text{ref}}^{N_{\max}=4}(\kappa_{\min})\rangle$ are used to construct the NO2B-approximated Hamiltonian \hat{H}_{NO2B} together with the scalar one and two-body density matrices. We emphasize that the non-scalar parts of the density matrices due to $J \neq 0$ contributions are discarded. As shown by the third row of fig. 6.19, the total angular momentum J of the reference state is degraded—a behavior which is to be expected and well-known as the eigenstates of the importance-truncated model space are not necessarily eigenstates of \hat{J}^2 anymore. As a consequence, the non-scalar admixtures to the density matrices are increasing. The effect of this projection of the density matrices is evident from the curve labeled as “IM-SRG Energy” in the upper row of fig. 6.19. It depicts the expectation value of the NO2B-approximated Hamiltonian \hat{H}_{NO2B} , where the expectation value is calculated by employing the projected density matrices $\gamma^{[1,2]}$.

Lastly, there is another curve labeled “ $N_{\max} = 4$ ” in the top panel: It depicts a subsequent NCSM calculation at $N_{\max} = 4$ employing \hat{H}_{NO2B} as input. The source for the discrepancies between the IT-NCSM based on \hat{H} and the NCSM calculation based on \hat{H}_{NO2B} is two-fold: Firstly, the reference state $|\psi_{\text{ref}}^{N_{\max}=4}(\kappa_{\min})\rangle$ does not necessarily have to be an eigenstate of \hat{H}_{NO2B} . Secondly, even while we are not performing an IM-SRG evolution per se, \hat{H}_{NO2B} goes once through the complete IM-SRG machinery implying an eventual single-particle transformation into the natural orbitals.³ Note that we verified that the dominant contribution here is the single-particle transformation into the natural orbitals, while $|\psi_{\text{ref}}\rangle$ being not an eigenstate of \hat{H}_{NO2B} is numerically negligible. Furthermore, we observe that this curve is mostly independent of κ_{\min} , which implies that the effect of κ_{\min} on the NO2B approximation is negligible.

The impact of κ_{\min} on IM-NCSM calculations is shown in the second row of fig. 6.19: It includes a curve labeled as “ $N_{\max} = 4$ ” showing the results of IM-NCSM calculations at $N_{\max} = 4$ employing a reference state $|\psi_{\text{ref}}^{N_{\max}=4}(\kappa_{\min})\rangle$. Additionally, there are two horizontally lines which depict the result of IM-NCSM calculations at $N_{\max} = 4$ employing $N_{\max}^{\text{ref}} = 2$ and 4 reference states without any importance truncation. It becomes evident that, as long as κ_{\min} is chosen within reasonable limits $\kappa_{\min} \leq 0.001$, the result of an IM-NCSM calculation with an importance-truncated reference state lies in between the results for regular $N_{\max}^{\text{ref}} = 2, 4$ IM-NCSM calculations. Thus, through a specific choice of κ_{\min} for an IM-NCSM calculation at N_{\max}^{ref} we may control the amount of correlations we are additionally including with regard to an IM-NCSM calculation at $(N_{\max}^{\text{ref}} - 2)$ while keeping the model-space sizes under control.

³Note that this kind of natural orbitals refer to the eigenbasis of the one-body density matrix constructed from the reference state—in contrast to the natural orbitals which are constructed at the very beginning of the IM-NCSM framework and are based on perturbation theory.

We could, e.g., halve the model-space size of an $N_{\max}^{\text{ref}} = 4$ calculation by using $\kappa_{\min} = 4 \times 10^{-4}$ while still retaining the regular $N_{\max}^{\text{ref}} = 4$ result to a large extent.

We have found that $\kappa_{\min} = 2 \times 10^{-4}$ is a good compromise between model-space size reduction and precision. In this context, the impact of κ_{\min} on the IM-NCSM result and the energy of the corresponding reference-state w.r.t. the untransformed Hamiltonian are correlated with each other: As long as the energy of the importance-truncated and full reference state w.r.t. the initial Hamiltonian are close to each other, also the two associated IM-NCSM calculations lie close to each other.

6.9. Evolution of Observables—Concepts

The IM-NCSM not only allows for the treatment of energies but also the full range of nuclear structure observables. This capability is founded in the fact that we directly obtain ground and excited states from the IM-NCSM and, therefore, the calculation of expectation values or transition matrix elements of an arbitrary observable is straightforward. However, the unitary transformation applied to the Hamiltonian through the IM-SRG framework is associated with a basis transformation and, as a consequence, observables have to be *consistently* transformed employing the same unitary transformation as for the Hamiltonian. For the consistent evolution of an observable \hat{O}_M^L there are two possible approaches within the IM-SRG framework:

1. the *direct* evolution of an observable through *simultaneously* solving the operator differential equations for the operator and the Hamiltonian

$$\frac{d}{ds} \hat{H}(s) = [\hat{\eta}(s), \hat{H}(s)] , \quad \frac{d}{ds} \hat{O}_M^L(s) = [\hat{\eta}(s), \hat{O}_M^L(s)] , \quad (6.9.1)$$

2. the *Magnus* evolution through a previous solution of the differential equation for $\hat{\Omega}(s)$ and an evaluation of the Baker-Campbell-Hausdorff series for the observable

$$\hat{O}_M^L(s) = \sum_{i=0}^{\infty} \left[\hat{\Omega}(s), \hat{O}_M^L(s) \right]_k . \quad (6.9.2)$$

Two scalar operators, whose transformation employing either of these two approaches is straightforward, are the intrinsic and center-of-mass Hamiltonian \hat{H}_{int} and \hat{H}_{cm} , respectively. Apart from these operators, we discuss the treatment of the (scalar) radius operator as well as general electromagnetic observables associated with non-scalar operators.

6.9.1. Theoretical Foundation of the Radius Operator

The translationally invariant (point-mass) mean-square radius is defined as

$$\hat{r}_{\text{ms}} \equiv \frac{1}{A} \sum_{i=1}^A (\hat{x}_i - \hat{R})^2, \quad (6.9.3)$$

where \hat{x}_i refers to the position operator of the i -th particle and \hat{R} denotes the center-of-mass position operator. Applying several elementary transformations to the right-hand side of this expression gives

$$\hat{r}_{\text{ms}} = \frac{1}{2A^2} \sum_{i,j=1}^A \hat{r}_{ij}^2 = \frac{1}{A^2} \sum_{i<j}^A \hat{r}_{ij}^2, \quad (6.9.4)$$

which only depends on relative distances $\hat{r}_{ij} \equiv \hat{x}_i - \hat{x}_j$. In second quantization the mean-square radius operator may then be written as

$$\hat{r}_{\text{ms}} = \frac{1}{A^2} \frac{1}{4} \sum_{\substack{q_1 q_2 \\ q_3 q_4}} \langle q_1 q_2 | \hat{r}_{12}^2 | q_3 q_4 \rangle \hat{a}_{q_3 q_4}^{q_1 q_2}. \quad (6.9.5)$$

For defining the point-proton and point-neutron mean-square radii, let us introduce the proton and neutron projectors $\hat{\Pi}_i^p$ and $\hat{\Pi}_i^n$, respectively. The point-proton mean-square radius, i.e., the mean-square radius, which exclusively considers the protons within the nucleus, can be defined as

$$\hat{r}_{\text{pms}} \equiv \frac{1}{Z} \sum_{i=1}^A (\hat{x}_i - \hat{R})^2 \hat{\Pi}_i^p. \quad (6.9.6)$$

Following similar steps as before, we obtain

$$\hat{r}_{\text{pms}} = \frac{1}{ZA} \sum_{i<j}^A \hat{r}_{ij}^2 (2\hat{\Pi}_i^p \hat{\Pi}_j^p + \hat{\Pi}_i^p \hat{\Pi}_j^n + \hat{\Pi}_i^n \hat{\Pi}_j^p) - \hat{r}_{\text{ms}}, \quad (6.9.7)$$

which may be written in second quantization as

$$\begin{aligned} \hat{r}_{\text{pms}} = & \frac{1}{4A^2} \frac{2A}{Z} \sum_{\substack{q_1 q_2 \\ q_3 q_4}} \langle q_1 q_2 | \hat{r}_{12}^2 \hat{\Pi}_1^p \hat{\Pi}_2^p | q_3 q_4 \rangle \hat{a}_{q_3 q_4}^{q_1 q_2} \\ & + \frac{1}{4A^2} \frac{A}{Z} \sum_{\substack{q_1 q_2 \\ q_3 q_4}} \langle q_1 q_2 | \hat{r}_{12}^2 (\hat{\Pi}_1^p \hat{\Pi}_2^n + \hat{\Pi}_2^p \hat{\Pi}_1^n) | q_3 q_4 \rangle \hat{a}_{q_3 q_4}^{q_1 q_2} - \hat{r}_{\text{ms}} \end{aligned} \quad (6.9.8)$$

The point-neutron mean-square radius operator \hat{r}_{nms} may now be easily obtained by an interchange $\hat{\Pi}_i^{\text{p}} \leftrightarrow \hat{\Pi}_i^{\text{n}}$ and $Z \leftrightarrow N$ within the analytical expression for \hat{r}_{pms} . Furthermore, it can easily be verified that the three operators \hat{r}_{ms} , \hat{r}_{pms} , and \hat{r}_{nms} are related through

$$\hat{r}_{\text{nms}} = \frac{A}{N} \hat{r}_{\text{ms}} - \frac{Z}{N} \hat{r}_{\text{pms}}. \quad (6.9.9)$$

It is important to note that the projections from which we obtain the individual operator structures within the expressions for \hat{r}_{pms} and \hat{r}_{nms} and the unitary transformation induced by the IM-SRG transformation for obtaining $\hat{r}_{\text{pms}}(s)$ and $\hat{r}_{\text{nms}}(s)$, respectively, are not commuting with each other. As a consequence, it is not possible to insert the IM-SRG-evolved mean-square radius operator $\hat{r}_{\text{ms}}(s)$ into eq. (6.9.8) for obtaining the evolved proton mean-square radius operator $\hat{r}_{\text{pms}}(s)$. Instead, we have to construct $\hat{r}_{\text{pms}}(0)$ and evolve it for obtaining $\hat{r}_{\text{pms}}(s)$. This is further elucidated by taking into account that the IM-SRG generally produces an induced one-body part for $\hat{r}_{\text{pms}}(s)$ which would be missing when simply employing eq. (6.9.8) for the calculation of $\hat{r}_{\text{pms}}(s)$ from $\hat{r}_{\text{ms}}(0)$.⁴

Employing the mean-square radius operators, we can define the point-mass, point-proton, and point-neutron root-mean-square radii

$$R_{\text{rms}} \equiv \sqrt{\langle \psi_i | \hat{r}_{\text{ms}} | \psi_i \rangle}, \quad R_{\text{prms}} \equiv \sqrt{\langle \psi_i | \hat{r}_{\text{pms}} | \psi_i \rangle}, \quad R_{\text{nrms}} \equiv \sqrt{\langle \psi_i | \hat{r}_{\text{nms}} | \psi_i \rangle}, \quad (6.9.10)$$

respectively, where $|\psi_i\rangle$ refers to an eigenstate of the Hamiltonian. The experimentally commonly measured charge radius is obtained through [Lu+13]

$$R_{\text{ch}}^2 \equiv R_{\text{prms}}^2 + \left(r_{\text{p}}^2 + \frac{3}{4m_{\text{p}}^2} \right) + \frac{N}{Z} r_{\text{n}}^2, \quad (6.9.11)$$

which takes the charge radius of the proton $r_{\text{p}}^2 = 0.770 \text{ fm}^2$, the charge radius of the neutron $r_{\text{n}}^2 = -0.1161 \text{ fm}^2$, and the so-called Darwin-Foldy term $\frac{3}{4m_{\text{p}}^2} = 0.033 \text{ fm}^2$ into account.

6.9.2. Theoretical foundation of Electromagnetic Observables

Let us now introduce the basics for the treatment of electromagnetic observables. These observables probe the structure of the wave functions involved through multipole moments and gamma decays. Furthermore, compared to, e.g., the Hamiltonian, they are sensitive to different aspects of the wave functions and are thus an excellent test for our nuclear models. For more information see, e.g., [Suh07; RS80].

The electromagnetic decay process has its roots in the interaction of the nucleus with an external electromagnetic field where this field consists of an electric \vec{E} and magnetic \vec{B} contribution. The interaction between the nucleus and the field is mediated by the four-potential

⁴Strictly speaking, such an approach is possible but the projection operators themselves would have to be transformed.

(ϕ, \vec{A}) where ϕ is the scalar potential that interacts with the nuclear charge density ρ and the vector potential interacts with the nuclear current density \vec{j} . The complete system consisting of nucleus and field, where the field is quantized in terms of photons, interacts weakly such that it can be treated perturbatively. The electromagnetic field can be expanded in multipoles giving the following result for the electric and magnetic tensor operators⁵

$$\hat{Q}_\mu^\lambda = \sum_{j=1}^A e_j r_j^\lambda Y_\mu^\lambda(\Omega_j), \quad (6.9.12)$$

$$\hat{M}_\mu^\lambda = \frac{\mu_N}{\hbar c} \sum_{j=1}^A \left(\frac{2}{\lambda+1} g_{l,j} \hat{l}_j + g_{s,j} \hat{s}_j \right) \nabla_j (r_j^\lambda Y_\mu^\lambda(\Omega_j)), \quad (6.9.13)$$

where e_j , \hat{l}_j , and \hat{s}_j indicate the charge, orbital, and spin angular momentum, respectively, of the j -th particle. The spin gyromagnetic factor g_s is either 5.586 (protons) or -3.826 (neutrons). The orbital gyromagnetic factor g_l is 1 (protons) or 0 (neutrons). The nuclear magneton is defined as $\mu_N = \frac{e\hbar}{2m_p}$, where m_p is the proton mass [Suh07].

Electromagnetic Transitions and Reduced Transition Probability. Let us consider an electromagnetic decay of an excited nucleus mediated by one of the multipole terms of the radiation field. The initial state is an excited state of the nucleus $|\psi_i\rangle$ and the final state consists of a photon and another eigenstate $|\psi_f\rangle$ of the underlying Hamiltonian. The transition probability of this decay is denoted as T_{fi} and the corresponding half life is $t_{1/2} = \ln(2)/T_{fi}$. The $\sigma\lambda\mu$ transition probability $T_{fi}^{\sigma\lambda\mu}$ describes the decay mediated by one of the multipole terms $\lambda\mu$ of the electromagnetic field and is either of electric ($\sigma=E$) or magnetic ($\sigma=M$) nature. Through the “golden rule” of time-dependent perturbation theory, we obtain the transition probability

$$T_{fi}^{\sigma\lambda\mu} = \frac{2}{\epsilon_0 \hbar} \frac{\lambda+1}{\lambda((2\lambda+1)!!)^2} \left(\frac{E_\gamma}{\hbar c} \right)^{2\lambda+1} \left| \langle \psi_f; J_f M_f | (\hat{\mathcal{M}}_\sigma)_\mu^\lambda | \psi_i; J_i M_i \rangle \right|^2, \quad (6.9.14)$$

where E_γ is the energy of the photon and $(\hat{\mathcal{M}}_\sigma)_\mu^\lambda$ denotes the electric or magnetic multipole field operator, i.e.,

$$(\hat{\mathcal{M}}_E)_\mu^\lambda \equiv \hat{Q}_\mu^\lambda, \quad (\hat{\mathcal{M}}_M)_\mu^\lambda \equiv \hat{M}_\mu^\lambda. \quad (6.9.15)$$

As magnetic substates are not observed experimentally, we may average over the initial substates M_i and sum over the final substates M_f and all projections μ of the operator which yields the transition probability

$$T_{fi}^{\sigma\lambda} = \frac{1}{2J_i+1} \sum_{M_i} \sum_{M_f \mu} T_{fi}^{\sigma\lambda\mu} \quad (6.9.16)$$

$$= \frac{2}{\epsilon_0 \hbar} \frac{\lambda+1}{\lambda((2\lambda+1)!!)^2} \left(\frac{E_\gamma}{\hbar c} \right)^{2\lambda+1} B(\sigma\lambda; \psi_i \rightarrow \psi_f), \quad (6.9.17)$$

⁵These expressions are derived by employing the long-wavelength approximation, i.e., the wavelength of the photon is assumed to be large compared to the extension of the nucleus.

where we have introduced the *reduced* transition probability

$$B(\sigma\lambda; \psi_i \rightarrow \psi_f) \equiv \frac{1}{2J_i + 1} \left| \langle \psi_f; J_f M_f | (\hat{\mathcal{M}}_\sigma)^\lambda | \psi_i; J_i M_i \rangle \right|^2. \quad (6.9.18)$$

Note that there are no $M0$ transitions since the magnetic multipole operator vanishes in this case, which is the result of the fundamental absence of magnetic monopoles in nature.

Selection Rules. Classifying electromagnetic transitions according to their multipoles is achieved by inspecting the general structure of the electric and magnetic multipole operators for each particle. Under parity the involved terms exhibit the behavior

$$r^\lambda \rightarrow r^\lambda, \quad Y_\mu^\lambda \rightarrow (-1)^\lambda Y_\mu^\lambda, \quad \hat{\mathbf{l}} \rightarrow \hat{\mathbf{l}}, \quad \hat{\mathbf{s}} \rightarrow \hat{\mathbf{s}}, \quad \nabla \rightarrow -\nabla. \quad (6.9.19)$$

Hence, we obtain

$$\hat{Q}_\mu^\lambda \rightarrow (-1)^\lambda \hat{Q}_\mu^\lambda, \quad \hat{M}_\mu^\lambda \rightarrow (-1)^{\lambda+1} \hat{M}_\mu^\lambda. \quad (6.9.20)$$

Consequently, we obtain the *parity* conservation selection rule for the parities of the initial and final state π_i and π_f , respectively,

$$\pi_i \pi_f \stackrel{!}{=} \begin{cases} (-1)^\lambda & \text{for } E\lambda \\ (-1)^{\lambda+1} & \text{for } M\lambda \end{cases}. \quad (6.9.21)$$

Furthermore, there is the *angular momentum* selection rule which states that for a transition associated with a multipole operator of rank λ from an initial state to a final state with angular momenta J_i and J_f , respectively, the triangular condition $\Delta(J_f \lambda J_i)$ has to be fulfilled. Note that the transition probabilities decrease significantly with increasing rank λ of the involved operator. Therefore, the transition with the greatest probability is the one with the lowest multipolarity which is allowed by the parity and angular momentum selection rules.

Multipole Moments. The general form of multipole moments can be written as

$$\mathcal{M}(\sigma\lambda) \equiv \langle \Psi; J_\Psi M_{J_\Psi} = 0 | (\hat{\mathcal{M}}_\sigma)_0^\lambda | \Psi; J_\Psi M_{J_\Psi} = 0 \rangle \quad (6.9.22)$$

$$= \begin{pmatrix} J & \lambda & J \\ -J & 0 & J \end{pmatrix} \langle \Psi; J_\Psi | (\hat{\mathcal{M}}_\sigma)^\lambda | \Psi; J_\Psi \rangle. \quad (6.9.23)$$

The magnetic dipole moment μ and electric quadrupole moment Q are now defined such that they coincide with their classical analogues which yields

$$\frac{\mu}{c} = \sqrt{\frac{4\pi}{3}} \mathcal{M}(M1) = \sqrt{\frac{4\pi}{3}} \sqrt{\frac{J}{(J+1)(2J+1)}} \langle \Psi; J_\Psi | \hat{M}^1 | \Psi; J_\Psi \rangle, \quad (6.9.24)$$

$$eQ = \sqrt{\frac{16\pi}{5}} \mathcal{M}(E2) = \sqrt{\frac{16\pi}{5}} \sqrt{\frac{J(2J-1)}{(J+1)(2J+1)(2J+3)}} \langle \Psi; J_\Psi | \hat{Q}^2 | \Psi; J_\Psi \rangle, \quad (6.9.25)$$

where we inserted analytical expressions for the corresponding 3j symbols. It becomes evident from the properties of the 3j symbol that a necessary condition for non-vanishing $M1$ and $E2$ moments is $J \geq \frac{1}{2}$ and $J \geq 1$, respectively.

6.10. Evolution of Observables—Applications

Now that we have discussed the theoretical foundation of the, for this work, most relevant observables, let us incorporate them into the IM-NCSM framework and compare the results to those of the NCSM and experiment. Note that this section mainly focuses on investigating methodological developments of the IM-NCSM. Especially comparisons with NCSM are—due to its exact nature—very useful for assessing the methodological uncertainties of the IM-NCSM. When comparing results obtained from the IM-NCSM with experimental values, however, it should always be kept in mind that the interaction we are employing throughout this chapter has a deficiency when it comes to the reproduction of particular observables like, e.g., radii [Bin+14; Her+13b; Her+14; Bin+13a]. This deficiency is well-known and one of the motivations for the construction and application of new generations of chiral interactions (see next chapter).

Carbon-12. Let us begin with a study of ^{12}C . Figure 6.20 depicts the evolution of various observables including the charge radius R_{ch} , electric and magnetic transitions $B(E2)$ and $B(M1)$, respectively, and the electric quadrupole moment Q . Similarly to the well-known behavior of ground and excited-state energies, also these new observables are changing throughout the IM-SRG evolution until, for large values of the flow parameter s , they stabilize. Considering the N_{max} convergence, however, things become slightly more complicated: Unlike the eigenstates of the Hamiltonian, other observables like, e.g., radii and electromagnetic transitions are not bound by the variational principle. This leads to a non-monotonic N_{max} convergence, making it difficult to obtain a reliable estimate for the observable with regard to $N_{\text{max}} \rightarrow \infty$. This observation is closely related to the fact that some observables are corresponding to operator structures that probe a different part of the wave function than the Hamiltonian. This becomes evident when considering the radius and the quadrupole operator: Both probe the *long-range* part of the wave function which manifests itself through a high sensitivity to higher- N_{max} contributions. These small contributions of higher- N_{max} basis states to the eigenstates obtained from the IM-NCSM arise due to residual couplings of the reference state $|\psi_{\text{ref}}\rangle$ to some of its particle-hole excitations i.e., a partially incomplete decoupling.

Through fig. 6.21 we are able to inspect the N_{max} convergence and the $N_{\text{max}}^{\text{ref}}$ dependence of numerical results obtained from the IM-NCSM and compare to results obtained from the NCSM and with experimental values. Compared to the NCSM, the ground-state energy obtained from the IM-NCSM is slightly overbound. Furthermore, the ground-state energy exhibits an $N_{\text{max}}^{\text{ref}}$ dependence that is slightly more pronounced than for oxygen isotopes and for all $N_{\text{max}}^{\text{ref}}$ the energies are converged w.r.t. N_{max} . The excitation energy of the first 2^+ state obtained from the IM-NCSM is above the corresponding NCSM energy by about 1 MeV, but differs only slightly from the experimental value. The experimentally observed 0_2^+ state—known as the Hoyle state—lying at about 7.7 MeV is not adequately described by the IM-NCSM, where it lies much too high at about 15 MeV, i.e., beyond the limits of our plot.⁶ For the charge radius

⁶The theoretical description of this state through shell-model-like approaches is a long-standing problem, which is eventually due to the fact that this state may be associated with an α cluster.

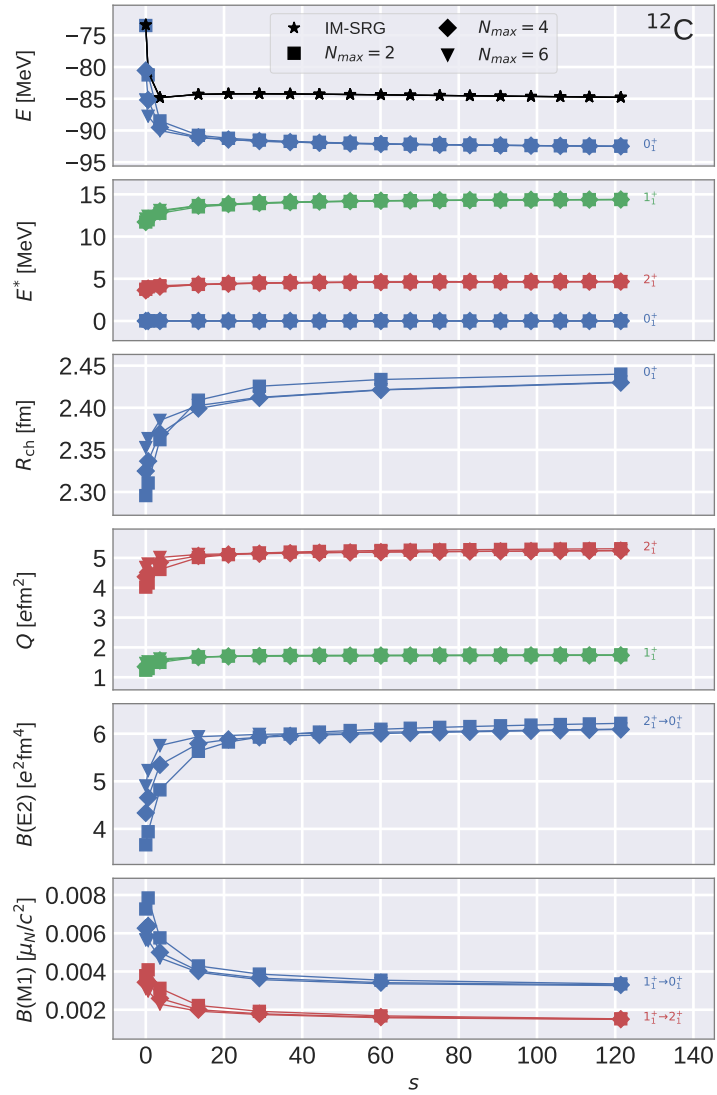


Figure 6.20.: Evolution of the ground-state energy, the lowest-lying excitation energies, the charge radius, the quadrupole moment, the $B(E2)$ transition, and the $B(M1)$ transition for ^{12}C . IM-NCSM calculations have been performed at $N_{\text{max}}^{\text{ref}} = 2$.

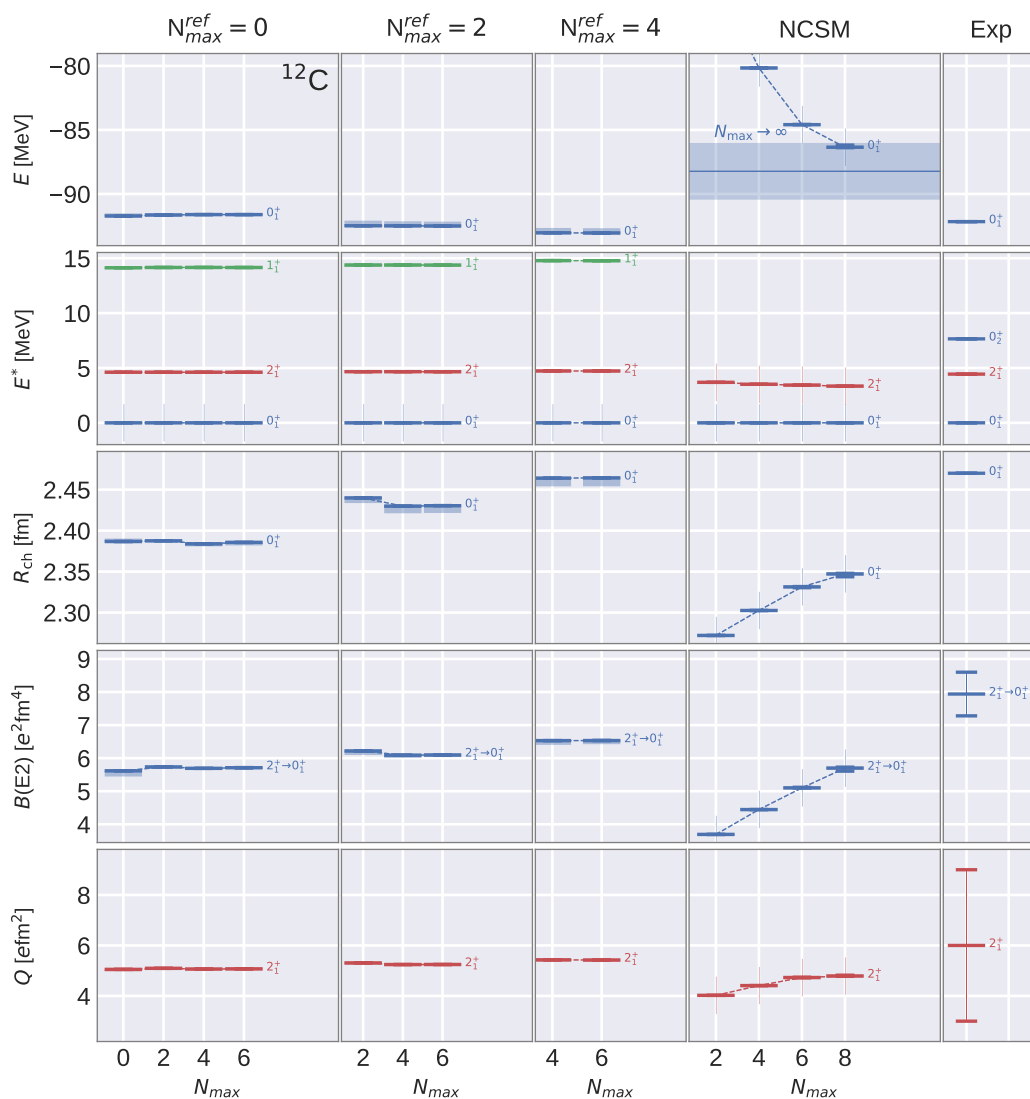


Figure 6.21.: Depiction of the N_{\max} convergence of various observables for ^{12}C employing the IM-NCSM at $N_{\max}^{\text{ref}} = 0$ to 4. Additionally, results obtained from the NCSM and experimental values are shown. For details on experimental data see appendix C.

we observe that the results are increasing w.r.t. N_{\max}^{ref} , which is a somewhat counterintuitive behavior as the ground-state energy is decreasing w.r.t. N_{\max}^{ref} and hints at the effects of correlations. For each N_{\max}^{ref} , however, the charge radii are practically converged w.r.t. N_{\max} . The radius obtained at $N_{\max}^{\text{ref}} = 4$ is compatible with the experimentally observed value, while the radius obtained from the NCSM is slowly increasing with N_{\max} and even at $N_{\max} = 8$, i.e., the largest N_{\max} available here, the radius is not fully converged. The $B(E2; 2_1^+ \rightarrow 0_1^+)$ transition shows an N_{\max}^{ref} dependency that is very similar to the radius. Likewise, also the NCSM exhibits a very similar behavior w.r.t. N_{\max} : The $B(E2)$ transition shows no clear sign of convergence and is still increasing at $N_{\max} = 8$. However, the result obtained from the IM-NCSM at $N_{\max}^{\text{ref}} = 4$ is compatible with the NCSM result. Additionally, the $B(E2; 2_1^+ \rightarrow 0_1^+)$ transition strength obtained from the IM-NCSM is within reach of the experimentally observed value. The quadrupole moments of the first 2^+ state obtained from the IM-NCSM, NCSM and experiment are in agreement.

In summary, this study for ^{12}C serves as a prime example for the advantages of the IM-NCSM and demonstrates its capabilities: We obtain converged results at very small N_{\max} , which are consistent with NCSM calculations, even though the NCSM calculations require much higher N_{\max} for getting close to convergence.

Oxygen-20. However, we found that specific nuclei show large discrepancies between theoretically predicted and experimentally measured electromagnetic observables. As we made the observation that usually nuclei with closed proton shells seem to be affected here, let us consider ^{20}O in the following. Figure 6.22 shows the evolution of various observables including radii, quadrupole moments, the $B(E2)$, and the $B(M1)$ transition. Figure 6.23 depicts the N_{\max} convergence and N_{\max}^{ref} dependence of IM-NCSM calculations as well as NCSM results and experimental values.

Figure 6.22 demonstrates that all observables shown are stabilizing w.r.t. to the flow parameter. By comparing the N_{\max} convergence of the ground and excited states in fig. 6.23 with the N_{\max} convergence of the $B(E2; 2^+ \rightarrow 0^+)$ transition, differences are evident: While the energies of the 2^+ and 0^+ states are practically converged, there is still a dependence on N_{\max} of the corresponding $B(E2; 2^+ \rightarrow 0^+)$ transition, where a similar pattern emerges for the quadrupole moment $Q(2^+)$.

Figure 6.24 further illustrates this observation: There are small residual contributions of $|\phi_i^{N=4}\rangle$ NCSM basis states to the eigenstate $|\psi_{\text{g.s.}}^{N_{\max}=2}\rangle$ for an $N_{\max}^{\text{ref}} = 2$ calculation. Those contribution seem to be irrelevant for the eigenvalues of the Hamiltonian, but have an impact on other observables probing the long-range properties of eigenstates. For the charge radius R_{ch} , the $B(E2)$ transition, and the quadrupole moment Q there is a slight N_{\max}^{ref} dependency which, however, seems to saturate such that the difference between $N_{\max}^{\text{ref}} = 2$ and $N_{\max}^{\text{ref}} = 4$ is only marginal. The charge radius and electromagnetic transition obtained from the IM-NCSM for the largest N_{\max}^{ref} lie above the corresponding values from the NCSM and the quadrupole moment lies below such that the IM-NCSM results are compatible with estimated extrapolated NCSM results—assuming that the trend with regard to N_{\max} is maintained.

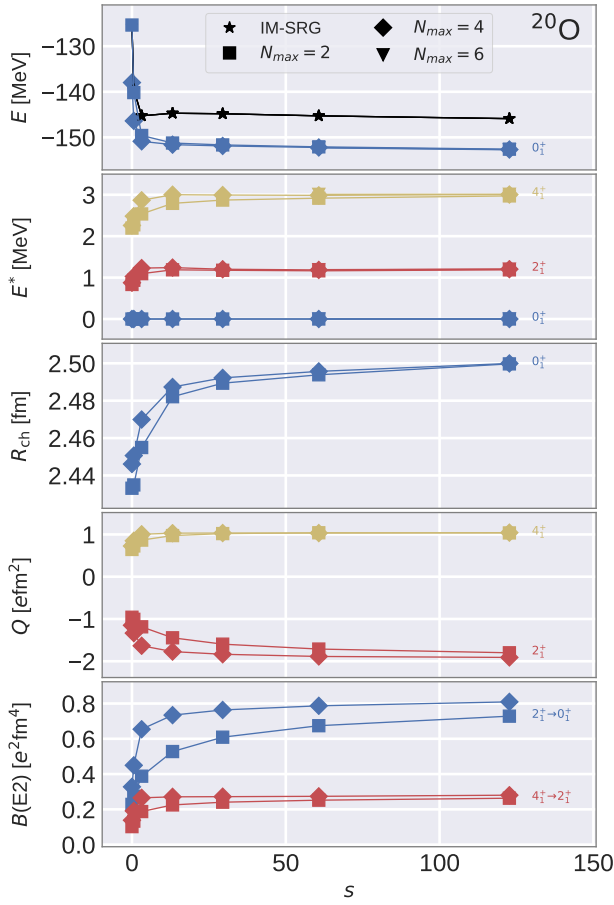


Figure 6.22.: Depiction of the evolution of the ground-state energy, the excitation energies of the lowest-lying states, the charge radius, the quadrupole moment, and the $B(E2)$ transition. IM-NCSM calculations have been performed for ^{20}O and at $N_{\text{max}}^{\text{ref}} = 2$.

All things considered, the results obtained from the IM-NCSM are compatible with those from the NCSM even though the NCSM results are not yet converged at the largest N_{max} available and there may still be some changes at even larger N_{max} . There is, however, a striking disagreement between the theoretically predicted transition $B(E2; 2^+ \rightarrow 0^+)$ and the experimentally measured one: The experimentally measured $B(E2; 2^+ \rightarrow 0^+)$ transition amounts to $5.6(4) e^2\text{fm}^4$, which lies beyond the range of our figure. Therefore, the theoretical and experimental value are differing from each other by about a factor of 5.

We would like to remark that the observation that there is still a sizeable dependence of electromagnetic $B(E2)$ on $N_{\text{max}}^{\text{ref}}$ and N_{max} raises questions about the adequateness of valence-space shell model calculations employing single-shell effective valence-space interactions derived from the IM-SRG [Par+17]—since such shell model calculations are largely equivalent to $N_{\text{max}}^{\text{ref}} = N_{\text{max}} = 0$.

Further Examples. The calculations for ^6He in fig. 6.25 show that there is a sizable depen-

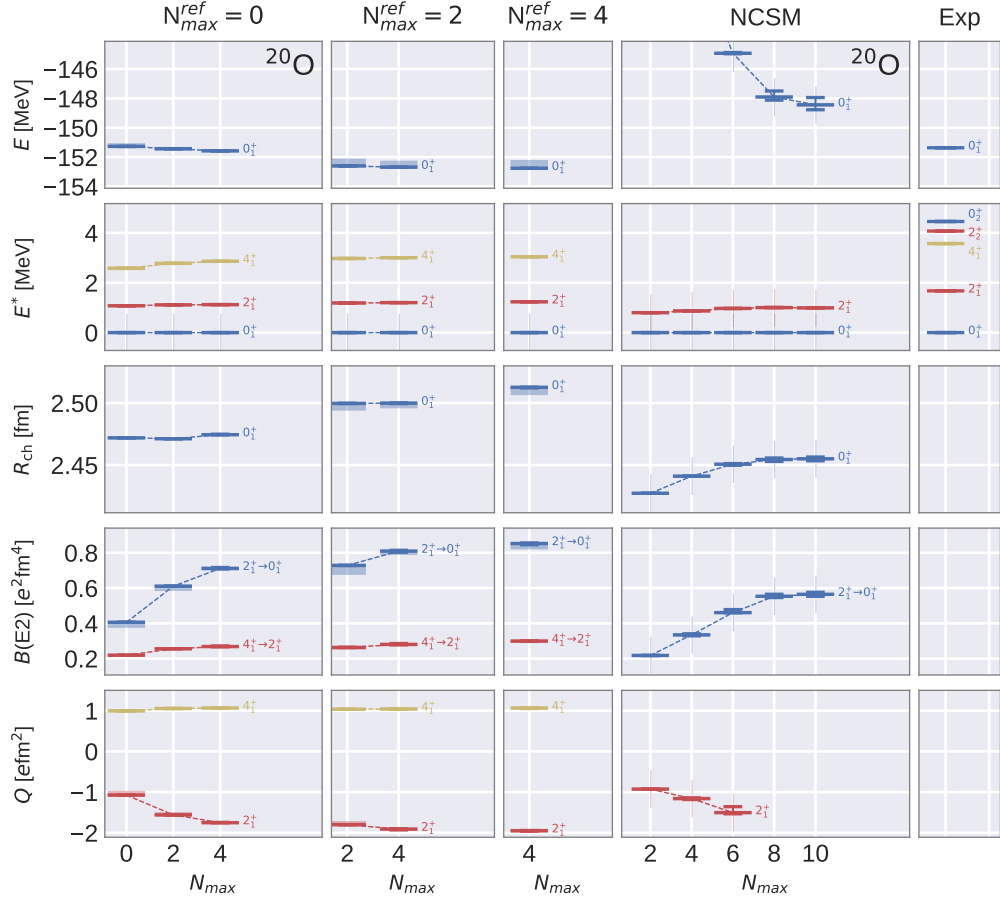


Figure 6.23.: Depiction of the N_{\max} convergence of various observables for ^{20}O employing the IM-NCSM at $N_{\max}^{\text{ref}} = 0, 2$ and 4 and the NCSM. Additionally, associated experimental values are shown. The experimental transition $B(E2; 2^+ \rightarrow 0^+) = 5.6(4) e^2\text{fm}^4$ is too high for showing it within the plot and still being able to inspect the N_{\max} behavior and perform a comparison of IM-NCSM and NCSM calculations. For details on experimental data see appendix C.

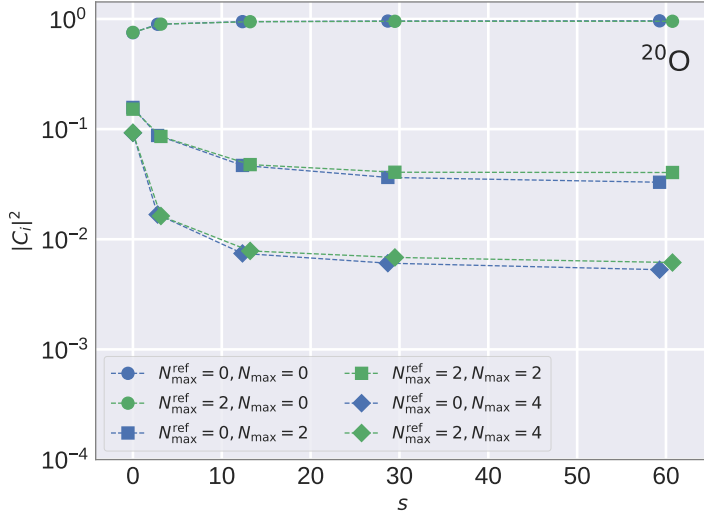


Figure 6.24.: Expressing the ground-state from an N_{\max}^{ref} model space as a superposition of NCSM basis states $|\phi_i^N\rangle$ where each basis state is associated with a coefficient c_i , this figure depicts $\sum_i |c_i^N|^2$ for $N = 0, 2$ and 4 and $N_{\max}^{\text{ref}} = 0$ and 2 .

dence on N_{\max}^{ref} . This may be rooted in the fact that ${}^6\text{He}$ is a halo nucleus and, as a consequence, larger N_{\max} are necessary such that the reference state captures the structure of the ground state. Furthermore, the experimental ground-state energy is underestimated by about 1 MeV, however, this behavior is commonly known within the context of shell-model-like approaches and hints at the relevance of neglected continuum degrees of freedom [Qua+18; NO03]. Taking excitation energies into account, we observe that the first 2^+ lies slightly too high, and that we predict the second excitation to be a 2^+ state. The $B(E2; 2^+ \rightarrow 0^+)$ transition obtained from the IM-NCSM lies, compared to the experimental value, much too low by about a factor of 10—where the neglected continuum might again play a dominant role here.

The calculations for ${}^{22}\text{O}$ in fig. 6.26 show that also here the IM-NCSM is largely consistent with the NCSM and properly predicts the experimental ground-state energy and the excitation energies of the first lowest-lying states. The $B(E2; 2^+ \rightarrow 0^+)$ transitions from the IM-NCSM and the NCSM are in agreement with each other, however, we observe a large difference with regard to the experimental value—similarly to ${}^{20}\text{O}$. In contrast to ${}^{20}\text{O}$, there is a low lying 3^+ state in the spectrum of ${}^{22}\text{O}$ which allows us to calculate the $B(M1; 3^+ \rightarrow 2^+)$ transition. The IM-NCSM and the NCSM differ from each other by about 20 %, however, the NCSM is still not converged at $N_{\max} = 8$.

Figure 6.26 depicts IM-NCSM calculations at $N_{\max}^{\text{ref}} = 0$ and 2 and experimental values for ${}^{22}\text{Ne}$, i.e., besides the previous study of ${}^{12}\text{C}$, another fully open-shell nucleus. The ground-state energy and excitation energies obtained from the IM-NCSM show a slight but negligible N_{\max}^{ref} dependence, are well converged w.r.t. N_{\max} , and are in good agreement with experimental values. The experimental radius, however, is underestimated by about 0.3 fm. The $B(E2; 2^+ \rightarrow 0^+)$ transition from the IM-NCSM underestimates the experimental value by about a factor of 2—which is much less pronounced than for ${}^{20}\text{O}$. Similarly to the $B(E2; 2^+ \rightarrow 0^+)$ transition, the

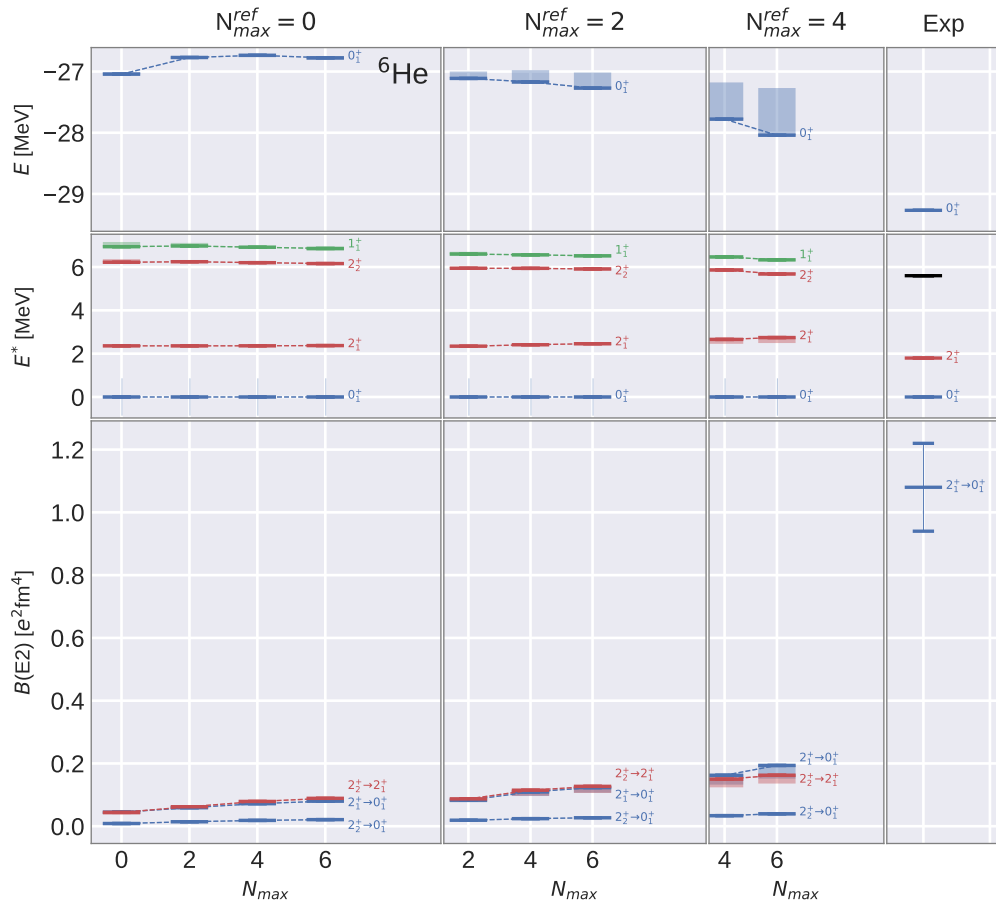


Figure 6.25.: Depiction of IM-NCSM calculations at $N_{\max}^{\text{ref}} = 0$ to 4 and experimental values for ${}^6\text{He}$. For details on experimental data see appendix C.

absolute value of the (negative) quadrupole moment is underestimated by about a factor of 2. Taking the underestimated radius and dependence of the quadrupole operator on the radius operator into account, it can be argued that the discrepancy observed here is an interaction issue.

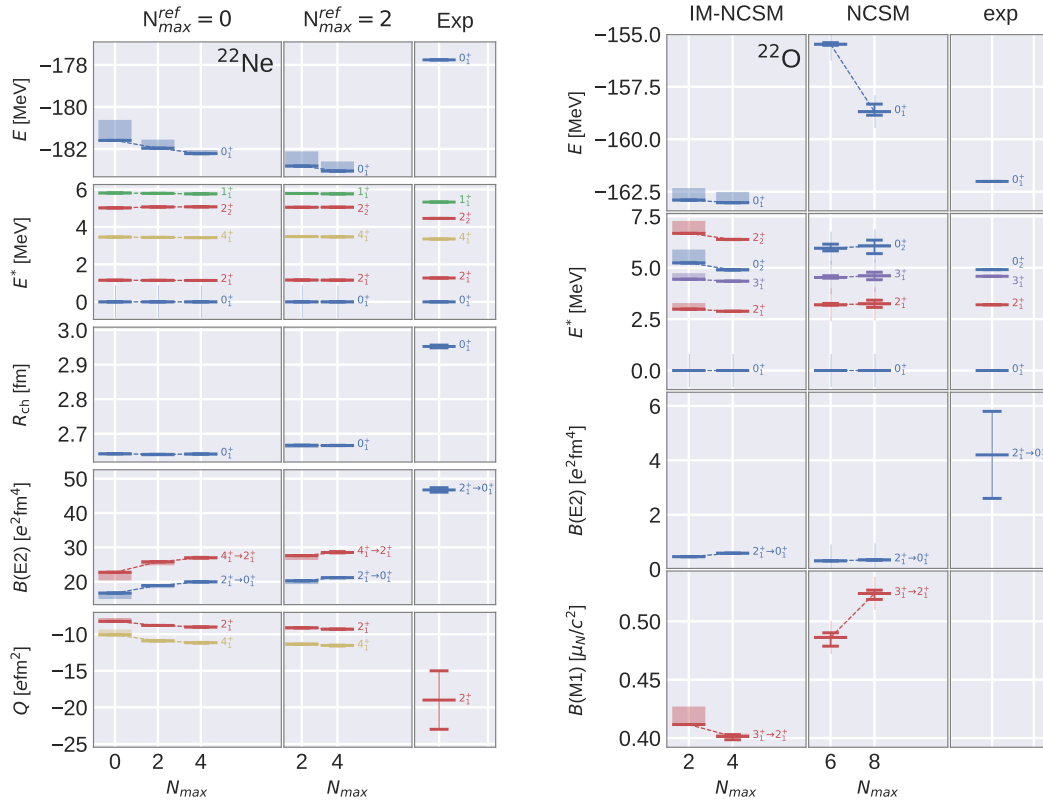


Figure 6.26.: Left: IM-NCSM calculations at $N_{\max}^{\text{ref}} = 0$ and 2 and experimental values for ^{22}Ne . Right: IM-NCSM calculations at $N_{\max}^{\text{ref}} = 2$, NCSM calculations, and experimental values for ^{22}O . For details on experimental data see appendix C.

Interpretation & Conclusion. Being concerned with electromagnetic observables and having now studied their theoretical prediction for several different nuclei, there seems to be a specific pattern emerging: While calculations for fully open-shell nuclei like ^{12}C and ^{22}Ne are already close to experimental values or at least close enough such that deficiencies of the interaction might explain the observed discrepancies, calculations for nuclei with a closed proton shell, i.e., ^{20}O , ^{22}O , and ^6He are giving $B(E2)$ transition strengths that are much too small with regard to their corresponding experimental ones.⁷

At the moment, the main source for these discrepancies is not entirely clear and several sources may be possible:

1. the interaction employed here may not adequately describe electromagnetic transition;

⁷Regarding the halo nucleus ^6He , also the continuum might play a special role.

2. free-space SRG induced electromagnetic operators of higher-particle rank may become of importance;
3. errors due to intrinsic truncations of our many-body methods become sizeably large .

The first issue will be further addressed in chapter 7 by employing new generations of chiral interactions. Nevertheless, we would like to remark that an increase of the $B(E2)$ by a factor of 5, as it would be necessary for ^{20}O , through the employment of another interaction is unlikely—an expectation that is confirmed by the studies of the following chapter.

Considering the second possible source, we have found that free-space SRG induced operators for these kind of observables are of minor importance [Sch+14; Sch+15]. This is also consistent with the naïve picture that the free-space SRG removes the “hard-core”, i.e., acts on the short-range part while preserving the physics of the long-range part of the wavefunction. The underlying operator \hat{Q}^2 of the $B(E2)$ transition exhibits a long-range character such that we may not expect a significant impact of the free-space SRG. However, we would like to note that this simple picture for assessing the effects of the free-space SRG on the \hat{Q}^2 operator may oversimplify things too much, as this operator also consists of tensor components the free-space SRG may have a sizeable impact after all.

Lastly, there is the possibility that the IM-SRG evolution of the \hat{Q}^2 operator induces a substantial amount of three or higher-body operators. As we are consistently truncating all our operators at the NO2B level throughout the evolution, these induced contributions are neglected which—assuming that these induced contributions are of major importance—could explain the large discrepancies with regard to experimental values. However, even if the transformation of electromagnetic observables is suffering from a massive amount of induced interaction whose inclusion would bring us closer to the experiment, there is still the question why the results obtained from the NCSM are also differing that much from the experiment even for relatively large values for N_{max} . Put differently, the possible explanation that the IM-SRG induces a substantial amount of three or higher-body parts goes hand in hand with the fact that, even at relatively high N_{max} , the eigenstates obtained from a regular NCSM calculation are not adequately describing electromagnetic observables.

6.10.1. Hierarchy Inversion

Similarly to other observables like, e.g., the Hamiltonian, also the non-scalar operators associated with electromagnetic observables are truncated at the NO2B level. An important question that always has to be kept in mind is to which extent the IM-SRG induces contributions beyond the NO2B level. It is the NO2B approximation which separates the IM-NCSM from an exact treatment—which would have to be carried out in A -body space—and, therefore, the amount of induced contributions directly governs the uncertainty of the calculated observables.

In the context of the transformation of electromagnetic observables, the corresponding untransformed, i.e., initial operators $\hat{X}_M^L(0)$ are usually consisting of a one-body part only.⁸ The IM-SRG transforms this initial one-body operator such that for $s > 0$ we naturally obtain a non-zero two-body contribution together with a transformed one-body part. The interrelation between the one and two-body and the manner in which they are feeding into each other during the solution of the operator differential equation for $\hat{X}_M^L(s)$ is highly non-trivial as can be seen by inspecting the commutator evaluation equations (see chapter 5). For examining the relative contribution of the transformed one-body and two-body operators to a specific observable of interest, we calculate these observables in two different ways. On the one hand, we applied the regular approach: Starting from an initial one-body operator, we obtain a transformed one and two-body part from the IM-SRG, which is then passed on to the subsequent NCSM calculation. On the other hand, only the transformed one-body part is taken into account for the subsequent NCSM calculation while the transformed two-body part is neglected. Comparing both results, we are able to assess the impact of the transformed two-body part on observables.

Oxygen-20. Figure 6.27 shows this analysis for the $B(E2; 2^+ \rightarrow 0^+)$ transition and the quadrupole moment $Q(2^+)$ in ^{20}O . Regarding the $B(E2)$ transitions an unsettling observation can be made: The contribution of the one-body part to the $B(E2)$ transition is completely removed and entirely shifted into the induced two-body part—a behavior that we are referring to as *hierarchy inversion*. As the complete operator structure is shifting from the one-body to the two-body part this hierarchy inversion raises the question about the importance of induced but neglected three-body terms. Furthermore, it might explain the rather significant discrepancies of the $B(E2)$ transition obtained from the IM-NCSM with experimental values. At this point one might wonder why the relative contribution of the transformed one-body of the $B(E2)$ transition is suppressed to such an extent. The answer to this question is simple: Throughout the IM-SRG evolution the Hamiltonian is transformed such that its eigenstates are forced into an “ N_{\max}^{ref} -sized box”, i.e., in a basis consisting of NCSM basis states the eigenstates are purely built from basis states contained within $\{|\phi_i^N\rangle \mid N \leq N_{\max}^{\text{ref}}\}$. Due to a deficiency of the IM-SRG generator each eigenstate is, in fact, only consisting of basis states $\{|\phi_i^N\rangle\}$ with one specific N with $N \leq N_{\max}^{\text{ref}}$. However, usually the eigenstates are transformed such that they end up being contained within the $N_{\max} = 0$ space which is also illustrated by fig. 6.24. The one-body part of \hat{Q}^2 , however, is only sensitive to protons⁹ and, therefore, only “sees” the closed proton shells of the $N_{\max} = 0$ eigenstates of ^{20}O based on which it may not contribute anything to the $B(E2)$ anymore. As the observable $B(E2; 2^+ \rightarrow 0^+)$ is supposed to be invariant under the unitary transformation imposed by the IM-SRG, the entire physics has to be shifted into the two-body part of \hat{Q}^2 . This may also be illustrated as follows: Initially, the $B(E2)$ transition obtains its value through eigenstates, which consists of NCSM basis states up to large N_{\max} . The IM-SRG, however, transforms the Hamiltonian such that its eigenstates are

⁸Throughout this consideration we neglect the two-body part induced by the free-space SRG as well as the two-body part arising due to a center-of-mass subtraction.

⁹The transformed one-body part may contain *induced* neutron-neutron matrix elements, however, these are numerically not observed.

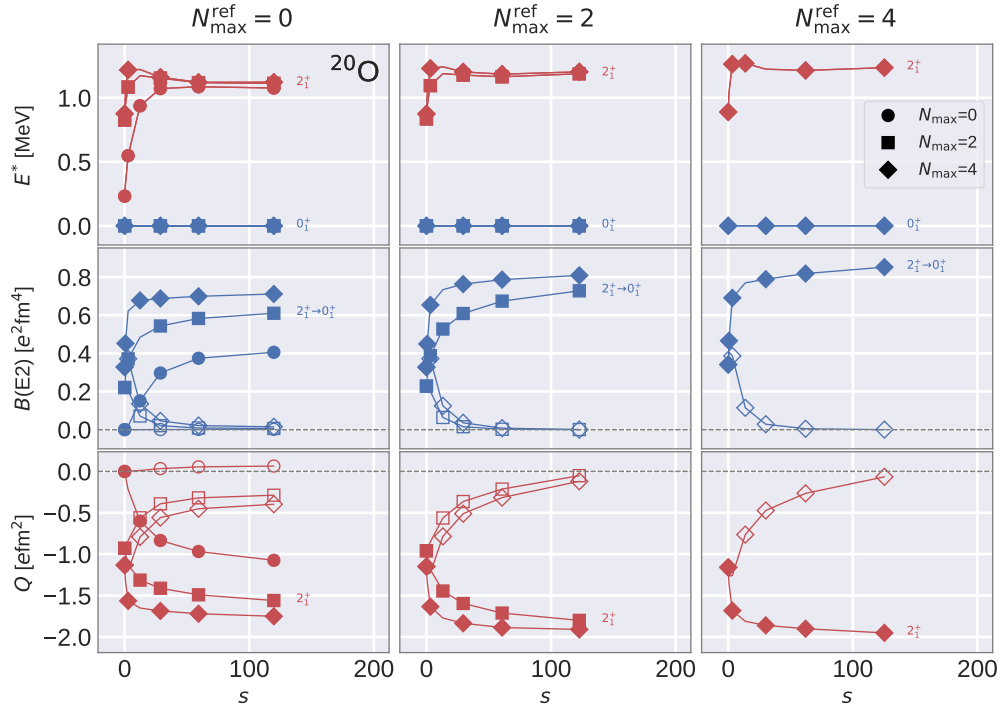


Figure 6.27.: Starting with an initial quadrupole operator \hat{Q}^2 consisting only of a one-body part, the IM-SRG evolution of this operator produces an evolved one and two-body part. This figure depicts the transition $B(E2; 2^+ \rightarrow 2^+)$ and the quadrupole moment $Q(2^+)$ we obtain from an IM-NCSM calculation when only the evolved one-body part (open symbols) or both the evolved one *and* two-body (solid symbols) are taken into account within the final NCSM calculation. In both cases, however, the one and two-body part are kept throughout the MR-IM-SRG evolution. The calculations shown here were performed for ^{20}O at $N_{\max}^{\text{ref}} = 0$ to 4.

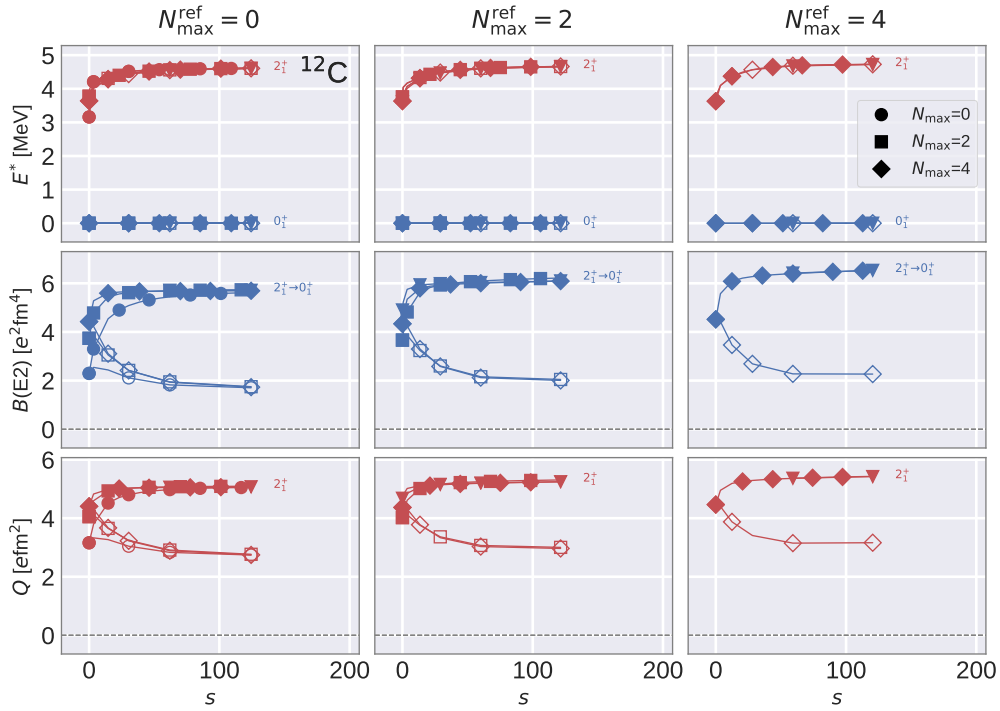


Figure 6.28.: Similarly to fig. 6.27, this figure shows calculations for ^{12}C .

built up from basis states with $N_{\max} = 0$ only and—as the observable has to be invariant—the transformation of the operator $\hat{Q}_M^L(0)$ is seeking to conserve the transition matrix element

$$\langle \psi(0) | \hat{Q}_M^L(0) | \psi'(0) \rangle \xrightarrow{\hat{U}} \langle \psi(s) | \hat{Q}_M^L(s) | \psi'(s) \rangle. \quad (6.10.1)$$

However, this is only possible through inducing two-body operators—or even higher particle ranks—acting in an $N_{\max} = 0$ space.

Carbon-12. Figure 6.28 is similar to fig. 6.27 only that it shows a study for ^{12}C . Obviously, we have a reduction of the importance of the one-body part, i.e., a partial shift of contributions into the induced two-body part, but this shift is much less pronounced than for ^{20}O . The contribution of the one-body part is not vanishing throughout the evolution but stabilizes at a value that corresponds to about half of its initial contribution at $s = 0$.

At first glance, this might seem surprising especially when compared to ^{20}O , but can be explained by considering the structure of the $N_{\max} = 0$ space for ^{12}C : Looking only at protons, it consists of all basis states in which 2 protons are filling up the $1s$ shell and 4 protons are partially occupying the $1p$ shell, i.e., the $1p$ shell is open in this case. As the $1p$ shell itself consists of $1p_{1/2}$ and $1p_{3/2}$ single-particle states the contribution of the one-body part is not

forced to be zero even for eigenstates that purely live within the $N_{\max} = 0$ space. The same picture applies for the quadrupole moment: The relative contribution of the one-body part is approximately halved but not completely removed as it is the case for ^{20}O .

6.10.2. Observables and Particle-Attached/Particle-Removed

The calculation of observables within the context of the IM-NCSM may also be combined with particle-attached/particle-removed extension.

Figure 6.29 depicts the fully open-shell nucleus ^{21}F . While energetic observables are only differing slightly from experimental values, the $B(E2; 5/2^+ \rightarrow 1/2^+)$ obtained from the IM-NCSM is about a factor of 2 too low. The magnetic dipole moment μ of the $5/2^+$ state, however, differs only slightly from the experimental value.

Figure 6.30 shows IM-NCSM calculations and experimental values for ^{19}O and ^{21}O . The calculations for ^{19}O show that the ground-state energy is overestimated by about 2 MeV and the two lowest-lying nearly degenerate $3/2^+$ and $5/2^+$ states are reversed compared to experiment. Surprisingly, the $B(E2; 1/2^+ \rightarrow 5/2^+)$ transition is much closer to experiment compared to ^{20}O , however, they are still differing by about a factor of 2. The $B(M1; 5/2^+ \rightarrow 3/2^+)$ transition is also in reach of the experimental value, even though it still seems to increase w.r.t. N_{\max} . The theoretically predicted magnetic dipole moment μ for the $3/2^+$ state lies within the experimental error range and also $\mu(5/2^+)$ is close to the experimental value. Compared to ^{19}O , ^{21}O exhibits a very similar behavior: The ground-state energy is slightly overbound, the excited states are compatible with their experimental counterpart—where the second excitation is predicted to be a $3/2^+$ state—and the observed discrepancy for the $B(E2; 1/2^+ \rightarrow 5/2^+)$ transition is by far less pronounced than for ^{20}O .

Why is the situation so much different for ^{19}O and ^{21}O than for ^{20}O and ^{22}O ? It might be the case that the excitations involved in the $B(E2)$ transitions are of a different nature within the even and the odd oxygen isotopes. This different nature is also hinted at by the large gap between the experimental transitions in those even and odd nuclei.

On the one hand, the relevant excitations in ^{20}O and ^{22}O might have larger contributions of highly collective multi-particle multi-hole excitations beyond the N_{\max}^{ref} reference space. Due to different operator structures, these collective contributions might have no substantial impact on energetic observables, but may critically govern the $B(E2)$ transition. If this is true, then it follows that the IM-SRG transformation—which aims to decouple simple two-particle two-hole excitations—is forced to induce operators beyond the NO2B rank and, therefore, relevant physical information that is essential for an adequate description of electromagnetic transitions is cut away. A possible solution for this problem is to choose a larger N_{\max}^{ref} such that correlations due to multi-particle multi-hole excitations are already captured at the level of the reference state. This might also yield an explanation why ^{19}O and ^{21}O do not suffer from the same amount of induced operators and discrepancies w.r.t. experimental values: The

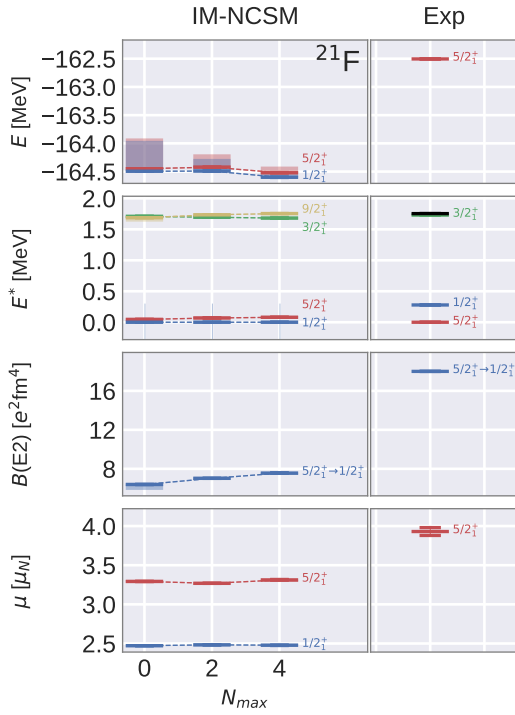


Figure 6.29.: IM-NCSM calculations for ^{21}F performed at $N_{\text{max}}^{\text{ref}} = 0$ and employing ^{22}Ne as parent nucleus. Furthermore, the corresponding experimental values are depicted. For details on experimental data see appendix C.

$N_{\text{max}}^{\text{ref}}$ chosen here might already be sufficient such that the residual correlations are purely associated with simple one-particle one-hole and two-particle two-hole excitations.

However, even if we chose an even larger $N_{\text{max}}^{\text{ref}}$, we are limited by the current implementation of the generator construction and the underlying decoupling pattern. In particular, our current decoupling pattern suffers from a partial decoupling of determinants with different excitation quanta N from each other—even for $N \leq N_{\text{max}}^{\text{ref}}$. As a consequence, the eigenstates are eventually dominated by determinants with a specific number of excitation quanta only—which is usually $N = 0$ —as can be seen in fig. 6.24. Therefore, we have to modify our decoupling pattern such that, e.g., an $N_{\text{max}}^{\text{ref}} = 2$ calculation meets our naïve expectations: A decoupling of $N = 0$ and $N = 2$ determinants from $N > 2$ determinants, but leaving the coupling of $N = 0$ and $N = 2$ determinants with each other intact.

Note that such a modification is part of future developments and is unfortunately not part of this work anymore. However, we would like to note that there are already several ideas how to optimize the decoupling pattern.

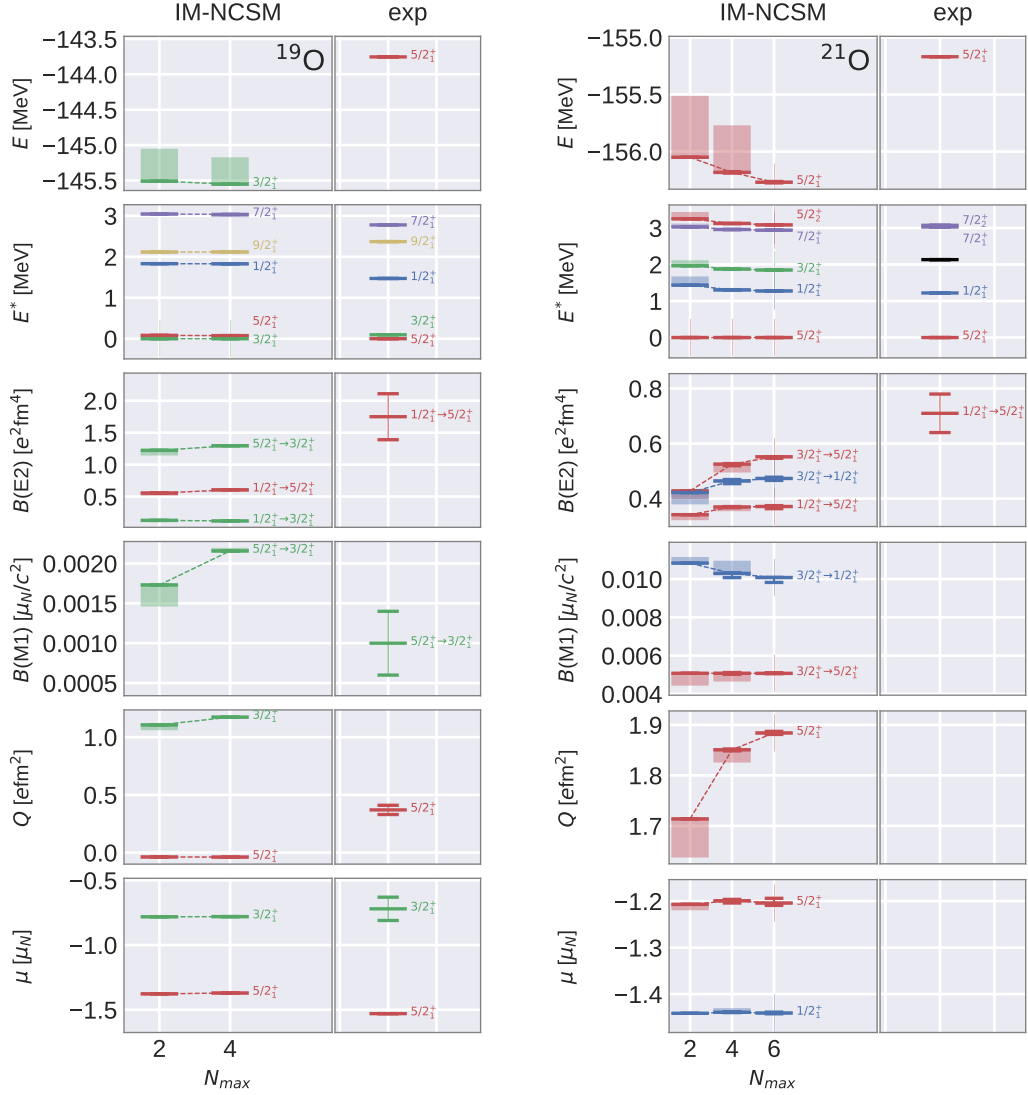


Figure 6.30.: IM-NCSM calculations at $N_{\max}^{\text{ref}} = 2$ and experimental values for ^{19}O (left) and ^{21}O (right), where ^{20}O and ^{22}O were employed as parent nuclei, respectively. For details on experimental data see appendix C.

In-Medium No-Core Shell Model—Applications and Outlook

Throughout the previous chapters we have thoroughly discussed the concept of the IM-NCSM as well as methodical improvements and comparisons with exact methods like the NCSM.

This chapter is mainly focused on applications of the IM-NCSM. We will study various observables in the oxygen and fluorine chain employing the $N^3LO_{EM}+N^2LO_{400,L}$ interaction. However, this interaction exhibits several deficiencies, namely, the underestimation of radii, the overbinding the oxygen chain, and an inconsistency regarding the determination of the low-energy constant c_D in the three-body sector, which has only recently been discovered [GQN19; Mar+18]. As a consequence, we will study the properties and characteristics of new generations of chiral interactions and the impact of some of its parameters on nuclear structure observables—some of which are surprising. Finally, we will employ such a new chiral interaction and explore its properties in the oxygen and neon chain.

7.1. Oxygen and Fluorine Chain

Oxygen Chain. Employing the $N^3LO_{EM}+N^2LO_{400,L}$ interaction at $\alpha = 0.08 \text{ fm}^4$, we study ground-states energies obtained from the IM-NCSM and the NCSM for oxygen isotopes from ^{14}O up to ^{26}O in fig. 7.1. The NCSM calculations have been performed employing either a full or an NO2B-approximated 3N interaction.

By comparing the NCSM calculations employing a full 3N interaction with those employing an NO2B-approximated 3N interaction, it becomes evident that for medium-mass nuclei the NO2B approximation leads to an overbinding of about 1 – 2%, which is consistent with previous findings [GCR16; Rot+12]. As both the IM-NCSM and the NCSM(NO2B) calculations are starting from the same NO2B-approximated initial Hamiltonian, we may assess the error

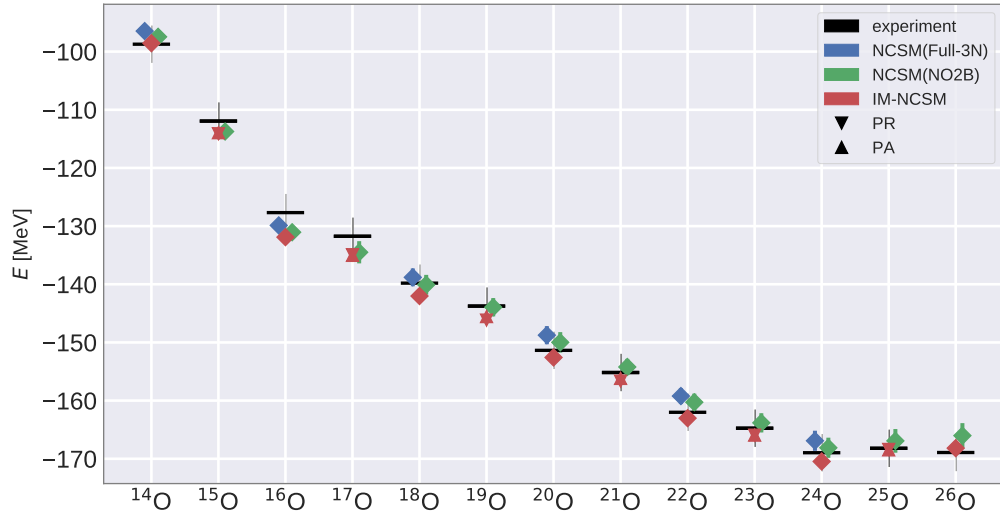


Figure 7.1.: Ground-state energies for oxygen chain isotopes. On the one hand, error bars with regard to NCSM calculations (either with full or NO2B-approximated 3N interactions) indicate $N_{\max} \rightarrow \infty$ extrapolation uncertainties. On the other hand, error bars for IM-NCSM calculations, which were performed at $N_{\max}^{\text{ref}} = 2$, indicate the difference between two subsequent NCSM calculations performed at $N_{\max} = 2, 4$ —which eventually is smaller than the plot marker itself. We employed the $N^3\text{LO}_{\text{EM}} + N^2\text{LO}_{400,\text{L}}$ interaction at $\alpha = 0.08 \text{ fm}^4$. For details on experimental data see appendix C.

introduced by the IM-NCSM, which solely originates from induced many-body pieces beyond the NO2B rank during the IM-SRG evolution. We observe that the IM-NCSM results lie slightly below the NCSM(NO2B) results but still within, or at least very close to, the corresponding error bars. Thus, the IM-NCSM introduces an additional error at the level of approximately 1% for ground-state energies. Furthermore, we can examine the dependence of the PA/PR extension on the parent nucleus for the IM-NCSM results for odd isotopes, where two different plot markers are employed for the specification of the specific parent nucleus. Obviously, this choice has practically no impact for the odd oxygen isotopes shown here. Lastly, we may compare our theoretical results to experimental values, showing that the general trend of the experimental ground-state energies is very well reproduced. Also the position of the neutron drip line is correctly predicted—with ^{24}O being the last stable neutron-rich isotope within the oxygen chain.

Note that fig. 7.1 introduces a new kind of theoretical uncertainty estimation: In these kind of plots, error bars of IM-NCSM calculation solely indicate differences between the largest two N_{\max} spaces. Uncertainties of experimental values, however, are shown as shaded bands.

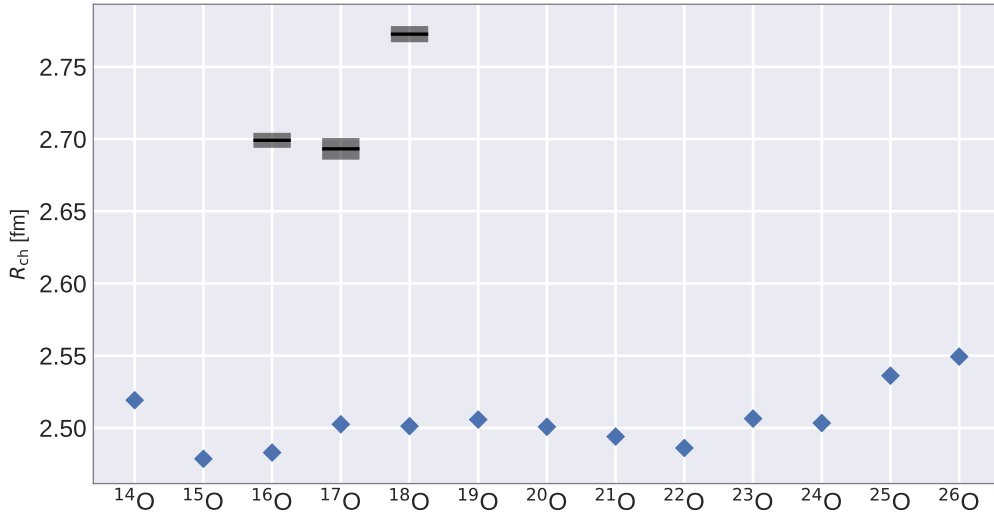


Figure 7.2.: Charge radii for oxygen chain isotopes from the IM-NCSM. Error bars indicate the difference between two subsequent NCSM calculations performed at $N_{\max} = 2, 4$ —which eventually is smaller than the plot marker itself. We employed the $N^3\text{LO}_{\text{EM}} + N^2\text{LO}_{400,\text{L}}$ interaction at $\alpha = 0.08 \text{ fm}^4$. IM-NCSM calculations have been performed at $N_{\max}^{\text{ref}} = 2$. For details on experimental data see appendix C.

Figure 7.2 depicts charge radii obtained from IM-NCSM calculations for oxygen chain isotopes and compares them to experimental values. Evidently, radii are underestimated by about 0.2 fm. Also the experimentally large increase of almost 0.1 fm from ^{17}O to ^{18}O is practically not reproduced. This is a deficiency of the chiral interaction we are employing and is also observed in other many-body methods.

Having discussed scalar ground-state observables of oxygen chain isotopes, let us now consider excitation energies, electromagnetic transitions and moments. Figure 7.3 depicts IM-NCSM calculations for various observables for the oxygen isotopes ^{17}O to ^{22}O and also shows corresponding experimental values.

Considering excitation spectra, the IM-NCSM reproduces the experimentally observed order of states and the excitation energies are mostly in good agreement. The $B(E2)$ transitions for the odd isotopes ^{19}O and ^{21}O lie—compared to the other nuclei shown here—close to the experimental values. However, for all even isotopes and ^{17}O we observe large discrepancies and, as already mentioned, we assume that these differences are rooted in deficiencies of the interaction employed here and the limitations of the IM-NCSM model space. The assumption that the $B(E2)$ transitions for ^{19}O and ^{21}O are, compared to the other nuclei shown here, of different nature is also hinted at by the fact that the absolute values for their transitions is rather small. The quadrupole moments $Q(5/2^+)$ of ^{17}O and $Q(2^+)$ of ^{18}O differ from the experimental

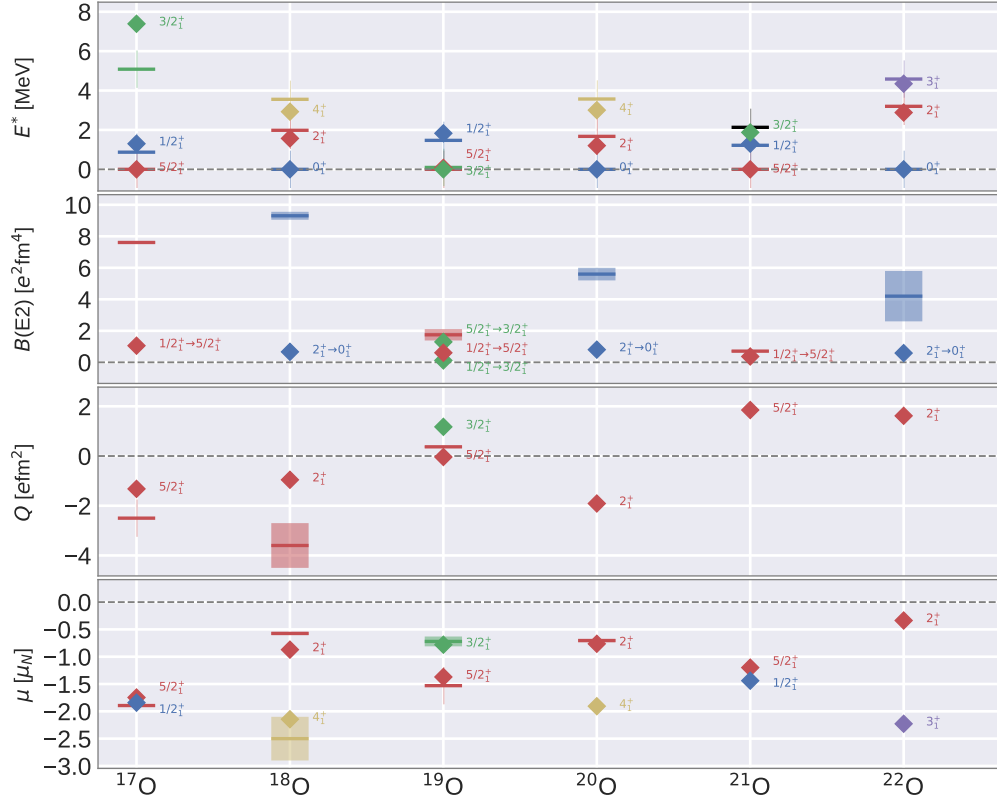


Figure 7.3.: IM-NCSM calculation for oxygen isotopes from ^{17}O to ^{22}O . Calculations were performed at $N_{\text{max}}^{\text{ref}} = 2$ and error bars indicate the difference between $N_{\text{max}} = 4$ and $N_{\text{max}} = 2$. Bars and shaded areas indicate experimental values and errors, respectively. Note that the sign of the dipole moments $\mu(4^+)$ in ^{18}O and $\mu(5/2^+)$ in ^{19}O and of the quadrupole moment $Q(5/2^+)$ in ^{19}O are experimentally unknown and theoretically predicted. We employed the $\text{N}^3\text{LO}_{\text{EM}} + \text{N}^2\text{LO}_{400,\text{L}}$ interaction at $\alpha = 0.08 \text{ fm}^4$. For details on experimental data see appendix C.

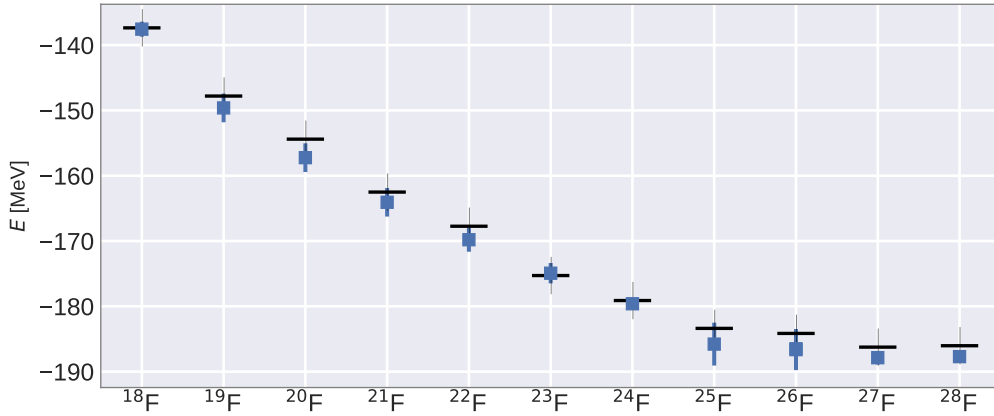


Figure 7.4.: IM-NCSM calculations at $N_{\max}^{\text{ref}} = 0$ and $N_{\max} = 2$ for the ground-state energies of various fluorine chain isotopes. Error bars indicate the difference between $N_{\max} = 2$ and $N_{\max} = 0$. We employed the $N^3\text{LO}_{\text{EM}} + N^2\text{LO}_{400,\text{L}}$ interaction at $\alpha = 0.08 \text{ fm}^4$. For details on experimental data see appendix C.

value by about 50 %, while $Q(5/2^+)$ of ^{18}O differs by about a factor of 10. However, both, the experimental and theoretical value are very small. The magnetic dipole moments μ for ^{17}O to ^{20}O agree surprisingly well with experimental values.

Fluorine chain. Let us now proceed with fully open-shell nuclei. Figure 7.4 depicts ground-state energies obtained from the IM-NCSM as well as experimental values for the isotopes throughout the fluorine chain. The uncertainties of the IM-NCSM calculations are more pronounced than for the oxygen isotopes discussed previously and the experimental values lie either within or very close to the error range of IM-NCSM results. Thus, also for these mostly fully open-shell nuclei w.r.t. both protons and neutrons the IM-NCSM results for the ground-state energies are in good agreement with experimental values. Note that fig. 7.4 does not include the isotopes ^{29}F and ^{30}F since the associated IM-SRG evolutions become very stiff and we are not able to obtain converged results—in contrast to calculations based on other chiral interactions.

Furthermore, fig. 7.5 shows the excitation energies of the first excited states for fluorine isotopes. Compared to the rather simple behavior of the oxygen isotopes, things are more complicated here: Experimentally, the excitation energies are rather small and the theoretically obtained absolute values or even the order of the ground and excited state are not always in accord with experiment. While the excitation energies show a sizeable dependence on N_{\max} for some isotopes, for others it is practically converged at $N_{\max} = 0$. Except for ^{24}F and ^{25}F , the IM-NCSM and the experiment are largely agreeing with each other and eventually only the order of states is reversed. For ^{25}F , however, only the quantum numbers of the ground state are correctly predicted and for ^{24}F the 3^+ shows a sizeable dependence on N_{\max} and probably

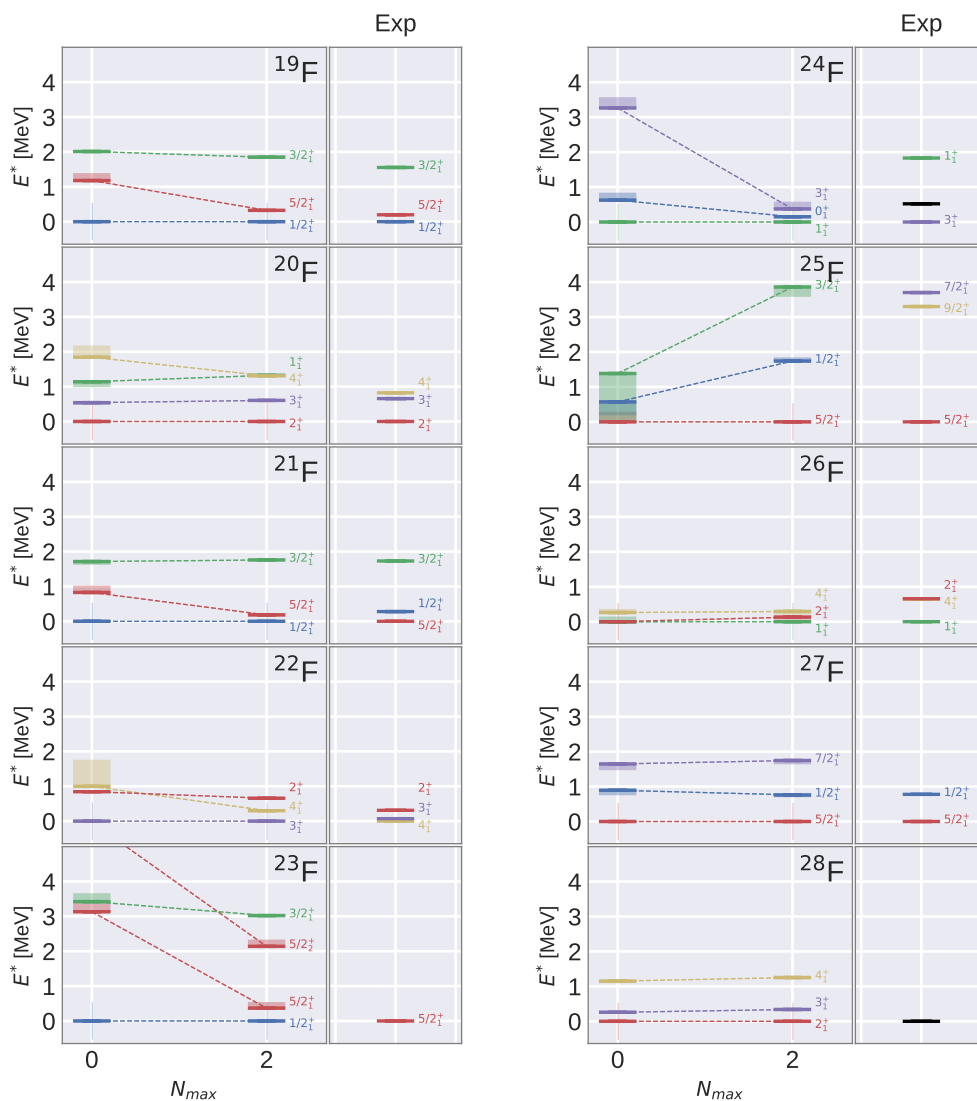


Figure 7.5.: Excitation energies for the fluorine isotopes ^{19}F up to ^{28}F from the IM-NCSM. Calculations have been performed at $N_{max}^{\text{ref}} = 0$. For details on experimental data see appendix C.

crosses the 1^+ and 0^+ state for higher N_{\max} such that the IM-NCSM and experiment would agree.

7.2. New Generations of Chiral Interactions

The dependence of observables on the interaction is illustrated in fig. 7.6, which depicts IM-NCSM calculations for ^{21}O employing three different chiral interactions.¹ Firstly, we employed the $\text{N}^3\text{LO}_{\text{EM}}+\text{N}^2\text{LO}_{400,\text{L}}$ interaction at $\alpha = 0.08 \text{ fm}^4$, which includes the NN interaction by Entem and Machleidt [EM03] with a cutoff $\Lambda_{\text{NN}} = 500 \text{ MeV}$ and an 3N interaction with local regulator and reduced cutoff $\Lambda_{3\text{N}} = 400 \text{ MeV}$ [Nav07; Rot+12]. Secondly, we used the $\text{N}^3\text{LO}_{\text{EM}}+\text{N}^2\text{LO}_{500,\text{NL}}$ interaction at $\alpha = 0.12 \text{ fm}^4$, which is an update of the $\text{N}^3\text{LO}_{\text{EM}}+\text{N}^2\text{LO}_{400,\text{L}}$ interaction, but employs a non-local regulator for the 3N interaction, $\Lambda_{3\text{N}} = 500 \text{ MeV}$, and a corrected c_D value [GQN19; Mar+18]. Thirdly, we use the $\text{N}^2\text{LO}_{\text{SAT}}+\text{N}^2\text{LO}_{\text{SAT}}$ interaction [Eks+15] by Ekström et al., which uses NN and 3N interactions at N^2LO , non-local regulators, cutoffs $\Lambda_{\text{NN}} = \Lambda_{3\text{N}} = 450 \text{ MeV}$, and includes many-body observables for the determination of its low-energy constants—in contrast to all other interactions employed throughout this work that only employ few-body data.

Considering the first two interactions, the ground-state energy and the excitation energies are in good agreement with experiment. Furthermore, we predict the third state as a $3/2^+$ state. The $B(\text{E}2)$ transitions differ drastically between the two first interactions by almost a factor of 2, where the result for the $B(\text{E}2; 1/2^+ \rightarrow 5/2^+)$ transition obtained from the interaction $\text{N}^3\text{LO}_{\text{EM}}+\text{N}^2\text{LO}_{500,\text{NL}}$ agrees well with the corresponding experimental value. The $B(\text{M}1)$ transitions, however, differ only slightly between these two interactions. Looking at the third interaction $\text{N}^2\text{LO}_{\text{SAT}}+\text{N}^2\text{LO}_{\text{SAT}}$, a different picture emerges: The binding energy is substantially overestimated and the excitation energies lie much too high compared to experimental values. While the $B(\text{E}2)$ transitions are mostly similar between the second and third interaction, the $B(\text{M}1; 3/2^+ \rightarrow 1/2^+)$ transition is much lower compared to the other two interactions. Due to the fact that already the excitation energies obtained from the $\text{N}^2\text{LO}_{\text{SAT}}+\text{N}^2\text{LO}_{\text{SAT}}$ interaction differ significantly from experimental values, questions about the trustworthiness of the other results are raised.

This study of ^{21}O demonstrates that the specific choice for the chiral interaction has a substantial impact on observables. Therefore, we will explore other, newer generations of chiral interactions in the following, which eventually lead to a better agreement with experimental values.

¹Note that the calculations presented here were performed in the context of a collaboration with experimentalists that measured electromagnetic transitions among the lowest-lying states in ^{21}O . A publication is currently in preparation.

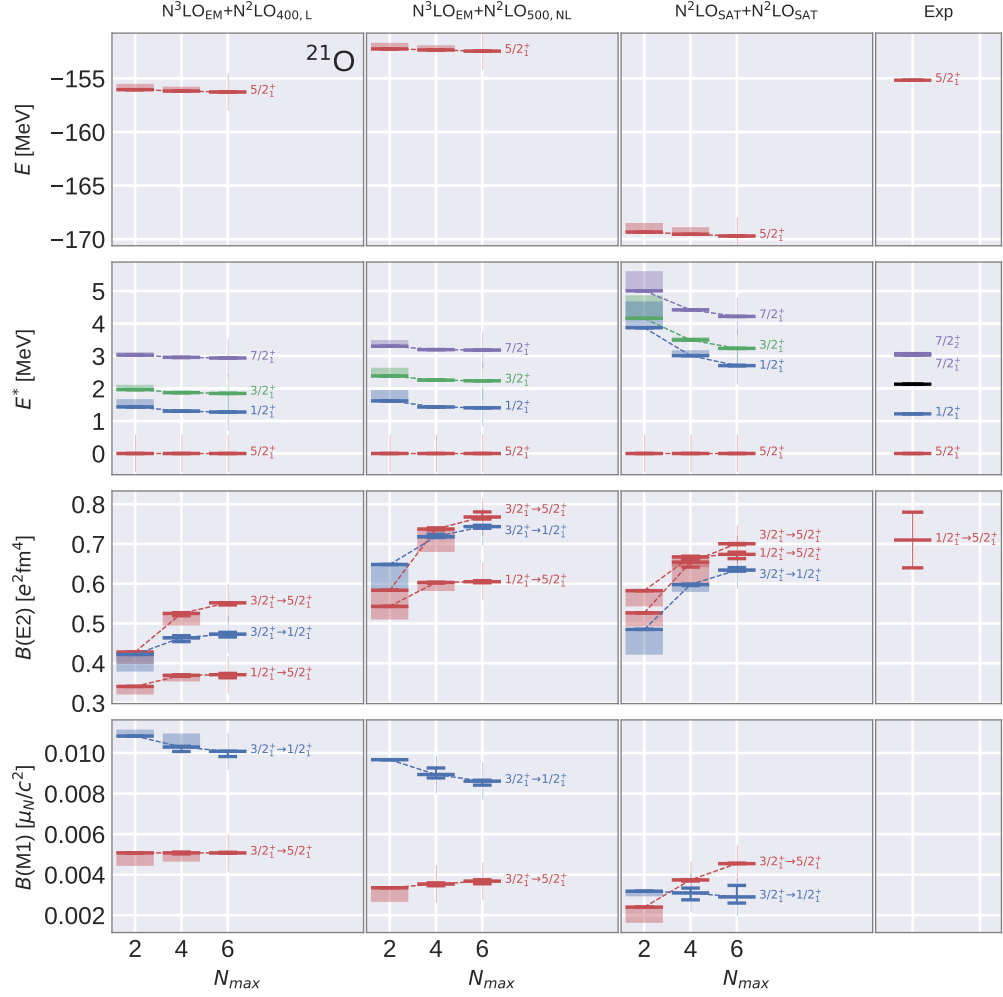


Figure 7.6.: IM-NCSM calculations at $N_{\text{max}}^{\text{ref}} = 2$ for ^{21}O employing several chiral interaction (see text for details). Calculations were performed employing ^{22}O as parent nucleus. For details on experimental data see appendix C.

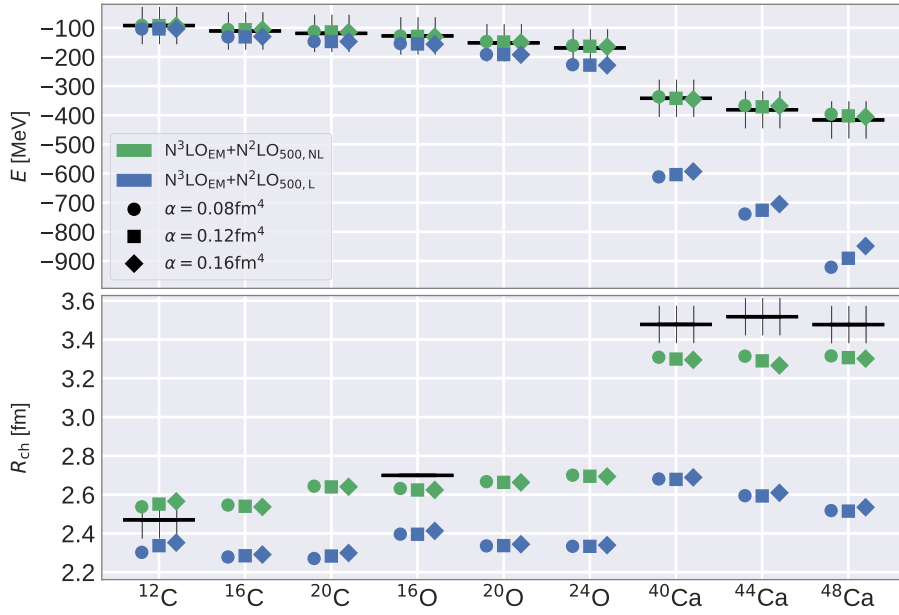


Figure 7.7.: IM-NCSM calculations at $N_{\max}^{\text{ref}} = 2$ and $N_{\max} = 2$ for several carbon, oxygen, and calcium isotopes. We employed a local and a non-local regulator and three different values for the free-space SRG flow parameter α . Experimental values are indicated through black bars (for details see appendix C).

7.2.1. Regulator Effects: Local vs. Non-Local Regulators

For avoiding infinities, interaction terms \hat{V} obtained from χ EFT have to be regularized, i.e., high momenta have to be cut off, which is consistent with χ EFT being only valid for momenta $Q \ll \Lambda_\chi \approx 1 \text{ GeV}$ [EM03; ME11]. While various regularization schemes are available, they fall in either of two classes or anything in between: local and non-local. For more information see, e.g., [EM03; EMN17; EKM15; ME11; EM09]

Figure 7.7 shows a comparison of IM-NCSM calculations employing local and non-local three-body regulators for the two interactions $N^3\text{LO}_{\text{EM}}+N^2\text{LO}_{500,\text{L}}$ and $N^3\text{LO}_{\text{EM}}+N^2\text{LO}_{500,\text{NL}}$, respectively. Both of these interactions are updates of the commonly used $N^3\text{LO}_{\text{EM}}+N^2\text{LO}_{400,\text{L}}$ interaction with a cutoff of $\Lambda_{3N} = 500 \text{ MeV}$ and a corrected c_D value.

There is a significant difference between the local and non-local regularization scheme. While the non-locally regularized interaction yields binding energies that are consistent with experimental values, the locally regularized interaction gives too much binding—in oxygen isotopes up to 50 MeV, in calcium more than 400 MeV. Except for the heavier calcium isotopes, the dependence on α is negligible. Looking at charge radii, a similar picture emerges: The

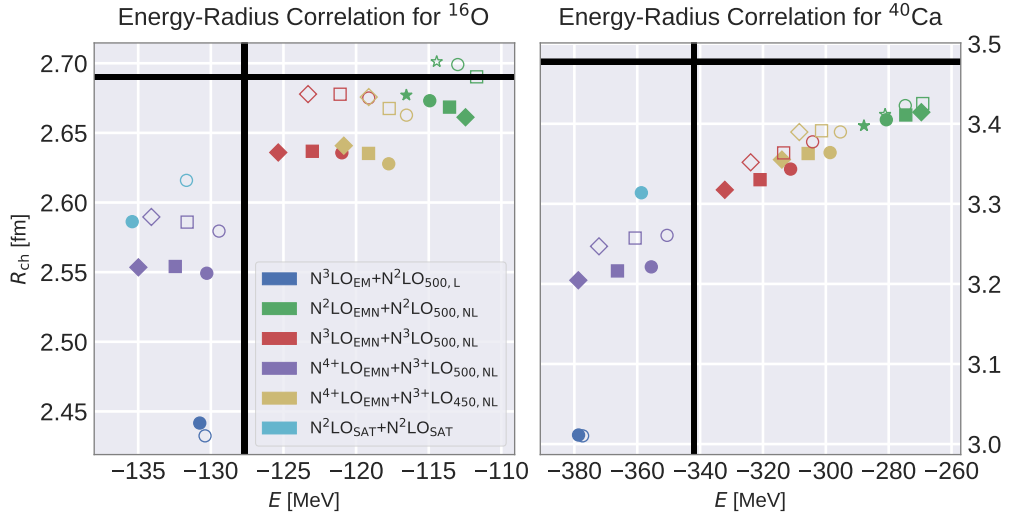


Figure 7.8.: Ground-state energies and radii obtained from the single-reference IM-SRG for ^{16}O and ^{40}Ca employing several chiral interactions. All interaction were softened through a free-space SRG transformation up to $\alpha = 0.04 \text{ fm}^4$ (open symbols) and $\alpha = 0.08 \text{ fm}^4$ (solid symbols). Furthermore, we employed a circle, a square, and a diamond-shaped symbol for indicating $c_D = -1.0, -2.0$ and -3.0 ($\text{N}^2\text{LO}_{\text{EMN}}+\text{N}^2\text{LO}_{500,\text{NL}}$); $c_D = 1.0, 2.0$ and 3.0 ($\text{N}^3\text{LO}_{\text{EMN}}+\text{N}^3\text{LO}_{500,\text{NL}}$); $c_D = 2.0, 3.0$ and 4.0 ($\text{N}^4\text{LO}_{\text{EMN}}+\text{N}^3+\text{LO}_{500,\text{NL}}$); and $c_D = 2.0, 3.0$ and 4.0 ($\text{N}^4\text{LO}_{\text{EMN}}+\text{N}^3+\text{LO}_{450,\text{NL}}$), respectively. Experimental values are indicated through horizontal and vertical lines (for details see appendix C).

$\text{N}^3\text{LO}_{\text{EM}}+\text{N}^2\text{LO}_{500,\text{NL}}$ interaction over or underestimates the charge radius in ^{12}C and ^{16}O , respectively, by about 0.1 fm , whereas the difference in calcium gets larger. However, the discrepancies of the local interaction with the experimental values are much larger.

In summary, we observe that the regularization scheme has a sizeable impact on observables. As a consequence, it might be necessary to reevaluate regulator effects in future investigations. For the time being, however, we decided to employ non-local regulators for our following calculations.

7.2.2. Study of Energy-Radius Correlations

Next, we conducted a survey, where we investigated ground-state energies and radii for ^{16}O and ^{40}Ca as shown in fig. 7.8. Besides the already discussed interactions $\text{N}^3\text{LO}_{\text{EM}}+\text{N}^2\text{LO}_{400,\text{L}}$ and $\text{N}^2\text{LO}_{\text{SAT}}+\text{N}^2\text{LO}_{\text{SAT}}$, this figure also shows results for the family of interactions referred to

via $N^{\nu_2}\text{LO}_{\text{EMN}}+N^{\nu_3}\text{LO}_{500/450,\text{NL}}$, which employ an NN interaction [EMN17] by Entem, Machleidt, and Nosyk (EMN) together with a non-local 3N interaction [Heb+15]. As these interactions are available for several chiral orders ν_2 and ν_3 for the NN and 3N interaction, respectively, we may investigate the convergence of the chiral expansion. Note that the notation $N^4\text{LO}_{\text{EMN}}+N^{3+}\text{LO}_{500,\text{NL}}$ indicates that selected 3N terms from $N^4\text{LO}$ are included.

Note that all interactions have been free-space SRG transformed up to either $\alpha = 0.04 \text{ fm}^4$ or $\alpha = 0.08 \text{ fm}^4$. Furthermore, we employed three different values for c_D for each interaction by EMN for investigating the dependence of observables on c_D , where c_D is obtained from a fit to the ${}^4\text{He}$ binding energy (the employed values for c_D are given in the caption of fig. 7.8).

The “old” $N^3\text{LO}_{\text{EM}}+N^2\text{LO}_{400,\text{L}}$ interaction yields results that lie farthest away from the intersection of the experimental ground-state energy and charge radius. Even though the interaction $N^2\text{LO}_{\text{SAT}}+N^2\text{LO}_{\text{SAT}}$ yields results that are closer to experimental values, especially through an improved prediction of radii, some interactions from EMN yield even better results—and include only few-body data for the determination of the LECs. Note that the $N^2\text{LO}_{\text{SAT}}+N^2\text{LO}_{\text{SAT}}$ interaction is originally designed to match the charge radius and binding energy of ${}^{16}\text{O}$, where the LECs are determined via a coupled cluster singles and doubles (CCSD) calculation employing bare interactions. In contrast, we are employing free-space SRG evolved interactions since bare interactions usually imply larger uncertainties due to an increased role of inherent truncations—raising questions about the trustworthiness of CCSD calculations with bare interactions after all. Furthermore, we made the observation that spectra obtained from the $N^2\text{LO}_{\text{SAT}}+N^2\text{LO}_{\text{SAT}}$ interaction do not agree very well with experimental data, which can also be seen in fig. 7.6.

Considering the family of interactions from EMN, we observe that there is not only a sizeable dependence on the chiral order, but also on c_D and Λ_{3N} for both ${}^{16}\text{O}$ and ${}^{40}\text{Ca}$. While the local interaction yields radii that are much too small, all non-local interaction give much larger radii. Looking at all non-local interactions, energies and radii seem to be approximately linearly correlated, however, the estimated line describing the correlation still lies too low, i.e., radii are still too small. Future investigations have to sort out the dependence on c_D and Λ_{3N} such that, eventually, an interaction that minimizes the difference to experimental values may be constructed.

For the time being, however, we decided to employ the $N^4\text{LO}_{\text{EMN}}+N^{3+}\text{LO}_{500,\text{NL}}$ interaction with $c_D = 3.0$ for our following studies. This interaction contains NN and 3N interactions at the highest order currently available and, compared to the $N^3\text{LO}_{\text{EM}}+N^2\text{LO}_{400,\text{L}}$ interaction, yields better radii in both ${}^{16}\text{O}$ and ${}^{40}\text{Ca}$ and better binding energies in ${}^{40}\text{Ca}$.

We would like to note at this point that there is another family of interactions under development within the LENPIC collaboration. For the construction of these interactions, semi-local regulators are employed and one of the goals is to study the convergence of the chiral expansion and to quantify theoretical uncertainties due to truncations of the chiral expansion [Bin+16; Bin+18; Epe+19]. However, in this work none of these interactions are employed.

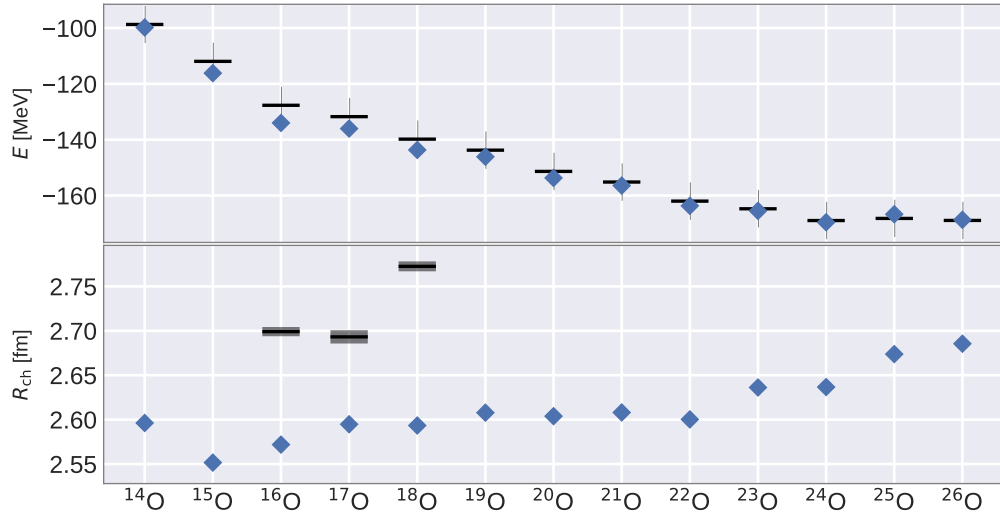


Figure 7.9.: Ground-state energies and charge radii from the IM-NCSM at $N_{\max}^{\text{ref}} = 2$ and $N_{\max} = 4$ for oxygen isotopes employing the $N^4\text{LO}_{\text{EMN}}+N^3+\text{LO}_{500,\text{NL}}$ interaction at $\alpha = 0.08 \text{ fm}^4$. For details on experimental data see appendix C.

7.3. Oxygen Chain—Revisited

Let us now reconsider oxygen isotopes by employing the $N^4\text{LO}_{\text{EMN}}+N^3+\text{LO}_{500,\text{NL}}$ interaction at $\alpha = 0.08 \text{ fm}^4$. Figure 7.9 shows ground-state energies and charge radii for all isotopes of the oxygen chain up to ^{26}O .

Similarly to applications employing the $N^3\text{LO}_{\text{EM}}+N^2\text{LO}_{400,\text{L}}$ interaction, also here the ground-state energies are in good agreement with experimental data and the neutron drip line is correctly predicted at ^{24}O .²

Looking at charge radii, we observe a similar pattern as in fig. 7.2, however, the radii obtained with the $N^4\text{LO}_{\text{EMN}}+N^3+\text{LO}_{500,\text{NL}}$ interaction are increased by about 0.1 fm—reducing the discrepancies with experiment. However, also calculations employing this newer interaction do not show the experimentally observed increase of the charge radius from ^{17}O to ^{18}O .

Nevertheless, the obtained radii are significantly larger and closer to experimental values, while—which is somewhat surprising—the ground-state energies are approximately invariant. Therefore, future investigations and developments of new generations of chiral interactions might eventually resolve the issue of too small radii.

²The correct prediction of the neutron drip line is insofar noteworthy as we also employed interactions that were in good agreement with experimental values up to approximately ^{20}O , but for heavier nuclei than that we observed a rapid decrease of the binding energy.

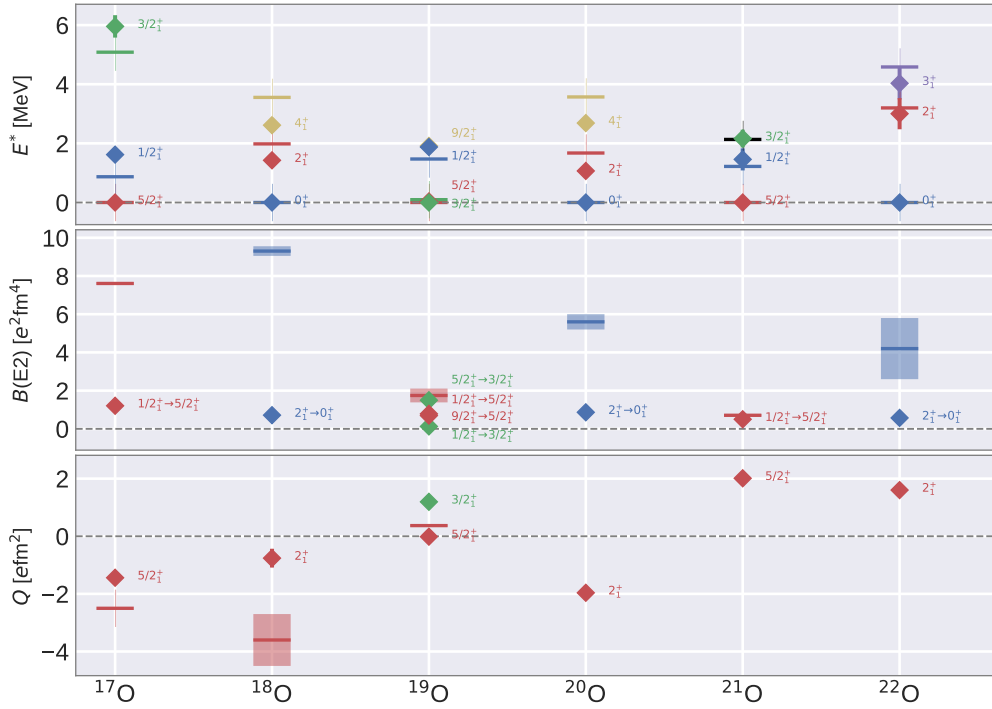


Figure 7.10.: Excitation energies, $B(E2)$ transitions, and quadrupole moments for oxygen chain isotopes obtained from the IM-NCSM at $N_{\max}^{\text{ref}} = 2$ and $N_{\max} = 4$ employing the $N^4\text{LO}_{\text{EMN}}+N^3+\text{LO}_{500,\text{NL}}$ interaction at $\alpha = 0.08 \text{ fm}^4$. Error bars indicate differences between $N_{\max} = 2$ and 4. For details on experimental data see appendix C.

Let us now move on to the discussion of spectra, transitions and moments of oxygen isotopes as depicted in fig. 7.10. Comparing the results shown here with fig. 7.3, a similar picture is drawn. There are slight discrepancies between theoretical and experimental values for the excitation energies, however, the order of states and their quantum numbers are in good agreement. Looking at $B(E2)$ transitions, we observe that, similarly to the $N^3\text{LO}_{\text{EM}}+N^2\text{LO}_{400,\text{L}}$ interaction, also this interaction yields results for ^{19}O and ^{21}O that are close to the experimentally observed values, however, for the other nuclei presented here there are again significant discrepancies. Naturally, also the quadrupole moments still not agree with experimental values.

A detailed comparison of $B(E2)$ transitions obtained from either the $N^4\text{LO}_{\text{EMN}}+N^3+\text{LO}_{500,\text{NL}}$ or the $N^3\text{LO}_{\text{EM}}+N^2\text{LO}_{400,\text{L}}$ interaction is shown in fig. 7.11. Evidently, the $B(E2)$ transition depend only slightly on the interaction and most results are approximately lying within the error bars of each other.

Thus, there are still open questions regarding the source for the rather large discrepancies

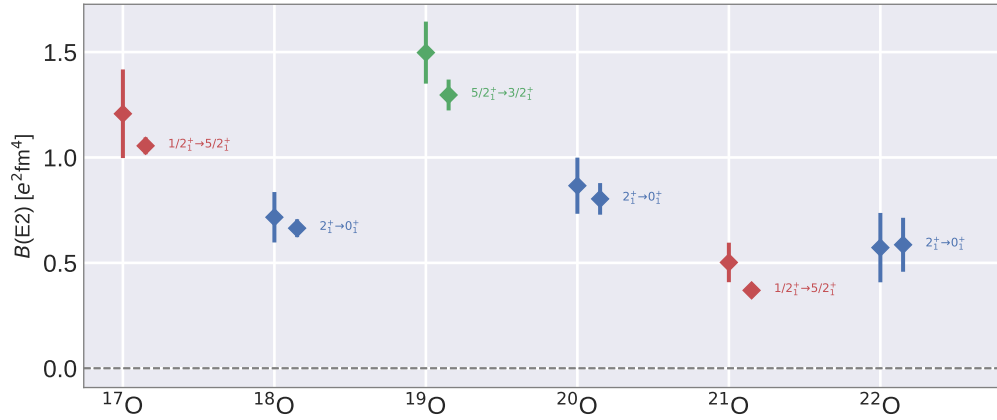


Figure 7.11.: This figure depicts a direct comparison of $B(E2)$ transitions for oxygen chain isotopes employing either the $N^4\text{LO}_{\text{EMN}}+N^{3+}\text{LO}_{500,\text{NL}}$ interaction (left symbols) or the $N^3\text{LO}_{\text{EM}}+N^2\text{LO}_{400,\text{L}}$ interaction (right symbols). Both interactions have been free-space SRG transformed up to $\alpha = 0.08 \text{ fm}^4$ and IM-NCSM calculations have been performed at $N_{\text{max}}^{\text{ref}} = 2$ and $N_{\text{max}} = 4$. Error bars indicate differences between $N_{\text{max}} = 2$ and 4.

between theoretically predicted and experimentally measured $B(E2)$ transition strengths for oxygen isotopes. Future investigations have to address these question and investigate if these differences are rooted within the interaction, the inherent truncations of the IM-NCSM, or both.

7.4. Neutron-Rich Fluorine Isotopes

We performed IM-NCSM calculations for the two neutron-rich fluorine isotopes ^{29}F and ^{30}F as shown in Figure 7.12. Both nuclei are in the direct vicinity of the neutron drip line and recently gained interest from experimentalists.

The calculations for ^{30}F show that the theoretically predicted ground state is a 2^- state lying at about -177 MeV , where we would like to note that the interaction that we were employing in this case has the tendency to underestimate the binding energy in neutron rich systems. The first two excitations are a 6^- and a 4^- state, which are nearly degenerate at $N_{\text{max}} = 6$, and lie at about 0.5 MeV —but show an inverse trend w.r.t. N_{max} . The next two states, however, are energetically clearly separated. Even though the N_{max} convergence is not as enhanced as for the oxygen isotopes, there are only slight changes from $N_{\text{max}} = 4$ to $N_{\text{max}} = 6$.

Figure 7.12 also shows results for ^{29}F obtained from IM-NCSM calculations employing ^{30}Ne as parent nucleus. We predict a $5/2^+$ ground-state lying at about -178.5 MeV . The first two

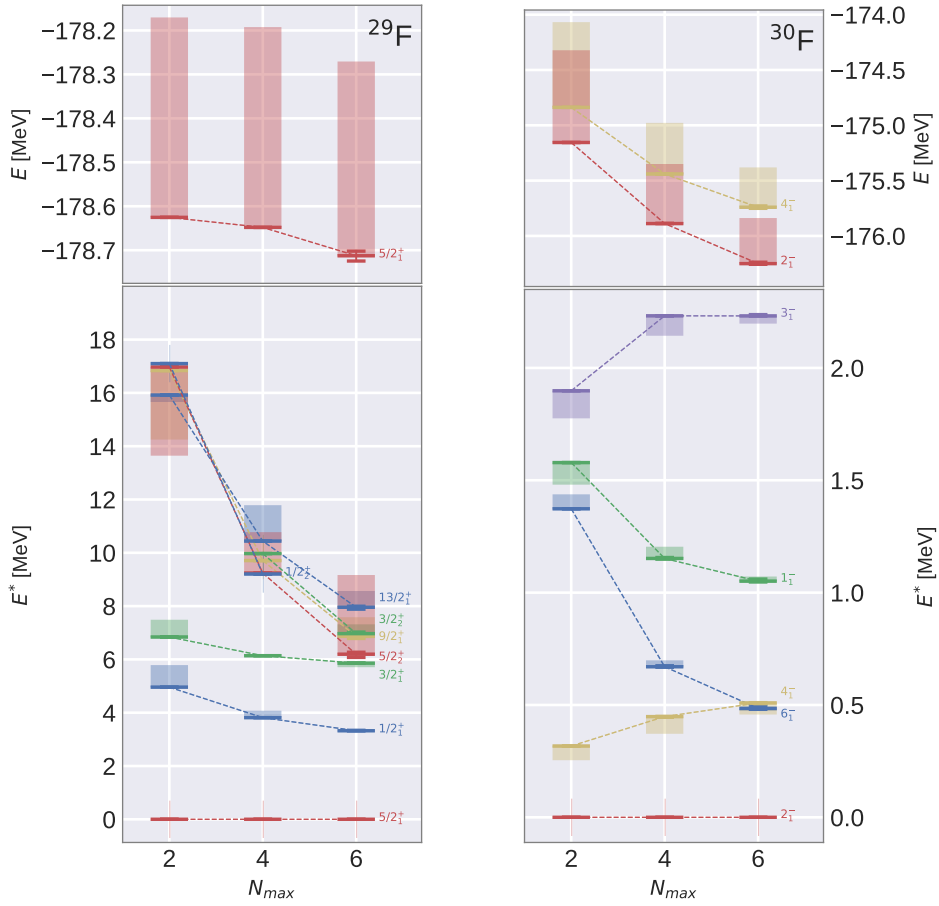


Figure 7.12.: IM-NCSM calculation at $N_{\text{max}}^{\text{ref}} = 2$ for ^{29}F employing ^{30}Ne as parent nucleus (left) and calculation for ^{30}F (right). We were employing the $\text{N}^3\text{LO}_{\text{EM}} + \text{N}^2\text{LO}_{500,\text{NL}}$ interaction at $\alpha = 0.12 \text{ fm}^4$.

excitations are a $1/2_1^+$ and a $3/2_1^+$ state, which both are reasonably well converged at the largest N_{\max} available. For higher-lying excitations, however, things get interesting: There is a whole bunch of energetically close states that is coming down from high excitation energies. Compared to the three lowest-lying states, their energies still show a pronounced dependence on N_{\max} and s . The lowest-lying states in this bunch of states are a $5/2_2^+$ state, followed by two nearly degenerate $9/2_1^+$ and $3/2_2^+$ states. As the $5/2_2^+$ state is nearly degenerate with the $3/2_1^+$ state and still moves to lower energies w.r.t. N_{\max} and s , it is likely that it turns out as the second excitation by moving past the $3/2_1^+$ state. However, we can not give a definite answer on the order of the excited states as these high-lying states are not fully converged.

We would like to remark that the behavior of those high-lying states resembles the behavior of spurious eigenstates. However, we performed calculations at several values for λ_{cm} and verified that—even though they show a larger dependence on λ_{cm} than the first two excited states—those higher-lying eigenstates are no spurious center-of-mass excitations.

7.5. Neon Chain

Let us now move on to the fully open-shell nuclei of the neon chain, whose ground-state energies and charge radii are shown in fig. 7.13.

Overall, the ground-state energies agree well with experimental values and reproduce the general trend for the binding energies. A prediction of the neutron drip line is difficult, as also experimentally the binding energies are almost constant between ^{30}Ne and ^{34}Ne , whereas there are small variations of the results obtained from the IM-NCSM. However, starting from ^{35}Ne , we see a significant decrease of the binding energy.

Looking at the charge radii shown in fig. 7.13, we observe the by now well-known pattern that theoretically obtained charge radii underestimate experimental values. The largest discrepancy is found for ^{20}Ne , where the difference amounts to approximately 0.2 fm. Taking error bars into account³, the discrepancy for ^{23}Ne to ^{26}Ne is much lower and in the region of 0.05 fm to 0.1 fm.

Interestingly, we observe that the experimental radius for ^{24}Ne lies within a local minimum—hinting at sub-shell closure effects of the $1d_{5/2}$ neutron shell. Furthermore, the IM-NCSM calculations for ^{23}Ne to ^{26}Ne are showing a slower N_{\max} convergence than the other neon isotopes. Both of these observations are consistent with previous findings that also oxygen chain isotopes—which have a closed proton shell—are showing a slowed down N_{\max} convergence for $N_{\max}^{\text{ref}} = 0$.

Excited states, $B(E2)$ transitions, and quadrupole moments for ^{20}Ne up to ^{34}Ne are shown in fig. 7.14. All in all, the spectra obtained from the IM-NCSM are compatible with the experimentally observed ones with regard to both excitation energies and quantum numbers.

³While the error bars are depicting a symmetric error, the radius is usually *increasing* w.r.t. N_{\max} .

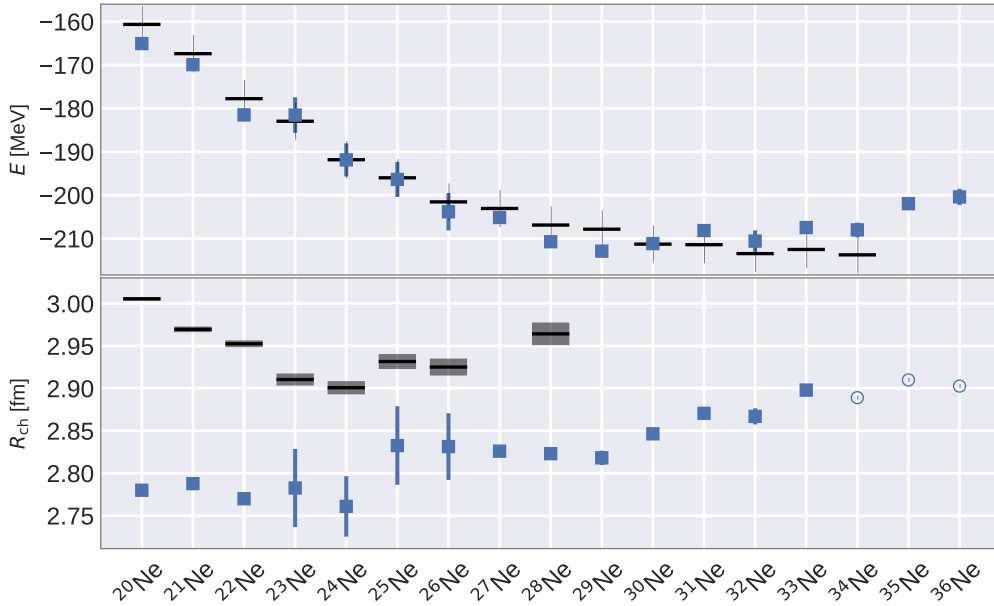


Figure 7.13.: Ground-state energies and charge radii obtained from the IM-NCSM at $N_{\max}^{\text{ref}} = 0$ and $N_{\max} = 2$ for ^{20}Ne up to ^{36}Ne . We employed the $N^4\text{LO}_{\text{EMN}} + N^3 + \text{LO}_{500,\text{NL}}$ interaction at $\alpha = 0.08 \text{ fm}^4$. IM-NCSM error bars indicate differences between $N_{\max} = 0$ and 2. For details on experimental data see appendix C.

Surprisingly, the $B(E2)$ transition strengths are in much better agreement with experiment than for oxygen isotopes. The largest discrepancies are observed for ^{20}Ne , ^{21}Ne , and ^{22}Ne , where the difference amounts to a factor of 2 to 3—which is still much smaller than the huge differences we found for the even oxygen isotopes. Furthermore, it is noteworthy that the order of the transitions in ^{22}Ne is correct: While both the $B(E2; 2^+ \rightarrow 0^+)$ and the $B(E2; 4^+ \rightarrow 2^+)$ transition are too small, also experimentally the latter is bigger than the former. For the more neutron-rich neon isotopes ^{24}Ne and ^{26}Ne , we obtain IM-NCSM results that are very close to the corresponding experimental values. Going even further, however, we see that the $B(E2; 2^+ \rightarrow 0^+)$ for ^{28}Ne differs by about a factor of 2. Regarding quadrupole moments, there is only experimental data for $^{20-22}\text{Ne}$ available, where we obtain IM-NCSM results that differ by about a factor of 2.

In summary, there are still differences between theoretical and experimental values regarding electromagnetic transitions and moments, however, those difference are less pronounced than in previous studies of oxygen isotopes and may very well be resolved by an optimization of the interaction. Regarding the different behavior of neon isotopes compared to oxygen isotopes, we believe that the open proton shell found in neon isotopes partially accounts for this different behavior. The IM-NCSM suffers much less from inherent truncations and deficien-

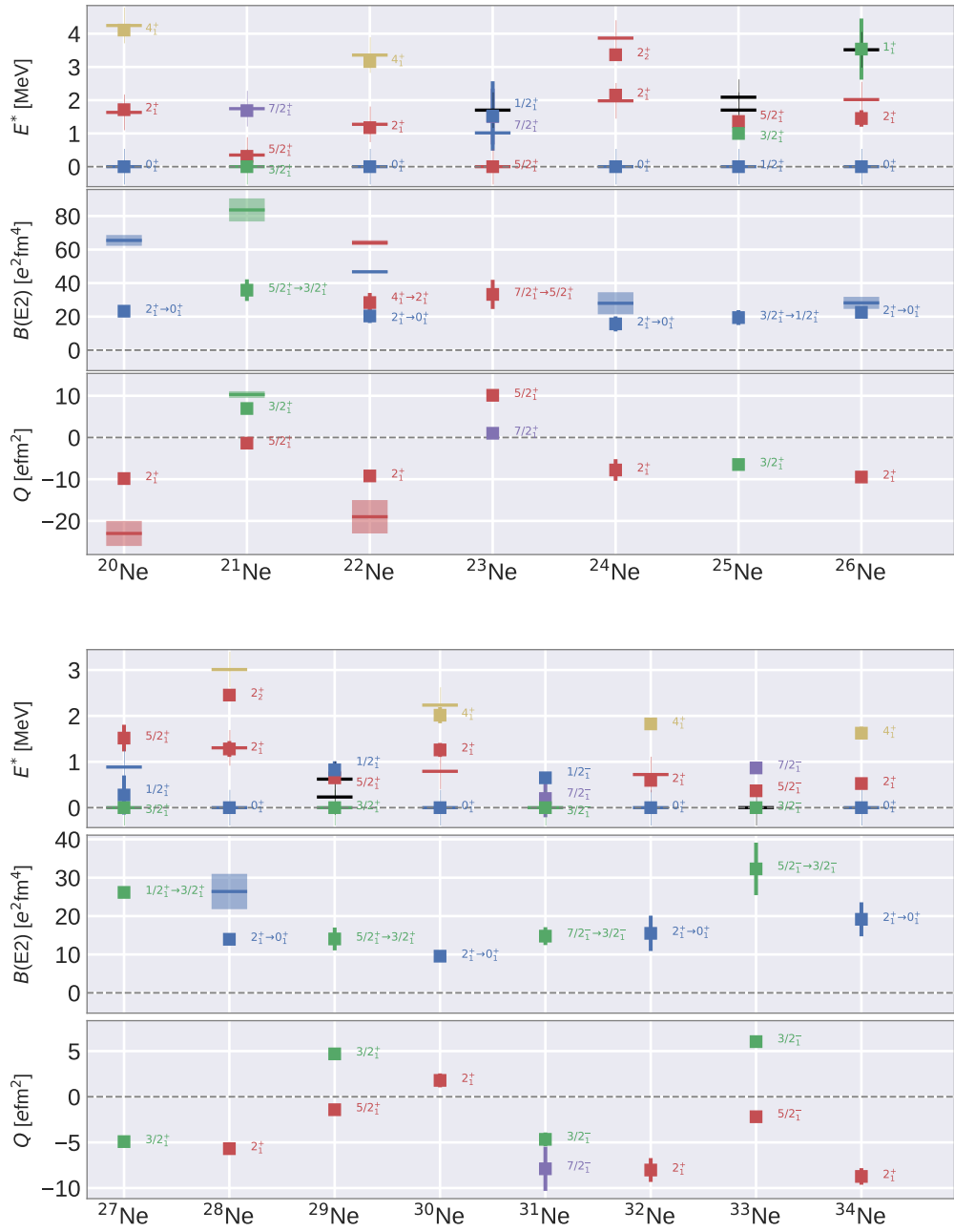


Figure 7.14.: Excited states, $B(E2)$ transitions, and quadrupole moments obtained from the IM-NCSM at $N_{\text{max}}^{\text{ref}} = 0$ and $N_{\text{max}} = 2$ for ^{20}Ne up to ^{36}Ne . IM-NCSM error bars indicate differences between $N_{\text{max}} = 0$ and 2 . We employed the $N^4\text{LO}_{\text{EMN}} + N^3\text{LO}_{500,\text{NL}}$ interaction at $\alpha = 0.08 \text{ fm}^4$. For details on experimental data see appendix C.

cies in fully open-shell nuclei as the reference state $|\psi_{\text{ref}}\rangle$ captures the main structure of the relevant eigenstates already at $N_{\text{max}}^{\text{ref}} = 0$. In contrast, it might be essential in oxygen isotopes to perform calculations at $N_{\text{max}}^{\text{ref}} = 2$, i.e., include $N_{\text{max}} = 2$ determinants in the expansion of eigenstates, for adequately describing electromagnetic observables and, as a consequence, oxygen isotopes are much more sensitive to eventual deficiencies of the IM-SRG decoupling pattern.

Thus, one of the main goals of future investigations towards extensions of the IM-NCSM is the optimization of decoupling patterns and generators such that we may eventually isolate the source for the observed discrepancies w.r.t. electromagnetic transitions and overcome it.

Summary and Outlook

Throughout this work, we discussed the foundations, extension, and applications of the IM-NCSM, which is a combination of two successful ab initio many methods: the IM-SRG and the NCSM.

On the one hand, the NCSM is an exact configuration interaction approach. It represents and diagonalizes the Hamiltonian w.r.t. a truncated many-body model space and gives direct access to ground and excited-state observables. However, due to the growth of the basis dimension it is limited to the description of p -shell nuclei—or lower sd -shell nuclei if an importance-truncation scheme is applied.

On the other hand, the IM-SRG is a medium-mass method that performs an unitary transformation of observables. This transformation is designed such that a reference state—usually chosen as the ground-state of the A -body system under consideration—is decoupled from particle-hole excitations. In this work, we employ the multi-reference IM-SRG that uses correlated reference states and, therefore, makes open-shell nuclei accessible. As the IM-SRG transformation is not carried out in A -body space, but all operators are truncated at the normal-ordered two-body rank, the transformation is not exactly unitary. It is solely this truncation that separates the IM-SRG from being an exact method and introduces an uncertainty.

The IM-NCSM consists of an initial NCSM calculation for the determination of the reference state. Based on this reference state, the IM-SRG performs a unitary transformation of observables, which is constructed such that the reference state gets decoupled. Subsequently, the IM-SRG-transformed observables enter a final NCSM calculation, whose convergence is substantially improved compared to a regular NCSM calculation—demonstrating the power of the IM-SRG decoupling scheme. As a consequence, the IM-NCSM may treat nuclei that are out of reach for traditional NCSM calculations. An essential aspect of the IM-NCSM is the complementarity of the two ab initio many-body methods it is built upon: Each stage employs its inherent truncations scheme and may capture different kinds of correlations such that, in total, a large portion of correlations is accounted for.

The initial formulation of the IM-NCSM had several restrictions that we eliminated in this work. One problem concerns the total angular momentum of the reference state, which is required to vanish due to the spherical formulation of the IM-SRG equations. The particle-attached/particle-removed extension overcomes this restriction and makes odd nuclei accessible by differentiating between a “parent” and a “target” nucleus. The parent nucleus defines the reference state that is decoupled from particle-hole excitations via the IM-SRG, while the target nucleus specifies the many-body system w.r.t. which the final NCSM calculation is performed. Similarly to the regular IM-NCSM approach, the NCSM calculation for the target nucleus greatly benefits from the IM-SRG transformation of observables, i.e., the convergence is substantially enhanced.

Furthermore, the spherical formulation of the IM-SRG equations—which is mandatory from a computational point of view—did not account for non-scalar operators and, therefore, the consistent transformation of electromagnetic observables was not possible. For overcoming this limitation, we derived analytical expressions for the spherical IM-SRG equations in which the spherical tensor rank of the observable may be chosen freely. In practical applications, however, directly solving the ordinary differential equations for non-scalar observables is not feasible due to a significantly increased computational effort. Fortunately, we can make use of the Magnus formulation of the IM-SRG that had been implemented at the beginning of this research project. Broadly speaking, the Magnus formulation determines the generator for the IM-SRG transformation and the computational effort for the subsequent transformation of observables is greatly reduced.

Considering numerical applications, we employ the IM-NCSM for the calculation of ground-state energies, excitation energies, radii, magnetic dipole moments, electric quadrupole moments, $B(M1)$ transitions, and $B(E2)$ transitions, where we study various medium-mass nuclei up to calcium isotopes. These calculations are already converged at very small model-space sizes—showing the great advantage of the IM-NCSM—and the results are compatible with large-scale NCSM calculations. While ground-state and excitation energies are mostly in agreement with the experiment for nuclei up to neon isotopes, radii are usually too small—a well-known deficiency of currently employed chiral interactions. In the context of electromagnetic observables the emerging picture is more diverse: Numerical applications for, e.g., ^{12}C show that $B(E2)$ transition strengths, and quadrupole moments are largely in agreement with the experiment, however, there are also cases where $B(E2)$ transition strengths and quadrupole moments suffer from large discrepancies with experimental values. On the one hand, the observed discrepancies might be an issue of the interaction and, in fact, we see a sizeable dependence of electromagnetic observables on the interaction. Employing newer generations of chiral interactions might, therefore, eventually lead to a better agreement with experimental values. On the other hand, there might be a substantial amount of induced many-body pieces beyond the NO2B rank, which is eventually rooted in deficiencies of the IM-SRG generator. In future applications, we will investigate whether a generator optimization resolves this issue and, thus, leads to a better agreement of the IM-NCSM with the experiment.

In this work, we were only looking at $B(E2)$ and $B(M1)$ transitions strengths. However, we laid the groundwork to employ the IM-NCSM for studying other non-scalar observables like, e.g., $B(E1)$ and Gamow-Teller transitions in future applications. An ongoing project deals with the estimation of induced many-body contributions beyond the normal-ordered three-body rank, which are neglected throughout the IM-SRG evolution. The Magnus formulation of the IM-SRG offers an opportunity to approximate these effects of induced three-body contributions. As a consequence, we would be able to give a quantitative assessment of the uncertainty of IM-NCSM calculations.

In summary, the IM-NCSM is now capable of addressing the full range of nuclear structure observables—including spectroscopic and electromagnetic observables—in fully open-shell nuclei and future developments will mostly treat optimizations of this framework. Furthermore, we obtain results that are largely compatible with NCSM calculations—at a fraction of the computational cost. The new possibility to calculate electromagnetic observables from the IM-NCSM is ideal for validating theoretical models and opens up new opportunities for fruitful collaborations with experimentalists. Assuming that the reference state captures the most relevant correlations already at small model-space sizes, the IM-NCSM is ready to be utilized for exploring the complete medium-mass range of the nuclear chart. Therefore, the IM-NCSM offers an *ab initio* framework that can be used to study, e.g., the structure of nuclei in the vicinity of the neutron drip line and island-of-inversion physics. Finally, the IM-NCSM will be a valuable tool for investigating new generations of chiral interactions and eventually may contribute to establish a new era of high-precision theoretical nuclear physics.

Effective Valence-Space Interactions from the In-Medium SRG

Formally, the valence-space shell model (VSSM) [KB66; Cau+05; Cor+14] belongs to the class of configuration interaction approaches as already discussed in chapter 2 in the context of the NCSM. However, in contrast to the NCSM the shell-model usually employs another truncation of its model space such that not all nucleons are active degrees of freedom. Pictorially, there is a “frozen core” of single-particle states that are all contributing equally to all many-body basis states contained within the model space. On top of this frozen core, there are a few nucleons that may move freely within a so-called valence space and which eventually account for the degrees of freedom of the basis states within the model space of the VSSM.

While, traditionally, effective valence-space interactions are constructed phenomenologically [KB66; Cau+05; Cor+09], the IM-SRG opens up the possibility to construct such interactions within an ab-initio framework and has already been successfully employed for the construction of single-shell valence space interactions [TBS12; Bog+14; Str+16; Str+17]. In the following, we will outline the principles of the construction of effective valence-space interactions.

Model Space of the Valence-Space Shell Model. The VSSM partitions the (truncated) set of single-particle basis states into a core (C), valence (V) and excluded (Q) space. Additionally, let us define the so-called particle space \mathbb{P} as the union of V and Q

$$\mathbb{C} = \{c_1, c_2 \dots\}, \quad \mathbb{V} = \{v_1, v_2 \dots\}, \quad \mathbb{Q} = \{q_1, q_2 \dots\}, \quad \mathbb{P} = \mathbb{V} \cup \mathbb{Q} = \{p_1, p_2 \dots\}. \quad (\text{A.0.1})$$

Note that we use specific labels c , v , q and p for referring to certain subsets throughout this chapter.

For the construction of the model space, the notion of a “core” is essential: It is a Slater determinant $|\Phi\rangle = |c_1 \dots c_{A_c}\rangle$ whose A_c occupied single-particle states define the core space. Furthermore, those core states are also occupied in all other many-body basis states contained in

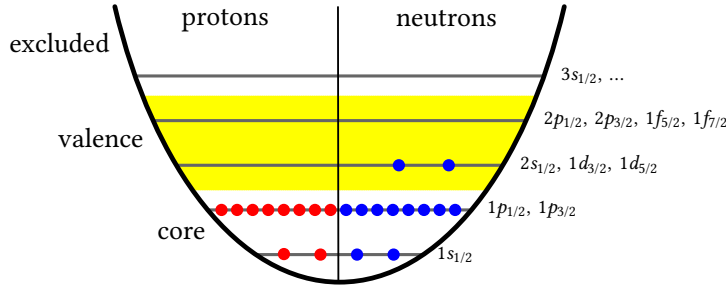


Figure A.1.: A schematic representation of an sd -shell model-space truncation of the VSSM: Only the two highest-lying neutrons may move within the yellow band. For more information see text.

the model space \mathcal{M} which can then be formally written as

$$\mathcal{M} = \text{span} \left(\left\{ \hat{a}^{v_1 v_2 \dots v_{A_v}} |\Phi\rangle : v_1, v_2, \dots, v_{A_v} \in \mathbb{V} \right\} \right). \quad (\text{A.0.2})$$

Evidently, the many-body basis of \mathcal{M} consists of all Slater determinants in which—on top of the A_c core-space states—exactly A_v valence space states are occupied. Consequently, the model space \mathcal{M} is a subspace of the antisymmetric A -body Hilbert space \mathcal{H}_a^A with $A = A_c + A_v$ particles. The complement of \mathcal{M} in \mathcal{H}_a^A is notated via

$$\overline{\mathcal{M}} = \mathcal{H}_a^A \setminus \mathcal{M}. \quad (\text{A.0.3})$$

IM-SRG Decoupling Pattern. For employing the IM-SRG framework for the construction of effective valence-space interactions that can be used as input for the VSSM, we first have to set up the corresponding decoupling pattern that the IM-SRG is aiming for during the transformation of operators.

The idea for the construction of effective valence-space interactions via the IM-SRG framework can be described as follows: We are aiming at unitarily transforming an initial Hamiltonian $\hat{H}(0)$ such that $\hat{H}(\infty)$ does not couple the model space \mathcal{M} with its complement $\overline{\mathcal{M}}$. Assuming that such a decoupling succeeds, a representation of $\hat{H}(\infty)$ in \mathcal{M} contains a subset of the exact eigenstates and eigenvalues. Formally, this decoupling condition can now be formulated as

$$\langle \psi | \hat{H} | \bar{\psi} \rangle = 0, \quad \forall |\psi\rangle \in \mathcal{M}, |\bar{\psi}\rangle \in \overline{\mathcal{M}}. \quad (\text{A.0.4})$$

Similarly to previous considerations, this decoupling scheme—formulated with regard to a decoupling of elements of an A -body model space—has to be translated into a decoupling pattern that is compatible with the formulation of the IM-SRG. That is why we have to identify the one and two-body matrix elements which are involved in the coupling of \mathcal{M} and $\overline{\mathcal{M}}$ with each other and include them in the off-diagonal Hamiltonian that we wish to suppress.

For that purpose, let us assume that all operators are in reference-state representation w.r.t. to the core state $|\Phi\rangle$ and contain up to two-body pieces

$$\hat{H}(s) = E_0 + \sum_{pq} f_q^p \{ \hat{a}_q^p \}_{|\Phi\rangle} + \frac{1}{4} \sum_{pqrs} \Gamma_{rs}^{pq} \{ \hat{a}_{rs}^{pq} \}_{|\Phi\rangle}. \quad (\text{A.0.5})$$

As a consequence, we only have to consider those states in $|\bar{\psi}\rangle \in \overline{\mathcal{M}}$ that may be associated with 1p1h or 2p2h excitations w.r.t. any element $|\psi\rangle \in \mathcal{M}$. This is due to the fact that a two-body Hamiltonian cannot connect higher-order excitations. It is easy to verify that the following set \mathbb{E} contains all excitation operators \hat{E} that eventually have to be taken into account

$$\mathbb{E} = \left\{ \hat{a}_c^v, \hat{a}_q^c, \hat{a}_q^v, \hat{a}_{cc'}^{vv'}, \hat{a}_{cc'}^{vq}, \hat{a}_{cc'}^{qq'}, \hat{a}_{cv}^{v'v'}, \hat{a}_{cv}^{v'q}, \hat{a}_{cv}^{qq'}, \hat{a}_{vv'}^{qq'} \right\}. \quad (\text{A.0.6})$$

It contains all excitation operators that, once acting on an element $|\psi\rangle \in \mathcal{M}$, produce an element $|\bar{\psi}\rangle \in \overline{\mathcal{M}}$. The original decoupling condition given through eq. (A.0.4) can now be reformulated to

$$\langle \Phi | \hat{a}_{v_1 \dots v_{A_v}} \hat{H} \hat{E} \hat{a}^{v'_1 \dots v'_{A_v}} | \Phi \rangle \stackrel{!}{=} 0, \quad \forall \hat{E} \in \mathbb{E}, \forall v_1, \dots, v_{A_v} \in \mathbb{V}. \quad (\text{A.0.7})$$

Employing once more that we are dealing with a two-body Hamiltonian, we can even further simplify our decoupling condition to

$$\langle \Phi | \hat{a}_{v_1 v_2} \hat{H} \hat{E} \hat{a}^{v'_1 v'_2} | \Phi \rangle \stackrel{!}{=} 0, \quad \forall \hat{E} \in \mathbb{E}, \forall v_1, v_2 \in \mathbb{V}. \quad (\text{A.0.8})$$

As the core $|\Phi\rangle$ is a single Slater determinant we can employ the single-reference version of the generalized Wick's theorem for evaluating $\langle \Phi | \hat{a}_{v_1 \dots v_{A_v}} \hat{H} \hat{E} | \Phi \rangle$ yielding fully-contracted terms of $\hat{a}_{v_1 \dots v_{A_v}} \hat{H} \hat{E}$ only. We performed this rather tedious task programatically, where we evaluated

$$h^{\text{od}}(|\Phi^{v_1 v_2}\rangle, \hat{E}) \equiv \langle \Phi^{v_1 v_2} | \hat{H} \hat{E} | \Phi^{v_1 v_2} \rangle, \quad (\text{A.0.9})$$

$$\Delta(|\Phi^{v_1 v_2}\rangle, \hat{E}) \equiv \langle \Phi^{v_1 v_2} | \hat{H} | \Phi^{v_1 v_2} \rangle - \langle \Phi^{v_1 v_2} | \hat{E}^\dagger \hat{H} \hat{E} | \Phi^{v_1 v_2} \rangle, \quad (\text{A.0.10})$$

for all possible $\hat{E} \in \mathbb{E}$ and with the definition $|\Phi^{v_1 v_2}\rangle \equiv \hat{a}^{v_1 v_2} |\Phi\rangle$. Note that the evaluation of $h^{\text{od}}(|\Phi^{v_1 v_2}\rangle, \hat{E})$ sometimes yields not one single matrix elements but superpositions of several types of one and two-body matrix elements. In such cases, we are requiring each matrix element to vanish individually.

- *Class I:* single excitation from h-space into p-space

$$h^{\text{od}}(|\Phi^{v_1 v_2}\rangle, \hat{a}_c^p) = -\Gamma_{pv_1}^{v_1 c} - \Gamma_{pv_2}^{v_2 c} + f_p^c, \quad (\text{A.0.11})$$

$$\Delta(|\Phi^{v_1 v_2}\rangle, \hat{a}_c^p) = f_c^c - f_p^p. \quad (\text{A.0.12})$$

- *Class II:* single excitation from v-space into q-space

$$h^{\text{od}}(|\Phi^{v_1 v_2}\rangle, \hat{a}_q^v) = -\Gamma_{v_1 q}^{v_2 v_1} + f_q^{v_2}, \quad (\text{A.0.13})$$

$$\Delta(|\Phi^{v_1 v_2}\rangle, \hat{a}_q^v) = -f_q^q + f_{v_2}^{v_2}. \quad (\text{A.0.14})$$

- *Class III*: double excitation from v-space into q-space

$$h^{\text{od}}(|\Phi^{v_1 v_2}\rangle, \hat{a}_{v_1 v_2}^{q_1 q_2}) = \Gamma_{q_1 q_2}^{v_1 v_2}, \quad (\text{A.0.15})$$

$$\Delta(|\Phi^{v_1 v_2}\rangle, \hat{a}_{v_1 v_2}^{q_1 q_2}) = -f_{q_1}^{q_1} - f_{q_2}^{q_2} + f_{v_1}^{v_1} + f_{v_2}^{v_2}. \quad (\text{A.0.16})$$

- *Class IV*: double excitation from h-space into p-space

$$h^{\text{od}}(|\Phi^{v_1 v_2}\rangle, \hat{a}_{c_1 c_2}^{p_1 p_2}) = \Gamma_{p_1 p_2}^{c_1 c_2}, \quad (\text{A.0.17})$$

$$\Delta(|\Phi^{v_1 v_2}\rangle, \hat{a}_{c_1 c_2}^{p_1 p_2}) = f_{c_1}^{c_1} + f_{c_2}^{c_2} - f_{p_1}^{p_1} - f_{p_2}^{p_2}. \quad (\text{A.0.18})$$

- *Class V*: double excitation from h-space into p-space and v-space into p-space

$$h^{\text{od}}(|\Phi^{v_1 v_2}\rangle, \hat{a}_{c v_2}^{p_1 p_2}) = \Gamma_{p_1 p_2}^{v_2 c}, \quad (\text{A.0.19})$$

$$\Delta(|\Phi^{v_1 v_2}\rangle, \hat{a}_{c v_2}^{p_1 p_2}) = f_c^c + f_{v_2}^{v_2} - f_{p_1}^{p_1} - f_{p_2}^{p_2}. \quad (\text{A.0.20})$$

The generator matrix elements may now be constructed by applying definition 4.7.1. For example, a White generator matrix element belonging to the class V may be constructed through

$$\eta_{p_1 p_2}^{v_2 c_1} = \frac{\Gamma_{p_1 p_2}^{v_2 c_1}}{f_{c_1}^{c_1} + f_{v_2}^{v_2} - f_{p_1}^{p_1} - f_{p_2}^{p_2}}. \quad (\text{A.0.21})$$

We would like to remark that we did not include any two-body matrix elements within our expression for Δ , i.e., we were constructing a Møller-Plesset-like generator.

Applications and Limitations. In the recent past, effective valence-space interactions derived from the IM-SRG have been applied in the context of nuclear structure theory [TBS12; Bog+14; Str+16; Str+17]. However, all of these applications aim for the construction of a single-shell valence-space interaction such that, e.g, the valence space for a calculation of ^{18}O based on an ^{16}O core only consists of single-particle states within the sd -shell. In contrast, a multi-shell valence-space interaction would employ the $sdpf$ -shell as valence space, i.e, two major shells. It is a vital aspect of any ab initio methods to explore the impact of its inherent truncations schemes. In the context of the VSSM and effective valence-space interactions from the IM-SRG, one of the inherent truncations is governed by the size of the valence space and it is important to assess the impact of an increase of this valence space in both directions since the exact result is only recovered in the limit of a vanishing core and a vanishing excluded space.

In a collaborative effort we tried to generalize the construction of effective interactions to multi-shell valence-space interactions, where the numerical results of our studies and applications of the VSSM are presented in [Stu18, p. 76]. However, we found out that an increase of the valence space to two major shells is not possible and already at the level of the IM-SRG the evolution of the Hamiltonian is not stable and eventually we suffer from a substantial amount

of induced many-body contributions beyond the NO2B rank. This instability is manifesting itself via a massive increase of the off-diagonal matrix elements belonging to class V, which hints at effects of intruder states—a long-standing problem in the context of VSSM. While we tried many approaches to solve this problem, to this day it remains unsolved.

This deficiency contributes to our preference of the IM-NCSM, i.e., a multi-reference approach. In contrast to VSSM calculations based on interactions derived from the IM-SRG, the IM-NCSM allows for an investigation of the impact of the model space by varying N_{\max} and N_{\max}^{ref} , which gives us an estimate of the uncertainties of this method. Furthermore, the NO2B approximation within the IM-NCSM framework, which employs multi-reference normal ordering, might be preferable since the normal-ordering is performed w.r.t. a particular target nucleus—in contrast to the targeted normal ordering in the context of effective interactions for the VSSM [Str+17].

Details on the Implementation of the In-Medium SRG

The necessary steps that have to be taken for the consistent transformation of observables via the IM-SRG may be summarized as follows:

1. read matrix elements of operators w.r.t vacuum normal order and a specific single-particle basis;
2. read density matrices $\gamma^{[1]}$ and $\gamma^{[2]}$;
3. construct the natural orbitals from the one-body density matrix;
4. perform a representation change from vacuum to reference-state representation;
5. perform transformation into natural orbitals;
6. solve the ODE for $\hat{\Omega}(s)$ and transform observables subsequently via the BCH series;
7. solve the ODE for the Hamiltonian directly and eventually evolve observables simultaneously;
8. evaluate occurring commutators efficiently;
9. perform representation change from reference-state to vacuum representation;
10. save the matrix elements of the transformed operators to hard disk.

Throughout this chapter, we are going to briefly address the most important details of our implementation of the IM-SRG, i.e., some selected items of the previous enumeration will be addressed.

B.1. Spherical Equations for Representation Change

The equation for changing the representation from vacuum to reference-state representation and vice versa given in eqs. (3.4.3) to (3.4.5) and eqs. (3.4.7) to (3.4.9) are m -scheme equations, i.e., they explicitly resolve the projection quantum numbers. Similarly to the transformation of the m -scheme commutator equations to spherical equations in chapter 5, also the equations for the representation change may be transformed such that they are expressed in terms of reduced matrix elements only. Note that the derivation was performed by employing the graphical technique of angular momentum coupling as presented in section 5.4. We can write the two operators in vacuum and reference-state representation as

$$\hat{R}_M^L = \sum_{pq} (R_M^L)_q^p + \frac{1}{4} \sum_{pqrs} (R_M^L)_{rs}^{pq} , \quad (\text{B.1.1})$$

$$\hat{V}_M^L = \sum_{pq} (V_M^L)_q^p + \frac{1}{4} \sum_{pqrs} (V_M^L)_{rs}^{pq} , \quad (\text{B.1.2})$$

where we assumed that $L \neq 0$ and, therefore, the zero-body part naturally vanishes. The spherical matrix elements of \hat{R}_M^L may now be expressed in terms of spherical matrix elements of \hat{V}_M^L

$$(R^L)_q^p = (V^L)_q^p + \sum_r \Pi_{j_r} n_r (\overline{V}^L)_{(rr)0}^{(pq)L} , \quad (\text{B.1.3})$$

$$(R^L)_{(rs)J'}^{(pq)J} = (V^L)_{(rs)J'}^{(pq)J} . \quad (\text{B.1.4})$$

The inverse relations may be written as

$$(V^L)_q^p = (R^L)_q^p - \sum_r \Pi_{j_r} n_r (\overline{R}^L)_{(rr)0}^{(pq)L} , \quad (\text{B.1.5})$$

$$(V^L)_{(rs)J'}^{(pq)J} = (R^L)_{(rs)J'}^{(pq)J} . \quad (\text{B.1.6})$$

B.2. Numerical Solution of ODEs

ODE for Observables. The ODE system for the Hamiltonian \hat{H} can be schematically written as

$$\frac{d}{ds} \vec{h}(s) = \vec{F}_\lambda(\vec{h}(s), \vec{\eta}(s)) , \quad (\text{B.2.1})$$

where $\vec{h}(s)$ and $\vec{\eta}(s)$ denote the entirety of all matrix elements of the Hamiltonian and the generator, respectively. In practical applications this ODE system, which reaches dimensions of

up to 6×10^7 , is solved numerically by employing an ODE solver from the GNU scientific library (GSL) together with the explicit Runge-Kutta-Fehlberg (RKF45) algorithm. The stepsize h is adaptive, i.e., controlled dynamically such that at each ODE integration step it is ensured that the numerical error is below a certain error threshold, where an absolute error threshold of $\epsilon_{\text{abs}} = 1 \times 10^{-3}$ is used. The initial stepsize h —chosen in such a way that the numerical error during the first integration is not exceeding the threshold—is strongly depending on the specific generator and ranges from 1×10^{-6} to 1×10^{-1} . Generally, the ODE system is integrated until some kind of convergence criterion is fulfilled. Considering the single-reference IM-SRG as an example, such a convergence criterion may be constructed from second-order perturbation theory.

ODE for Magnus operator. Similarly to the ODE for observables, the ODE for the Magnus operator can be schematically written as

$$\frac{d}{ds} \vec{\Omega}(s) = \vec{\mathcal{F}}_{\lambda}(\vec{\Omega}(s), \vec{\eta}(s)). \quad (\text{B.2.2})$$

As $\hat{\Omega}(s)$ always corresponds to a unitary transformation, unitarity is always formally conserved and, eventually, this leads to the fact that we could even solve the ODE for $\hat{\Omega}(s)$ via a simple Euler method at a fixed stepsize leading to reduced computational memory requirements. However, for the solution of the ODE for $\hat{\Omega}(s)$ we are employing—similarly to the IM-SRG(2)—an ODE solver from GSL and the RKF45 algorithm with automatically adjusted stepsizes. Having specified a numerical error threshold, the automatic stepsize control readjusts the stepsize at each integration step of the ODE accordingly, where the absolute and relative errors are $\epsilon_{\text{abs}} = \epsilon_{\text{rel}} = 1 \times 10^{-3}$. We are choosing this approach as the memory requirement of this implementation of the Magnus expansions is not too high and may, therefore, benefit from the enhanced stepsize control. Note that the generator $\hat{\eta}(s)$ depends on $\hat{H}(s)$ such that $\hat{H}(s)$ has to be calculated at each integration step of the ODE for $\hat{\Omega}(s)$. For reducing the memory requirements of our implementation, we are applying the BCH series for the calculation of $\hat{H}(s)$ at each integration step. However, in future applications one might as well prefer to simultaneously evolve $\hat{H}(s)$ with $\hat{\Omega}(s)$ —implying an increase of memory requirements but also a decrease of computing time.

B.3. Commutator Equations and Matrix Products

The evaluation of the right-hand side of the ODE for observables as well as for the Magnus operator requires the repeated evaluation of commutators and, as a matter of fact, the evaluation of commutators is the computationally most expensive part. The evaluation of commutators is carried out through calculating the spherical commutator equations. However, instead of directly implementing the spherical commutator equations derived in chapter 5 via simple loops, we employ a computationally more efficient approach by expressing the right-hand side of these equations in terms of linear algebra operations, i.e., matrix-matrix and matrix-vector

products. This allows an implementation that relies on Basic Linear Algebra Subprograms (BLAS), which are highly optimized library functions [BLA17].

One-Body Matrix. Regarding the one-body part, there is no need to exploit additional symmetries since the computational effort is basically determined by terms involving the two-body part. As a consequence, we are usually employing the single-particle index set

$$\mathbb{B}_{1B} = \{ p \mid e_p \leq e_{\max} \} , \quad (\text{B.3.1})$$

for representing one-body operators as matrices.

Two-Body Matrices. Regarding two-body matrix elements, we construct sets of collective two-particle indices

$$\mathbb{B}_{2B}^{J\Pi M_T} \equiv \{ (p, q) \mid \Delta(j_p j_q J) \text{ and } (-)^{l_p+l_q} = \Pi \text{ and } m_{t_p} + m_{t_q} = M_T \} , \quad (\text{B.3.2})$$

such that each two-particle index contained in a particular index set $\mathbb{B}_{2B}^{J\Pi M_T}$ may be associated with a two-particle state that is coupled to a total angular momentum J , has parity P and isospin projection M_T .

Then, we may construct matrices $(\underline{X}_{J'\Pi'M'_T}^{J\Pi M_T})$ containing two-body matrix elements, where rows and columns of such a matrix refer to two-particle indices contained exclusively in $\mathbb{B}_{2B}^{J\Pi M_T}$ and $\mathbb{B}_{2B}^{J'\Pi'M'_T}$, respectively.

Due to the symmetry properties of the operator \hat{X} , there are certain restrictions on which two index sets $\mathbb{B}_{2B}^{J\Pi M_T}$ and $\mathbb{B}_{2B}^{J'\Pi'M'_T}$ lead to non-zero matrices. Assuming that the operator \hat{X} is a spherical tensor operator of rank L_X , has parity Π_X , and is a spherical tensor in isospin space of rank τ_X , these restrictions read

$$|J - J'| \leq L_X , \quad \Pi \Pi' = \Pi_X , \quad |M_T - M'_T| = \tau_X . \quad (\text{B.3.3})$$

As a consequence, there are only very specific non-zero matrices $\underline{X}_{J'\Pi'M'_T}^{J\Pi M_T}$ that have to be taken into account.

The advantage of such an approach becomes obvious by considering the expression

$$(\underline{C}^L)_{(34)J'}^{(12)J} = \sum_{pqJ''} (\underline{A}^0)_{(pq)J}^{(12)J} (\underline{B}^L)_{(34)J'}^{(pq)J} , \quad (\text{B.3.4})$$

which, assuming that all operators are iso-scalars and have positive parity, may be translated to

$$\underline{C}_{J'\Pi M_T}^{J\Pi M_T} = \underline{A}_{J\Pi M_T}^{J\Pi M_T} \cdot \underline{B}_{J'\Pi M_T}^{J\Pi M_T} , \quad (\text{B.3.5})$$

where the expression on the right-hand side refers to a matrix-matrix product. In fact, most of the terms that are occurring in the context of the commutator equations can be expressed in terms of such matrix-matrix products.

Note that Pandya-transformed matrix elements may also be represented as matrices, however, a slightly different definition of the collective two-particle index has to be employed in this case since, e.g., Pandya transformed matrix elements of iso-scalars conserve the *difference* of the single-particle isospin projection quantum numbers—instead of the sum.

For more information on the subject of an efficient implementation of the spherical IM-SRG equations see [Geb17], where the scalar multi-reference case is treated.

APPENDIX C.

Experimental Data

Ground-state energies are taken from [Wan+12; Wan+17] and charge radii are taken from [AM13]. For converting charge radii and point-proton radii into each other, eq. (6.9.11) may be employed. Electric quadrupole and magnetic dipole moments are taken from [Sto05]. Experimental $B(M1)$ transition strengths are taken from [Til+95; Fir15] Experimental $B(E2)$ transition strengths for various helium, carbon, oxygen, fluorine, and neon isotopes are taken from [Pri+16; TWC93; Til+95; Ram+87; Thi+00; Fir15; Fir07] Values for $B(E2)$ transitions are also listed in table C.1. In the literature, these transitions are sometimes given in Weisskopf units (W.u.) and have to be converted to SI units for our purposes (see [Suh07, p. 131]). If not contained within the aforementioned references, excitation energies are taken from [NND19].

| nucleus | ψ_i | ψ_f | $B(E2)$ [$e^2\text{fm}^4$] | nucleus | ψ_i | ψ_f | $B(E2)$ [$e^2\text{fm}^4$] |
|-------------------|-----------|-----------|------------------------------|--------------------|-----------|-----------|------------------------------|
| ${}^6\text{He}$ | 0_1^+ | 2_1^+ | 5.4(7) | ${}^{20}\text{Ne}$ | 2_1^+ | 0_1^+ | 65.46(322) |
| ${}^{12}\text{C}$ | 0_1^+ | 2_1^+ | 39.7(33) | ${}^{20}\text{Ne}$ | 4_1^+ | 2_1^+ | 70.94(644) |
| ${}^{17}\text{O}$ | $1/2_1^+$ | $5/2_1^+$ | 7.60(8) | ${}^{21}\text{Ne}$ | $5/2_1^+$ | $3/2_1^+$ | 83.63(688) |
| ${}^{18}\text{O}$ | 2_1^+ | 0_1^+ | 9.30(25) | ${}^{21}\text{Ne}$ | $7/2_1^+$ | $3/2_1^+$ | 32.00(275) |
| ${}^{18}\text{O}$ | 4_1^+ | 2_1^+ | 3.33(17) | ${}^{21}\text{Ne}$ | $7/2_1^+$ | $5/2_1^+$ | 37.85(1376) |
| ${}^{18}\text{O}$ | 2_2^+ | 0_1^+ | 3.64(56) | ${}^{22}\text{Ne}$ | 2_1^+ | 0_1^+ | 46.72(65) |
| ${}^{19}\text{O}$ | $1/2_1^+$ | $5/2_1^+$ | 1.75(36) | ${}^{22}\text{Ne}$ | 4_1^+ | 2_1^+ | 64.08(146) |
| ${}^{20}\text{O}$ | 0_1^+ | 2_1^+ | 28(2) | ${}^{23}\text{Ne}$ | $1/2_1^+$ | $5/2_1^+$ | 2.91(19) |
| ${}^{21}\text{O}$ | $1/2_1^+$ | $5/2_1^+$ | 0.71(7) | ${}^{24}\text{Ne}$ | 2_1^+ | 0_1^+ | 27.96(657) |
| ${}^{22}\text{O}$ | 0_1^+ | 2_1^+ | 21(8) | ${}^{26}\text{Ne}$ | 0_1^+ | 2_1^+ | 141(18) |
| ${}^{21}\text{F}$ | $1/2_1^+$ | $5/2_1^+$ | 54 | ${}^{28}\text{Ne}$ | 0_1^+ | 2_1^+ | 132(23) |

Table C.1.: Experimental $B(E2; \psi_i \rightarrow \psi_f)$ transition strengths for various helium, carbon, oxygen, fluorine, and neon isotopes.

Bibliography

- [AM13] I. Angeli and K. P. Marinova. “Table of experimental nuclear ground state charge radii: An update”. In: *Atomic Data and Nuclear Data Tables* 99 (2013), 69–95. DOI: 10.1016/j.adt.2011.12.006.
- [BNV13] B. R. Barrett, P. Navrátil, and J. P. Vary. “Ab initio no core shell model”. In: *Progress in Particle and Nuclear Physics* 69 (2013), 131–181. DOI: 10.1016/j.pnpnp.2012.10.003.
- [BS09] R. J. Bartlett and I. Shavitt. *Many-Body Methods in Chemistry and Physics: MBPT and Coupled Cluster Theory*. Cambridge University Press, 2009.
- [Bin+16] S. Binder, A. Calci, E. Epelbaum, et al. “Few-nucleon systems with state-of-the-art chiral nucleon-nucleon forces”. In: *Physical Review C* 93 (2016), 044002. DOI: 10.1103/PhysRevC.93.044002.
- [Bin+18] S. Binder, A. Calci, E. Epelbaum, et al. “Few-nucleon and many-nucleon systems with semilocal coordinate-space regularized chiral nucleon-nucleon forces”. In: *Physical Review C* 98 (2018), 014002. DOI: 10.1103/PhysRevC.98.014002.
- [Bin+13a] S. Binder, J. Langhammer, A. Calci, et al. “Ab initio calculations of medium-mass nuclei with explicit chiral 3N interactions”. In: *Physical Review C* 87 (2013), 021303(R). DOI: 10.1103/PhysRevC.87.021303.
- [Bin+14] S. Binder, J. Langhammer, A. Calci, et al. “Ab Initio Path to Heavy Nuclei”. In: *Physics Letters B* 736 (2014), 119–123.
- [Bin+13b] S. Binder, P. Piecuch, A. Calci, et al. “Extension of coupled-cluster theory with a noniterative treatment of connected triply excited clusters to three-body Hamiltonians”. In: *Physical Review C* 88 (2013), 054319. DOI: 10.1103/PhysRevC.88.054319.
- [Bla+09] S. Blanes, F. Casas, J. Oteo, et al. “The Magnus expansion and some of its applications”. In: *Physics Reports* 470 (2009), 151–238. DOI: 10.1016/j.physrep.2008.11.001.
- [BLA17] BLAS. *Basic Linear Algebra Subprograms*. <http://www.netlib.org/blas/>, 2017.
- [BFP07] S. K. Bogner, R. J. Furnstahl, and R. J. Perry. “Similarity renormalization group for nucleon-nucleon interactions”. In: *Physical Review C* 75 (2007), 061001. DOI: 10.1103/PhysRevC.75.061001.

- [BFS10] S. K. Bogner, R. J. Furnstahl, and A. Schwenk. “From low-momentum interactions to nuclear structure”. In: *Progress in Particle and Nuclear Physics* 65 (2010), 94–147. DOI: 10.1016/j.ppnp.2010.03.001.
- [Bog+14] S. K. Bogner, H. Hergert, J. D. Holt, et al. “Nonperturbative shell-model interactions from the in-medium similarity renormalization group”. In: *Physical Review Letters* 113 (2014), 142501. DOI: 10.1103/PhysRevLett.113.142501.
- [Bro01] B. Brown. “The nuclear shell model towards the drip lines”. In: *Progress in Particle and Nuclear Physics* 47 (2001), 517–599. DOI: 10.1016/S0146-6410(01)00159-4.
- [Car+15] J. Carlson, S. Gandolfi, F. Pederiva, et al. “Quantum Monte Carlo methods for nuclear physics”. In: *Reviews of Modern Physics* 87 (2015), 1067–1118. DOI: 10.1103/RevModPhys.87.1067.
- [Cau+05] E. Caurier, G. Martínez-Pinedo, F. Nowacki, et al. “The shell model as a unified view of nuclear structure”. In: *Reviews of Modern Physics* 77 (2005), 427–488. DOI: 10.1103/RevModPhys.77.427.
- [CBN13] A. Cipollone, C. Barbieri, and P. Navrátil. “Isotopic Chains Around Oxygen from Evolved Chiral Two- and Three-Nucleon Interactions”. In: *Physical Review Letters* 111 (2013), 062501. DOI: 10.1103/PhysRevLett.111.062501.
- [Cor+09] L. Coraggio, A. Covello, A. Gargano, et al. “Shell-model calculations and realistic effective interactions”. In: *Progress in Particle and Nuclear Physics* 62 (2009), 135–182. DOI: 10.1016/j.ppnp.2008.06.001.
- [Cor+14] L. Coraggio, A. Covello, A. Gargano, et al. “From Kuo–Brown to today’s realistic shell-model calculations”. In: *Nuclear Physics A* 928 (2014), 43–50. DOI: 10.1016/J.NUCLPHYSA.2014.03.018.
- [Eck30] C. Eckart. “The Application of Group theory to the Quantum Dynamics of Monatomic Systems”. In: *Reviews of Modern Physics* 2 (1930), 305–380. DOI: 10.1103/RevModPhys.2.305.
- [Eks+15] A. Ekström, G. R. Jansen, K. A. Wendt, et al. “Accurate nuclear radii and binding energies from a chiral interaction”. In: *Physical Review C* 91 (2015), 051301. DOI: 10.1103/PhysRevC.91.051301.
- [EM03] D. R. Entem and R. Machleidt. “Accurate charge-dependent nucleon-nucleon potential at fourth order of chiral perturbation theory”. In: *Physical Review C* 68 (2003), 041001. DOI: 10.1103/PhysRevC.68.041001.
- [EMN17] D. R. Entem, R. Machleidt, and Y. Nosyk. “High-quality two-nucleon potentials up to fifth order of the chiral expansion”. In: *Physical Review C* 96 (2017), 024004. DOI: 10.1103/PhysRevC.96.024004.
- [Epe+19] E. Epelbaum, J. Golak, K. Hebeler, et al. “Few- and many-nucleon systems with semilocal coordinate-space regularized chiral two- and three-body forces”. In: *Physical Review C* 99 (2019), 024313. DOI: 10.1103/PhysRevC.99.024313.

-
- [EKM15] E. Epelbaum, H. Krebs, and U.-G. Meißner. “Precision Nucleon-Nucleon Potential at Fifth Order in the Chiral Expansion”. In: *Physical Review Letters* 115 (2015), 122301. DOI: 10.1103/PhysRevLett.115.122301.
- [EM09] E. Epelbaum and U.-G. Meißner. “Modern theory of nuclear forces”. In: *Reviews of Modern Physics* 81 (2009), 1773–1825. DOI: 10.1103/RevModPhys.81.1773.
- [Fir07] R. Firestone. “Nuclear Data Sheets for $A = 23$ ”. In: *Nuclear Data Sheets* 108 (2007), 1–78. DOI: 10.1016/j.nds.2007.01.002.
- [Fir15] R. Firestone. “Nuclear Data Sheets for $A = 21$ ”. In: *Nuclear Data Sheets* 127 (2015), 1–68. DOI: 10.1016/j.nds.2015.07.001.
- [GQN19] D. Gazit, S. Quaglioni, and P. Navrátil. “Erratum: Three-Nucleon Low-Energy Constants from the Consistency of Interactions and Currents in Chiral Effective Field Theory”. In: *Physical Review Letters* 122 (2019), 029901. DOI: 10.1103/PhysRevLett.122.029901.
- [Geb17] E. Gebrerufael. “In-Medium No-Core Shell Model for Ab Initio Nuclear Structure Calculations”. PhD thesis. TU Darmstadt, 2017.
- [GCR16] E. Gebrerufael, A. Calci, and R. Roth. “Open-shell nuclei and excited states from multireference normal-ordered Hamiltonians”. In: *Physical Review C* 93 (2016), 031301. DOI: 10.1103/PhysRevC.93.031301.
- [Geb+16] E. Gebrerufael, K. Vobig, H. Hergert, et al. “Ab Initio Description of Open-Shell Nuclei: Merging No-Core Shell Model and In-Medium Similarity Renormalization Group”. In: *Physical Review Letters* 118 (2016), 152503. DOI: 10.1103/PhysRevLett.118.152503.
- [GL74] D. H. Gloeckner and R. D. Lawson. “Spurious center-of-mass motion”. In: *Physics Letters B* 53 (1974), 313–318. DOI: 10.1016/0370-2693(74)90390-6.
- [Hag+16] G. Hagen, M. Hjorth-Jensen, G. R. Jansen, et al. “Emergent properties of nuclei from ab initio coupled-cluster calculations”. In: *Physica Scripta* 91 (2016), 063006. DOI: 10.1088/0031-8949/91/6/063006.
- [Hag+07] G. Hagen, T. Papenbrock, D. J. Dean, et al. “Coupled-cluster theory for three-body Hamiltonians”. In: *Physical Review C* 76 (2007), 034302. DOI: 10.1103/PhysRevC.76.034302.
- [Hag+08] G. Hagen, T. Papenbrock, D. J. Dean, et al. “Medium-Mass Nuclei from Chiral Nucleon-Nucleon Interactions”. In: *Physical Review Letters* 101 (2008), 092502. DOI: 10.1103/PhysRevLett.101.092502.
- [Hag+14] G. Hagen, T. Papenbrock, M. Hjorth-Jensen, et al. “Coupled-cluster computations of atomic nuclei”. In: *Reports on Progress in Physics* 77 (2014), 96302. DOI: 10.1088/0034-4885/77/9/096302.
- [Heb12] K. Hebeler. “Momentum-space evolution of chiral three-nucleon forces”. In: *Physical Review C* 85 (2012), 021002. DOI: 10.1103/PhysRevC.85.021002.

- [Heb+15] K. Hebeler, H. Krebs, E. Epelbaum, et al. “Efficient calculation of chiral three-nucleon forces up to N³LO for ab initio studies”. In: *Physical Review C* 91 (2015), 044001. DOI: 10.1103/PhysRevC.91.044001.
- [Her17] H. Hergert. “In-medium similarity renormalization group for closed and open-shell nuclei”. In: *Physica Scripta* 92 (2017), 023002. DOI: 10.1088/1402-4896/92/2/023002.
- [Her+13a] H. Hergert, S. Binder, A. Calci, et al. “Ab Initio Calculations of Even Oxygen Isotopes with Chiral Two-Plus-Three-Nucleon Interactions”. In: *Physical Review Letters* 110 (2013), 242501. DOI: 10.1103/PhysRevLett.110.242501.
- [Her+13b] H. Hergert, S. K. Bogner, S. Binder, et al. “In-medium similarity renormalization group with chiral two- plus three-nucleon interactions”. In: *Physical Review C* 87 (2013), 034307. DOI: 10.1103/PhysRevC.87.034307.
- [Her+14] H. Hergert, S. K. Bogner, T. D. Morris, et al. “Ab initio multireference in-medium similarity renormalization group calculations of even calcium and nickel isotopes”. In: *Physical Review C* 90 (2014), 041302. DOI: 10.1103/PhysRevC.90.041302.
- [Her+16] H. Hergert, S. K. Bogner, T. D. Morris, et al. “The In-Medium Similarity Renormalization Group: A novel ab initio method for nuclei”. In: *Physics Reports* 621 (2016), 165–222. DOI: 10.1016/j.physrep.2015.12.007.
- [HR09] H. Hergert and R. Roth. “Treatment of the intrinsic Hamiltonian in particle-number nonconserving theories”. In: *Physics Letters B* 682 (2009), 27–32. DOI: 10.1016/j.physletb.2009.10.100.
- [Jan+16] G. R. Jansen, M. D. Schuster, A. Signoracci, et al. “Open sd-shell nuclei from first principles”. In: *Physical Review C* 94 (2016), 011301. DOI: 10.1103/PhysRevC.94.011301.
- [JNF09] E. D. Jurgenson, P. Navrátil, and R. J. Furnstahl. “Evolution of Nuclear Many-Body Forces with the Similarity Renormalization Group”. In: *Physical Review Letters* 103 (2009), 082501. DOI: 10.1103/PhysRevLett.103.082501.
- [KNM10] L. Kong, M. Nooijen, and D. Mukherjee. “An algebraic proof of generalized Wick theorem”. In: *The Journal of Chemical Physics* 132 (2010), 234107. DOI: 10.1063/1.3439395.
- [KB66] T. Kuo and G. Brown. “Structure of finite nuclei and the free nucleon-nucleon interaction: An application to ¹⁸O and ¹⁸F”. In: *Nuclear Physics* 85 (1966), 40–86. DOI: 10.1016/0029-5582(66)90131-3.
- [Kuo+81] T. Kuo, J. Shurpin, K. Tam, et al. “A simple method for evaluating Goldstone diagrams in an angular momentum coupled representation”. In: *Annals of Physics* 132 (1981), 237–276. DOI: 10.1016/0003-4916(81)90068-3.
- [KM97] W. Kutzelnigg and D. Mukherjee. “Normal order and extended Wick theorem for a multiconfiguration reference wave function”. In: *The Journal of Chemical Physics* 107 (1997), 432–449. DOI: 10.1063/1.474405.

-
- [KM04] W. Kutzelnigg and D. Mukherjee. “Irreducible Brillouin conditions and contracted Schrödinger equations for n-electron systems. IV. Perturbative analysis”. In: *The Journal of Chemical Physics* 120 (2004), 7350–7368. DOI: 10.1063/1.1652490.
- [Lu+13] Z. T. Lu, P. Mueller, G. W. Drake, et al. “Colloquium: Laser probing of neutron-rich nuclei in light atoms”. In: *Reviews of Modern Physics* 85 (2013), 1383–1400. DOI: 10.1103/RevModPhys.85.1383.
- [Mac01] R. Machleidt. “High-precision, charge-dependent Bonn nucleon-nucleon potential”. In: *Physical Review C* 63 (2001), 24001. DOI: 10.1103/PhysRevC.63.024001.
- [ME11] R. Machleidt and D. R. Entem. “Chiral effective field theory and nuclear forces”. In: *Physics Reports* 503 (2011), 1–75. DOI: 10.1016/j.physrep.2011.02.001.
- [Mag54] W. Magnus. “On the exponential solution of differential equations for a linear operator”. In: *Communications on Pure and Applied Mathematics* 7 (1954), 649–673. DOI: 10.1002/cpa.3160070404.
- [Mar+18] L. E. Marcucci, A. Kievsky, S. Rosati, et al. “Erratum: Chiral Effective Field Theory Predictions for Muon Capture on Deuteron and 3-He”. In: *Physical Review Letters* 121 (2018), 049901. DOI: 10.1103/PhysRevLett.121.049901.
- [MVS09] P. Maris, J. P. Vary, and A. M. Shirokov. “Ab initio no-core full configuration calculations of light nuclei”. In: *Physical Review C* 79 (2009), 014308. DOI: 10.1103/PhysRevC.79.014308.
- [MPB15] T. D. Morris, N. M. Parzuchowski, and S. K. Bogner. “Magnus expansion and in-medium similarity renormalization group”. In: *Physical Review C* 92 (2015), 034331. DOI: 10.1103/PhysRevC.92.034331.
- [Nav+07] P. Navrátil, V. G. Gueorguiev, J. P. Vary, et al. “Structure of A=10-13 Nuclei with Two- Plus Three-Nucleon Interactions from Chiral Effective Field Theory”. In: *Physical Review Letters* 99 (2007), 042501. DOI: 10.1103/PhysRevLett.99.042501.
- [Nav07] P. Navrátil. “Local three-nucleon interaction from chiral effective field theory”. In: *Few-Body Systems* 41 (2007), 117–140. DOI: 10.1007/s00601-007-0193-3.
- [NO03] P. Navrátil and W. E. Ormand. “Ab initio shell model with a genuine three-nucleon force for the p-shell nuclei”. In: *Physical Review C* 68 (2003), 034305. DOI: 10.1103/PhysRevC.68.034305.
- [Nav+09] P. Navrátil, S. Quaglioni, I. Stetcu, et al. “Recent developments in no-core shell-model calculations”. In: *Journal of Physics G: Nuclear and Particle Physics* 36 (2009), 083101. DOI: 10.1088/0954-3899/36/8/083101.
- [NND19] NNDC. *ENSDF* (<https://www.nndc.bnl.gov/>). 2019.
- [Par+17] N. M. Parzuchowski, S. R. Stroberg, P. Navrátil, et al. “Ab initio electromagnetic observables with the in-medium similarity renormalization group”. In: *Physical Review C* 96 (2017), 034324. DOI: 10.1103/PhysRevC.96.034324.
-

- [PR08] S. Perez-Martin and L. M. Robledo. “Microscopic justification of the equal filling approximation”. In: *Physical Review C* 78 (2008), 014304. DOI: 10.1103/PhysRevC.78.014304.
- [Pri+16] B. Pritychenko, M. Birch, B. Singh, et al. “Tables of E2 transition probabilities from the first 2+ states in even – even nuclei”. In: *Atomic Data and Nuclear Data Tables* 107 (2016), 1–139. DOI: 10.1016/j.adt.2015.10.001.
- [Qua+18] S. Quaglioni, C. Romero-Redondo, P. Navrátil, et al. “Three-cluster dynamics within the ab initio no-core shell model with continuum: How many-body correlations and α clustering shape He 6”. In: *Physical Review C* 97 (2018), 034332. DOI: 10.1103/PhysRevC.97.034332.
- [Ram+87] S. Raman, C. Malarkey, W. Milner, et al. “Transition probability, $B(E2)_{\uparrow}$, from the ground to the first-excited 2+ state of even-even nuclides”. In: *Atomic Data and Nuclear Data Tables* 36 (1987), 1–96. DOI: 10.1016/0092-640X(87)90016-7.
- [RS80] P. Ring and P. Schuck. *The Nuclear Many-Body Problem*. Springer, 1980.
- [RN07] R. Roth and P. Navrátil. “Ab Initio Study of 40Ca with an Importance Truncated No-Core Shell Model”. In: *Physical Review Letters* 99 (2007), 071302. DOI: 10.1103/PhysRevLett.99.071302.
- [Rot09] R. Roth. “Importance Truncation for Large-Scale Configuration Interaction Approaches”. In: *Physical Review C* 79 (2009), 064324. DOI: 10.1103/PhysRevC.79.064324.
- [Rot+12] R. Roth, S. Binder, K. Vobig, et al. “Medium-Mass Nuclei with Normal-Ordered Chiral NN+3N Interactions”. In: *Physical Review Letters* 109 (2012), 052501. DOI: 10.1103/PhysRevLett.109.052501.
- [Rot+14] R. Roth, A. Calci, J. Langhammer, et al. “Evolved chiral NN+3N Hamiltonians for ab initio nuclear structure calculations”. In: *Physical Review C - Nuclear Physics* 90 (2014), 024325. DOI: 10.1103/PhysRevC.90.024325.
- [RGP09] R. Roth, J. R. Gour, and P. Piecuch. “Center-of-mass problem in truncated configuration interaction and coupled-cluster calculations”. In: *Physics Letters B* 679 (2009), 334–339. DOI: 10.1016/J.PHYSLETB.2009.07.071.
- [Rot+11] R. Roth, J. Langhammer, A. Calci, et al. “Similarity-Transformed Chiral NN+3N Interactions for the Ab Initio Description of 12-C and 16-O.” In: *Physical Review Letters* 107 (2011), 072501. DOI: 10.1103/PhysRevLett.107.072501.
- [RNF10] R. Roth, T. Neff, and H. Feldmeier. “Nuclear structure in the framework of the unitary correlation operator method”. In: *Progress in Particle and Nuclear Physics* 65 (2010), 50–93. DOI: 10.1016/j.pnpnp.2010.02.003.
- [RRH08] R. Roth, S. Reinhardt, and H. Hergert. “Unitary correlation operator method and similarity renormalization group: Connections and differences”. In: *Physical Review C - Nuclear Physics* 77 (2008), 064003. DOI: 10.1103/PhysRevC.77.064003.

-
- [Sch+14] M. D. Schuster, S. Quaglioni, C. W. Johnson, et al. “Operator evolution for ab initio theory of light nuclei”. In: *Physical Review C* 90 (2014), 011301. DOI: 10.1103/PhysRevC.90.011301.
- [Sch+15] M. D. Schuster, S. Quaglioni, C. W. Johnson, et al. “Operator evolution for ab initio electric dipole transitions of He 4”. In: *Physical Review C* 92 (2015), 014320. DOI: 10.1103/PhysRevC.92.014320.
- [Som+14] V. Somà, A. Cipollone, C. Barbieri, et al. “Chiral two- and three-nucleon forces along medium-mass isotope chains”. In: *Physical Review C* 89 (2014), 061301. DOI: 10.1103/PhysRevC.89.061301.
- [Sto05] N. Stone. “Table of nuclear magnetic dipole and electric quadrupole moments”. In: *Atomic Data and Nuclear Data Tables* 90 (2005), 75–176. DOI: 10.1016/j.adt.2005.04.001.
- [Str+17] S. R. Stroberg, A. Calci, H. Hergert, et al. “Nucleus-Dependent Valence-Space Approach to Nuclear Structure”. In: *Physical Review Letters* 118 (2017), 032502. DOI: 10.1103/PhysRevLett.118.032502.
- [Str+16] S. R. Stroberg, H. Hergert, J. D. Holt, et al. “Ground and excited states of doubly open-shell nuclei from ab initio valence-space Hamiltonians”. In: *Physical Review C* 93 (2016), 051301. DOI: 10.1103/PhysRevC.93.051301.
- [Stu18] C. Stumpf. “Nuclear Spectra and Strength Distributions from Importance-Truncated Configuration-Interaction Methods”. PhD thesis. 2018.
- [Suh07] J. Suhonen. *From Nucleons to Nucleus*. 2007. DOI: 10.1007/978-3-540-48861-3.
- [SO96] A. Szabo and N. S. Ostlund. *Modern Quantum Chemistry: Introduction to Advanced Electronic Structure Theory*. Dover, 1996, p. 466.
- [Thi+00] P. Thirolf, B. Pritychenko, B. Brown, et al. “Spectroscopy of the 21+ state in 22O and shell structure near the neutron drip line”. In: *Physics Letters B* 485 (2000), 16–22. DOI: 10.1016/S0370-2693(00)00720-6.
- [Tic+18] A. Tichai, E. Gebrerufael, K. Vobig, et al. “Open-shell nuclei from No-Core Shell Model with perturbative improvement”. In: *Physics Letters B* 786 (2018), 448–452. DOI: 10.1016/j.physletb.2018.10.029.
- [Tic+19] A. Tichai, J. Müller, K. Vobig, et al. “Natural orbitals for ab initio no-core shell model calculations”. In: *Physical Review C* 99 (2019), 034321. DOI: 10.1103/PhysRevC.99.034321.
- [TWC93] D. Tilley, H. Weller, and C. Cheves. “Energy levels of light nuclei A = 16–17”. In: *Nuclear Physics A* 564 (1993), 1–183. DOI: 10.1016/0375-9474(93)90073-7.
- [Til+95] D. Tilley, H. Weller, C. Cheves, et al. “Energy levels of light nuclei A = 18–19”. In: *Nuclear Physics A* 595 (1995), 1–170. DOI: 10.1016/0375-9474(95)00338-1.
- [TBS11] K. Tsukiyama, S. K. Bogner, and A. Schwenk. “In-Medium Similarity Renormalization Group For Nuclei”. In: *Physical Review Letters* 106 (2011), 222502. DOI: 10.1103/PhysRevLett.106.222502.
-

- [TBS12] K. Tsukiyama, S. K. Bogner, and A. Schwenk. “In-medium similarity renormalization group for open-shell nuclei”. In: *Physical Review C* 85 (2012), 061304. DOI: 10.1103/PhysRevC.85.061304.
- [VMK88] D. A. Varshalovich, A. N. Moskalev, and V. K. Khersonskii. *Quantum Theory of Angular Momentum*. World Scientific Publishing, 1988.
- [Vob14] K. Vobig. “In-Medium Similarity Renormalization Group with Chiral NN + 3N Interactions”. PhD thesis. 2014.
- [Wan+12] M. Wang, G. Audi, A. H. Wapstra, et al. “The Ame2012 atomic mass evaluation”. In: *Chinese Physics C* 36 (2012), 1603–2014. DOI: 10.1088/1674-1137/36/12/003.
- [Wan+17] M. Wang, G. Audi, F. G. Kondev, et al. “The AME2016 atomic mass evaluation (II). Tables, graphs and references”. In: *Chinese Physics C* 41 (2017), 030003. DOI: 10.1088/1674-1137/41/3/030003.
- [Weg94] F. Wegner. “Flow-equations for Hamiltonians”. In: *Annalen der Physik* 3 (1994), 77–91.
- [Weg00] F. Wegner. “Flow equations for Hamiltonians”. In: *Nuclear Physics B (Proc. Suppl.)* 90 (2000), 141–146.
- [Wei79] S. Weinberg. “Phenomenological Lagrangians”. In: *Physica A: Statistical Mechanics and its Applications* 96 (1979), 327–340. DOI: 10.1016/0378-4371(79)90223-1.
- [Wei90] S. Weinberg. “Nuclear forces from chiral lagrangians”. In: *Physics Letters B* 251 (1990), 288–292. DOI: 10.1016/0370-2693(90)90938-3.
- [Whi02] S. R. White. “Numerical canonical transformation approach to quantum many-body problems”. In: *The Journal of Chemical Physics* 117 (2002), 7472. DOI: 10.1063/1.1508370.
- [Wig31] E. Wigner. *Gruppentheorie und ihre Anwendung auf die Quantenmechanik der Atomspektren*. Wiesbaden: Vieweg+Teubner Verlag, 1931. DOI: 10.1007/978-3-663-02555-9.
- [WSS95] R. B. Wiringa, V. Stoks, and R. Schiavilla. “Accurate nucleon-nucleon potential with charge-independence breaking”. In: *Physical Review C* 51 (1995), 38–51. DOI: 10.1103/PhysRevC.51.38.
- [Wło+05] M. Włoch, D. J. Dean, J. R. Gour, et al. “Ab-Initio Coupled-Cluster Study of O 16”. In: *Physical Review Letters* 94 (2005), 212501. DOI: 10.1103/PhysRevLett.94.212501.

Danksagung

Es gibt einige Menschen, welche mich während meiner Promotion und der Anfertigung dieser Arbeit unterstützt haben und denen ich hier ausdrücklich danken möchte.

Meinem Doktorvater Prof. Robert Roth möchte ich dafür danken, dass er es mir ermöglicht hat unter seiner Leitung diese Arbeit anzufertigen und dieses spannende Thema zu bearbeiten. Außerdem danke ich ihm für seine hilfreichen Ratschläge, sein jederzeit offenes Ohr und das Schaffen einer sehr angenehmen Arbeitsatmosphäre.

Prof. Achim Schwenk danke ich für das übernehmen des Zweitgutachtens.

Ein großer Dank geht an meine Arbeitsgruppe für die hilfreichen Diskussionen und die Wohlfühlatmosphäre in der Uni, wobei ich insbesondere Christina Stumpf, Roland Wirth, Alexander Tichai, Julius Müller, Laura Mertes, Stefan Schulz, Richard Trippel, Tobias Wolfgruber, Thomas Hüther, Stefan Alexa, Marco Knöll, Eskendr Gebrerufael und Tobias Mongelli danken möchte. Auch an die gemeinsame Zeit, die wir außerhalb der Uni zusammen verbracht haben – zum Beispiel während Kurzurlauben nach einer Konferenz oder Spieleabenden – werde ich mich gerne erinnern.

Besonders danken möchte ich Roland Wirth, ohne dessen Hilfe ich wahrscheinlich immer noch an dem ein oder anderen Problem physikalischer oder IT-technischer Natur sitzen würde. Außerdem danke ich natürlich all denen, die einen Teil meiner Arbeit gelesen haben und so zum Gelingen dieser Arbeit beigetragen haben.

Bei meinen Eltern Ute und Erich Vobig möchte ich mich für ihre Unterstützung während meines Studiums und meiner Promotion bedanken, und dass sie sonst auch jederzeit hinter mir stehen.

Bei meiner Freundin Helge Schaller möchte ich mich dafür bedanken, dass sie für mich da ist, mich zum Lachen bringt, mir oft einen anderen Blickwinkel eröffnet und mich gerade in der Endphase dieser Arbeit unterstützt hat sowie Geduld und Verständnis hatte.

Werdegang

Zur Person

| | |
|--------------|-------------------|
| Name | Klaus Vobig |
| Geburtsdatum | 17.02.1987 |
| Geburtsort | Erlenbach am Main |
| Nationalität | Deutsch |

Bildungsweg

| | |
|-----------|---|
| 1993-1997 | Grundschule , Klein-Welzheim |
| 1997-2006 | Gymnasium , Einharschule, Seligenstadt |
| 2007-2011 | Bachelorstudium Physik , TU Darmstadt |
| 2011-2014 | Masterstudium Physik , TU Darmstadt |
| 2014-2019 | Promotionstudium Physik , TU Darmstadt |

Publikationen

- R. Roth, S. Binder, K. Vobig, et al., Phys. Rev. Lett. 109, 052501 (2012).
- E. Gebrerufael, K. Vobig, H. Hergert, et al., Phys. Rev. Lett. 118, 152503 (2016).
- S. Binder, A. Calci, E. Epelbaum, Phys. Rev. C 98, 014002 (2018).
- A. Tichai, E. Gebrerufael, K. Vobig, et al., Phys. Lett. B 786, 448 (2018).
- E. Epelbaum, J. Golak, K. Hebeler, et al., Phys. Rev. C 99, 024313 (2019).
- A. Tichai, J. Müller, K. Vobig, et al., Phys. Rev. C 99, 034321 (2019).

Erklärung gemäß §9 Promotionsordnung

Hiermit versichere ich, dass ich die vorliegende Dissertation selbstständig angefertigt und keine anderen als die angegebenen Quellen und Hilfsmittel verwendet habe. Alle wörtlichen und paraphrasierten Zitate wurden angemessen kenntlich gemacht. Die Arbeit hat bisher noch nicht zu Prüfungszwecken gedient.

Datum

Ort

(Klaus Vobig)

